Doctoral Thesis

Control of Proton Exchange Membrane Fuel Cell System

Candidate:
Mohamed Derbeli

Director:
Prof. Oscar Barambones

Academic Year 2021-2022

Doctoral Thesis

Control of Proton Exchange Membrane Fuel Cell System

In partial fulfilment of the requirements for the degree of doctor of philosophy in control engineering, automation and robotics

Candidate:
Mohamed Derbeli

Director:
Prof. Oscar Barambones

Academic Year 2021-2022

Universidad del Paìs Vasco
Department of Automatic Control and System Engineering
Engineering School of Vitoria-Gasteiz
Barrio Sarriena, s/n, 48940 Leioa, Biscay, Spain

To my whole Family
To those whom i love & those who love me
I dedicate this work.

Acknowledgments

I would like to thank all my collaborators and colleagues for creating a friendly environment, giving me useful advices, and for their continued support.

I am deeply thankful to my supervisor Professor *Oscar Barambones* for accepting me to enrol a doctorate at the Advanced Control Group Lab of the Universidad del Paìs Vasco, Spain, and for his permission to use all the electrical devices and systems available on his lab. I am also grateful to him for his invaluable guidance and excellent follow-ups, spirited discussions and consistent encouragements, as well as for sharing his deep insights and clear thinking with me during our numerous discussions.

I am grateful to *Dr. Amira Zrelli* and *Dr. Aicha Abid* for reviewing my thesis report.

I am also grateful to *Josean Ramos*, *Maissa Farhat*, *Dhia Chariag*, and *Lassaad Sbita* for their valuable help and support during my Ph.D.

I thank all who in one way or another contributed in the completion of this thesis.

Finally, I owe my deepest gratitude to my dearest *Family* who inspired me all the time. My thesis work might not have been fulfilled without their consistent encouragement and of course their immense love.

Vitoria-Gasteiz, March 2022

Mohamed Derbeli

Resumen

El calentamiento global es el resultado del efecto invernadero causado por el aumento de la concentración de CO_2 en la atmósfera, lo que resulta en desastres que afectan a la población. Se cree que este efecto ha generado fenómenos meteorológicos como el conocido "El Niño", que perturba la región del Pacífico Sur y causa desastres naturales como inundaciones, tornados y sequía. Además, la desaparición del hielo polar es también es uno de los principales resultados del calentamiento global, por lo que conduce a aumentos del nivel del mar, lo que puede causar inundaciones en las regiones costeras.

Las energías limpias, tanto solar y eólica, se consideran una forma importante de superar estos problemas al reducir las emisiones de CO_2. Sin embargo, estas energías dependen de las condiciones climáticas. Por ejemplo, la energía solar solo está disponible cuando el sol brilla y el viento cuando tiende a soplar de forma intermitente. Además, el almacenamiento del exceso de energía producido durante la época de buenas condiciones climáticas es una tarea costosa y complicada.

Una tecnología que puede basarse en fuentes sostenibles es la pila de combustible. Las pilas de combustible podrían ser una alternativa ideal de energía limpia renovable. Estos son dispositivos que convierten directamente la energía química, almacenada en algunos combustibles, en energía eléctrica y calor. Esto implica que pueden proporcionar electricidad en todos los climas, siempre que haya combustible disponible. Por esto, han atraído la atención mundial en las últimas décadas. Las celdas de combustible generalmente se clasifican en cinco categorías diferentes según su temperatura de funcionamiento o el tipo de química de sus electrolitos: celda de combustible de carbonato fundido (MCFC), celda de combustible de óxido sólido (SOFC), celda de combustible alcalina (AFC), celda de combustible de membrana de intercambio de protones. (PEMFC), pila de combustible de ácido fosfórico (PAFC) y pila de combustible de metanol directo (DMFC).

El combustible preferido en muchas pilas de combustible es el hidrógeno, ya que es una fuente de energía renovable. Por lo tanto, las celdas de combustible de membrana de intercambio de protones (PEMFC), que tienen hidrógeno como combustible, se consideran uno de los dispositivos de conversión de energía más confiables y prometedores. Pueden proporcionar un suministro de energía continuo durante de forma ininterrumpida, siempre que se le proporcione hidrógeno. Además, a diferencia de los motores de combustión interna, en las PEMFC no se realiza ningún tipo de combustión, sino que la energía se produce a través de una reacción química. Esto se traduce en varios beneficios, como alta eficiencia (hasta más del 50 %), cero emisiones

de gases, baja temperatura de funcionamiento (20-100 °C), bajo mantenimiento y funcionamiento silencioso. Así, por la misma cantidad de combustible, las pilas de combustible pueden extraer un 90 % más de energía que la gasolina tradicional. Las celdas de combustible también tienen un mantenimiento muy simple ya que no tienen partes móviles en su construcción. Además, la ausencia de partes mecánicas en su composición les permite operar en silencio. Las PEMFC tienen muchas ventajas no solo en comparación con los combustibles fósiles tradicionales, sino incluso en comparación con otros tipos de celdas. Se caracterizan por su baja temperatura de operación, rápida reacción electroquímica (arranque rápido), larga vida útil, que es un punto muy importante, y su alta densidad de potencia. Por lo tanto, son ampliamente conocidas como la fuente de energía más confiable y prometedora. Este tipo de pilas de combustible, se han desarrollado y utilizado en muchos campos, como fuentes de energía de respaldo, fuentes de energía portátiles, sistemas de energía híbridos, sistemas de generación distribuida, microredes, automóviles urbanos, autobuses, tranvías, locomotoras y aviones.

Una PEMFC se compone de una capa catalizadora, una capa de difusiva de gas y una membrana de electrolito. Cada uno de estos componentes se fabrica individualmente y luego se unen entre sí a altas presiones y temperaturas. La capa catalizadora y la capa difusiva de gas se colocan en los lados del ánodo y el cátodo. La membrana electrolítica permite que solo los iones apropiados (protones) migren hacia el cátodo. El PEMFC se alimenta de hidrógeno (H_2) y oxígeno (O_2) presurizados como combustible y genera electricidad, agua y calor. Los átomos de hidrógeno (H_2) entran en la PEMFC por el lado del ánodo, donde la capa catalizadora divide en protones (H^+) y electrones (e^-). Los protones fluyen hacia el cátodo a través de la membrana electrolítica, mientras que los electrones van por el circuito externo para proporcionar energía eléctrica a lo largo del camino. Los átomos de oxígeno (O_2) entran en la PEMFC por el lado del cátodo y reaccionan con los electrones que regresan del circuito externo y con los protones que han viajado a través de la membrana para producir agua y calor.

Los modelos PEMFC se dividen en “mecanismos operativos” y de “datos experimentales”. En cuanto a la primera categoría mencionada, en función del régimen, estos se dividen en estáticos y dinámicos. Hay tres modelos bien conocidos que se utilizan en el análisis estático, como el modelo de Amphlett, el modelo de Larminie y Dicks y el modelo de Chamberlin-Kim. Estos tres enfoques tuvieron diferentes resultados donde Amphlett produjo los resultados más precisos con una implementación de alta complejidad como desventaja (la misma desventaja para Larmini-Dicks). Por el contrario, Chamberlin-Kim mostró ser el más simple pero con baja precisión. En otros términos, los modelos dinámicos se utilizan en regímenes no transitorios donde el efecto de doble capa encabeza esta condición. A menudo, este fenómeno se modela con un capacitor eléctrico que depende de los electrodos y las características individuales de la pila. Por otro lado, los métodos experimentales comprenden mecanismos como identificación difusa. Sin embargo, una de las principales desventajas de esta

estrategia es el requisito computacional cuando se aumentan la complejidad y, por lo tanto, se expanden las reglas. Otro enfoque diferente que se utilizó es la máquina de vectores de soporte (SVM) basada en datos para el diagnóstico de fallas en PEMFC. A pesar de la alta precisión, algunas desventajas están relacionadas con la dinámica de período corto donde ciertos cambios no se pueden mostrar en el modelo propuesto. Además, en ciertos casos, SVM requiere altos recursos computacionales de acuerdo a la precisión del modelo a entrenar. A pesar de las desventajas de las estrategias mencionadas, otro enfoque es el uso de herramientas como las redes neuronales artificiales (ANN). Este esquema algorítmico se basa en un origen biológico de las neuronas del cerebro humano que tienen la capacidad de reconocer, adquirir información y autoajustarse de acuerdo con acciones pasadas (esto también se conoce como neuroplasticidad). Por lo tanto, en esta tesis, se llevó a cabo una investigación en profundidad con un PEMFC comercial para generar una amplia variedad de ANN con el objetivo de encontrar una configuración adecuada que pueda modelizar el comportamiento del PEMFC real. Después de encontrar una configuración ANN adecuada, esta se utilizó como planta para el proceso de control.

En muchas aplicaciones, la PEMFC generalmente se combina con un convertidor electrónico de potencia CC-CC que proporciona una conversión de energía eficiente a la carga y también ofrece un voltaje de salida altamente regulado. Este equipo, que podría ser un convertidor de conmutación inductivo o un convertidor de condensador conmutado, es un circuito de etapa de adaptación que se inserta entre la carga y la pila PEMFC. Muchos tipos de convertidores se han diseñado durante los últimos años, el más simple es el convertidor reductor, que disminuye el voltaje de entrada a salida, y el convertidor elevador, que lo aumenta, otros tipos son los convertidores reductor-elevador y Cuk. Estos convertidores proporcionan un voltaje de salida de CC controlado con la técnica de conmutación PWM de modulación de ancho de pulso. Las ventajas y desventajas de cada topología se basan en el recuento de sus componentes. Por lo tanto, debido a su mayor eficiencia y menos componentes en comparación con las topologías de otros convertidores, es posible que se apliquen convertidores de CC-CC elevadores para interconectar el PEMFC con la carga. Este último ha sido catalogado como uno de los convertidores más sencillos que se han utilizado. Este convertidor tiene la capacidad de aumentar un voltaje de entrada más bajo a un voltaje de salida más alto a través de una técnica de conmutación de modulación de ancho de pulso (PWM) controlada. Por lo tanto, se necesita un lazo de control para obtener un voltaje de CC de salida aplicable. Además, dado que la celda de combustible está muy influenciada por la carga y las variaciones de sus insumos (temperatura, oxígeno e hidrógeno), se desea la aplicación del controlador para mantener la PEMFC operando en un punto de potencia adecuado.

En esta tesis se han diseñado muchas técnicas de control y algoritmos para tener una conversión de energía eficiente de las PEMFC al enlace de CC (o carga). Los controladores lineales pueden ser una opción inicial adecuada para controlar un convertidor CC-CC. Por lo tanto, se ha implementado un primer enfoque típico y

clásico mediante un control proporcional-integral-derivativo (PID). El diseño del controlador lineal se basa en el modelo de convertidor linealizado alrededor de un punto de operación. La estrategia de ajuste de Ziegler-Nichols se ha utilizado en entornos de simulación, mientras que diferentes estrategias como el error cuadrático medio (MSE), el error absoluto medio (MAE), el error cuadrático medio (RMSE), el error cuadrático medio relativo (RRMSE) se han utilizado en las validaciones experimentales. Sin embargo, debido a la no linealidad del sistema, con estas estrategías de control es difícil compensar la variación de los parámetros del sistema, debido a la influencia de la dinámica no lineal en el punto de operación del convertidor. Además, los transitorios que generan grandes variaciones de la señal, como en el arranque o frente a cambios en la carga, no pueden tratarse con estas técnicas. Por lo tanto, las aplicaciones de técnicas de control lineal para el control de estos convertidores no son efectivas cuando el sistema está experimentando grandes cambios de parámetros de modelo y variaciones de carga.

El diseño de una estrategia no lineal puede mejorar la eficacia, especialmente cuando se integra un controlador en tiempo real. Por lo tanto, en esta tesis se han propuesto muchas estrategias no lineales diferentes. Controladores de modo deslizante robustos como control de deslizante convencional (CSMC), control deslizante integral proporcional (ISMC), control deslizante terminal integral (ITSMC), control de modo deslizante de terminal rápido integral (IFTSMC) y SMC integral terminal rápido combinado con ley de alcance rápido (IFTSMC-QRL), se utilizaron para mejorar el rendimiento del seguimiento del sistema de pila de combustible. Estos algoritmos se implementaron y contrastaron como diseños novedosos para resaltar las características que podrían definir la efectividad de cada uno en diferentes escenarios, como el seguimiento de cambios constantes y dinámicos. Se utilizó un equipo de prueba ensamblado con una pila PEMFC comercial de Heliocentric con un convertidor elevador junto a un dSPACE DS1102, que es el sistema encargado de procesar el control en tiempo real.. Para probar el desempeño de los controladores, se aplicaron dos cambios de carga en t= 25 y t= 45 s. Los resultados experimentales mostraron que durante los cambios dinámicos, las cinco técnicas propuestas han mostrado alta robustez frente a variaciones de la resistencia de carga. Se encontró que el IFTSMC-QRL tiene un rendimiento superior en términos de precisión (oscilación de estado estable) sobre los otros algoritmos. Por lo tanto, se obtuvo una oscilación de estado estacionario de 0,25 Win the stack power, donde los estados estacionarios de CSMC, ISMC, ITSMC, IFTSMC fueron respectivamente 6,5 W, 0,7 W, 0,35 W y 0,4 W. Además, el IFTSMC-QRL ha mostrado una respuesta más rápida y una mejor robustez sobre ISMC, ITSMC e IFTSMC. Por lo tanto, se obtuvo un tiempo de respuesta de 1,5 s, donde el tiempo de respuesta del ISMC, ITSMC, IFTSMC fueron respectivamente 6,2 s, 2,1 s, 1,8 s. Por otro lado, el SMC convencional proporciona una mayor robustez sobre los modos deslizantes de terminales. Por lo tanto, se obtuvo un sobreimpulso de 6,5 W en la potencia de la pila, donde el sobreimpulso de ISMC, ITSMC, IFTSMC, IFTSMC-QRL son respectivamente 8,1 W, 6,43 W, 9,1 W,

6,66 W. Sin embargo, aunque el SMC convencional ha mostrado una gran robustez, su efecto de oscilación sigue siendo uno de sus inconvenientes.

Para superar el inconveniente del modo deslizante de primer orden, que es el efecto de oscilación, en esta tesis se propusieron diferentes controladores de modo deslizante de alto orden. Por lo tanto, se han diseñado e implementado cinco tipos de control de modo deslizante de alto orden que incluyen algoritmo de torsión (TA), algoritmo de súper torsión (STA), algoritmo de ley de convergencia prescrita (PCL), algoritmo cuasi continuo (QCA) y algoritmo de deriva (DA). para un PEMF comercial heliocéntrico. Los resultados experimentales mostraron que, durante los cambios dinámicos, las técnicas propuestas han demostrado una gran capacidad para reducir el fenómeno de oscilación al tiempo que proporcionan una gran robustez frente a las variaciones de la resistencia de carga. Por lo tanto, en comparación con el SMC convencional, se obtuvo una reducción del 87 %, 89 %, 91 %, 89 %, 94 % en la oscilación de estado estacionario respectivamente a través de TA, STA, PCL, QCA y DA. En esta tesis también se han propuesto algoritmos alternativos como proporcional-integral (PI), control de lógica difusa (FLC), control predictivo de módulo (MPC) y control de retroceso (BSC). Se encontró que, en comparación con el controlador PI convencional, las técnicas FLC, MPC y BSC han demostrado una gran capacidad para reducir el tiempo de respuesta al tiempo que proporcionan una gran robustez frente a las variaciones de la resistencia de carga. Así, en comparación con el IP convencional, se obtuvo una reducción de más de 4 veces mediante el uso de FLC, una reducción de más de 12 veces mediante el uso de MPC y una reducción de 2 veces mediante el uso de uso del BSC.

Finalmente, en esta tesis también se proponen diferentes métodos de seguimiento del punto de máxima potencia aplicados a celdas de combustible PEM y sistemas fotovoltaicos. Se diseñaron e implementaron en los sistemas experimentales métodos MPPT modernos y avanzados, como el estimador de voltaje de referencia (RVE), el estimador de corriente de referencia (RCE) y las redes neuronales recurrentes (RNN). Para el caso de PV, y bajo las condiciones climáticas disponibles durante los experimentos y el hardware disponible, se demostró que MPC empleando una predicción de un paso es capaz de proporcionar los mejores resultados en comparación con P&O, FLC y SMC. En cuanto al caso de la pila de combustible PEM, los resultados obtenidos del RCE basado en HO-PCL han demostrado el éxito del método propuesto para extraer la máxima potencia del FC-42 con un alto rendimiento de seguimiento.

Abstract

Global warming is a result of the greenhouse effects caused by the propagation of CO_2 in the atmosphere, resulting in many disasters that influencing human populations. It is thought to have caused meteorological phenomena such the well known “El Nino", which disturbs the south Pacific region and causes some natural disasters as inundations, tornadoes, and dryness. Besides, melting of the polar ice mountains is also one of the major results of global warming. Hence, it leads to a rise in the sea level that may cause floods in coastal regions.

Clean energy such as solar and wind are considered as an important way to overcome these issues by reducing CO_2 emissions. However, these energies are dependent on the weather conditions. Thus, the solar energy is only available when the sun is shining and the wind tends to blow intermittently. Besides, storing excess energy produced during the time of abundance is a tricky task.

One technology which can be based upon sustainable sources of energy is fuel cell. Fuel cell technologies could be an ideal alternative renewable clean energy. Fuel cells are devices that directly convert the chemical energy stored in some fuels into electrical energy and heat. This means that they can provide electricity throughout all weathers as long as fuel is available. Therefore, they have attracted the worldwide attention in the recent few decades. Fuel cells are generally classified into five different categories based on their operating temperature or the type of their electrolyte chemistry: molten carbonate fuel cell (MCFC), solid oxide fuel cell (SOFC), alkaline fuel cell (AFC), proton exchange membrane fuel cell (PEMFC), phosphoric acid fuel cell (PAFC) and direct methanol fuel cell (DMFC).

The preferred fuel for many fuel cells is hydrogen, since it is a renewable source of energy. Thereby, proton exchange membrane fuel cells (PEMFCs), which have hydrogen as fuel, are considered as one of the most reliable and promising energy conversion devices. They can provide a continuous power supply throughout all seasons as long as hydrogen is provided. Moreover, unlike internal combustion engines, PEMFCs are not combusted, the energy instead is produced through a chemical reaction. This results in several benefits such as high efficiency (up to more than 50%), zero gas emissions, low operating temperature (20-100 °C), low maintenance, and quiet operation. Thus, for the same quantity of fuel, fuel cells can extract 90% more efficient power than traditional gasoline. Fuel cells are also very simple in maintenance since they have no moving parts in their construction. In addition, the absence of mechanical parts in their composition allows them to operate silently. PEMFCs have many advantages not only when compared with traditional fossil fuels,

but also even when compared with other types of cells. They are characterized by their low operating temperature, fast electrochemical reaction (quick start up), long cycle life which is a very important point, and their high power density. Therefore, they are widely known as the most reliable and promising source of energy. They have been developed and used in many fields, such as back-up power sources, portable power supplies, hybrid power systems, distributed generation systems, micro-grids, urban cars, buses, tramways, locomotives, and air-crafts.

A PEMFC is composed of a catalyst layer, a gas diffusion layer, and an electrolyte membrane. Each of these components is fabricated individually and then pressed to each other at high pressures and temperatures. The catalyst layer and gas diffusion layer are placed on both anode and cathode sides. The electrolyte membrane permits only the appropriate ions (protons) to migrate toward the cathode. The PEMFC is supplied by pressurized hydrogen (H_2) and oxygen (O_2) as a fuel and generates electricity, water, and heat. The hydrogen atoms (H_2) enter the PEMFC at the anode side, where the catalyst layer divides them into protons (H^+) and electrons (e^-). The protons flow to the cathode via the electrolyte membrane, while the electrons flow through the external circuit to provide electric energy along the way. The oxygen atoms (O_2) enter the PEMFC at the cathode side and react with electrons returning from the external circuit and with protons that have traveled through the membrane to produce water and heat.

PEMFC models are divided into operational mechanism and experimental data ones. In regards to the first mentioned category, based on the regime, these are divided into static and dynamic. There are three well known models used in static analysis such as the Amphlett model, Larminie and Dicks model, and Chamberlin-Kim model. These three approaches had different outcomes where the Amphlett produced the most accurate results with high complexity implementation as a downside (same disadvantage for Larmini-Dicks). Oppositely, Chamberlin-Kim showed to be the most simple one but with low precision. Contrarily, dynamic models are used in transient regimes where the double layer effect heads this condition. Often, this phenomenon is modeled as with an electrical capacitor that depends on the electrodes and individual stack features. On the other hand, experimental methods comprise mechanisms such as fuzzy identification where the dehydration of the PEMFC was analysed through classification based on the knowledge from an operator over a FC. However, one of the main disadvantages of fuzzy logic strategies is the computational requirement when features are increased and thus, rules are expanded. Another different approach was used is support vector machine (SVM) based on data-driven for fault diagnosis in PEMFC. In spite of the high accuracy, some disadvantages are related to dynamics that can happen in a short period of time such as switches that are unable to be shown by the proposed model. Additionally, in certain cases, SVM required high computational resources which is associated with the accuracy of the model to be trained. Despite the disadvantages of the mentioned strategies, another approach is the usage of trend tools such as artificial neural networks (ANN). This

algorithmic scheme is based on a biological approach of human brain neurons which have the capabilities of recognizing, acquire information and self-adjust according to past actions (this is also known as neuroplasticity). Therefore, in this thesis, an in-depth investigation was conducted with a commercial PEMFC to generate a spread variety of ANNs with the aim of finding a suitable configuration that can match the behaviour of the real PEMFC. After finding a proper ANN configuration, this was used as a plant for the control process.

In many applications, the PEMFC is usually coupled with a DC-DC power electronic converter that provides an efficient power conversion to the load, and also offers highly regulated output voltage. The DC-DC power converter, which could be an inductive switching converter or a switched capacitor converter, is an adaptation stage circuit that is inserted between the load and the PEMFC stack. Many types of converters have been designed during the previous years, the most simple are the buck converter, that decreases voltage from input to output, and the boost converter, that increases it, other types are the buck-boost and the Cuk converters. They provide a dc output voltage controlled with pulse width-modulation PWM switching technique. The advantages and disadvantages of each topology is based on the count of its components. Therefore, due to their higher efficiency and fewer components compared with other converters topologies, high step-up dc-dc converters could possibly be applied to interface the PEMFC to the load. This latter has been classified as one of the most and simplest used converters. It has the ability to step-up a lower input voltage into a higher output voltage via controlled pulse-width-modulation (PWM) switching technique. Therefore, the control loop is needed so as to obtain an applicable output dc voltage. Besides, since the fuel cell is largely influenced by the load and its inputs variations (temperature, oxygen, and hydrogen), the application of the controller is desired so as to keep the PEMFC operating at the adequate power point.

In order to have an efficient power conversion from the PEMFCs to the DC link (or load), many control techniques and algorithms have been designed in this thesis. Linear controllers can be a suitable initial option to control a DC-DC converter. Hence, a typical first and classic approach like a proportional integral derivative (PID) has been implemented. The design of the linear controller is based on the linearized converter model around an equilibrium point. Ziegler-Nichols tuning strategy has been used in simulation environments, whereas different strategies like mean squared error (MSE), mean absolute error (MAE), root mean squared error (RMSE), relative root mean squared error (RRMSE) have been used in the experimental environments. However, due to the nonlinearity of the system, it is difficult to account the variation of the system parameters, due to the influence of the small signal model parameters to the converter operating point. Moreover, large signal variations transients such as in the start-up or against changes in the load, cannot be dealt with these techniques. Therefore, the application of linear control techniques for the control of these converters are not effective when the system is

experiencing large model parameters and load variations.

A nonlinear strategy design can improve the effectiveness, specially when a real-time controller is embedded. Therefore, many different nonlinear strategies have been proposed in this thesis. Robust sliding mode controllers like conventional sliding mode control (CSMC), proportional integral sliding mode control (ISMC), integral terminal sliding mode control (ITSMC), integral fast terminal sliding mode control (IFTSMC) and integral fast terminal SMC combined with quick reaching law (IFTSMC-QRL), were used as a first attempt to improve the tracking performance of the fuel cell system. These algorithms were implemented and contrasted with novel designs to highlight the features that could define the effectiveness of each in different scenarios such as constant and dynamic change following. An assembled test rig with a commercial PEMFC from Heliocentric with a boost converter were used to evaluate each structure in a dSPACE DS1102. To test the performance of the controllers, two load changes at t= 25 s and t= 45 s were applied. The experimental results showed that during the dynamic changes, the five proposed techniques have shown high robustness against variations of the load resistance. It was found that the IFTSMC-QRL has the superior performance in terms of accuracy (steady state oscillation) over the other algorithms. Hence, a steady state oscillation of 0.25 W in the stack power was obtained, where the steady states of the CSMC, ISMC, ITSMC, IFTSMC were respectively 6.5 W, 0.7 W, 0.35 W, and 0.4 W. Moreover, the IFTSMC-QRL has shown faster response and better robustness over the ISMC, ITSMC, and IFTSMC. Hence, a response time of 1.5 s was obtained, where the response time of the ISMC, ITSMC, IFTSMC were respectively 6.2 s, 2.1 s, 1.8 s. On the other hand, the conventional SMC provides higher robustness over the terminal sliding modes. Hence, an overshoot of 6.5 W in the stack power was obtained, where the overshoot of the ISMC, ITSMC, IFTSMC, IFTSMC-QRL are respectively 8.1 W, 6.43 W, 9.1 W, 6.66 W. However, although the conventional SMC has shown high robustness, its chattering effect is still one of its drawbacks.

To overcome the drawback of the first order sliding mode, which is the chattering effect, different high order sliding mode controllers were proposed in this thesis. Hence, five types of high order sliding mode control including twisting algorithm (TA), super twisting algorithm (STA), prescribed convergence law algorithm (PCL), quasi-continuous algorithm (QCA) and drift algorithm (DA) have been designed and implemented for a Heliocentric commercial PEMF. The experimental results showed that during the dynamic changes, the proposed techniques have shown high capability to reduce the chattering phenomenon while providing high robustness against variations of the load resistance. Hence, in comparison with the conventional SMC, a reduction of 87 %, 89 %, 91 %, 89 %, 94 % in the steady state oscillation were obtained respectively via TA, STA, PCL, QCA, and DA.

Alternative algorithms such as proportional integral (PI), fuzzy logic control (FLC), module predictive control (MPC) and back-stepping control (BSC) also have been proposed in this thesis. It was found that when comparing to the conventional PI

controller, the FLC, MPC, and BSC techniques have shown high capability to reduce the response time while providing high robustness against variations of the load resistance. Hence, in comparison with the conventional PI, a reduction of more than 4 times were obtained via the use of the FLC, a reduction of more than 12 times were obtained via the use of the MPC, and a reduction of 2 times were obtained via the use of the BSC.

Finally, different maximum power point tracking methods applied on PEM fuel cell and PV system, are proposed in this thesis. Modern and advanced MPPT methods such as reference voltage estimator (RVE), reference current estimator (RCE) and recurrent neural networks (RNN) were designed and implemented in the experimental systems. For the PV case, and under the weather conditions available during experiments and available hardware, it was shown that MPC under a simple settle, can provide the best results in comparison with P&O, FLC, and SMC. Regarding the case of PEM fuel cell, the obtained results of the HO-PCL based RCE have proven the success of the proposed method in extracting the maximum power from the FC-42 with high tracking performance.

Contents

List of Figures

List of Tables

Chapter 1

Introduction

1.1. Motivation

At present, the entire world is becoming aware of the problems derived from traditional energies such as fossil fuels and non-renewable energies which have destructive environmental impacts. On the other hand, the ever-increasing energy demand and rising crude oil prices, as well as predictable expiration of fossil fuels reserves, have also caused high ambitions toward renewable and sustainable energy resources. In this context, renewable energy sources (RES) such as wind and solar are considered as suitable and viable alternative options to generate electrical power [1–5]. However, despite the environmental friendly features of these energies, their dependency on the weather conditions is still a considerable obstacle. Thus, the solar energy is lower in winter months and cloudy days below, as it is only available during the daytime. On the other hand, the wind energy is only available when the wind blows.

Due to its low amount of contamination, its abundance on the Earth's surface, as well as its high volatility and efficiency, hydrogen has been chosen as the most suitable alternative fuel to traditional fossil fuels. Hydrogen represents up to more than 75% of all normal matter mass, and it accounts for over 90% of all atoms on earth [6]; can reach an energy density value of 120 MJ/kg which is almost 5 times higher compared to the coal [7]. It could be produced by either simple methods, such as the electrolysis of water, or industrial methods using steam reforming. Regarding production costs, the target had been reduced from 4.2USD in 2015 and aimed to be 1.7USD in 2020 [8]; it is expected to fall by 50% by the middle of this century, and that could pave the way for more sustainable sources of energy [9]. Therefore, it has encouraged thousands of scientists and researchers to pursue research in hydrogen cells since it could replace fossil fuels in the automotive sector (with properly modification in the motor), or also could be used with oxygen in fuel cells to produce electricity.

The electro-chemical conversion of hydrogen as a gas into useful electricity can be achieved through fuel cells, devices that drew the attention since they were discovered by William Grove in 1838 [10]. Thenceforth, the attractiveness of fuel cells represents a trend in research as it is expected that this technology could reach its maturity near 2030 [11]. Additionally, because of the groundbreaking

innovation of fuel cell electric vehicles (FCEV) and large capacity stationary fuel cells (LCSFC), the interest has been growing exponentially since 2007 [12]. This is principally due to their emissions level that could reach up to 0% (depending on the type of fuel) and a high efficiency that yields up to 60% [13, 14]. Despite that an assorted variety of fuel cells had been developed, proton exchange membrane fuel cells (PEMFC) had a significant enhancement in recent years. The production costs not only provided a downsizing feature but also a performance improvement which covers high energy density and robustness [15]; thus, it has been a matter of research for several applications like automotive, stationary and portable power supplies [16–19]. For most of those applications, the PEMFC is usually used in conjunction with a DC–DC power converter that generates highly regulated DC voltage for end-use. Therefore, the control design plays the main role in a PEMFC power system, not only for performance improvement reasons but also for safety operation. Figure 1.1 shows the configuration of a typical fuel cell power system which is constructed with fuel cell, DC/DC converter and the controller.

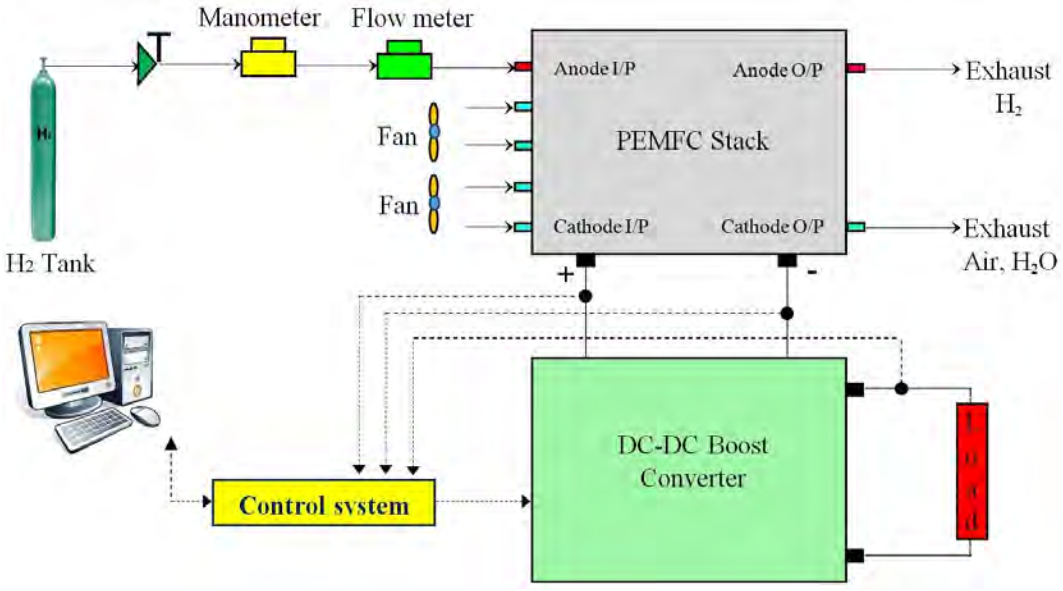

Figure 1.1: Configuration of a typical fuel cell power system

1.2. Objective of the thesis

The objective of this thesis is the application of advanced control algorithms for a commercial Proton exchange membrane fuel cell system aiming to optimise the performance of the stack. To achieve this objective, the following partial objectives have been considered:

1. Review the most frequent PEM fuel cell models that have been designed in the recent years.

2. Modeling of a commercial PEM fuel cell stack based on mathematical equations.
3. Application of artificial intelligence (AI) for modeling a commercial PEM fuel cell stack.
4. Investigate the effect of temperature and humidity on the PEM fuel cell stack performance.
5. Review the most frequent DC-DC power converters used in renewable energy systems.
6. Review the most frequent control algorithms that have been designed for the PEM fuel cell in the recent years.
7. Design and optimisation of the most commonly used control algorithms for the PEM fuel cell system.
8. Development of a new maximum power point tracking algorithm (MPPT) for the PEM fuel cell system.
9. Validation of the proposed algorithms on a real PEM fuel cell system.

1.3. Structure of the thesis

This thesis is divided into acknowledgments, abstract, bibliography and ten chapters. The first chapter introduces the thesis, it presents motivation that led the author to study and carry out the thesis subject; the goals of the thesis and the plan are presented in the first chapter as well.

The second chapter includes the state of the art in control used for the fuel cell system. The state of the art starts with a short introduction about the importance of the clean energies nowadays, then, a short review in the PEM fuel cells models, and finally, the main and the long part was focused on the controls review including the linear and non linear controllers.

The third chapter focused on the proton exchange membrane fuel cell. The first part of the chapter discus the principle of operation of the PEM fuel cell, the advantages, the inconvenient, and the applications. The second part of the chapter focused on the static and dynamic model of the PEM fuel cell.

The forth chapter introduces the application of machine learning in fuel cell systems. First, the artificial neural networks are introduced, then the data collection and analysis are discussed, and finally different structure of ANNs are tested to find out the most efficient predicted model.

The fifth chapter reviews different types of DC-DC power converter. The chapter starts with introducing the modes of operation (CCM and DCM) and then, it discuses the following power converters: boos, buck, back-boost, sepic, zeta and Cuk.

The sixth chapter describes the experimental system. The hardware system including the PEM fuel cell, the power converter, the dSPACE and the electronic load are clearly presented in this chapter.

The seventh chapter discusses the application of sliding mode control (SMC) on the PEM fuel cell system. The conventional sliding mode (CSMC) is tested first, then a proportional integral sliding mode (PISMC), integral terminal sliding mode (ITSMC), integral fast terminal sliding mode (IFTSMC) and integral fast terminal sliding mode combined with quick reaching law ((IFTSMC-QRL), were also designed and implemented in the real system.

The eighth chapter discusses the application of high order sliding mode (HOSM) on the PEM fuel cell. Hence, HOSM based on twisting algorithm (TA), super twisting algorithm(STA), prescribed convergence law algorithm (PCL), quasi-continuous algorithm (QCA) and finally drift algorithm (DA) are designed and implemented to improve the power quality and to remain the fuel cell functioning at an adequate power point.

The ninth chapter discusses the application of alternative control methods on the PEM fuel cell. In this chapter different controllers are designed and implemented in the system. The linear proportional integral (PI) is firstly designed, then, a peak current mode (PCM), a fuzzy logic control (FLC), a model predictive control (MPC) and a back-stepping control (BSC) were also designed and implemented to improve the output power quality of the fuel cell.

The tenth chapter discuses the application of novel maximum power point tracking methods on a PEM fuel cell and PV system. In this chapter we design novel techniques such as reference voltage estimator, reference current estimator and neural notworks model that used to obtain the reference corresponds to the maximum power point. For the control process, different algorithms such as sliding mode control (SMC), fuzzy logic control (FLC), model predictive control (MPC) and prescribed convergence law (PCL), have been used. As a reference of comparison of these algorithms we used the well known P&O.

Finally, conclusions and future perspectives were summarised in chapter 11.

1.4. Derived publication

The following is a list of the published works derived from this thesis:

- **Journal articles**

  1. Napole, C., **Derbeli, M.**, Barambones, O. Experimental Analysis of a Fuzzy Scheme against a Robust Controller for a Proton Exchange Membrane Fuel Cell System. *Symmetry* 2022, 14, 139. **Q1, IF=2.71**.
  2. **Derbeli, M.**, Napole, C., Barambones, O., Sanchez, J., Calvo, I., Fernández-Bustamante, P. Maximum Power Point Tracking Techniques for Photo-

voltaic Panel: A Review and Experimental Applications. *Energies* 2021, 14, 7806. **Q3, IF=3**.

3. **Derbeli, M.**, Charaabi, A., Barambones, O., & Napole, C. (2021). High-performance tracking for protonexchange membrane fuel cell system pemfc using model predictive control. *Mathematics* , 9(11), 1158. **Q1, IF=2.26**.

4. **Derbeli, M.**, Napole, C., & Barambones, O. (2021). Machine learning approach for modeling andcontrol of a commercial heliocentris fc50 pem fuel cell system. *Mathematics*, 9(17), 2068. **Q1, IF=2.26**.

5. Fernández-Bustamante, P., Barambones, O., Calvo, I., Napole, C., **Derbeli, M.** Provision of Frequency Response from Wind Farms: A Review. *Energies* 2021, 14, 6689. **Q3, IF=3**.

6. Bo Wang, **Derbeli, M.**, Barambones, O., Yousefpour, A., Jahanshahi, H., Bekiros, S., Aly, A.A., Alharthi, M.M., Experimental validation of disturbance observer-based adaptive terminal sliding mode control subject to control input limitations for SISO and MIMO systems, *European Journal of Control*, 2021, ISSN 0947-3580, **Q2, IF=2.39**

7. Napole, C.,**Derbeli, M.**, & Barambones, O. (2021). A global integral terminal sliding mode controlbased on a novel reaching law for a proton exchange membrane fuel cell system. *Applied Energy*, 301, 117473. **Q1, IF=9.75**.

8. Napole, C., Barambones, O.,**Derbeli, M.**, & Calvo, I. (2021). Advanced trajectory control forpiezoelectric actuators based on robust control combined with artificial neural networks. *Applied Sciences*, 11(16), 7390. **Q2, IF=2.28**.

9. Napole, C., Barambones, O.,**Derbeli, M.**, Calvo, I., Silaa, M. Y., & Velasco, J. (2021). High-performancetracking for piezoelectric actuators using super-twisting algorithm based on artificial neural networks. *Mathematics*, 9(3), 244. **Q1, IF=2.26**.

10. Napole, C., Barambones, O.,**Derbeli, M.**, Cortajarena, J. A., Calvo, I., Alkorta, P., & Bustamante, P. F.(2021). Double fed induction generator control design based on a fuzzy logic controller for anoscillating water column system. *Energies*, 14(12), 3499. **Q3, IF=3**.

11. Napole, C.,**Derbeli, M.**, & Barambones, O. (2021). Fuzzy logic approach for maximum power pointtracking implemented in a real time photovoltaic system. *Applied Sciences*, 11(13), 5927. **Q2, IF=2.28**.

12. Silaa, M. Y.,**Derbeli, M.**, Barambones, O., Napole, C., Cheknane, A., & Gonzalez De Durana, J. M.(2021). An efficient and robust current control for polymer electrolyte membrane fuel cell powersystem. *Sustainability*, 13(4), 2360. **Q2, IF=3.25**.

13. **Derbeli, M.**, Barambones, O., Farhat, M., Ramos-Hernanz, J. A., & Sbita, L. (2020). Robust high ordersliding mode control for performance improvement of pem fuel cell power systems. *International Journal of Hydrogen Energy*, 45(53), 29222–29234. **Q2, IF=5.81**.
14. **Derbeli, M.**, Barambones, O., Silaa, M. Y., & Napole, C. (2020). Real-time implementation of a newmppt control method for a dc-dc boost converter used in a pem fuel cell power system. *Actuators*, 9(4),105. **Q2, IF=1.99**.
15. Napole, C., Barambones, O., Calvo, I.,**Derbeli, M.**, Silaa, M. Y., & Velasco, J. (2020). Advances intracking control for piezoelectric actuators using fuzzy logic and hammerstein-wiener compensation. *Mathematics*, 8(11), 2071. **Q1, IF=2.26**.
16. Silaa, M. Y.,**Derbeli, M.**, Barambones, O., & Cheknane, A. (2020). Design and implementation of highorder sliding mode control for pemfc power system. *Energies*, 13(17), 4317. **Q3, IF=3**.
17. **Derbeli, M.**, Barambones, O., Ramos-Hernanz, J. A., & Sbita, L. (2019). Real-time implementation of asuper twisting algorithm for pem fuel cell power system. *Energies*, 12(9), 1594. **Q3, IF=3**.
18. **Derbeli, M.**, Barambones, O., & Sbita, L. (2018). A robust maximum power point tracking controlmethod for a pem fuel cell power system. *Applied Sciences*, 8(12), 2449. **Q2, IF=2.28**.
19. **Derbeli, M.**, Farhat, M., Barambones, O., & Sbita, L. (2017). Control of pem fuel cell power systemusing sliding mode and super-twisting algorithms. *International Journal of Hydrogen Energy*, 42(13), 8833–8844. **Q1, IF=4.2**.

- **Conference proceedings**

1. Napole, C.; Barambones, O.; **Derbeli, M.**; Yousri Silaa, M.; Calvo, I.; Velasco, J. Tracking Control for Piezoelectric Actuators with Advanced Feed-forward Compensation Combined with PI Control., *in Proceedings of the 1st International Electronic Conference on Actuator Technology: Materials, Devices and Applications*, 23–27 November 2020, MDPI: Basel, Switzerland.
2. **M. Derbeli**, O. Barambones, M. Farhat and L. Sbita, "Efficiency Boosting for Proton Exchange Membrane Fuel Cell Power System Using New MPPT Method," *2019 10th International Renewable Energy Congress (IREC)*, 2019, pp. 1-4,
3. **M. Derbeli**, A. Charaabi, O. Barambones and L. Sbita, "Optimal Energy Control of a PEM Fuel Cell/Battery Storage System," *2019 10th International Renewable Energy Congress (IREC)*, 2019, pp. 1-5

4. **M. Derbeli**, I. Mrad, L. Sbita and O. Barambones, "PEM fuel cell efficiency boosting — Robust MPP tracking," *2018 9th International Renewable Energy Congress (IREC)*, 2018, pp. 1-5,
5. N. Boukrich, **M. Derbeli**, M. Farhat and L. Sbita, "Smart auto-tuned regulators in electric vehicule PMSM drives," *2017 International Conference on Green Energy Conversion Systems (GECS)*, 2017, pp. 1-5
6. **M. Derbeli**, M. Farhat, O. Barambones and L. Sbita, "Control of Proton Exchange Membrane Fuel Cell (PEMFC) power system using PI controller," *2017 International Conference on Green Energy Conversion Systems (GECS)*, 2017, pp. 1-5,
7. **M. Derbeli**, M. Farhat, O. Barambones and L. Sbita, "A robust MPP tracker based on backstepping algorithm for Proton Exchange Membrane Fuel Cell power system," *2017 11th IEEE International Conference on Compatibility, Power Electronics and Power Engineering (CPE-POWERENG)*, 2017, pp. 424-429,
8. **M. Derbeli**, L. Sbita, M. Farhat and O. Barambones, "Proton exchange membrane fuel cell — A smart drive algorithm," *2017 International Conference on Green Energy Conversion Systems (GECS)*, 2017, pp. 1-5,
9. **M. Derbeli**, L. Sbita, M. Farhat and O. Barambones, "PEM fuel cell green energy generation — SMC efficiency optimization," *2017 International Conference on Green Energy Conversion Systems (GECS)*, 2017, pp. 1-5,
10. I. Mrad, **M. Derheli**, L. Shita, J. P. Barhot, M. Farhat and O. Baramhones, "Sensorless and robust PEMFEC power system drive based on Z(Tn) observability," *2017 International Conference on Green Energy Conversion Systems (GECS)*, 2017, pp. 1-6,
11. W. Torki and **M. Derbeli**, "Modeling and control of a stand-alone PEMFC for AC load-PMSM application," *2017 International Conference on Green Energy Conversion Systems (GECS)*, 2017, pp. 1-6,

Chapter 2

State of the art in control of fuel cell power systems

2.1. Introduction

During the recent few years, several clean energy sources such as solar, wind, geothermal etc., have been developed to generate electric energy and replace conventional fuel [20–26]. However, these alternative sources necessitate sophisticated and high-cost technologies, and they are not suitable for plenty of applications. Moreover, most of these sources are depending on certain climatic and geographical conditions. For example, solar energy needs the sun and it could not be used in countries where clouds abundant throughout the year. The same for the wind energy which could also be used only when the wind is blowing. The use of tidal phenomenon and waves movement necessitate to be near the sea and this is also not available everywhere etc.

By virtue of its abundance in the earth, hydrogen has emerged as an available and advantageous fuel. In this sense, PEM fuel cells which use hydrogen as the main fuel have shone the horizon as a comprehensive and general alternative to fossil fuel. They have been considered as the energy source of the twenty-first century due to their high power densities, lightweight, low operating temperature (quick start-up), long cycle life, as well as zero pollution [27, 28]. Thereby, they have been used in many fields such as transportation, aircraft, distributed generation, and especially in stationary and mobile applications [29–35].

2.2. Comprehensives review of fuel cell models

To achieve a suitable system design in terms of efficiency, several PEMFC mathematical models had been developed in the recent years to understand the main phenomena that can alter the device performance. According to Fang, Di and Ru, PEMFC models are divided into operational mechanism and experimental data ones [36]. In regards to the first mentioned category, based on the regime, these are divided into static and dynamic. Saadi et al. [37] studied three well known models used in static analysis such as the Amphlett et al. [38, 39], Larminie and Dicks [40] and Chamberlin-Kim [41]. A simulation showed that the three approaches had

different outcomes where the Amphlett produced the most accurate results with high complexity implementation as a downside (same disadvantage for Larmini-Dicks). Oppositely, Chamberlin-Kim showed to be the most simple one but with low precision. Contrarily, dynamic models are used in transient regimes where the double layer effect heads this condition. Often, this phenomenon is modeled as with an electrical capacitor that depends on the electrodes and individual stack features [42, 43].

On the other hand, experimental methods comprise mechanisms such as fuzzy identification which has been carried by authors of [44]. In this study, the dehydration of a PEMFC was analysed through classification based on the knowledge from an operator over a FC. Results revealed that suitable non-linearities like electrical features and uncertainties can be mirrored with linguistic rules, an essential feature of this tool [45]. However, one of the main disadvantages of fuzzy logic strategies is the computational requirement when features are increased and thus, rules are expanded [46]. Another different approach was used by authors of [47] where they employed support vector machine (SVM) based on data-driven for fault diagnosis in PEMFC. In spite of the high accuracy obtained, the disadvantages are related to dynamics that can happen in a short period of time such as switches that are unable to be shown by the proposed model. Additionally, in certain cases, SVM required high computational resources which is associated with the accuracy of the model to be trained [48].

Despite the disadvantages of the mentioned strategies, another approach is the usage of trend tools such as artificial neural networks (ANN). This algorithmic scheme is based on a biological approach of human brain neurons which have the capabilities of recognizing, acquire information and self-adjust according to past actions (this is also known as neuroplasticity) [49]. Recently, Nanadegani et al. [50] provided a PEMFC study based on ANNs to increase the output power with a multilayer perceptron (MLP).

2.3. Comprehensives review of power converters

In many applications, the PEMFC is usually coupled with a DC-DC power electronic converter that provides an efficient power conversion to the load, and also offers highly regulated output voltage [51–55]. The DC-DC power converter, which could be an inductive switching converter or a switched capacitor converter [56], is an adaptation stage circuit that is inserted between the load and the PEMFC stack. According to Luo and Ye [57], there are more than 500 different topologies of converters. The most simple are the buck converter, that decreases voltage from input to output, and the boost converter, that increases it, other types are the buck-boost and the Cuk converters. They provide a dc output voltage controlled with pulse width-modulation PWM switching technique. Yet, the advantages and disadvantages of each topology based on the count of components, are discussed and compared in [58]. Therefore, due to their higher efficiency and fewer components compared with

other converter topologies, high step-up dc-dc converters could possibly be applied to interface the PEMFC to the load. This latter has been classified as one of the most and simplest used converters. It has the ability to step-up a lower input voltage into a higher output voltage via controlled pulse-width-modulation (PWM) switching technique. Therefore, the control loop is needed so as to obtain an applicable output dc voltage. Besides, since the fuel cell is largely influenced by the load and its inputs variations (temperature, oxygen, and hydrogen), the application of the controller is desired so as to keep the PEMFC operating at the adequate power point.

2.4. Comprehensives review of linear controllers applied in fuel cell systems

In order to have an efficient power conversion from the PEMFCs to the DC link (or load), many control techniques and algorithms have been adopted during the recent years. Linear controllers can be a suitable initial option to control a DC-DC converter. Hence, a typical first and classic approach like a proportional integral derivative (PID) has been implemented several times in a DC-DC boost converters. A striking aspect has been accomplished in the research conducted by the authors of [59] where they compared controller tuning strategies in simulation environments. Procedures like Ziegler-Nichols, Chien-Hrones-Reswick and online optimization achieved respectively, 11.8%, 17.1% and 2.16% of overshoot reduction. Authors of [60] used a proportional integral (PI) control to keep the PEMFC working in an efficient power point. The proportional derivative (PD) has been proposed by [61] to keep the PEMFC operating at an appropriate power point. Choe [62] used PID control for a DC–DC boost converter with a fuel cell dynamic model. The PID was designed to control the fuel cell by adjusting the pulse width modulation (PWM) of the boost converter. Results have demonstrated that the objective is attained through the proposed method with improved dynamics and high tracking performance. The PID also was applied by [63] to obtain an appropriate power point for a PEMFC power system. Results showed that by selecting the accurate parameters, the proposed approach could provide satisfactory results in terms of high tracking efficiency. Although these controllers are especially sensitive when they face a large load variation, results showed a gradual and smooth rise to the desired operating power point with an acceptable tracking performance. Andujar [64] used a small signal model with a linearized PEMFC model for controlling the DC–DC converter, given that the parameters of the controller should be changed for any variation in the operating conditions. Diversely, an advance linear structure used in boost converters control is μ-synthesis approach as it was developed in the investigation of [65]. In that work, simulations were performed with the robust strategy and compared with a PI controller where further reduction of overshoot was observed along a step function. On the other hand, a classic linear quadratic

regulator (LQR) strategy has been proposed for a PEMFC in [66] where the maximum overshoot reached 96.21%. However, a main drawback of this analysed study is that only simulation results were provided. To increase the robustness of the PID and obtain a better dynamic performance, various research groups/researchers [67] have applied a fractional order proportional integral derivative (FOPID) controller to a DC–DC four-switch buck-boost (FSBB) converter used in a PEMFC power system. The obtained results have shown that the proposed method achieved better performance in comparison with the integer-order and Two-Zero/Three-Pole (TZTP) controller. Hence, an overall efficiency of 92%, more than the one obtained with TZTP, can be retained using the FOPID. A novel PID based grey wolf optimizer PID-GWM is proposed by authors of [68] to track the maximum power. The authors used the $\frac{dP}{dI}$ feedback control scheme. The presented results have indicated the effectiveness of the proposed MPPT algorithm over the P&O, INC, and PID based PSO. The performances of the PID have also been improved by various research groups/researchers [69] via the application of the slap swarm algorithm (PID-SSA). Comparative results with other methods, such as incremental resistance algorithm (IRA), mine-blast algorithm (MBA), and grey wolf optimizer (GWM), grey ant-lion optimizer (GAO) and fuzzy logic control (FLC), have indicated better performance of the proposed PID-SSA in terms of efficiency and reliability. However, despite the massive work done on improving the performance of the PID, it is still sensitive to cope with the non-linearity of the power converter, which leads many researchers to focus on the non-linear algorithms.

2.5. Comprehensives review of nonlinear controllers applied in fuel cell systems

A nonlinear strategy design can improve the effectiveness, specially when a real-time controller is embedded. Fuzzy-logic controller (FLC) represents a non-linear strategy which its construction is based on the designer expertise within the system and traduced through if-then causal rules in fuzzy sets. FLC is known for its simplicity and robustness which are the main advantages when it is employed in complex models [70]. For instance, authors of [71] demonstrated experimentally that the efficiency of the fuel cell can be improved from 14.67% when using a conventional PID controller to 37% when using a fuzzy controller. However, some oscillations are accrued in the electrical characteristics, which may cause serious life-shortening and severe cell deterioration. Various research groups/researchers [72] have proposed fuzzy logic control (FLC) to overcome the drawbacks of the conventional P&O, where the results have indicated a chattering reduction of 78.6% and an improvement of 63% in the settling time. To improve the performance of the FLC, various research groups/researchers [73] have proposed particle swarm optimization (FLC-PSO) for a 53KW PEMFC interfaced with a high step-up dc-dc converter aiming to maintain the

stack power extremely close to the maximum operating power point. Comparative results with the FLC have demonstrated the effectiveness of the FLC-PSO in reducing the overshoot from 65.833% to 63.115% while ensuring high tracking efficiency (99.39%). However, despite the reduction of 2%, an overshoot up to more than 63% is still undesirable. Reddy and Sudhakar [74] optimized the FLC via an adaptive neuro-fuzzy inference system (ANFIS). Simulation and experimental results have indicated that an increase of 1.95% in the average DC link and a reduction of 17.74% in the average time taken to reach the operating power point can be achieved using the proposed ANFIS algorithm. In [75], a variable step-size fuzzy logic control (VSS-FLC) is used to track the output power of a 7KW PEMFC power system. Comparative results with fixed step-size FLC, variable step-size INC, and fuzzy scaled INC, have shown that reductions of 82.35% in response time, 70.93% in current ripples, and 100% in overshoot could be attained using the proposed algorithm. The VSS-FLC also was used by authors of [76] aiming to reduce the current ripple caused by the conventional perturb and observe (P&O). Simulation results have demonstrated that ripple reduction of 88% could be attained through the use of the VSS-FLC algorithm. The authors of [77] used an adaptive FLC strategy for a boost converter linked to a PEMFC where simulations were carried and a final experiment was performed: results showed the chattering amplitude reached 2.4 V in the real device outcomes. However, the implementation of FLC has a significant drawback when complex strategies are required; the fuzzy-set growth implies that the computational requirements need to increment as well [78].

Due to their significant benefits, predictive control methods have attracted the intention of many researches and they have been implemented in a wide range of applications, including power converters, actuator faults, pharmaceuticals industry, chemical processes, and induction motors [79–94]. Model predictive control (MPC) is another non-linear approach that explicitly uses a plant model to calculate an optimal control action subject to constraints on actuation and states [79]. In comparison with the conventional P&O algorithm, an improvement of 10.52% in the overall system efficiency was achieved by various research groups/researchers [80] via the application of the MPC technique. In [81], an overall efficiency of 90% for a grid connected system was achieved by applying the MPC for a three-phase inverter, where the efficiency was approximately 98% for the maximum power point tracking (MPPT) control method and 92% for the inverter. A Lyapunov-function-based MPC was proposed by authors of [82], where the results showed that the proposed control strategy maintains the active and reactive powers close to the desired values with an error of less than 3%. Various research groups/researchers [83] have proposed a combination of MPC with an extended Kalman filter (EKF) for a two-level inverter. High performances in terms of robustness and potential noise rejection were obtained. Successful MPP tracking with an efficiency of up to 98% was obtained by various research groups/researchers [84]. In the latter, the MPC is proposed for a boost converter used in a renewable energy system. Various research groups/researchers [85]

have compared the MPC with different algorithms, such as IncCond, hill climbing, PSO, and FLC. Except for the design complexity, results have demonstrated that the proposed MPC has succeeded over the other methods in terms of efficiency, steady-state oscillation, tracking speed and accuracy. In [92], the MPC was designed to optimize the durability of the PEM fuel cell in renewable micro-grid. Although the effectiveness of the MPC to extend the lifespan of the fuel cell, it still encountered by many obstacles like lack of flexibility and high complexity. The study made by the authors of [93] showed the design and implementation of an MPC in a hardware in the loop (HIL) where a boost converter was emulated for voltage tracking. Despite that the error was enough reduced, the computational resources were one of the main highlights because a leading disadvantage of MPC are the requirements over low cost processors [94].

Smart and advanced computing techniques such as eagle strategy control (ESC), particle swarm optimization (PSO), ant colony optimization (ACO), neural network control (NNC), and genetic algorithms (GAs) have also been commonly used in the last few years [18, 95–117]. Hence, in comparison with FLC, efficiency improvements and a faster response of 45% are obtained by various research groups/researchers [95] via the application of the neural network algorithm (NNA) in a 1.26KW PEMFC electric vehicle power-train. Authors of [96] used the NNA to overcome the drawbacks of the P&O. The obtained results showed that a reduction of 86% and 74%, respectively, in power oscillations and settling time can be achieved. Authors of [97] proposed neural generalized model predictive control (NGMPC) aiming to track the maximum efficiency or the MPP of a grid-connected fuel cell power system. Simulation results have demonstrated the effectiveness of the proposed method to track the desired power point. The NNA also was developed by authors of [98]. However, an intelligent algorithm based chaotic particle swarm optimization (CPSO) is used to optimize the weights of the proposed algorithm. Simulation results have demonstrated the effectiveness of the proposed algorithm to track the MPP with high robustness and low steady-state oscillations. Rezazadeh [99] designed an adaptive inverse controller, known as radial basis function neural network (RBFNN), for the PEMFC system. This control scheme did not require any parameter identification of the system, which means that the needed experimental data for the control design can be reduced. In [100], a genetic algorithm (GA) was used to improve the power quality of the PV generator. Results have demonstrated that in comparison with the conventional P&O and the incremental conductance (IC), the proposed GA can achieve a reduction of 97% in the oscillations of output power. In [101], to obtain an accurate controller, feedback linearization control applied to a PEMFC power system was optimized via a non-dominated sorting genetic algorithm II (NSGA-II). The optimization process was performed on the linear gains of the designed controller. Khanam et al. [102] made a comparative study among ant colony optimization (ACO), particle swarm optimization (PSO), differential evolution (DE) and P&O. Results have demonstrated the effectiveness of the ACO in terms of convergence

time over the other proposed methods. Hence, in comparison with P&O, a reduction of 90.61% and 5.13% are, respectively, obtained via the application of ACO and PSO. İnci and Caliskan [103] proposed a novel optimization method called dynamic cuckoo search algorithm for performance enhancement of a fuel cell system. Comparative results with P&O, IC, and particle swarm optimization (PSO) have demonstrated the effectiveness of the proposed method in reducing the high switching frequency, fast convergence speed, as well as high efficiency (between 98.95% and 99.39%). In [104–109], a variable step-size incremental resistance algorithm (VSIR), gradient descent algorithm (GRD), as well as ripple correlation control (RCC), were proposed to overcome the drawbacks of the P&O and IC methods. In [110], a novel single sensor algorithm was designed to track the MPP of a 7KW PEMFC. Comparative results with conventional two sensors algorithm have demonstrated the effectiveness of the proposed algorithm to enhance the efficiency and the lifetime of the PEMFC. In [18], an extremum seeking control (ESC) is used for a hybrid fuel cell power system. The maximum efficiency power point is achieved by controlling the hydrogen flow-rate through the boost converter. Good results such as an increase of 2% in the overall system's efficiency and 12% in the fuel economy have been obtained. However, it should be noted that each method of these existing algorithms is characterized by its complexity in hardware implementation, convergence speed, the sensors required, the sensed parameters, and the cost.

Backstepping technique (BSTP) has recently attracted considerable attention. It is a recursive design methodology developed in 1990 by P. V. Kokotovic and his coauthors for designing stabilizing controls. It is a Lyapunov-based design that intents to split the whole feedback-system into sub-systems with the aim of developing a controller that considers the sub-parts [118]. Therefore, the mechanics of this approach through a Lyapunov-design can ensure the stability of the entire close-loop system. It has become an important robust algorithm due to its ability to control chaos and its flexibility in the construction of control law. It is commonly used for numerous applications, especially nonlinear uncertain systems [119–129]. Authors of [119, 120] implemented a BSTP for a high step-up converter to keep the PEMFC power system operating at the maximum power point. Comparative results with the well-known PI have indicated the out-performance of the proposed method in terms of robustness, settling time, and control precision. In [121], it is used for a smart grid-connected distributed PV system; where it is designed to drive the system to operate at its maximum power point in order to power up the telecommute towers. Similarly, it is also proposed in [122, 123] to track the reference voltage, which is generated using the incremental conductance algorithm. In [124], it is used to adapt the turbine speed at its maximum generator speed value. However, pitch control and PI regulators are used to determine the optimal specific speed at which the turbine generates its maximum power. In [125], it is proposed for a PV water desalination system to dissipates the maximum produced power in a resistive load to generate heat, which is then used for the desalination process. In [126], it is proposed to reduce

the steady state error, which degrades the efficiency of the MPPT controller. The authors used a regression plane to determine the reference voltage, which corresponds to the peak power. Recently, an advance implementation included a neural adaptive BSTP controller, and it was embedded in a boost converter for voltage regulation where an overshoot of 11.6% with low settling time was achieved [127]. Nevertheless, BSTP drawbacks are associated to its complex design since an advance Lyapunov analysis is involved to reach a suitable control law [128]; in addition, the robustness is limited because of its sensibility to uncertainties and disturbances [129].

Sliding mode control (SMC) is a nonlinear controller which main advantage over previously described tools is that it provides a prompt response, robustness, stability in undetermined environments and low computation is required [130–132]. This technique gathers a control law that changes the dynamics of a system based on a sliding surface that ensures the convergence [133]. Nevertheless, a severe deficiency of this strategy is the infinite time in which the states can achieve the equilibrium [134]. In the literature, the application of the SMC for the PEMFC system was proposed by various research groups/researchers [135–138]. A comprehensive study of SMC implementation in a PEMFC power system is addressed in [135]. The control process is performed using first order SMC, which applied to a DC–DC buck converter in order to ensure low and stable output voltage. The SMC also was proposed by authors of [136] aiming to extract the maximum power from a fuel cell/battery storage system. Satisfactory results in terms of robustness have been achieved. Authors of [137] used conventional sliding mode control (SMC) aiming to overcome the drawbacks of the classical linear PI controller; their proposed method showed acceptable results in terms of robustness against sharp load variation, but since the SMC was used, the chattering phenomenon was present during the tests. According to [138], despite its hardware implementation complexity, the sliding mode control technique shows high accuracy compared with conventional methods. However, in the presence of large load disturbance and uncertainties, its switching gain becomes higher, which leads to the production of a large amplitude of chattering. The computing techniques yield a high tracking efficiency, but the whole system cost becomes too expensive. Consequently, to counteract the chattering phenomenon of the SMC, many algorithm such as terminal sliding mode control (TSMC), integral terminal sliding mode control (ITSMC), high-order sliding mode based on twisting (TA), super-twisting (STA), prescribed convergence law (PCL) and quasi continue (QC) have been proposed [139–156]. In 1988, the terminal sliding mode control (TSMC) was introduced like a terminal attractor [139] and then as a control strategy in 1993 by Gulati and Venkataraman [140] where they aimed to achieve a finite time response. The TSMC is characterised by its capabilities to overcome the drawbacks of the conventional SMC while offering several superior properties such as speeding up the convergence rate and providing high precision control [141]. Shotorbani et al. [142] compared the performance of the distributed terminal sliding mode controller (DTSMC) with divers control schemes such as PI, SMC, proportional

finite-time control (PFTC), proportional asymptotic convergent control (PACC) and proportional-integral finite-time control (PIFTC). Results have confirmed the effectiveness of the proposed DTSMC over the other controllers; in terms of accuracy, smooth tracking and robustness when facing external disturbances. Despite this mentioned advantage, the TSMC is still slow when the system states are distant from the origin and singularities were found which could yield to an unbounded control signal [143]. An option proposed to counter the singularity problem is using high order sliding mode control (HOSMC); traditionally, it is also used to reduce the chattering, which represents an ordinary feature of SMC because it generates an increment in the energy consumption. Authors of [144–147] have, respectively, proposed quasi-continuous, twisting, super twisting, and prescribed convergence law algorithms. Results have demonstrated that chattering reduction of 82%, 84% 90%, and 91%, can be achieved via the proposed algorithms. Regardless the advantages of the HOSMC, the main issues are related to: complex stability proof [148] and it requires high order derivatives which can increase the noise in a feedback loop [149]. Integral terminal sliding mode control (ITSMC) is a composed approach that not only improves the time convergence but also enhances the chattering avoidance properties and the system dynamics [150]. For instance, authors of [151] used an ITSMC for a hybrid AC/DC grid based on a wind turbine and PEMFC generator source. Improved performance in terms of robustness was obtained using the proposed ITSMC scheme with respect to control Lyapunov function (CLF) and SMC. In regards to the implementation in converters, it was uncovered that a fractional ITSMC was designed and embedded in a buck converter type where the outcomes showed an improvement of time convergence even with unknown uncertainties [152]. A fast terminal sliding mode control (FTSMC) was designed by Gudey and Gupta [153], for a low-voltage PEMFC based micro-grid system. Experimental results have demonstrated the effectiveness of the proposed FTSMC (faster convergence and slighter steady-state error) to overcome the inability of the classical SMC to regulate the micro-grid bus voltage. Authors of [154] used an integral fast terminal sliding mode control (IFTSMC), which is a combination of ITSMC [151] and FTSMC [153], aiming to keep the PEMFC system operating at an appropriate and efficient power point. The authors also designed a digital filter to smooth the signals from the chattering effect of the IFTSMC. Another recent developed scheme is the usage of global terminal sliding mode control (GTSMC) with quick reaching law (QRL) [155]; this combines the benefits of TSMC with the global strategy that includes a linear design and pretends the system to reach an equilibrium in a limited time [156]. The QRL is entrenched to reduce the chattering at a cost of shrinking the reaching speed [155].

Chapter 3

Proton Exchange Membrane (PEM) fuel cell system

3.1. Introduction

One technology which can be based upon sustainable sources of energy is fuel cell. Fuel cells are devices that directly convert the chemical energy stored in some fuels into electrical energy and heat. Fuel cells are generally classified into five different categories based on their operating temperature or the type of their electrolyte chemistry: molten carbonate fuel cell (MCFC), solid oxide fuel cell (SOFC), alkaline fuel cell (AFC), proton exchange membrane fuel cell (PEMFC), phosphoric acid fuel cell (PAFC) and direct methanol fuel cell (DMFC). Table 3.1 [157] gives an overview of the main classes of fuel cells with their associated fuels, operating temperatures and electrolyte types [158].

The preferred fuel for many fuel cells is hydrogen, since it is a renewable source of energy. Thereby, proton exchange membrane fuel cells (PEMFCs), which have hydrogen as fuel, are considered as one of the most reliable and promising energy conversion devices. They can provide a continuous power supply throughout all seasons as long as fuel is provided. Moreover, unlike internal combustion engines, fuel cells are not combusted, the energy instead is produced through a chemical reaction. This results in several benefits such as high efficiency, low maintenance, and quiet operation. Thus, for the same quantity of fuel, fuel cells can extract 90% more efficient power than traditional gasoline. Fuel cells are also very simple in maintenance since they have no moving parts in their construction. In addition, the absence of mechanical parts in their composition allows them to operate silently. PEMFCs have many advantages not only when compared with traditional fossil fuels, but also even when compared with other types of cells. They are characterized by their low operating temperature, fast electrochemical reaction (quick start up), long cycle life which is a very important point, and their high power density [159–161]. Therefore, PEMFCs are ideally suited for a wide range of applications, such as stationary, automotive, and portable power supplies.

Table 3.1: Comparison of different fuel cells and their operating characteristics.

Cell Type	**Electrolyte**	**Charge Carrier**	**Temperature**	**Fuel**
PEMFC	solid	H^+	$50 - 90°C$	H_2
DMFC	solid	H^+	$50 - 90°C$	CH_3OH
AFC	liquid	OH^-	$60 - 250°C$	H_2
PAFC	liquid	H^+	$160 - 250°C$	H_2
MCFC	liquid	CO^{2-}	$\approx 650°C$	H_2, CO, CH_4
SOFC	solid	O^{2-}	$750 - 1000°C$	H_2, CO, CH_4

3.2. fuel cell basics

3.2.1. Basic fuel cell Structure

A fuel cell is a device that generates electricity by a chemical reaction. Every fuel cell has two electrodes, one positive and one negative, called respectively, the anode and cathode. The reactions that produce electricity take place at the electrodes.

Every fuel cell also has an electrolyte, which carries electrically charged particles from one electrode to the other, and a catalyst, which speeds the reactions at the electrodes.

Hydrogen is the basic fuel, but fuel cells also require oxygen. One great appeal of fuel cells is that they generate electricity with very little pollution [162].

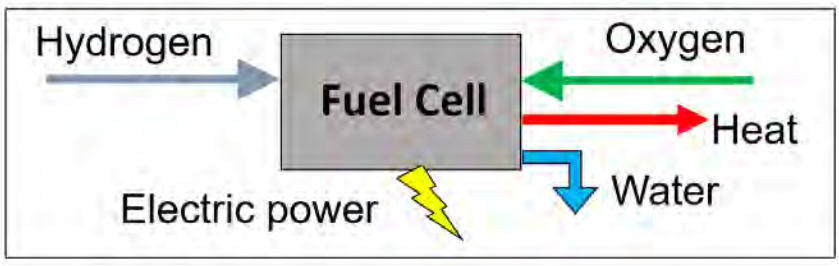

Figure 3.1: Schematic representation of fuel cell energy

3.2.2. A breif history of fuel cell

Fuel cells are actually quite old, although they sound like a modern innovation. Sir William Robert Grove created the first fuel cell in Wales in 1843 as shown in Figure 3.2. This latter was called “Grove Gas Battery”. In the beginning, it was

thought that the fuel cell generates electricity because of the physical contact between materials. However, several scientists such as Christian Schonbein have revealed and explained its principle of operation which is a chemical reaction that generates electricity.

In 1959, the British engineer Francis Bacon developed a fuel cell that characterised by high output power (5 kilowatts); which was enough to power a flat. Since that time, researchers were developing several different types of fuel cells aiming to improve the performance of cell. NASA was the first agency that put fuel cells in use with Apollo series spacecrafts and the Space Shuttles.

In the 1960s, auto companies began working with fuel cells in vehicles. During the oil crisis in the 1970s, automakers began seriously looking at alternative fuels and power-trains. With time, fuel cells have become smaller, more powerful and longer lasting. Most of the major automakers have fuel cells in vehicles such as cars and city buses. However, in the recent years, automakers brought fuel cells vehicles (FCVs) to the consumer market. They consider FCVs as a technology that can meet consumer demand for full-function cars, buses and pick-up trucks that create zero pollution, reduce greenhouse gas emissions and do not depend on fossil fuels [163, 164].

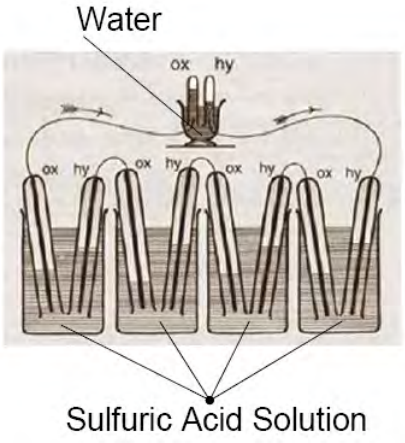

Figure 3.2: Schematic representation of William Grove's 1839 fuel cell

3.2.3. Basic principle of operation

As shown in Figure 3.3, a PEMFC is composed of a catalyst layer, a gas diffusion layer, and an electrolyte membrane. Each of these components is fabricated individually and then pressed to each other at high pressures and temperatures. The catalyst layer and gas diffusion layer are placed on both anode and cathode sides. The electrolyte membrane permits only the appropriate ions (protons) to migrate toward the cathode. The PEMFC is supplied by pressurized hydrogen (H_2) and oxygen (O_2) as a fuel and generates electricity, water, and heat. The hydrogen atoms (H_2) enter the PEMFC at the anode side, where the catalyst layer divides them into protons (H^+) and electrons (e^-). The protons flow to the cathode via the electrolyte

membrane, while the electrons flow through the external circuit to provide electric energy along the way. The oxygen atoms (O_2) enter the PEMFC at the cathode side and react with electrons returning from the external circuit and with protons that have traveled through the membrane to produce water and heat [165]. The electrochemical reactions occurring on the electrodes can be described in Equations (3.1), (3.2), and (3.3). The first and the second equations show the anode and the cathode side reactions, respectively, and the third equation shows the overall electrochemical reaction [166].

$$H_2 \implies 2H^+ + 2e^- \tag{3.1}$$

$$2H^+ + \tfrac{1}{2}O_2 + 2e^- \implies H_2O \tag{3.2}$$

$$H_2 + \tfrac{1}{2}O_2 \implies H_2O + \text{Energy.} \tag{3.3}$$

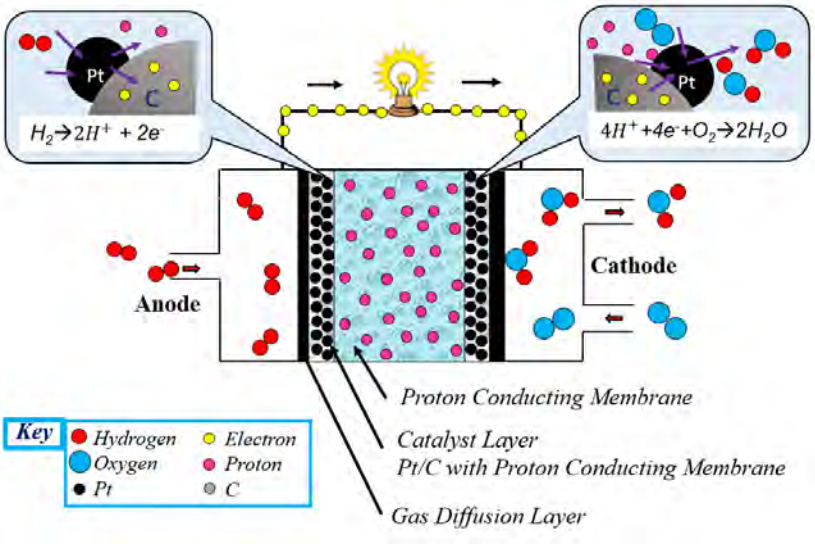

Figure 3.3: Fuel cell operation diagram

3.3. Advantages and disadvantages of PEM fuel cell

3.3.1. Advantages

The main advantages of fuel cells with respect to traditional energy converters are:

- **High conversion efficiency**: PEM fuel cells are characterised by high conversion efficiency, which can reaches up to $50°C$, comparatively with traditional energy [167]. Moreover, the efficiency increases with diminishing the load which is a very interesting characteristic for the transportation sector where part load

operation is the rule and the Internal Combustion Engine systems (ICEs) run at reduced efficiency in low load conditions.

- **Very low emissions**: by using PEM fuel cells, zero-emission performance is achieved since the only reaction product is water. Even with other types of fuel cells where natural gas or petrol is used as a fuel through a reforming process, CO_2 emissions will be lower than the ICE due to the fuel cell's higher efficiency [160].

- **Low noise levels**: due to the electrochemical reaction which is a conversion process that requires no moving parts, operation of the fuel cell is completely silent.

- **Low operating temperature**: the temperature operating range of PEM fuel cells is between $25°C$ and $100°C$, which leads to quick start up in comparison with other types of fuel cells [168].

3.3.2. Disadvantages

The biggest obstacle of fuel cells is their cost. Although many fuel cell systems are in use today, very few are currently cost-effective. For instance, for stationary fuel cells, typical capital cost to install the system is greater than 5000$/KW, while the target capital cost used by most energy generation developers is less than 1500$ [169]. Also, the need for high pressure of H_2 for efficient operation, the lifetime of the cell and the potential for the poisoning of the sensitive catalysts are all issues standing in the way of integration of fuel cell technology into the energy systems of the nations.

3.4. Fuel cell applications

PEM fuel cells have many potential shapes and sizes for several applications. The three main applications of PEM fuel cells are: transportation, portable uses and stationary installations.

3.4.1. Automotive applications

- Automobiles: many vehicle manufacturers like Ford, Nissan, Mazda, Hyundai, Fiat, Volkswagen.. are interesting in fuel cells, for that, they are researching and developing transportation fuel cells for future use in cars, buses and trucks [170–172].

- Scooters: in countries like India, many of the population use scooters, so this is a great application for fuel cells to eliminate emissions in Asia [173].

- Forklifts: fuel cells forklifts have potential lower total logistic cost because they require minimal refilling and less maintenance than electric forklifts, whose batteries must be periodically charged and refilled with water [174].
- Trains: an international consortium is developing the largest fuel cell vehicle, a 109 metric-ton, 1Mw locomotive for military and commercial railway applications [175].
- Planes: fuel cells represent an attraction for aviation because they offer low emissions and make no noise, and especially the army is interested in this application because of the noise. Companies like Boeing are developing a fuel cell plane [176].
- Boats: many countries have decided to use fuel cells in boats. For example, Iceland has decided to use fuel cells like auxiliary power in the boats of its large fishing fleet and, eventually, like primary power [177].
- Buses: many fuel cell buses have been developed in North and South America, Europe, Asia and Australia [178].
- Trucks: the department of Energy (DOE) has estimated that using fuel cell in 8 trucks would save 670 million gallons of diesel fuel per year and 4.64 million tons of CO_2 per year.

3.4.2. Stationary fuel cells

The primary stationary application of fuel cell technology is for the combined generation of electricity and heat, for buildings, industrial facilities or stand-by generators. Because the efficiency of fuel cell power systems is nearly unaffected by size, the initial stationary plant development has focused on the smaller, several hundred kw to low Mw capacity plants.

3.4.3. Portable power

Miniature fuel cells could replace batteries that power consumer electronic products such as cellular telephones, portable computers, and video cameras. Small fuel cells could be used to power telecommunications and satellites [179].

3.5. Static model of PEMFC

3.5.1. Reversible cell potential (E_{Cell})

The energy obtained in Equation (3.3) is called the enthalpy of formation $\triangle H$ (-285.84 J/mol). It can be divided into two kinds of energies: the first one is the thermal energy represented by the specific entropy $\triangle S$ (J/mol) multiplied by the temperature T (K), and the second is the useful work $\triangle G$ (J/mol). $\triangle G$ is also called

the negative thermodynamic potential (or Gibbs free energy). Therefore, the total energy as given in [180] is

$$\triangle H = \triangle G + T \times \triangle S. \tag{3.4}$$

$\triangle G$ can be extracted as an electric work, defined by the charge Q (coulombs) across the potential E_{Cell}. Q is the number of electrons (released from the anode), multiplied by the Faraday constant F (96485.309 C/mol). Therefore, the useful work can be calculated by Equation (3.5):

$$\triangle G = -Q \times E_{Cell} = -2 \times F \times E. \tag{3.5}$$

Using Equations (3.4) and (3.5), the PEMFC potential can be calculated by Equation (3.6), where $\triangle G$, $\triangle H$, and $\triangle S$ are negative due to the exothermic reaction (yields energy).

$$E_{Cell} = -\frac{\triangle G}{2 \times F} = -\frac{\triangle H - T \times \triangle S}{2 \times F}. \tag{3.6}$$

The values of the useful work $\triangle G$, which is given in Equation (3.5), also depend on the reactants. Therefore, it can also be calculated using Equation (3.7):

$$\triangle G = \triangle G^0 - RT[ln(P_{\mathrm{H_2}}) + \frac{1}{2} ln(P_{\mathrm{O_2}})] \tag{3.7}$$

where

- $\triangle G^0$: is the Gibbs free energy at standard condition (J/mol).
- R : is the universal gas constant (83.143 J/mol·K).
- T : is the cell operating temperature [K].
- P_{H2}: is the hydrogen partial pressure in [atm].
- P_{O2}: is the oxygen partial pressure in [atm]

The model equations so far accept as inputs the partial pressures of the gases. Deriving the perfect gas equation, a specific relation is derived between the partial pressure and the input flow rate of the fuel, the partial pressure of hydrogen and oxygen are given in Equations (3.8) and (3.9) [181–183].

$$P_{H2} = \frac{1/K_{H2}}{(1 + \tau_{H2})}(q_{H2} - 2I.K_r) \tag{3.8}$$

$$P_{O2} = \frac{1/K_{O2}}{(1 + \tau_{O2})}(q_{O2} - I.K_r) \tag{3.9}$$

Where:

- K_{H2} is the valve molar constant for hydrogen (kmol/s.atm).

- K_{O2} is the valve molar constant for oxygen (kmol/s.atm).
- q_{H2} is the hydrogen flow rate (kmol/s).
- q_{O2} is the hydrogen flow rate (kmol/s).
- K_r is a modeling parameter constant (kmol/ (sA)), which has a value of N/4F.

The response time of hydrogen τ_{H2} (s) and oxygen τ_{O2} (s) can be determined using Equation (3.10) and (3.10) respectively.

$$\tau_{H2} = \frac{V_{an}}{R.T.K_{H2}} \tag{3.10}$$

$$\tau_{O2} = \frac{V_{an}}{R.T.K_{O2}} \tag{3.11}$$

Where

- V_{an} is volume of the anode.

By replacing Equation (3.7) into Equation (3.6), the PEMFC potential can be given as

$$E_{Cell} = -\frac{\Delta G}{2F} = -\frac{\Delta G^0}{2F} + \frac{RT}{2F}[ln(P_{\mathrm{H_2}}) + \frac{1}{2}ln(P_{\mathrm{O_2}})] \tag{3.12}$$

At the standard condition ($T_{std} = 25$ °C, $1atm$). The term $\frac{\triangle G^0}{2.F}$ is equal to $E_0 = 1.229$ V. It varies with the temperature according to the following expression:

$$-\frac{\Delta G}{2F} = 1.229 + (T - 298)(\frac{\Delta S^0}{2F}). \tag{3.13}$$

Using the standard thermo-dynamical relations as developed in [184], Equation (3.12) becomes

$$E_{Cell} = 1.229 - 0.85 \times 10^{-3}(T - 298) + 4.3 \times 10^{-5} \times T[ln(P_{\mathrm{H_2}}) + \frac{1}{2}ln(P_{\mathrm{O_2}})]. \tag{3.14}$$

Using Equation (3.14), the implementation of the thermodynamic potential of the PEMFC in Matlab/Simulink is represented in Figure 3.4; while the output signal of this equation is shown in Figure 3.5.

However, the potential of the PEMFC is significantly less than the values of the theoretical potential, which is given in the above equation, due to the existence of losses, including polarization and interconnection losses. According to [184], the main voltage losses in a PEMFC are the electric losses, which can be classified into three main polarization losses: the activation polarization losses V_{act}, the ohmic polarization losses V_{ohm}, and the concentration polarization losses V_{conc}.

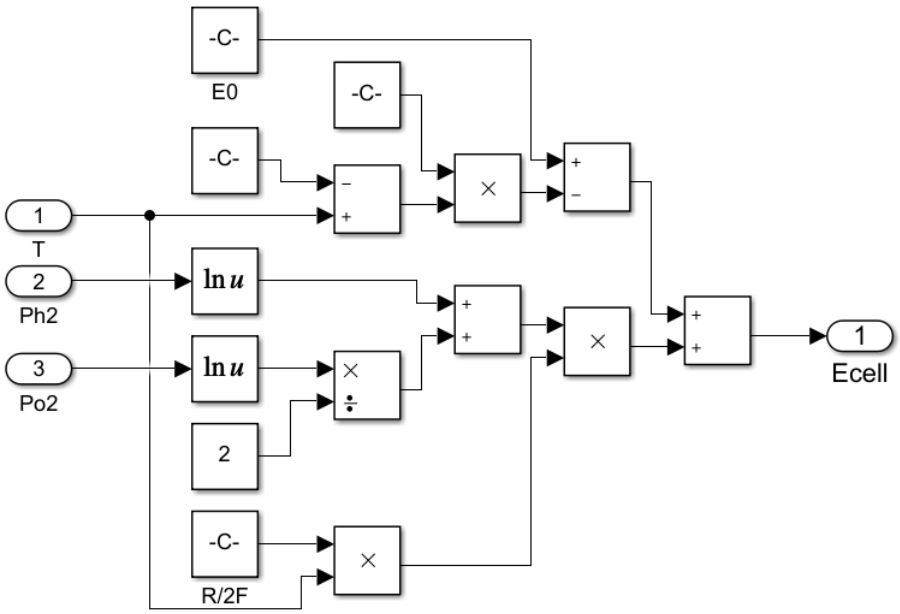

Figure 3.4: Synoptic diagram of the thermodynamic potential of the PEMFC

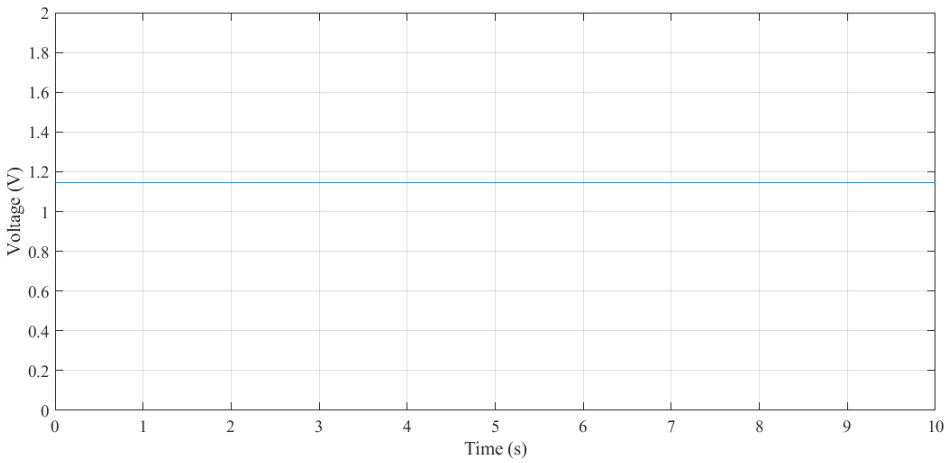

Figure 3.5: Thermodynamic potential of the PEMFC

3.5.2. Activation polarization loss

The activation polarization loss V_{act} is characterized by a strong non-linear demeanour. This is due to the reaction kinetics at the electrode of the PEMFC. The activation polarization is important at low current densities (mostly affect in the initial part of the polarization curve) due to the slowness and maintenance of the chemical reaction. The activation polarization loss can be calculated by Equation (3.15) [181].

$$V_{act} = \xi_1 + \xi_2.T + \xi_3.T.ln(C_{O2}) + \xi_4.T.ln(I) \tag{3.15}$$

Where

- I : is the cell load current in [A].
- $\xi_{(1-4)}$: are parametric coefficients ,defined on the basis of kinetic, thermodynamic and electrochemical phenomena. Their values in the semi-empirical equations are given as follows: Parametric coefficients $k_1 = 0.9514(V), k_2 = -0.00312(V/K), k_3 = -7.4.10^{-5}(V/K), k_4 = 1.87.10^{-4}(V/K)$.
- C_{O2} : is the concentration of oxygen dissolved in a water film interface in the catalytic surface of the cathode in (mol/cm^3), estimated on the basis of the oxygen partial pressure and cell temperature by the law of Henry.

The concentration of oxygen C_{O2} can be calculated using Equation (3.16).

$$C_{O2} = \frac{P_{O2}}{5.08 \times 10^6 . exp^{(\frac{-498}{T})}} \tag{3.16}$$

Using Equation (3.15) and (3.16), the implementation of the activation polarization loss V_{act} in Matlab/Simulink is represented in Figure 3.6; while the output signal of this equation is shown in Figure 3.7.

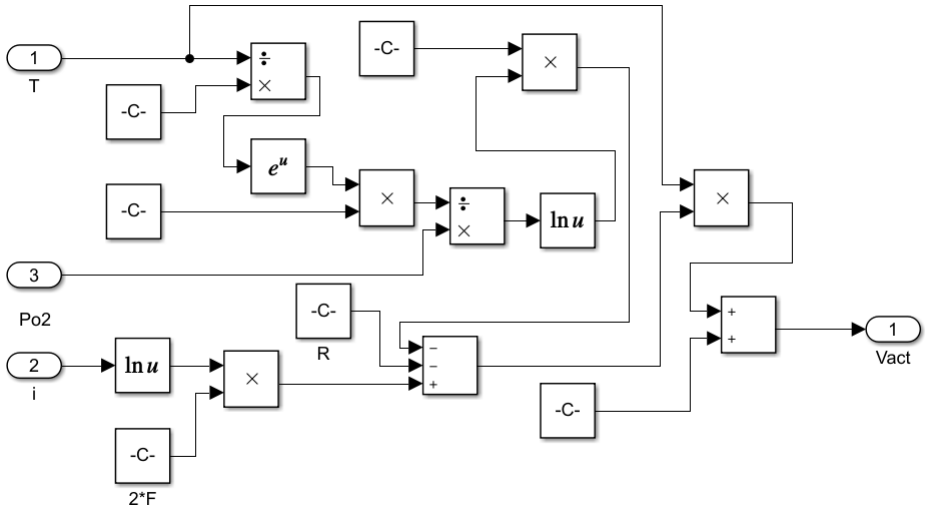

Figure 3.6: Synoptic diagram of the activation polarization loss

3.5.3. Ohmic polarization loss

The ohmic polarization loss V_{ohm} is affected by the ohmic losses of energy derived from the impedance of the membrane. It is also influenced by the resistances of the construction materials (collecting plates and carbon electrodes). The ohmic losses can be formulated as Equation (3.17) [181].

$$V_{ohm} = I.(R_m + R_c) \tag{3.17}$$

Where

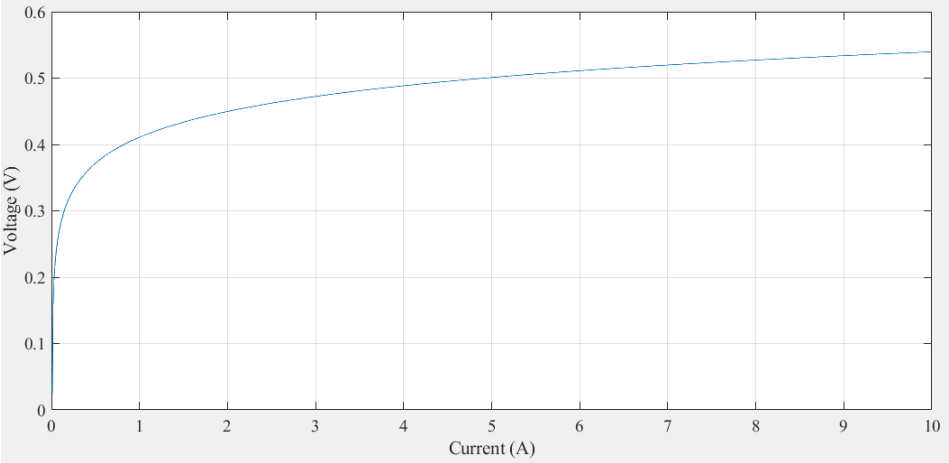

Figure 3.7: Activation polarization loss

- R_m : is the equivalent resistance of the electron flow.
- R_c : is the proton resistance considered as constant.

The equivalent resistance can be calculated using Equation (3.18), where the expression of the specific resistance ρ_M (Ω.cm) is given in Equation (3.19) [181–183].

$$R_m = \frac{\rho_M . l}{A} \tag{3.18}$$

$$\rho_M = \frac{181.6[1 + 0.03(\frac{T}{A}) + 0.062(\frac{T}{303})^2.(\frac{I}{A})^{2.5}]}{[\psi - 0.634 - 3(\frac{I}{A})].exp^{[4.18(T-303)/T]}} \tag{3.19}$$

Where

- A : is the membrane active area (cm^2).
- l : is the thickness of the membrane (cm).
- ψ is an adjustable parameter with a possible maximum value of 23.
- The exponential term in the denominator is the temperature factor correction if the cell is not at 30°C.
- $\frac{181.6}{\psi - 0.634}$ is the specific resistance (Ω.cm) at no current and at 30°C.

Using Equation (3.17), (3.18) and (3.19), the implementation of the ohmic polarization loss V_{ohm} in Matlab/Simulink is represented in Figure 3.8; while the output signal of this equation is shown in Figure 3.9.

3.5.4. Concentration polarization loss

The concentration polarization loss V_{con} (also called mass transportation loss) is the phenomenon that occurs due to the propagation of ions through the electrolyte

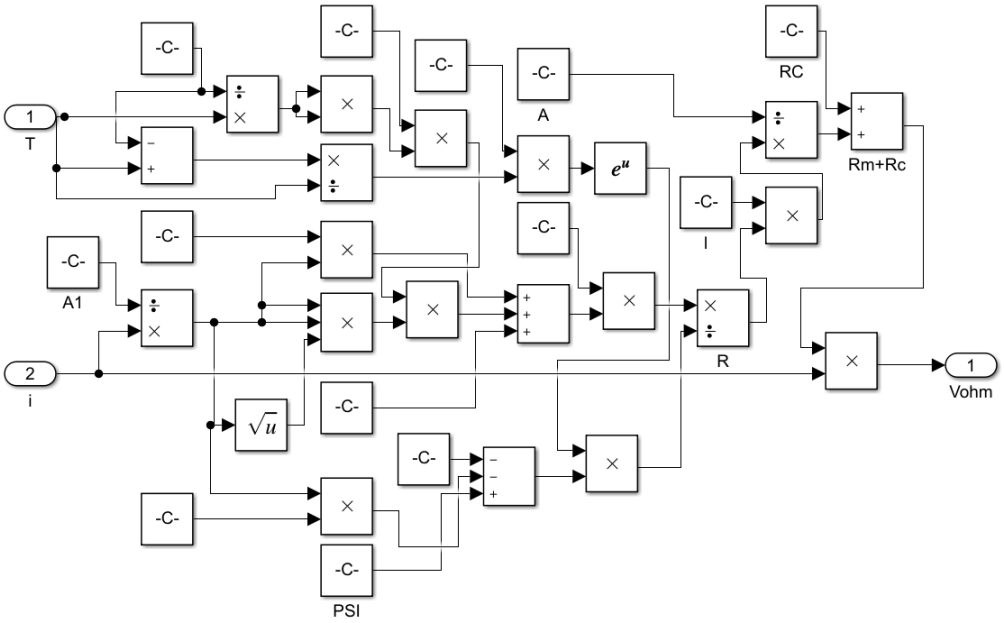

Figure 3.8: Synoptic diagram of the ohmic polarization loss

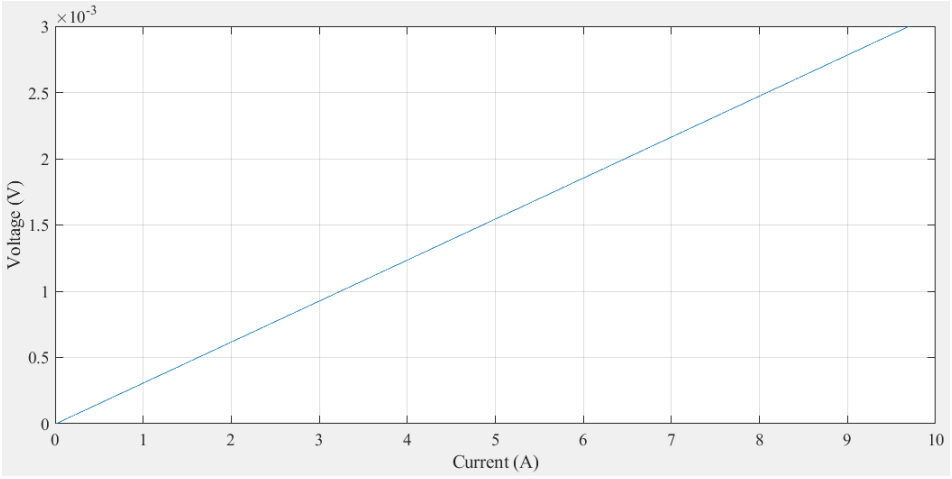

Figure 3.9: Ohmic polarization loss

membrane which leads to the lack of reactants mass transfer at the electrode caused by the rapid consumption of the respective reactant. Therefore, it can be represented by the loss of the chemical reaction. This loss is important especially at higher current densities. The concentration polarization loss V_{con} can be calculated using Equation (3.20)

$$V_{con} = -B \times ln(1 - \frac{J}{J_{max}}) \tag{3.20}$$

Where

- B is a parameter that depends on the type of cell.

- J represents the current density passing through the cell at each moment (A/cm^2).

The current density J can be determined using Equation (3.21).

$$J = \frac{I}{A} \tag{3.21}$$

Using Equation (3.20) and (3.21), the implementation of the concentration polarization loss V_{con} in Matlab/Simulink is represented in Figure 3.10; while the output signal of this equation is shown in Figure 3.11.

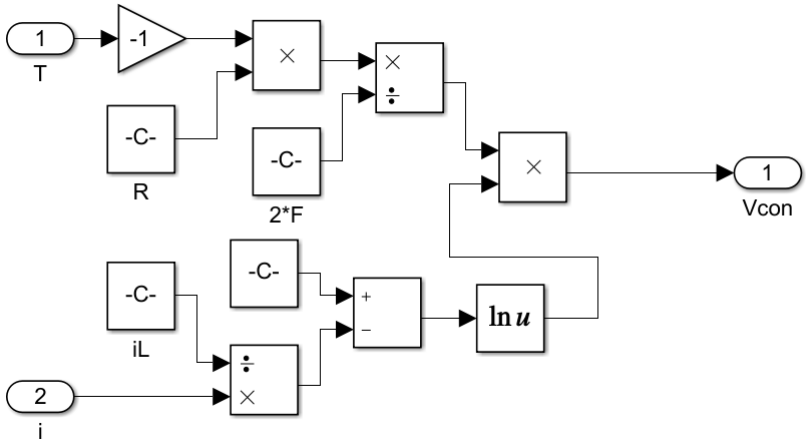

Figure 3.10: Synoptic diagram of the concentration polarization loss

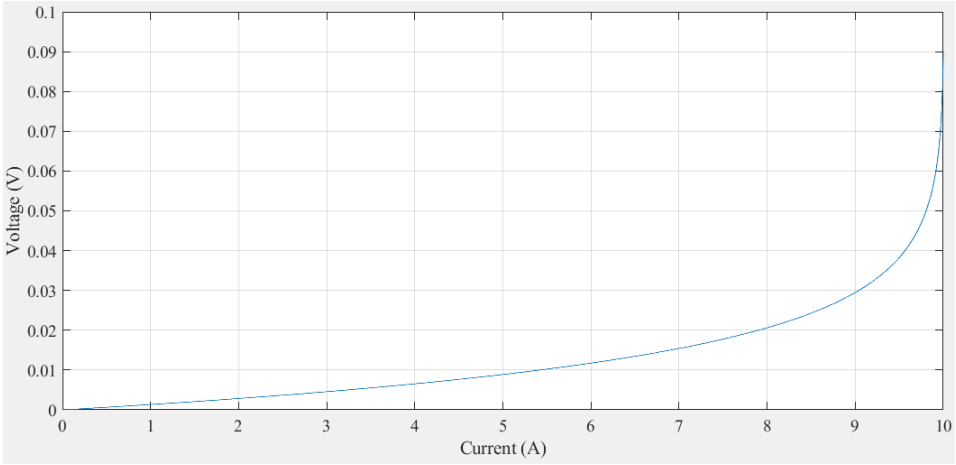

Figure 3.11: Concentration polarization loss

3.5.5. PEMFC potential

The fuel cell potential not only varies with the activation, ohmic, and concentration losses; but also varies with fuel crossover and internal currents due to the waste of

fuel and electron conduction through the electrolyte. However, these internal currents and fuel losses are very small and their effects are usually negligible. Therefore, according to [60], the voltage generated by an individual fuel cell can be expressed as Equation (3.22), where the voltage-current characteristic is shown in Figure 3.12.

$$V_{fc} = E_{Cell} - V_{act} - V_{ohm} - V_{con}. \tag{3.22}$$

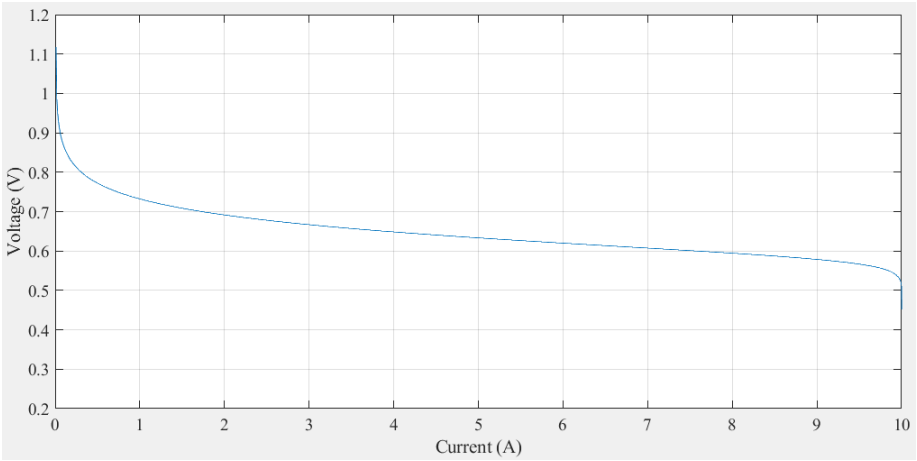

Figure 3.12: PEMFC voltage

However, to generate the required power, N_{cell} individual cells are lumped together and stacked in series. These cells are called stack and their potential can be calculated using Equation (3.23) [60].

$$V_{stack} = N_{cell}.V_{Fc} = N_{cell}.(E_{Cell} - V_{act} - V_{ohm} - V_{con}) \tag{3.23}$$

Where

- N_{cell} is the number of individual cells used in the stack (N_{cell}=10)

The parameters of the fuel cell model used in the above equations are summarized and enlisted in Table 3.2.

The implementation of the PEMFC stack voltage V_{stack} in Matlab/Simulink is represented in Figure 3.13; while the output signal of this equation is shown in Figure 3.14.

3.5.6. PEMFC stack power

The PEMFC stack power can be linked to any load without restriction related to the load type, whereas the power supplied by the stack is enough to feed it. The electrical power supplied by the stack to the load can be determined by Equation

Table 3.2: Parameter explanations of the PEMFC model.

Parameter	**Symbole**	**Value**
Cell operating temperature	T	[K]
Cell standard temperature	T_{std}	298.15 [K]
Cell operating current	I	[A]
Universal constant of the gases	R	83.143 [J.mol^{-1}.K^{-1}]
Constant of Faraday	F	96,485.309 [C.mol^{-1}]
Maximum current density	J_{max}	0.062 A cm^{-1}
Current density	J	[A.cm^{-2}]
Change in the free Gibbs energy	ΔG	[J.mol^{-1}]
Change of entropy	ΔS	[J.mol^{-1}]
Enthalpy of formation	ΔH	-285.84 [kJ.mol^{-1}]
Change in the Gibbs free energy at standard condition	ΔG^0	-237.2 [kJ.mol^{-1}]
Change of entropy at standard condition	ΔS^0	[J.mol^{-1}]
Electrochemical thermodynamics potential	E	[V]
Standard potential of the fuel cell	E_0	1.229 [V]
Nombre of cells	N_{cell}	10
Membrane active area	A	[162 cm^2]
Membrane thickness	l	175.10^{-6} cm
Adjustable parameter	ψ	23
Hydrogen and oxygen partial pressures	P_{H2},P_{O2}	[atm]
Oxygen concentration	C_{O2}	[mol.cm^{-3}]
Fuel cell voltage	V_{fc}	[V]
Activation losses	V_{act}	[V]
Ohmic losses	V_{ohm}	[V]
Concentration losses	V_{conc}	[V]
Constant parameters	λ	0.1 [V]
Electric charge	Q	[coulombs]
Equivalent resistance of the electron flow	R_{eq}	Ω
Proton resistance	R_p	Ω
Experimental coefficient	ξ_1	0.9514 V
Experimental coefficient	ξ_2	-0.00312 V/K
Experimental coefficient	ξ_3	-7.4 .10^{-5} V/K
Experimental coefficient	ξ_4	1.87 .10^{-4} V/K

(3.24), where the output signal of this equation is shown in Figure 3.15.

$$P_{stack} = I.V_{stack} \tag{3.24}$$

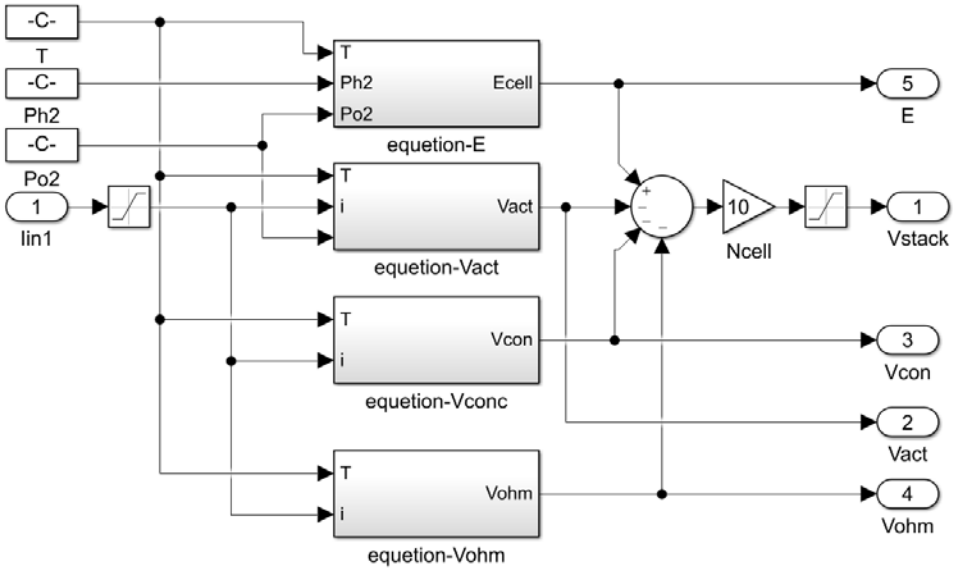

Figure 3.13: Synoptic diagram of the PEMFC voltage

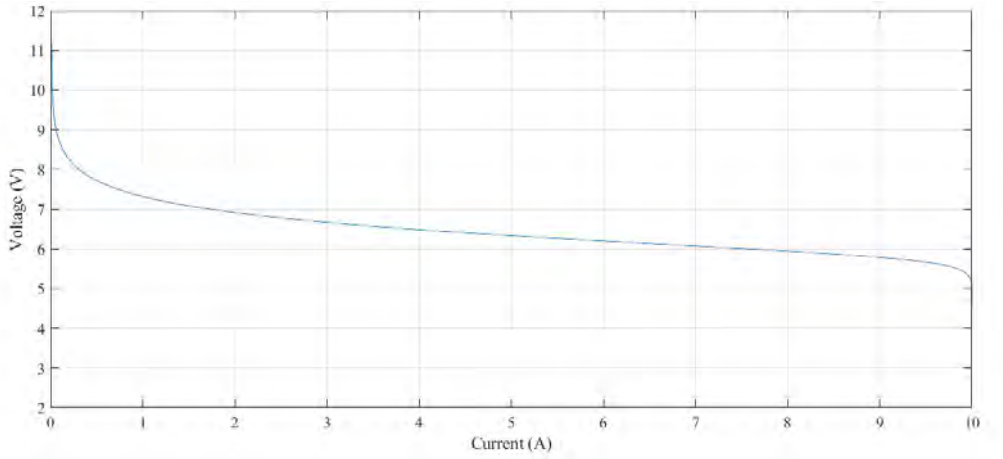

Figure 3.14: PEMFC stack voltage

3.5.7. Effect of temperature and hydrogen on the performance of the PEM fuel cell stack

The polarization curves of the PEM fuel cell stack at different operating temperatures of Figure 3.16a showed that the stack performance is improved by increasing temperature from 298.15 K to 313.15 K. However, according to the results, although the temperature variation was large, only slight improvement in the fuel cell efficiency is accrued. On the other hand, The polarization curves for different operating pressure presented in Figure 3.16b have demonstrated that the stack performance is also largely influenced by varying the operating hydrogen pressure. Hence, the operating pressure of the hydrogen was varied from 0.2 atm to 0.8 atm at a constant operating temperature of 313.15 K. When the hydrogen partial pressure is equal to

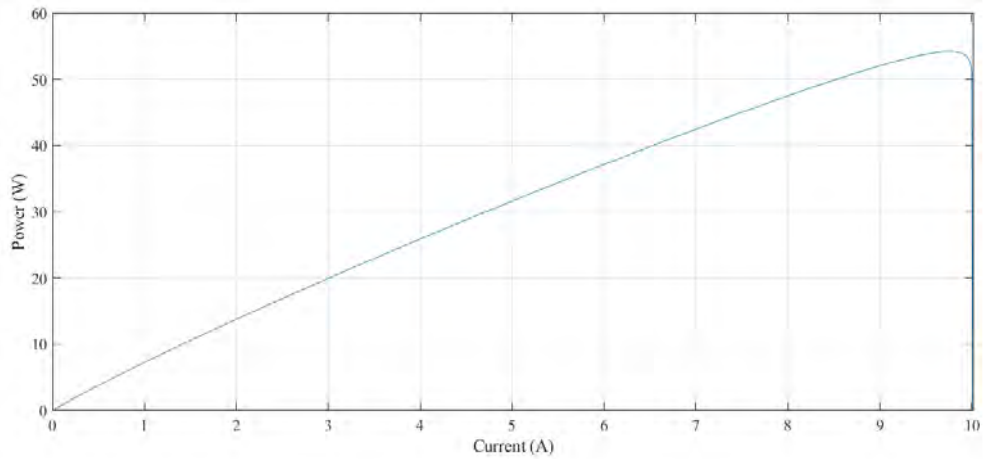

Figure 3.15: PEMFC stack power

0.2 atm, the voltage and the power generated by the stack are the lowest compared to other gasses partial pressure. When the hydrogen partial pressure is increased to 0.8 atm, the output voltage and the power produced by the fuel cell are the highest values. Therefore, the efficiency of the fuel cell is improved by increasing the hydrogen partial pressure.

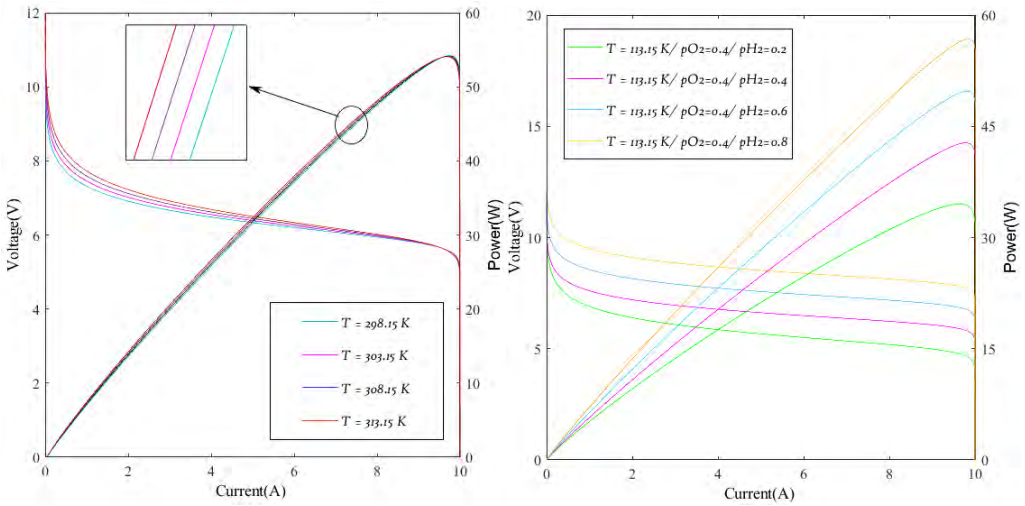

(a) Different operating temperatures. (b) Different hydrogen partial pressures.

Figure 3.16: Effect of temperature and hydrogen on the performance of the PEM fuel cell stack.

3.6. Dynamic model of PEMFC

In a PEM fuel cell the two layer separated by the membrane act as double charged layer, which can store electrical energy, due to this property this can be

treated as a capacitor. R_{act}, R_{con} and R_{ohm} are the equivalent resistance for different types of fuel cell losses [28]. The equivalent electrical circuit model of fuel cell by considering all the effect discussed above is shown in Figure 3.17.

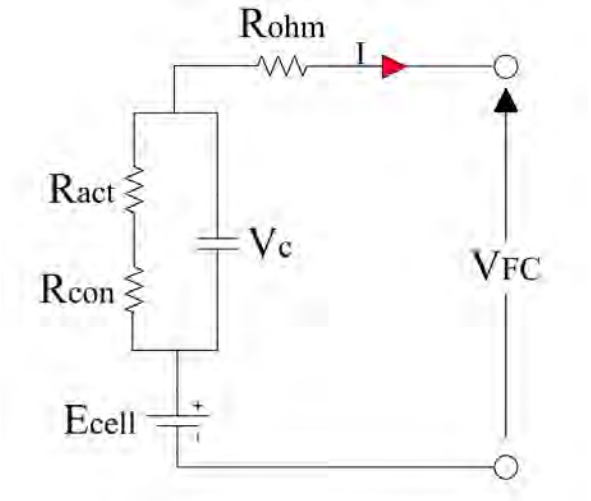

Figure 3.17: Equivalent electrical circuit of PEM fuel cell

The kirshof law gives the following equation:

$$I = C\frac{dV_d}{dt} + \frac{V_d}{R_{con} + R_{act}} \tag{3.25}$$

Tt can be writen as the equation below:

$$\frac{dV_d}{dt} = \frac{1}{C}I - \frac{1}{\tau}V_d \tag{3.26}$$

Where

- V_d represents the dynamical voltage across the equivalent capacitor (associated with η_{act} and η_{con}).
- C is the equivalent electrical capacitance.
- τ is the fuel cell electrical time constant dependant of the cell temperature given by the equation (3.27)

$$\tau = C(R_{act} + R_{con}) = C\left(\frac{\eta_{act} + \eta_{con}}{I}\right) \tag{3.27}$$

Including this electrical dynamic behavior term, the resulting FC voltage in (2.3)is then changed by the equation as given below:

$$V_{cell} = E_{Cell} - V_d - I.R_{ohm} \tag{3.28}$$

Where

- $R_{ohm}, R_{act}, R_{con}$ are respectively the representation for the ohmic, the activation and the concentration resistance.
- C corresponding to the membrane capacitance due to the double layer effect.

Using (2.14), (2.15) and Laplace transformations, transfer function (2.16) was obtained, in which s represents Laplace operator:

$$V_{cell} = E_{Cell} - \left(\frac{R_{act} + R_{con}}{(R_{act} + R_{con})C.s + 1} + R_{ohm} \right) I \tag{3.29}$$

3.7. Conclusion

In this chapter, the basics, advantages and disadvantages of the PEM fuel cell are reviewed. It has been proven that although that the fuel cell suffers from several disadvantages such us the high cost, it has received growing attention due to its considerable advantages which make it the energy of the future.

In the second part of this chapter, the static and dynamic model of the PEM fuel cell are developed on Matlab-Simulink. Finally the effect of temperature and hydrogen on the fuel cell efficiency are studied and it has been proven that the efficiency can improve by increasing the cell temperature and input fuel.

Chapter 4

PEM Fuel Cell Model Based Artificial Neural Networks (ANNs)

4.1. Introduction

ANNs have been considered as attractive and powerful tools to predict and approximate linear, nonlinear and even complex models, based only on input-output data mapping [185–187]. Actually, an ANN consists of input and output layers and at least one hidden interconnection layer. A general architecture of ANN with N_1 inputs, N_2 outputs and L hidden layers is depicted in Figure 4.1.

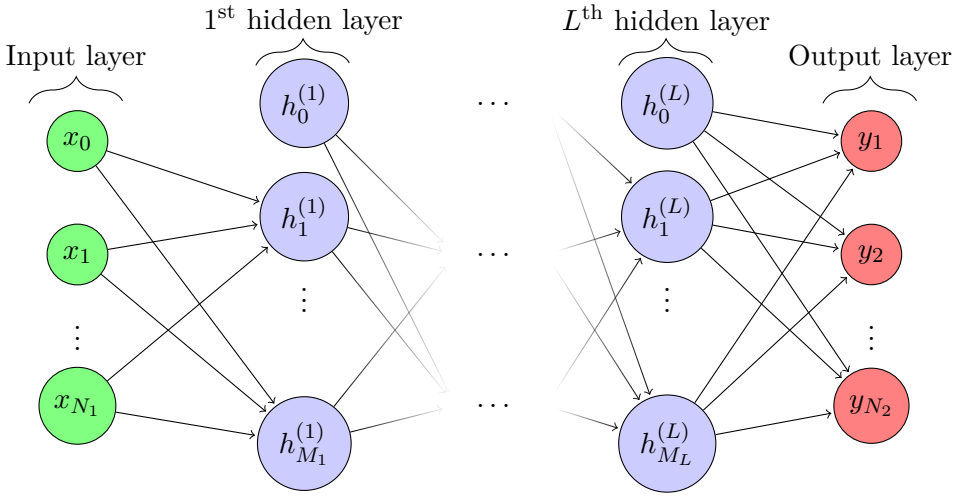

Figure 4.1: Network graph of N_1 input units, N_2 output units and L-layer perceptron where each hidden layer contains M_j hidden units.

ANNs can manipulate information just like the human brain thanks to the computational features of their basic units (also called nodes or neurons) which take a set of inputs, multiply them by weighted values and put them through an activation function. The schematic structure of the ith hidden artificial neuron at the jth hidden layer can be depicted as Figure 4.2.

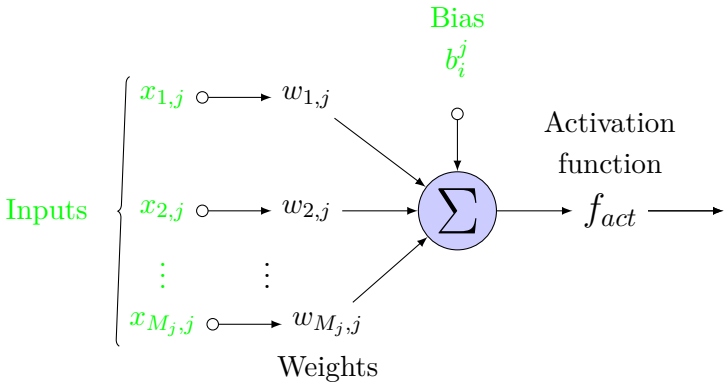

Figure 4.2: Structure of a single artificial neuron in a neural network.

There are several topologies of NNs in deep learning and they can be classified into two groups of algorithms. The first group contains the ones that were used for supervised deep learning problems such as fully-connected feed-forward algorithms (Multi-Layer Perceptron, Radial Basis Network, etc.), recurrent NNs algorithms (long short term memory, gated recurrent unit, gated feed-forward, etc.) and convolutions NNs algorithms (deep convolutional NNs, deep convolutional inverse graphics network, deconvolutional network, etc.). The second group contains the ones that were used for unsupervised deep learning problems such as restricted Boltzmann machine algorithms (deep belief network, deep Boltzmann machine, etc.) and ML auto-encoder algorithms (variational auto-encoder, denoising auto-encoder, sparse auto-encoder, etc.). However, since modelling the fuel cell is a supervised learning problem, different structures of feed-forward neural network perceptron (FFNNP) with back-propagation learning rule have been implemented in Matlab/Simulink^R and Neureal Network Toolbox^{TM} to predict the performance of a commercial fuel cell system (Heliocentris FC50).

4.2. Data Collection and Analysis

4.2.1. Data collection

The first and the most important step in the supervised learning process is gathering the data. In other words, to carry out good training, vast amounts of real-world data is required since the more data we provide, the more predictive power can be obtained. Besides, the collected dataset should be well distributed throughout the operation range so as to represent the behaviour of the fuel cell in each operating power point. To this end, a continuous triangular signal with a period of 15 s (7.5 s for each positive/negative slop) was built and supplied to the duty cycle of the boost converter so as to vary the stack current from the minimum to the maximum operating value. The selection of the period was made based on the characteristics of the fuel cell data acquisition software since it measures the data each 0.5 s. In other

words, 15 samples in different operating current values will be measured fore each positive/negative slop. Figures 4.3 and 4.4 show, respectively, the Simulink blocks used to design the triangular signal and the generated signal. The maximum value of this signal (0.8) drives the fuel cell to operate at the highest current value [8–9A] where the minimum value (0.5) drives the fuel cell to operate at the lowest operating current [0.2–0.5A]. These values can be adjusted via the increase/decrease of the output load resistance value. We have avoided operating currents above 9A since the fuel cell used in this study (Heliocentris FC50) is occupied with a security system that turns off the fuel cell in case of higher currents/temperatures [145, 188].

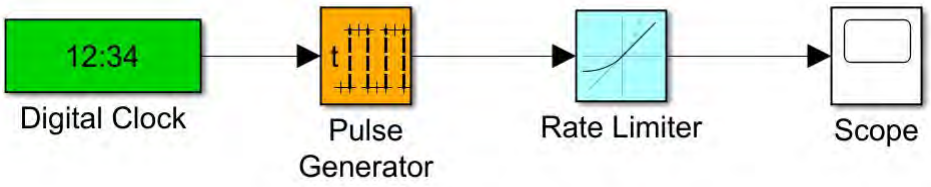

Figure 4.3: Triangular signal design.

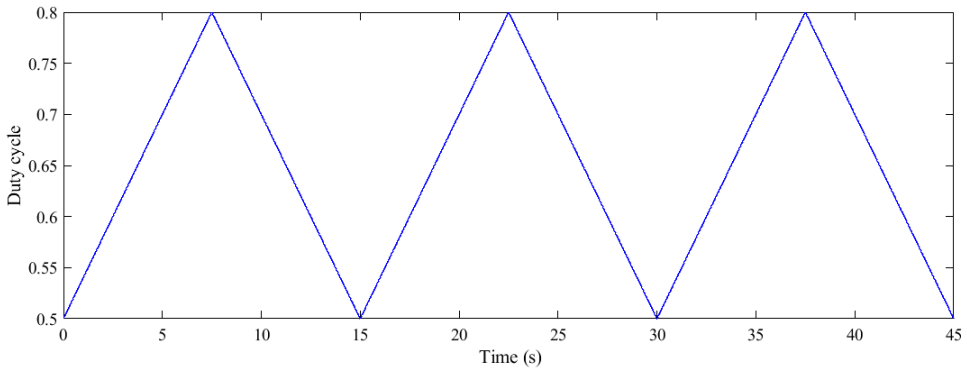

Figure 4.4: Triangular signal output.

To obtain data for different operating conditions, variations in temperature, humidity, hydrogen and airflow are required. It should be noted that the fuel cell contains an integrated control system that not only controls the supplied hydrogen but also provides an option to set the fans of the fuel cell at the automatic mode. By using the auto mode, the fans will automatically control the temperature, the humidity and the supplied airflow. However, to provide large degrees of freedom, the auto mode option of the fans was not considered. Therefore, a database containing 20,512 samples for different operating current, temperature and fan power were recorded and presented in Figure 4.5. This latter also shows the influence of the air flow on the fuel cell performance but the effect of temperature is still not well presented. Therefore, a 3D graph that clearly shows the effect of both temperature and air flow on the stack performance is presented in Figure 4.6.

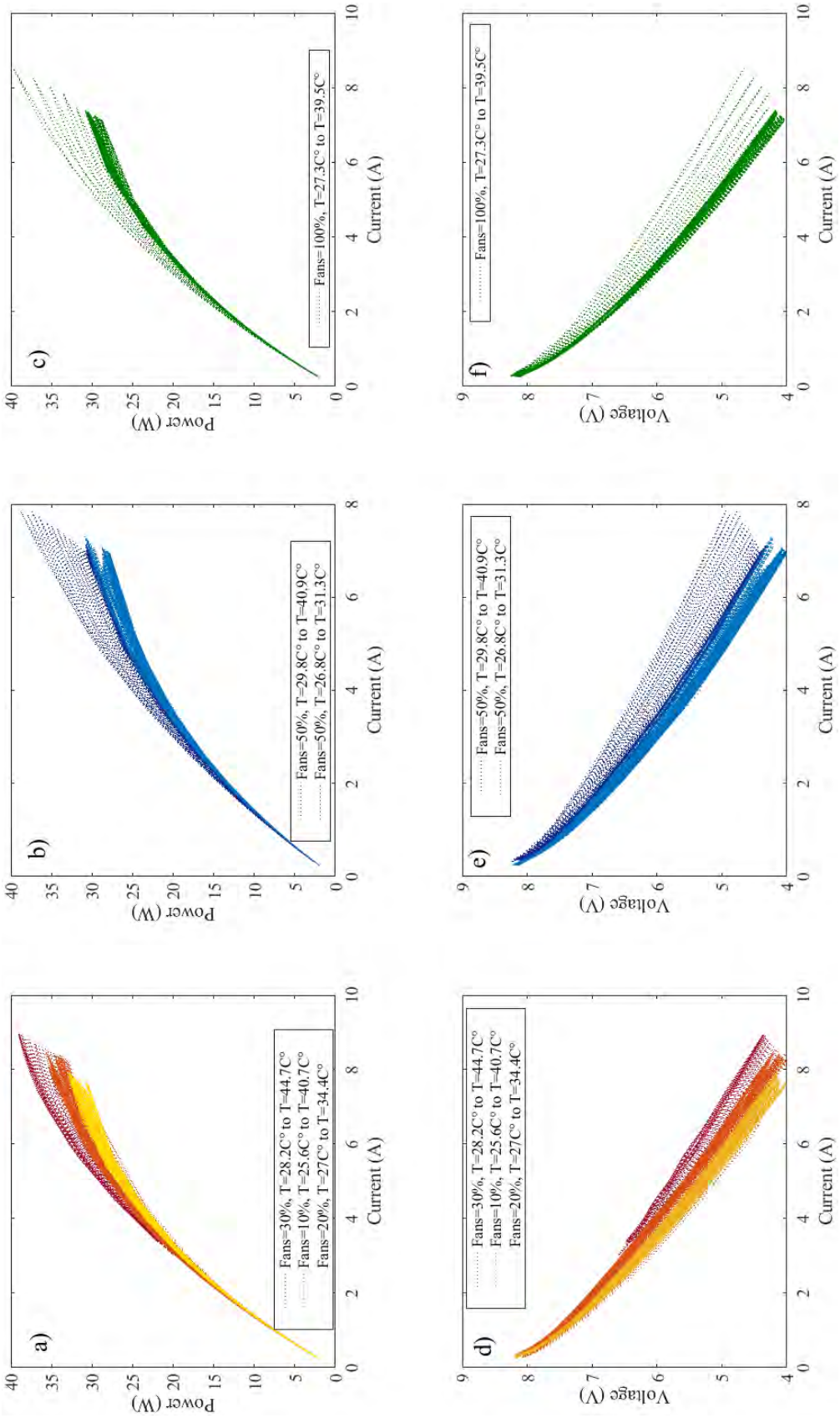

Figure 4.5: I_{stack}-P_{stack} and I_{stack}-V_{stack} measured data of Heliocentris FC50 fuel cell.

According to this latter, it is shown that at low air flow (fans power = 10%), by varying the temperature from 25 °C to 43 °C the stack performance improves in the beginning, then becomes almost constant and finally, it deteriorates for higher temperatures. At medium air flow (fans power = 50%), the stack performance improves with increasing temperature. However, for higher temperatures only slight improvements occur since the membrane requires an additional amount of water content. Regarding the last case at which the air flow is set at its maximum value (fans power = 100%), the stack performance improves largely with a temperature increase from $T = 25$ °C to over 40 °C. It is noticed that even for higher temperatures, the stack performance is still improving and this is due to the well humidification provided by the fans.

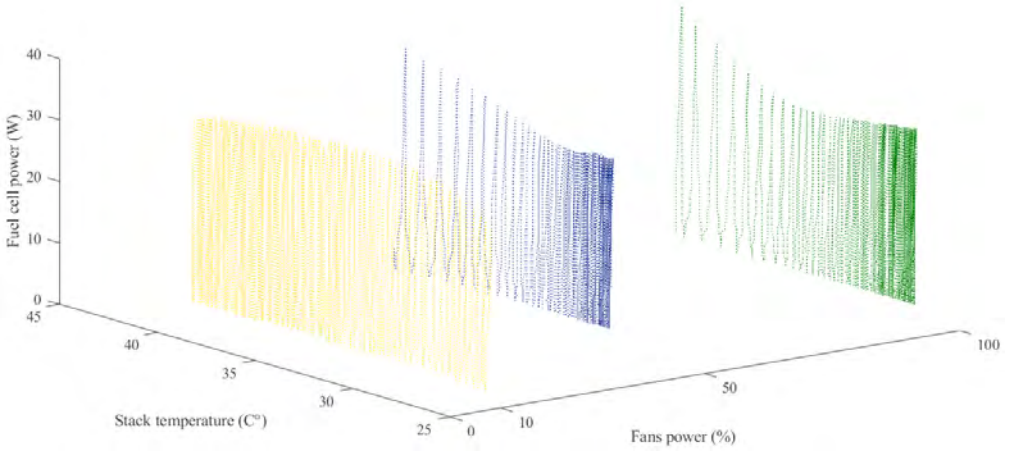

Figure 4.6: The Heliocentris FC50 stack power according to air flow and stack temperature.

4.2.2. Inputs and outputs selection

Another factor that can improve the accuracy of the learned function is the selection of the inputs and outputs since the accuracy is strongly dependent on how the inputs are represented. The inputs should be entered as a feature vector that contains enough information to properly predict the output; but also, it should not be too large due to the dimensionality curse effect. In this study, the input variables are selected as: stack current I_{stack} (A), stack temperature T (°C) and fans power (%), to predict the stack voltage V_{stack} (V)

4.2.3. Data division (training, validation and test)

When enough data is available, the next step is to split this data into three subsets which are training, validation and test. The training dataset needs to be fairly large and contains a variety of data in order to contain all the needed information. Many researchers have proposed a training set of 70%, 80% and 90% [189–192]; where the

rest of data were divided between the validation and test. In this study, the recorded data was divided as the following: training = 14,358 data points (70% of whole data), validation = 3077 data points (15% of whole data) and test = 3077 data points (15% of whole data). The training subset is used to adjust the network via minimising its error. In other words, it is used for computing the gradient and updating the weights and biases of the NNs. The validation subset is used for measuring the network generalisation and to stop the training when the generalisation stops improving. In more detail, when the training begins to over-fit the data, the validation error starts to rise. Therefore, the weights and biases of the network are saved at the minimum validation error point so as to balance the accuracy of the learned function versus over-fitting. The test subset is used to evaluate the performance of learned function when applying a new set. Actually, the test subset has no influence on the determination of the learned function parameters, but it is a kind of 'final exam' to test the performance of each predicted function.

4.3. Designing the Network

Based on Figure 4.2, the output of the $h_i^{(j)}$ hidden layer unit can be calculated as Equation (4.1) [193].

$$h_i^{(j)} = f_{act}\left[\left(\sum_{i=0}^{M_j} w_{i,j}x_{i,j}\right) + b_i^j\right] \tag{4.1}$$

where, j = [1,2, ..., L] refers to the jth hidden layer, i = [1,2, ..., M_j] refers to the ith neuron in the hidden layer j, M_j = [M_1,M_2, ..., M_L] refers to the number of neurons at each layer, $x \in \mathbb{R}^m$ are numerical inputs, $w \in \mathbb{R}^m$ are weights associated with the inputs, $b \in \mathbb{R}$ are biases. f_{act} is the activation function which is used to introduce non-linearity into the output of the artificial neuron. Actually, this is important since most of data in the real world is nonlinear and the neurons should learn these nonlinear representations. There are many activation functions that can be used in practice such as sigmoid, tanh, ReLu, etc. [194]. In this work a tansig function which is given in Equation (4.2) is used.

$$f_{act}(x) = \frac{2}{1+e^{-2x}} - 1 \tag{4.2}$$

By using Equations (4.1) and (4.2), the k^{th} output layer unit can be calculated as Equation (4.3).

$$y_k = f_{act}^{out}\left[\left(\sum_{i=0}^{M_L} w_{i,L}h_i^{(j)}\right) + b_k\right] \tag{4.3}$$

where k = [1,2, ..., N_2] and f_{act}^{out} is a linear transfer function or also known as *purelin*,

its mathematical expression is given in Equation (4.4)

$$purelin(x) = x \tag{4.4}$$

To train the FFNNP, several optimisation algorithms can be used to minimise the performance function (also known as loss/cost function) [189, 195–197]. These algorithms use either the Jacobian of the network errors or the gradient of the network performance. Both Jacobian and gradient are computed via the back-propagation algorithm which is an efficient computational trick for calculating derivatives inside the deep feed-forward NNs. In this work, we made a comparison study among the four major used algorithms including the Levenberg–Marquardt (LM), Bayesian regularization (BR), BFGS quasi-Newton and Scaled conjugate gradient (SCG). For each training algorithm, the following basic system training parameters are used: maximum number of epochs = 5000, learning rate = 0.01, performance goal = 0, time of training = Infinity. All these parameters were checked for different number of neurons and hidden layers as presented in Table 4.1.

The performance of each training algorithm was measured via the mean squared error (mse) which is given in Equation (4.5), where y_i^* is the desired output (target), y_i is the actual (predicted) output, and N is the number of dataset.

$$F = mse = \frac{1}{N}\sum_{i=0}^{N}(e_i)^2 = \frac{1}{N}\sum_{i=0}^{N}(y_i^* - y_i)^2 \tag{4.5}$$

The best performance, in terms of training time and mean squared error mse, of each algorithm is tinted with green colour (Table 4.1). The predicted output results as well as the error that corresponds to the best performance (green cells) for each training algorithm are respectively shown in Figures 4.7 and 4.8.

Table 4.1: Mean squared error of different FFNNP structures/algorithms.

Training algorithms	Hidden layers	MSE/ Time(s)	Number of neurons for each hidden layer							
			1	**5**	**10**	**15**	**20**	**25**	**30**	**35**
LM	**1**	**MSE**	0.0241	0.0052	0.0025	0.0016	0.0017	0.0015	0.0015	0.0014
		Time	1.9520	9.3870	17.1920	6.9760	6.6720	24.9600	21.1340	16.2700
	2	**MSE**	0.0248	0.0036	0.0017	0.0014	0.0014	0.0012	0.0013	0.0012
		Time	8.1680	8.1740	4.4090	31.4030	29.4810	90.1620	54.3320	235.6880
	3	**MSE**	0.0244	0.0017	0.0015	0.0012	0.0012	0.0011	0.0011	0.0012
		Time	6.9090	10.7930	6.9720	38.5620	43.3770	304.0570	193.9730	346.6590
BR	**1**	**MSE**	0.0242	0.0106	0.0022	0.0015	0.0015	0.0015	0.0014	0.0014
		Time	4.3540	6.5850	33.0220	20.9350	40.8840	69.8870	225.6650	268.2380
	2	**MSE**	0.0243	0.0022	0.0014	0.0011	0.0010	0.0009	0.0008	0.0008
		Time	41.7	6.5	132.6	260.6	657.3	1583.5	2954.5	5438.6
	3	**MSE**	0.0243	0.0015	0.0012	0.0009	0.0008	0.0007	0.0006	0.0006
		Time	41.4	67.6	126	518.2	1064.3	4741.2	6936.3	13217.4
BFG	**1**	**MSE**	0.0245	0.0082	0.0065	0.0036	0.0030	0.0029	0.0022	0.0023
		Time	2.2560	2.4880	1.8110	4.7750	5.3230	7.8430	13.4960	7.9190
	2	**MSE**	0.0245	0.0088	0.0024	0.0017	0.0016	0.0020	0.0019	0.0017
		Time	1.6280	2.2800	8.2930	26.7120	25.1810	20.8690	66.0140	223.0960
	3	**MSE**	0.0251	0.0048	0.0053	0.0019	0.0017	0.0016	0.0018	0.0018
		Time	1.6	8.1	15.6	27.8	85.0	278.1	601.0	1125.1
SCG	**1**	**MSE**	0.0258	0.0145	0.0100	0.0090	0.0070	0.0052	0.0096	0.0070
		Time	1.2110	1.1140	1.5290	2.4660	2.8820	5.4720	2.0470	4.3250
	2	**MSE**	0.0261	0.0204	0.0317	0.0040	0.0041	0.0023	0.0051	0.0027
		Time	1.0180	1.0500	0.7660	5.9290	6.2720	11.5320	5.1960	27.5590
	3	**MSE**	0.0261	0.0082	0.0061	0.0055	0.0028	0.0025	0.0024	0.0027
		Time	1.5150	4.1530	4.7230	6.3070	12.4290	21.7610	24.7390	42.3530

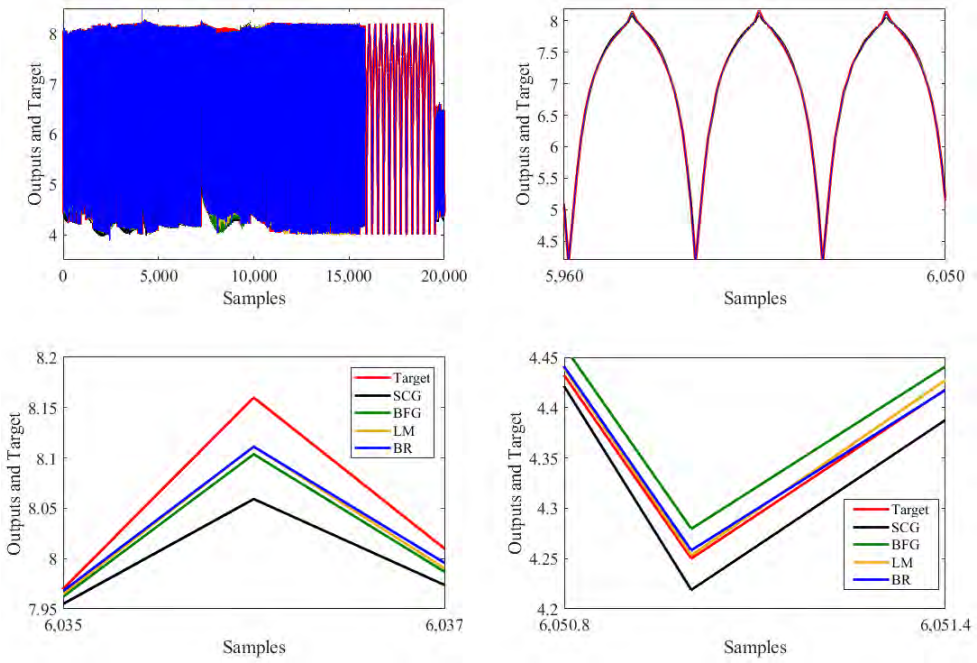

Figure 4.7: Predicted output results when using SCG, BFG, LM and BR.

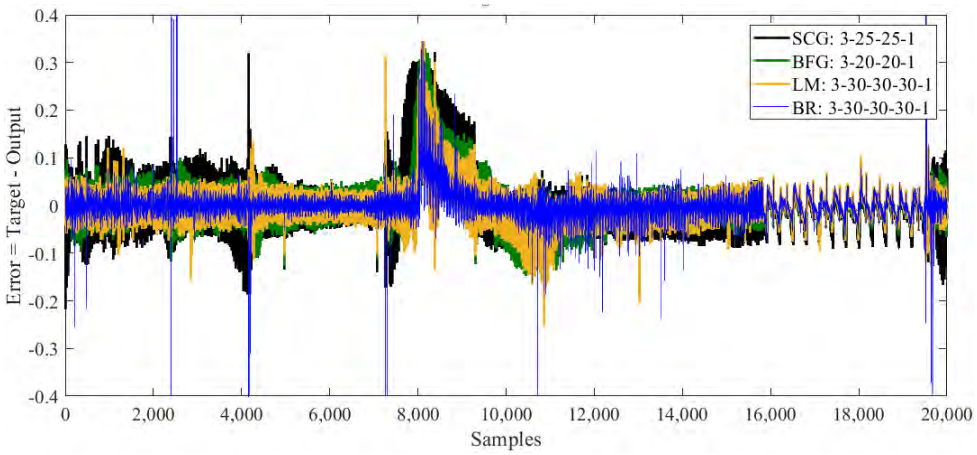

Figure 4.8: Obtained training errors when using SCG, BFG, LM and BR.

According to these figures, it is clear that the BR training algorithm with the structure of 3 hidden layers and 30 neurons for each predicts the best output results in terms of accuracy, where the SCG shows the worst predicted results in comparison with the rest of the algorithms. In terms of time, the SCG shows the fastest training since it takes only around 11 s to predict the output while the BR needs around 6930 s. However, although the BR takes around 2 h for the training, it finally provides a highly accurate model which is one of the main goals of this study.

Figure 4.9 shows the training regression plot. This measure is used to see how well the neural network has fit the data. According to this figure, the predicted model is characterised by high accuracy since most of the data points fall along a 45 degree

line, where the output is equal to the target.

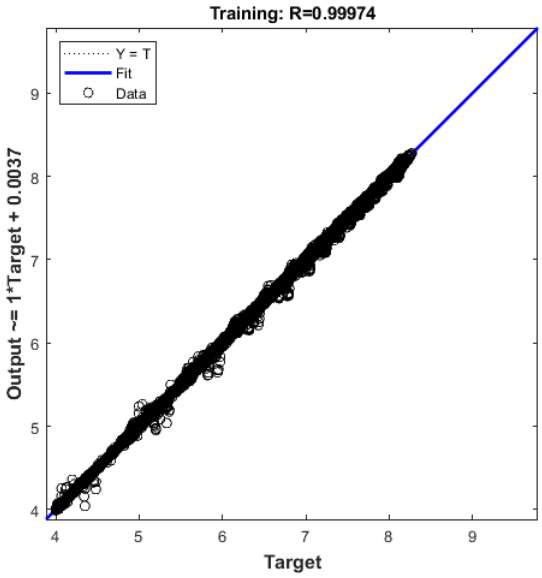

Figure 4.9: Training regression performance of the predicted model.

Figure 4.10 shows the testing regression plot. According to this figure, although some data are not fell on the 45 degree line, the testing accuracy still high since thousands of data are equal to the target.

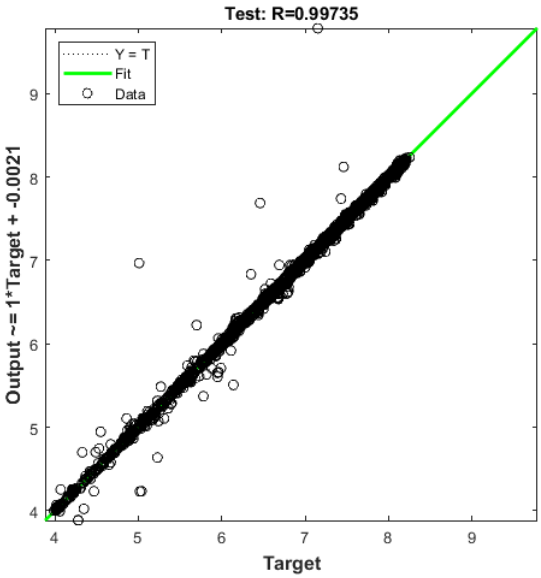

Figure 4.10: Testing regression performance of the predicted model.

Figure 4.11 shows the all regression plot, which takes into account the training and testing regression. According to this figure, it is clear that the predicted model is characterised by high accuracy. It should be noted that the goodness of the model also can be analysed via the R values which ranged between 0 (lowest accuracy) and

1 (ideal model). In our case, the accuracy of the obtained model is proven by the following R values: training, R = 0.99974, test, R = 0.99735 and all, R = 0.99938.

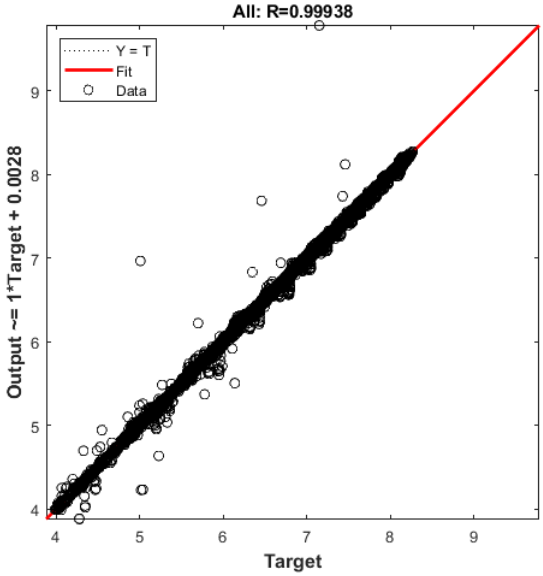

Figure 4.11: All regression performance of the predicted model.

4.4. Conclusion

This chapter presented an analysis of a commercial Heliocentris FC50 PEM fuel cell system; the objective was to model the device via the application of a deep machine learning based artificial neural network. Due to its several input variations, such as stack temperature, humidity and oxygen, which results in nonlinearities and high model complexity, extensive tests with various ANN parameters were required to predict an efficient model.

Since the ANN model requires a large dataset, an efficient automatic method was designed to simplify and facilitate the data collection. This was obtained by generating a triangular signal which varies the duty cycle of the power converter that was inserted between the stack and the load. An experimental dataset composed of 20,512 samples over a wide operating range (different operating current, temperature and fan power) of a commercial stack was recorded and saved for the training process.

Different structures of feed-forward neural network perceptron with backpropagation learning rule were tested to predict the performance of the Heliocentries FC50 fuel cell system. A comparison study including various ANN parameters such as the training algorithm, the number of hidden layers and the number of neurons at each layer was made to obtain the highest accurate model. Finally, an accurate model composed of 3 hidden layers and 90 neurons trained by BR algorithm was used for a comparison study with the real results.

Chapter 5

DC-DC Power Converters

5.1. Introduction

The main objective of using a power converter is to provide an efficient power conversion from the source (fuel cell stack) to the load and offer a regulated output voltage that may be used for various applications. A DC power converter must provide its output with a DC voltage of a desired value in spite of the fluctuations that may occurs in the input and the output current. DC converters use one or more switches to transform a DC voltage level to another DC level; this is done by controlling the conduction time of the switches (T_{on}) [198, 199]. A desirable characteristic in the study of any electronic circuit is the use of linear techniques. However, switched power converters are non-linear and discontinuous circuits. The time during which the switch S_1 is closed called conduction time, T_{on}. On the other hand, the time that the switch remains open is called the blocking time, T_{off}. The sum of T_{on} and T_{off} forms the converter period T, which is also called the switching time T_s.

In a DC-DC converter, the power delivered to the load is calculated by a function of the duty cycle, δ, which is defined as the ratio between the conduction time at which the converter is in the "ON" position and the switching time T_s. In the literature, the duty cycle is also called by the letter "D".

$$\delta = D = \frac{T_{on}}{T_s} \qquad 0 < \delta < 1 \tag{5.1}$$

$$T_s = T_{on} + T_{off} \tag{5.2}$$

$$T_s = \delta \cdot T_s + T_{off} \tag{5.3}$$

$$T_{off} = (1 - \delta) \cdot T_s \tag{5.4}$$

Typically, DC-DC power converters used for fuel cell and PV systems can be divided into isolated and non-isolated types [200–202], where the latter possesses a higher efficiency for high-power applications due to the absence of the transformer

which causes a reduction in the conversion efficiency. As for the non-isolated type, several existing DC-DC power converter topologies inherently have the capability of voltage boosting [200]. However, it is usually desired to use a power converter that provides continuous input current since the fuel cell stack current should be continuous for reduced capacitor sizing and proper efficient energy extraction [203].

Figure 5.1 shows the representation of a DC-DC converter, which can be used as an interface between the source and the load [204].

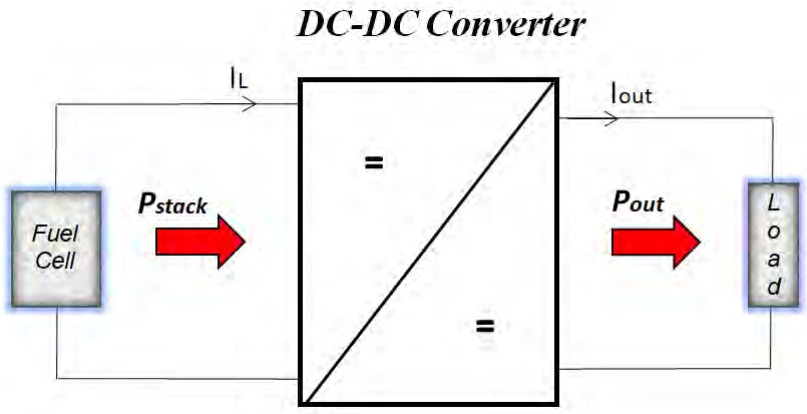

Figure 5.1: DC-DC power converter

For the sake of this study, the most common available types of DC-DC power converters will be analyzed so as to understand the features of each topology as well as its principle of operation. The five most common topologies used in the literature are: boost (step up), buck (step down), buck-boost (step up/down), Cuk (step up/down), and SEPIC (step up/down).

5.2. Modes of Operation

One of the most important elements of a DC-DC power converter is the inductor [205–207]. Selecting the proper size of the inductor and setting its operation mode makes the power converter operates correctly. The shape and magnitude of the inductor current I_L are dictated by the inductance L of the inductor itself. Hence, choosing the right and appropriate inductor value is very important. Usually, the current I_L that moves across the inductor L can be classified in three types; continuous, boundary, or discontinuous.

- The continuous inductor current, as presented in Figure 5.2a, means that the minimum level of the I_L waveform is never fall to zero in any switching period T_s [205].
- The boundary inductor current, as presented in Figure 5.2b, is occurred when the minimum level of the inductor current waveform touch the zero value at one point every switching cycle.

- A discontinuous inductor current, Figure 5.2c, is occurred when the minimum level of the inductor current is touching zero for a period of time before the next ON state occurs.

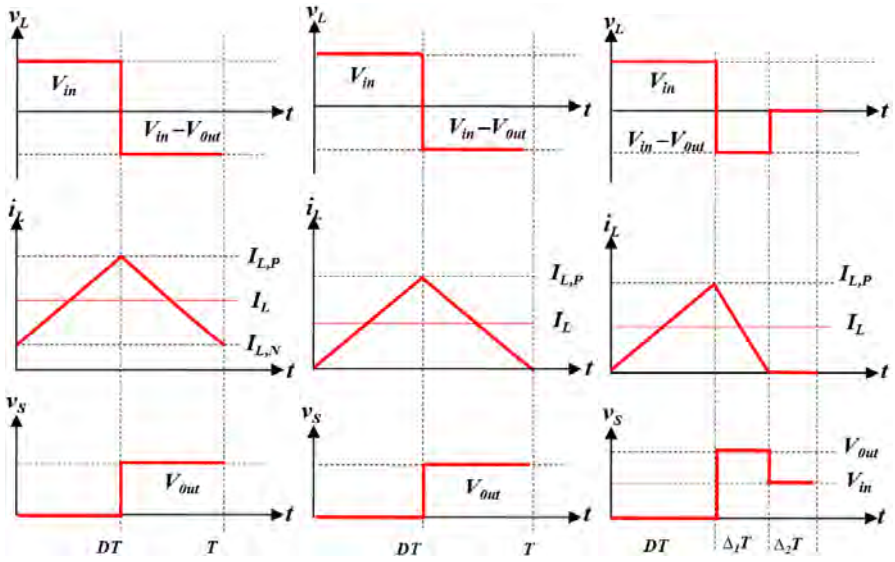

(a) Continuous current. (b) Boundary region. (c) Discontinuous current.

Figure 5.2: Voltage and current waveforms for DC-DC boost converter.

5.2.1. Continuous Conduction Mode (CCM)

As presented in Figure 5.3, the continuous conduction mode (CCM) is characterized by current flowing continuously in the inductor throughout the whole switching cycle T_s. In order to ensure and maintain the operation of the power converter in the CCM, the inductance L should be big enough such that its energy will not discharged until the next conductance T_{on} [200]. To guarantee the operation in this mode, the output current of the converter I_{out} (load current) must be higher than half of the ripple current that pass through the inductor I_L. In this case, I_L is continues and it will never go to zero which will results in a small ripple. It should be noted that a smaller ripple current ΔI_L corresponds to lower losses in the inductor L and in the active power devices. Therefore, the CCM is more desired for higher efficiency requirement. On the other hand, one drawback should be mentioned for the case when operating in CCM is that the inductor needs a larger inductance; which means a large physical size and an increased price.

5.2.2. Discontinuous Conduction Mode

As presented in Figure 5.4, the discontinuous conduction mode (DCM) is characterized by zero current for a portion of the switching cycle T_s. During each switching cycle, the inductor current I_L starts from zero, reaches the peak value, and then

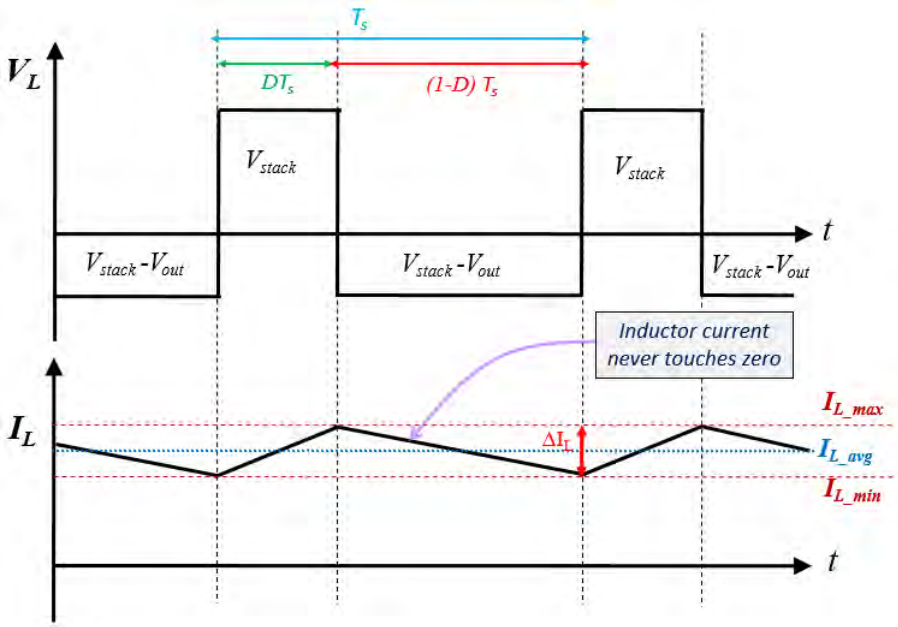

Figure 5.3: Continuous Conduction Mode (CCM)

returns to the zero value until the next switching cycle starts. When the current across the inductor becomes zero, the power to the load will be supplied only by the capacitor. Therefore, the output voltage V_{out} will be depending only on the circuit component values and the duty ratio of the MOSFET. It should be noted that in the discontinuous conduction mode, the current across the inductor as well as the current across the active devices are characterised by high peak value and their root mean square (RMS) also is high. This behavior leads to high power losses which as a consequence jeopardize the efficiency of the converter [205].

The DCM can be obtained by three methods; decreasing the inductor inductance L, decreasing the switching frequency T_s, or decreasing the load current I_{out} (increasing the load resistance). The effect of these parameters on the inductor current I_L is presented in Figure 5.5.

Concerning the current delivered to the load, if it is less than half of the inductor ripple current ($I_{out} < \frac{\Delta I_L}{2}$), the current I_L through the inductor will go into the discontinuous conduction mode. The behaviour of I_L when decreasing the load current is presented in Figure 5.6.

5.3. DC-DC boost converters

DC-DC boost converter is a high step up power converter which is used to boost and regulate an input DC voltage [208–210]. As shown in Figure 5.7, an ideal boost converter is consisted of linear (filtering capacitor C, load resistor R, inductor L) and nonlinear (switching transistor S_1, diode S_2) elements.

Under continuous conduction mode (CCM), the operation of DC-DC boost con-

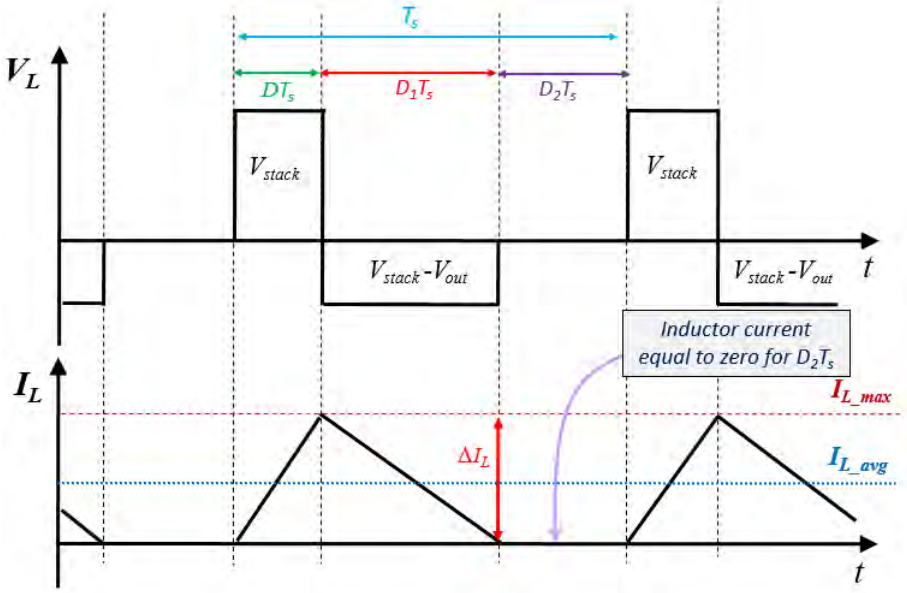

Figure 5.4: Discontinuous Conduction Mode (DCM)

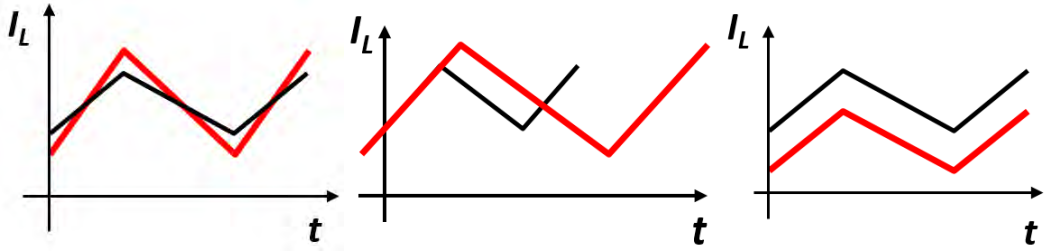

(a) reduction in L. (b) Reduction in T_s. (c) Reduction in I_{out}.

Figure 5.5: Methods for obtaining the DCM.

verter becomes fairly simple. Thus, using the inductor L and the two switches S_1 and S_2, the circuit alternates between two states (ON and OFF) for each complete switching cycle T_s. Each state of ON and OFF has a varying duration. The ON time T_{on} can be calculated by multiplying the switching cycle T_s with the duty cycle D. The OFF time T_{off} can be found by subtracting the ON time T_{on} from the complete switching cycle T_s. The configuration of the boost converter circuit in the ON state and OFF state is shown in Figure 5.8a and Figure 5.8b respectively.

ON state: When the switch S_1 turns ON, the inductor L connects to the DC source voltage. Therefore, the current I_L moves across the inductor L and the transistor switch S_1 which results an increase in the magnitude of I_L and I_s, while V_L is approximately equal to the input voltage V_{in}. On the other hand, during this state, the capacitor C discharges through the load R. Therefore, the voltage V_L across the inductor and the current I_c across the capacitor are simply can be given as Equation (5.5) and (5.6).

$$V_L = V_{stack} \tag{5.5}$$

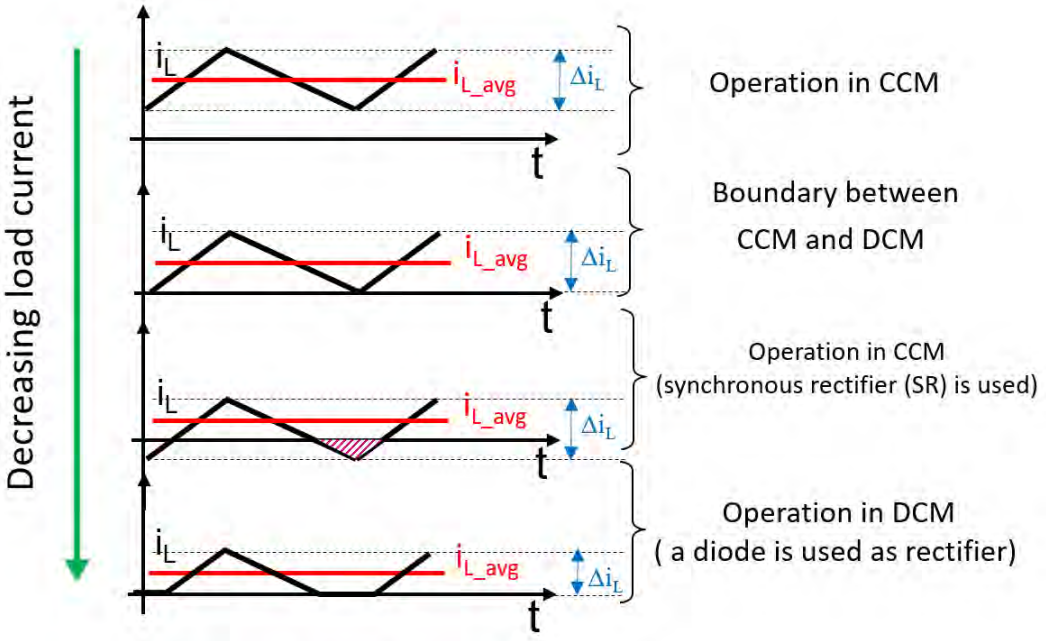

Figure 5.6: Effect of load current reduction on the inductor current

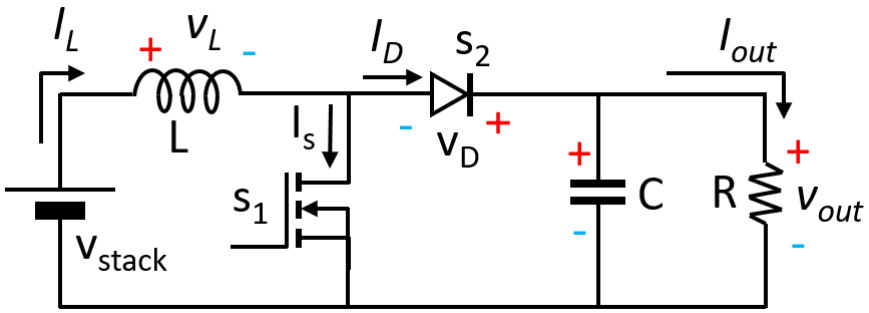

Figure 5.7: Boost converter circuit.

$$I_C = -\frac{V_{out}}{R} \tag{5.6}$$

During the on state, the current I_L through the inductor is rising linearly; and it can be calculated as Equation (5.9).

$$V_L = L \cdot \frac{dI_L}{dt} \tag{5.7}$$

$$\frac{dI_L}{dt} = \frac{1}{L}V_L = \frac{1}{L}V_{stack} \tag{5.8}$$

$$\Delta I_{L(ON)} = \frac{1}{L}\int_0^{T_{on}} V_L \cdot dt = \frac{1}{L}V_{stack} \cdot DT_s \tag{5.9}$$

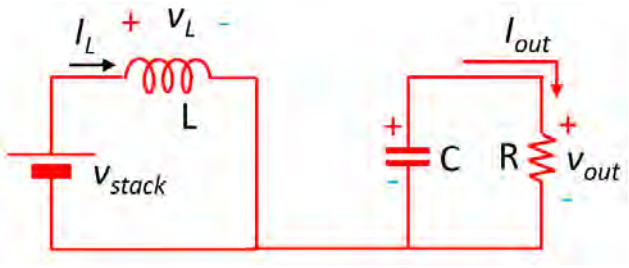

(a) ON state.

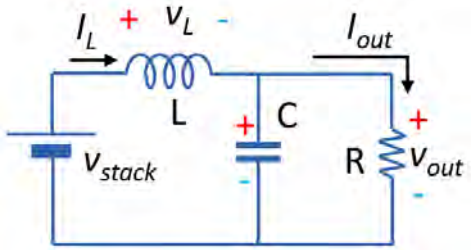

(b) OFF state.

Figure 5.8: Configurations of the boost converter circuit.

The voltage V_C across the capacitor is can be calculated as Equation (5.12).

$$I_C = C \cdot \frac{dV_{out}}{dt} \tag{5.10}$$

$$\frac{dV_{out}}{dt} = \frac{I_C}{C} = -\frac{V_{out}}{R \cdot C} \tag{5.11}$$

$$\Delta V_{C(ON)} = \frac{1}{C} \int_0^{T_{on}} I_C \cdot dt = -\frac{V_{out}}{R \cdot C} \cdot DT_s = \frac{-I_{out}}{C} \cdot DT_s \tag{5.12}$$

OFF state: When the switch S_1 turns OFF, the inductor L connects to the capacitor C and the load R. Therefore, the current i_L moves across the inductor L, the diode S_2, the capacitor C and the load R, which results a decrease in the magnitude of i_L and i_d (discharging of the inductor L into the load R and the capacitor C). During this state, the voltage V_L across the inductor, and the current I_c through the capacitor are simply can be given as Equation (5.13) and (5.14)

$$V_L = V_{stack} - V_{out} \tag{5.13}$$

$$I_C = I_L - \frac{V_{out}}{R} \tag{5.14}$$

During the off state, the current I_L through the inductor is decreasing linearly; it

can be calculated as Equation (5.17).

$$V_L = L \cdot \frac{dI_L}{dt} \tag{5.15}$$

$$\frac{dI_L}{dt} = \frac{1}{L} V_L = \frac{1}{L}(V_{stack} - V_{out}) \tag{5.16}$$

$$\Delta I_{L(OFF)} = \frac{1}{L} \int_{T_{on}}^{T_s = T_{on} + T_{off}} V_L \cdot dt = \frac{1}{L}(V_{stack} - V_{out}) \cdot (D-1) T_s \tag{5.17}$$

The voltage V_C across the capacitor can be calculated as Equation (5.20).

$$I_C = C \cdot \frac{dV_{out}}{dt} \tag{5.18}$$

$$\frac{dV_{out}}{dt} = \frac{I_C}{C} = \frac{I_L - \frac{V_{out}}{R}}{C} \tag{5.19}$$

$$\Delta V_{C(OFF)} = \frac{1}{C} \int_{T_{on}}^{T_s} I_C \cdot dt = \frac{I_L - \frac{V_{out}}{R}}{C} \cdot (D-1) T_s = \frac{I_L - I_{out}}{C} \cdot (D-1) T_s \tag{5.20}$$

When the converter is in steady state operation, the energy stored in each component is the same at the start and at the end of each switching cycle T_s. Therefore, the current I_L through the inductor is the same at the start and at the end of each switching cycle. By applying the inductor volt-second balance equation for the boost converter, Equation (5.25) can be obtained.

$$V_L = L \cdot \frac{dI_L}{dt} \tag{5.21}$$

$$\Rightarrow \int_0^{T_s} V_L \cdot dt = \int_0^{T_s} L \cdot dI_L = L\left[I_L(T_s) - I_L(0)\right] = 0 \tag{5.22}$$

$$\Rightarrow The \;\; overage \;\; voltage \;\; < V_L >= \frac{1}{T_s} \int_0^{T_s} V_L \cdot dt = 0 \tag{5.23}$$

$$\Rightarrow \frac{1}{L} \int_0^{T_s} V_L \cdot dt = \frac{1}{L} \int_0^{T_{on}} V_L \cdot dt + \frac{1}{L} \int_{T_{on}}^{T_s = T_{on} + T_{off}} V_L \cdot dt = 0 \tag{5.24}$$

$$\Rightarrow \Delta I_{L(ON)} + \Delta I_{L(OFF)} = 0 \tag{5.25}$$

Therefore, by replacing Equation (5.9) and Equation (5.17) in Equation (5.25), the relationship between input and output voltage in a boost converter can be written as Equation (5.26).

$$V_{out} = \left(\frac{1}{1-D}\right) \cdot V_{stack} \tag{5.26}$$

When the converter is in steady state operation, the voltage V_C through the capacitor C is the same at the start and at the end of each switching cycle. Therefore, by applying the capacitor charge balance equation for the boost converter, Equation (5.31) can be obtained.

$$I_C = C \cdot \frac{dV_C}{dt} \tag{5.27}$$

$$\Rightarrow \int_0^{T_s} I_C \cdot dt = \int_0^{T_s} C \cdot dV_C = C\left[V_C(T_s) - V_C(0)\right] = 0 \tag{5.28}$$

$$\Rightarrow The\ \ overage\ \ current\ \ < I_C >= \frac{1}{T_s}\int_0^{T_s} I_C \cdot dt = 0 \tag{5.29}$$

$$\Rightarrow = \frac{1}{C}\int_0^{T_s} I_C \cdot dt = \frac{1}{C}\int_0^{T_{on}} I_C \cdot dt + \frac{1}{C}\int_{T_{on}}^{T_s=T_{on}+T_{off}} I_C \cdot dt = 0 \tag{5.30}$$

$$\Rightarrow \Delta V_{C(ON)} + \Delta V_{C(OFF)} = 0 \tag{5.31}$$

Therefore, by replacing Equation (5.12) and Equation (5.20) in Equation (5.31), the relationship between input and output current in a boost converter can be written as Equation (5.32).

$$I_L = \left(\frac{1}{1-D}\right) \cdot I_{out} \tag{5.32}$$

The waveforms of the inductor voltage V_L, inductor current I_L, transistor current I_T, diode current I_D, and capacitor current I_c during the ON and OFF state, are presented in Figure. 5.9.

5.3.1. Inductance and capacitance Selection (L and C)

From Figure 5.9, it can be seen that the current flowing through the inductor L has a ripple ΔI_L (the ripple of the current is defined as being the difference between the maximum value and the minimum value of the current) which can be calculated as Equation (5.34) [211–213].

$$\Delta I_L = I_{L,max} - I_{L,min} = \frac{V_{stack}}{L} \cdot DT_s = \frac{V_{stack}}{L \cdot f_s} \cdot D \tag{5.33}$$

$$\Rightarrow L \geq \frac{V_{stack,min}}{\Delta I_{L,max} \cdot f_s} \cdot D_{boost} \tag{5.34}$$

Where:

- $V_{stack,min}$= minimum input voltage.
- $\Delta I_{L,max}$=maximum desired inductor current ripple.
- f_s= $\frac{1}{T_s}$ = switch frequency.

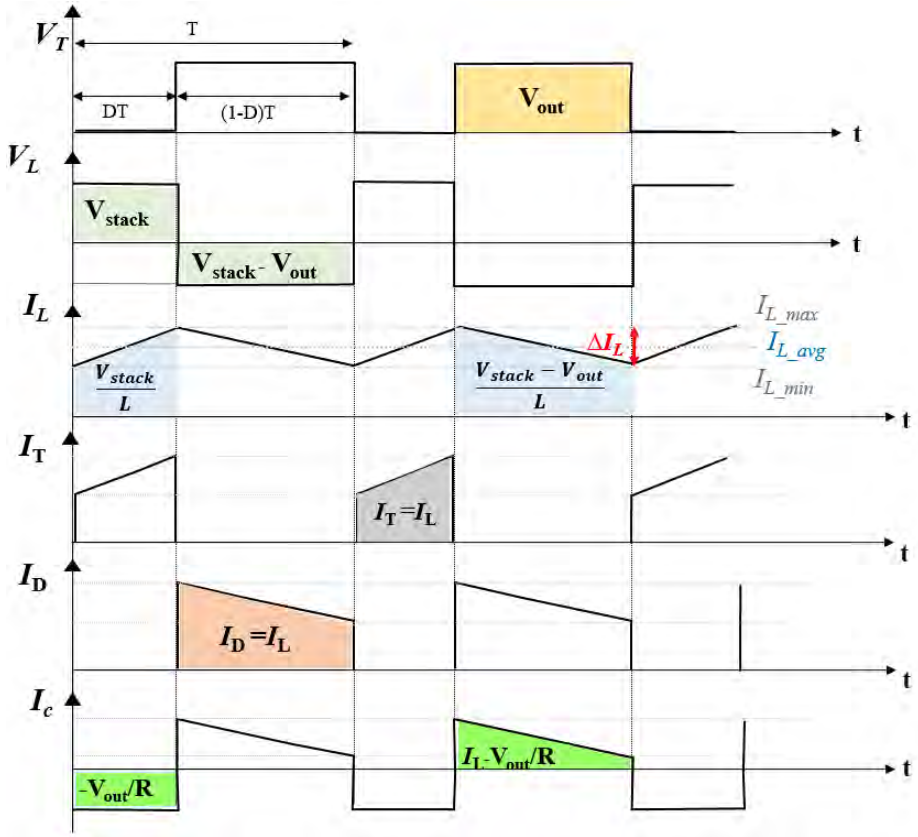

Figure 5.9: Waveforms of different currents and voltages under CCM operation.

- $D_{boost} = 1 - \frac{V_{stack,min} \cdot \eta}{V_{out}}$ duty cycle for the minimum input voltage since the minimum input voltage leads to the maximum switch current.
- η= efficiency of the converter.

Using Equation (5.12), the capacitance C can be calculated as Equation (5.35) [213, 214].

$$\Delta V_C = \frac{I_{out}}{C} \cdot DT_s \Rightarrow C = \frac{I_{out}}{\Delta V_C \cdot f_s} \cdot D \tag{5.35}$$

Therefore, the value of the capacitor C that allowing to have a ripple lower than the maximum ripple $\Delta V_{C,max}$ must satisfy Equation (5.36)

$$\Rightarrow C \geq \frac{I_{out,max}}{\Delta V_{C,max} \cdot f_s} \cdot D_{boost} \tag{5.36}$$

5.3.2. State-space representation

The state-space representation of the ON state circuit can be written as Equation (5.37).

$$\begin{cases} \dot{x} = A_1.x + B_1.v \\ \\ y = C_1.x + E_1.v \end{cases} \tag{5.37}$$

Where:

- $x = [x_1, x_2]^T = [I_L, V_{out}]^T$
- $A_1 = \begin{bmatrix} 0 & 0,0 & -\frac{1}{RC} \end{bmatrix}^T$
- $B_1 = \begin{bmatrix} \frac{1}{L} & 0 \end{bmatrix}^T$
- $C_1 = \begin{bmatrix} 0 & 1 \end{bmatrix}$
- $E_1 = 0$
- $v = V_{stack}$

The state-space representation of the OFF state circuit can be written as Equation (5.38).

$$\begin{cases} \dot{x} = A_2 \cdot x + B_2 \cdot v \\ \\ y = C_2 \cdot x + E_2 \cdot v \end{cases} \tag{5.38}$$

Where:

- $A_2 = \begin{bmatrix} 0 & -\frac{1}{L}, \frac{1}{C} & -\frac{1}{RC} \end{bmatrix}^T$
- $B_2 = \begin{bmatrix} \frac{1}{L} & 0 \end{bmatrix}^T$
- $C_2 = \begin{bmatrix} 0 & 1 \end{bmatrix}$
- $E_2 = 0$

Consequently, the state-space representation of the boost converter for both ON and OFF states can be expressed as Equation (5.39).

$$\begin{cases} \dot{x} = A \cdot x + B \cdot v \\ \\ y = C \cdot x + E \cdot v \end{cases} \tag{5.39}$$

Where A, B, C, and E are defined in Equation (5.40).

$$\begin{cases} A = u \cdot A_1 + (1-u)A_2 \\ \\ B = u \cdot B_1 + (1-u)B_2 \\ \\ C = u \cdot C_1 + (1-u)C_2 \\ \\ E = u \cdot E_1 + (1-u)E_2 \end{cases} \tag{5.40}$$

The state-space representation of the boost converter given in Equation (5.39) also can be written and detailed as Equation (5.41)

$$\begin{cases} \dot{x} = \begin{bmatrix} 0 & \frac{u-1}{L} \\ \frac{1-u}{C} & -\frac{1}{RC} \end{bmatrix} x + \begin{bmatrix} \frac{1}{L} \\ 0 \end{bmatrix} v, \\ y = \begin{bmatrix} 0 & 1 \end{bmatrix} x, \end{cases} \tag{5.41}$$

5.4. DC-DC buck converters

DC-DC buck converter is a high step down power converter which is used to decrease and regulate an input DC voltage [215–218]. As shown in Figure 5.10, an ideal back converter is consisted of linear (filtering capacitor C, load resistance R, inductor L) and nonlinear (switching transistor S_1, diode S_2) elements.

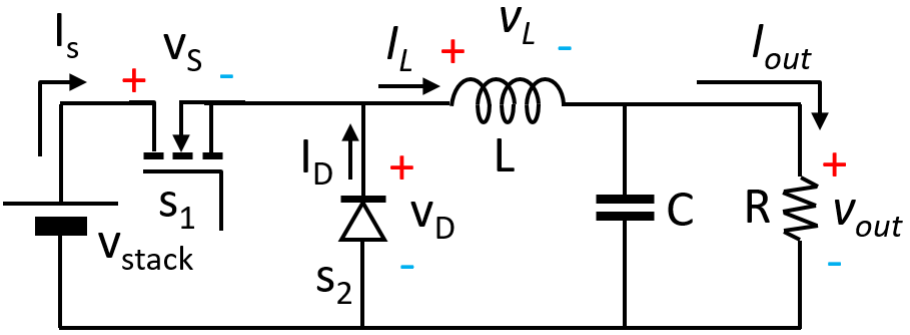

Figure 5.10: Buck converter circuit.

The configuration of the buck converter circuit in the ON state and OFF state is shown in Figure 5.11a and Figure 5.11b respectively.

ON state: When the switch S_1 turns ON, the inductor L connects to the DC source voltage. Therefore, the current I_s moves across the inductor L, the capacitor C and the load resistance R which results an increase in the magnitude of I_L and I_C, while V_L is approximately equal to the input voltage V_{stack} minus the load voltage V_{out}. Therefore, the voltage V_L across the inductor, and the current I_c through the capacitor are simply can be given as Equation (5.42) and (5.43).

$$V_L = V_{stack} - V_{out} \tag{5.42}$$

$$I_C = I_L - \frac{V_{out}}{R} \tag{5.43}$$

During the on state, the current I_L through the inductor is rising linearly; it can

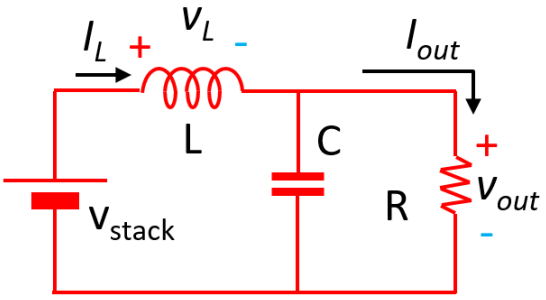

(a) ON state.

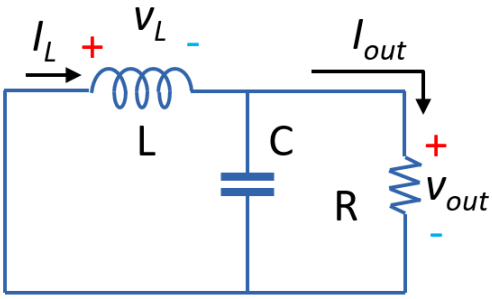

(b) OFF state.

Figure 5.11: Configurations of the buck converter circuit.

be calculated as Equation (5.46).

$$V_L = L \cdot \frac{dI_L}{dt} \tag{5.44}$$

$$\frac{dI_L}{dt} = \frac{1}{L} V_L = \frac{1}{L}(V_{stack} - V_{out}) \tag{5.45}$$

$$\Delta I_{L(ON)} = \frac{1}{L} \int_0^{T_{on}} V_L \cdot dt = \frac{1}{L}(V_{stack} - V_{out}) \cdot DT_s \tag{5.46}$$

The voltage V_C across the capacitor can be calculated as Equation (5.49).

$$I_C = C \cdot \frac{dV_{out}}{dt} \tag{5.47}$$

$$\frac{dV_{out}}{dt} = \frac{I_C}{C} = \frac{I_L - \frac{V_{out}}{R}}{C} \tag{5.48}$$

$$\Delta V_{C(ON)} = \frac{1}{C} \int_0^{T_{on}} I_C \cdot dt = \frac{I_L - \frac{V_{out}}{R}}{C} \cdot DT_s = \frac{I_L - I_{out}}{C} \cdot DT_s \tag{5.49}$$

OFF state: When the switch S_1 turns OFF, the inductor L connects to the capacitor C and the load R. Therefore, the current I_L moves across the inductor L, the capacitor C, the load R, and the diode S_2, which results a decrease in the

magnitude of I_L and I_D (discharging of the inductor L into the load R and the capacitor C). During this state, the voltage V_L across the inductor, and the current I_c through the capacitor are simply can be given as Equation (5.50) and (5.51)

$$V_L = -V_{out} \tag{5.50}$$

$$I_C = I_L - \frac{V_{out}}{R} \tag{5.51}$$

During the off state, the current I_L through the inductor is decreasing linearly; it can be calculated as Equation (5.54).

$$V_L = L \cdot \frac{dI_L}{dt} \tag{5.52}$$

$$\frac{dI_L}{dt} = \frac{1}{L} V_L = \frac{-V_{out}}{L} \tag{5.53}$$

$$\Delta I_{L(OFF)} = \frac{1}{L} \int_{T_{on}}^{T_s = T_{on} + T_{off}} V_L \cdot dt = \frac{-V_{out}}{L} \cdot (1 - D) T_s \tag{5.54}$$

The voltage V_C across the capacitor can be calculated as Equation (5.57).

$$I_C = C \cdot \frac{dV_{out}}{dt} \tag{5.55}$$

$$\frac{dV_{out}}{dt} = \frac{I_C}{C} = \frac{I_L - \frac{V_{out}}{R}}{C} \tag{5.56}$$

$$\Delta V_{C(OFF)} = \frac{1}{C} \int_{T_{on}}^{T_s} I_C \cdot dt = \frac{I_L - \frac{V_{out}}{R}}{C} \cdot (D - 1) T_s = \frac{I_L - I_{out}}{C} \cdot (1 - D) T_s \tag{5.57}$$

When the converter is in steady state operation, the energy stored in each component is the same at the start and at the end of each switching cycle T_s. Therefore, the current I_L through the inductor is the same at the start and at the end of each switching cycle. By applying the inductor volt-second balance equation for the back converter, Equation (5.58) can be obtained.

$$\Rightarrow \Delta I_{L(ON)} + \Delta I_{L(OFF)} = 0 \tag{5.58}$$

Therefore, by replacing Equation (5.46) and Equation (5.54) in Equation (5.58), the relationship between input and output voltage in a buck converter can be written as Equation (5.59).

$$V_{out} = D \cdot V_{stack} \tag{5.59}$$

When the converter is in steady state operation, the voltage V_C through the

capacitor C is the same at the start and at the end of each switching cycle. Therefore, by applying the capacitor charge balance equation for the buck converter, Equation (5.60) can be obtained.

$$\Rightarrow \Delta V_{C(ON)} + \Delta V_{C(OFF)} = 0 \tag{5.60}$$

Therefore, by replacing Equation (5.49) and Equation (5.57) in Equation (5.60), the relationship between input and output current in a back converter can be written as Equation (5.61).

$$I_L = I_{out} \tag{5.61}$$

The waveforms of the inductor voltage V_L, inductor current I_L, transistor current I_T, diode current I_D, and capacitor current I_c, during the ON and OFF state, are presented in Figure. 5.12.

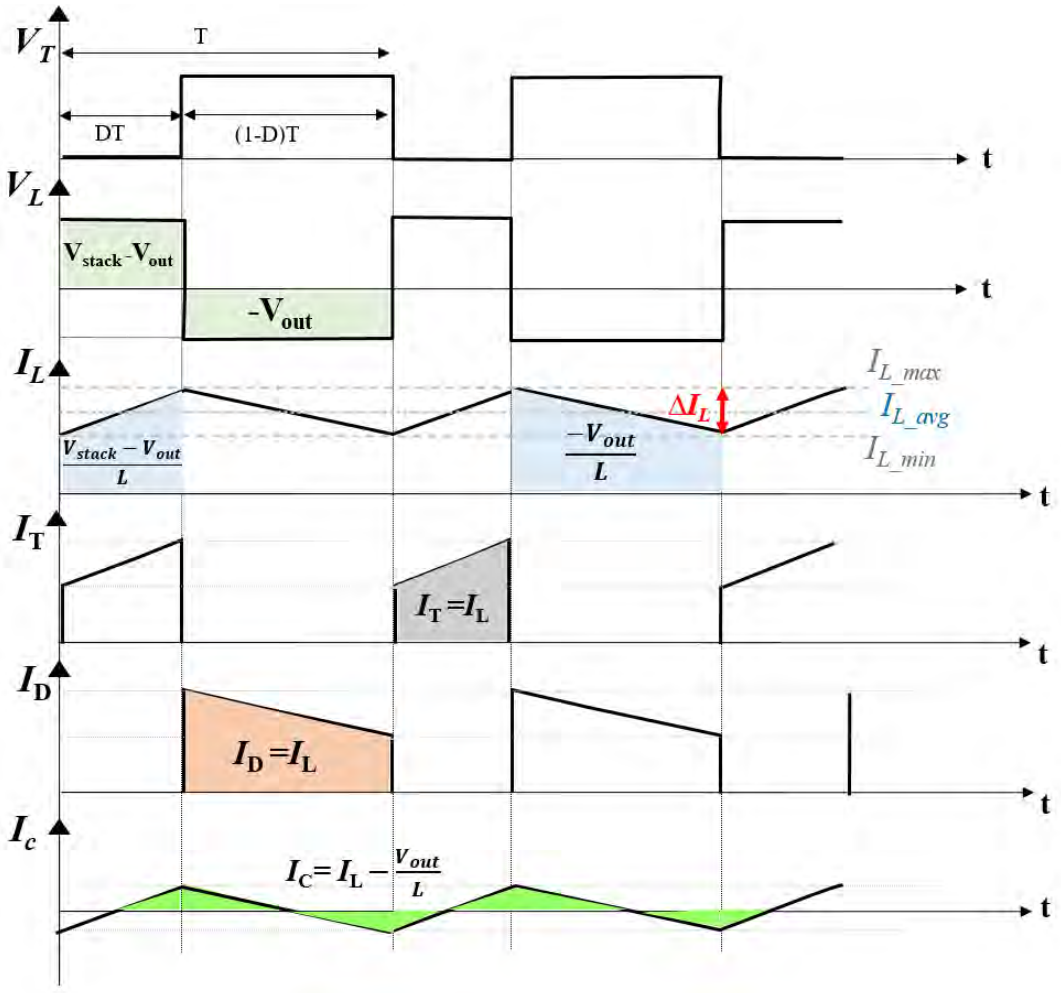

Figure 5.12: Waveforms of different currents and voltages under CCM operation.

5.4.1. State-space representation

Using the same principle that used in the boost converter section, the state-space representation of the buck converter for both ON and OFF states can be written and detailed as Equation (5.62)

$$\begin{cases} \dot{x} = \begin{bmatrix} 0 & -\frac{1}{L} \\ \frac{1}{C} & -\frac{1}{RC} \end{bmatrix} x + \begin{bmatrix} \frac{D}{L} \\ 0 \end{bmatrix} v, \\ y = \begin{bmatrix} 0 & 1 \end{bmatrix} x, \end{cases} \tag{5.62}$$

5.5. DC-DC buck-boost converters

DC-DC buck-boost converter is a high step up/down power converter which is used to increase/decrease and regulate an input DC voltage [219–223]. It is a circuit that combines the principles of the buck and the boost converters in a single circuit. As shown in Figure 5.13, an ideal back-boost converter is consisted of linear (filtering capacitor C, load resistance R, inductor L) and nonlinear (switching transistor S_1, diode S_2) elements.

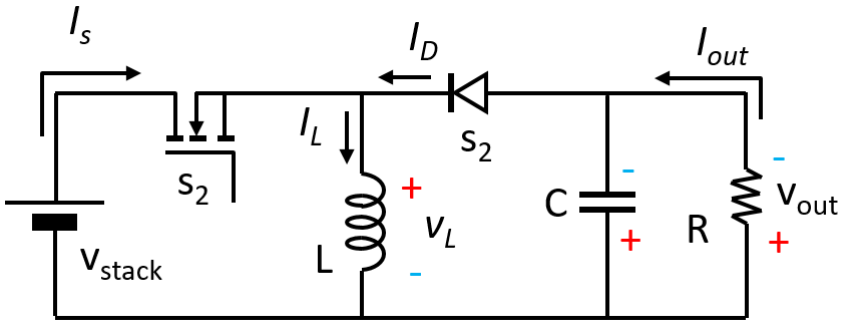

Figure 5.13: Buck-boost converter circuit.

The configuration of the buck-boost converter circuit in the ON state and OFF state is shown in Figure 5.14a and Figure 5.14b respectively.

ON state: When the switch S_1 turns ON, the inductor L connects to the DC source voltage. Therefore, the current I_s moves across the inductor L which results an increase in the magnitude of I_L and I_s, while V_L is approximately equal to the input voltage V_{stack}. On the other hand, during this state, the capacitor C discharges through the load R. Therefore, the voltage V_L across the inductor, and the current I_c through the capacitor are simply can be given as Equation (5.63) and (5.64).

$$V_L = V_{stack} \tag{5.63}$$

$$I_C = -\frac{V_{out}}{R} \tag{5.64}$$

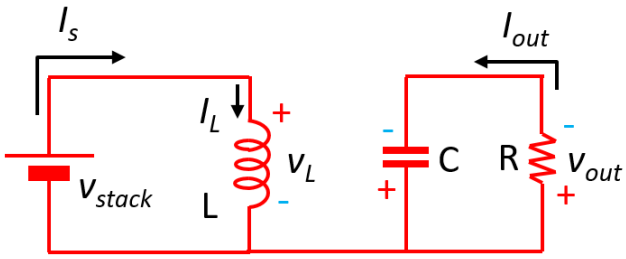

(a) ON state.

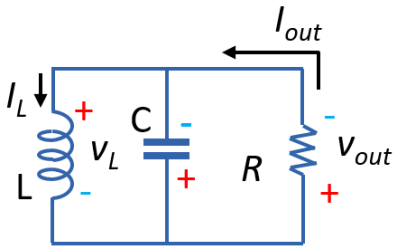

(b) OFF state.

Figure 5.14: Configurations of the buck-boost converter circuit.

During the on state, the current I_L through the inductor is rising linearly; it can be calculated as Equation (5.67).

$$V_L = L \cdot \frac{dI_L}{dt} \tag{5.65}$$

$$\frac{dI_L}{dt} = \frac{1}{L} V_L = \frac{1}{L} V_{stack} \tag{5.66}$$

$$\Delta I_{L(ON)} = \frac{1}{L} \int_0^{T_{on}} V_L \cdot dt = \frac{1}{L} V_{stack} \cdot DT_s \tag{5.67}$$

The voltage V_C across the capacitor can be calculated as Equation (5.70).

$$I_C = C \cdot \frac{dV_{out}}{dt} \tag{5.68}$$

$$\frac{dV_{out}}{dt} = \frac{I_C}{C} = -\frac{V_{out}}{R \cdot C} \tag{5.69}$$

$$\Delta V_{C(ON)} = \frac{1}{C} \int_0^{T_{on}} I_C \cdot dt = -\frac{V_{out}}{R \cdot C} \cdot DT_s = \frac{-I_{out}}{C} \cdot DT_s \tag{5.70}$$

OFF state: When the switch S_1 turns OFF, the inductor L connects to the capacitor C and the load R. Therefore, the current I_L moves across the inductor L, the capacitor C, the load R, and the diode S_2, which results a decrease in the magnitude of I_L (discharging of the inductor L into the load R and the capacitor C). During this state, the voltage V_L across the inductor, and the current I_c through the

capacitor are simply can be given as Equation (5.71) and (5.72)

$$V_L = -V_{out} \tag{5.71}$$

$$I_C = I_L - \frac{V_{out}}{R} \tag{5.72}$$

During the off state, the current I_L through the inductor is decreasing linearly; it can be calculated as Equation (5.75).

$$V_L = L \cdot \frac{dI_L}{dt} \tag{5.73}$$

$$\frac{dI_L}{dt} = \frac{1}{L} V_L = \frac{-V_{out}}{L} \tag{5.74}$$

$$\Delta I_{L(OFF)} = \frac{1}{L} \int_{T_{on}}^{T_s = T_{on} + T_{off}} V_L \cdot dt = \frac{-V_{out}}{L} \cdot (1 - D) T_s \tag{5.75}$$

The voltage V_C across the capacitor can be calculated as Equation (5.78).

$$I_C = C \cdot \frac{dV_{out}}{dt} \tag{5.76}$$

$$\frac{dV_{out}}{dt} = \frac{I_C}{C} = \frac{I_L - \frac{V_{out}}{R}}{C} \tag{5.77}$$

$$\Delta V_{C(OFF)} = \frac{1}{C} \int_{T_{on}}^{T_s} I_C \cdot dt = \frac{I_L - \frac{V_{out}}{R}}{C} \cdot (D - 1) T_s = \frac{I_L - I_{out}}{C} \cdot (1 - D) T_s \tag{5.78}$$

When the converter is in steady state operation, the energy stored in each component is the same at the start and at the end of each switching cycle T_s. Therefore, the current I_L through the inductor is the same at the start and at the end of each switching cycle. By applying the inductor volt-second balance equation for the back-boost converter, Equation (5.79) can be obtained.

$$\Rightarrow \Delta I_{L(ON)} + \Delta I_{L(OFF)} = 0 \tag{5.79}$$

Therefore, by replacing Equation (5.67) and Equation (5.75) in Equation (5.79), the relationship between input and output voltage in a buck-boost converter can be written as Equation (5.80).

$$V_{out} = \frac{D}{1 - D} \cdot V_{stack} \tag{5.80}$$

When the converter is in steady state operation, the voltage V_C through the

capacitor C is the same at the start and at the end of each switching cycle. Therefore, by applying the capacitor charge balance equation for the buck-boost converter, Equation (5.81) can be obtained.

$$\Rightarrow \Delta V_{C(ON)} + \Delta V_{C(OFF)} = 0 \tag{5.81}$$

Therefore, by replacing Equation (5.70) and Equation (5.78) in Equation (5.81), the relationship between input and output current in a back converter can be written as Equation (5.82).

$$I_L = \frac{1}{1-D} \cdot I_{out} \tag{5.82}$$

The waveforms of the inductor voltage V_L, inductor current I_L, transistor current I_T, diode current I_D, and capacitor current I_c, during the ON and OFF state, are presented in Figure. 5.15.

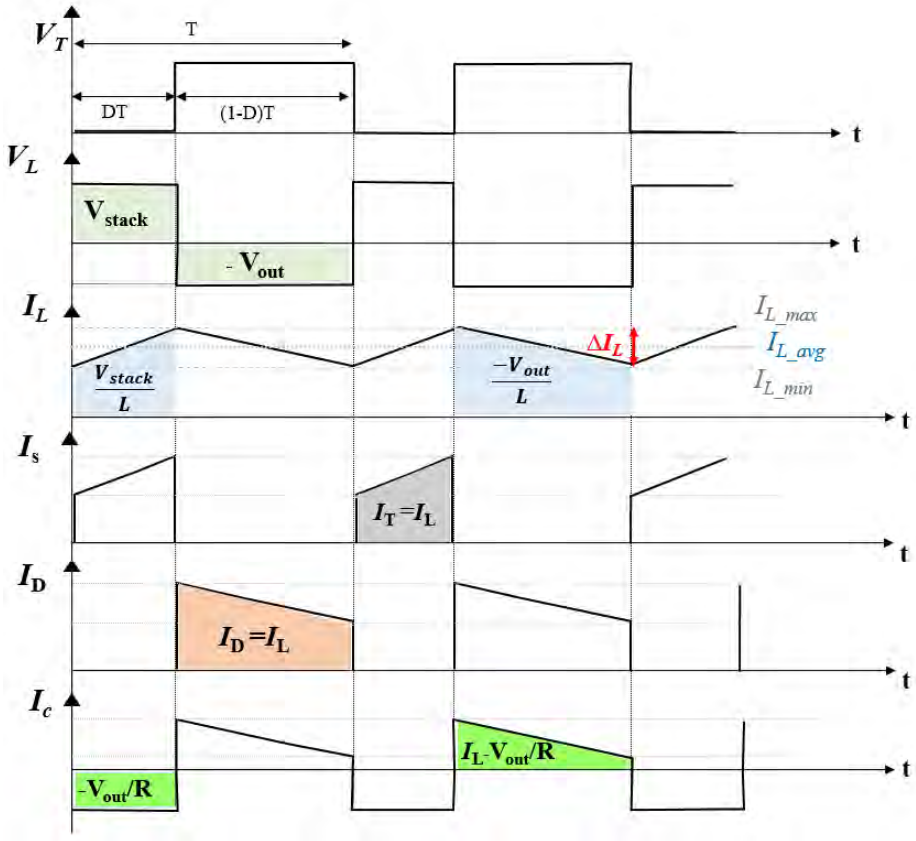

Figure 5.15: Waveforms of different currents and voltages under CCM operation.

5.5.1. State-space representation

Using the same principle that used in the boost converter section, the state-space representation of the buck-boost converter for both ON and OFF states can be

written and detailed as Equation (5.83)

$$\begin{cases} \dot{x} = \begin{bmatrix} 0 & \frac{1-D}{L} \\ -\frac{1-D}{C} & -\frac{1}{RC} \end{bmatrix} x + \begin{bmatrix} \frac{D}{L} \\ 0 \end{bmatrix} v, \\ y = \begin{bmatrix} 0 & 1 \end{bmatrix} x, \end{cases} \tag{5.83}$$

5.6. DC-DC SEPIC converters

The DC-DC single-ended primary-inductor converter (SEPIC) is a high step up/down power converter which is used to increase/decrease and regulate an input DC voltage [224–229]. The SEPIC converter is similar to the traditional buck-boost converter, but it has advantages of having non-inverted output. Besides, another important advantage is the continuous current at the input side; whereas its main disadvantage is the high number of reactive components. As shown in Figure 5.16, an ideal SEPIC converter is consisted of linear (input inductor L_1, energy transfer capacitor C_1, filtering inductor L_2, filtering capacitor C_2, load resistance R) and nonlinear (switching transistor S_1, diode S_2) elements. Since the overage voltage of the inductor L_1 and the inductor L_2 is equal to zero, then the voltage across the energy transfer capacitor C_1 is equal to V_{stack}.

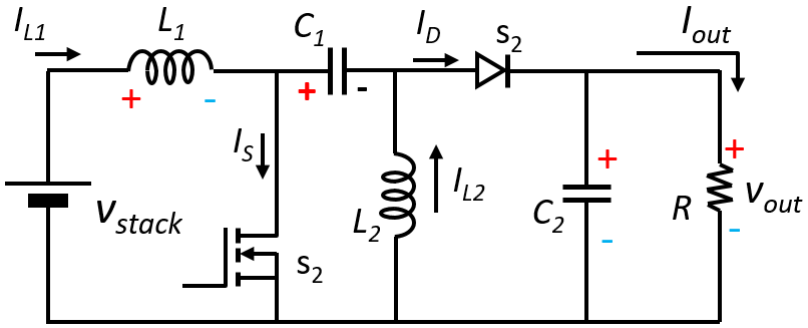

Figure 5.16: SEPIC converter circuit.

The equivalent circuits when the switching element is ON and OFF are respectively presented in Figure 5.17a and Figure 5.17b.

When the switch is on, the current from the source I_{L1} provides energy to the inductor L_1, whereas the capacitor C_1 is discharged via the inductor L_2. In the second part of the circuit, the capacitor C_2 leads the switch S_2 (diode) to open and it is discharged via the load resistor R. When the switch is OFF, the current from the source I_{L1} will flow through the switch S_2 (diode). At this time, the energy transfer capacitor C_1 is charged via the input inductor L_1, whereas the inductor L_2 will provide energy to the capacitor C_2 and to the load resistor R. The main waveforms of current and voltage in the converter are presented in Figure 5.18.

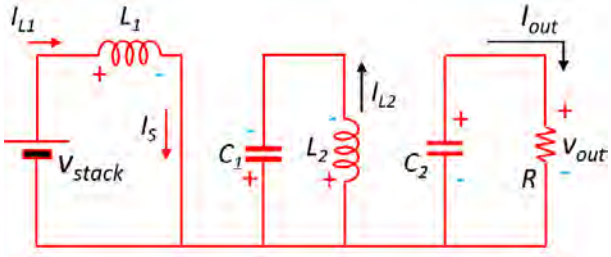

(a) ON state.

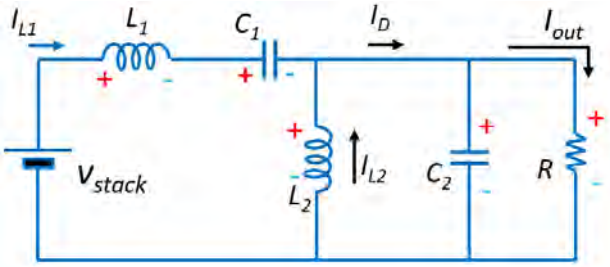

(b) OFF state.

Figure 5.17: Configurations of the SEPIC converter circuit.

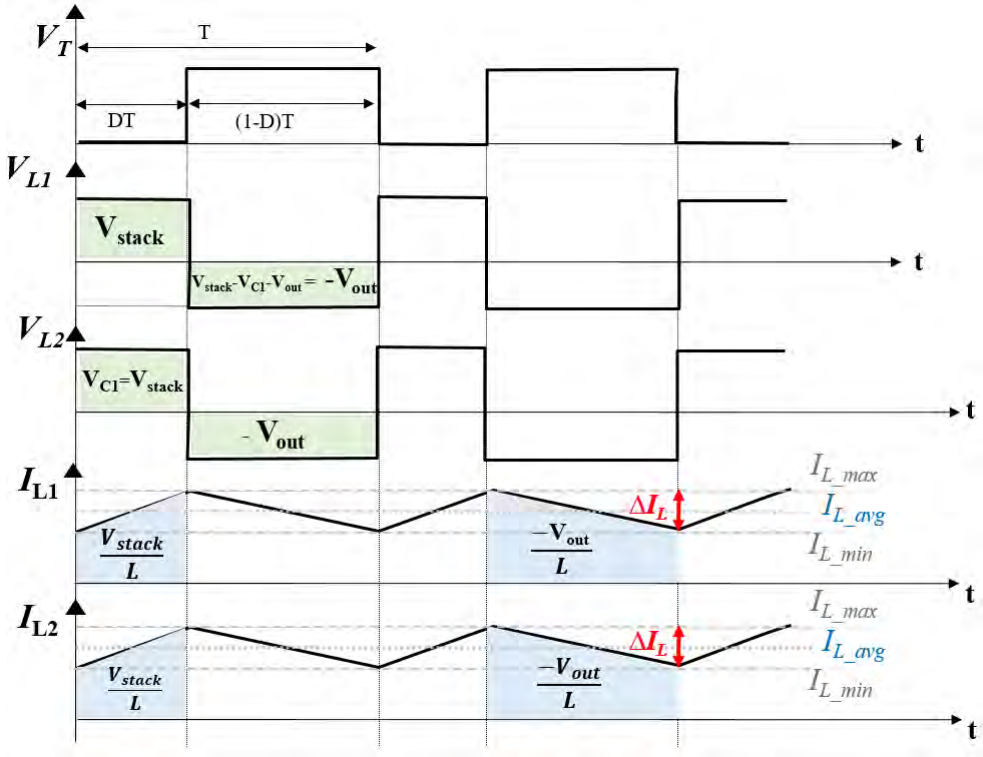

Figure 5.18: Waveforms of different currents and voltages under CCM operation.

5.7. DC-DC Zeta (dual SEPIC) converters

The DC-DC Zeta (also called duel SEPIC) is a high step up/down power converter which is used to increase/decrease and regulate an input DC voltage [230–235]. The Zeta converter is similar to the SEPIC converter, but it has the advantage of providing continuous output current (which is pulsed in the SEPIC topology). As shown in Figure 5.19, an ideal Zeta converter is consisted of linear (input inductor L_1, energy transfer capacitor C_1, filtering inductor L_2, filtering capacitor C_2, load resistance R) and nonlinear (switching transistor S_1, diode S_2) elements. Since the overage voltage of the inductor L_1 and the inductor L_2 is equal to zero, then the voltage across the energy transfer capacitor C_1 is equal to V_{out}.

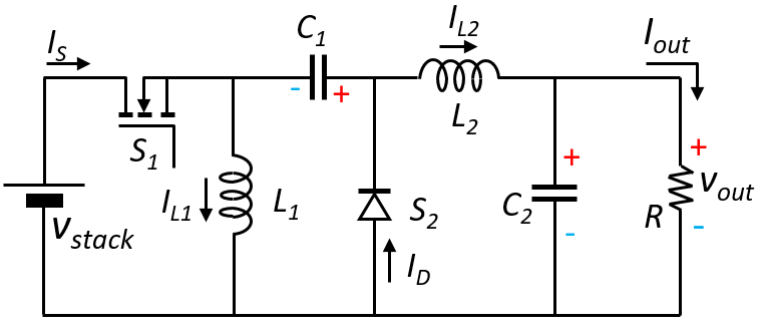

Figure 5.19: Zeta converter circuit.

The equivalent circuits when the switching element is ON and OFF are respectively presented in Figure 5.20a and Figure 5.20b.

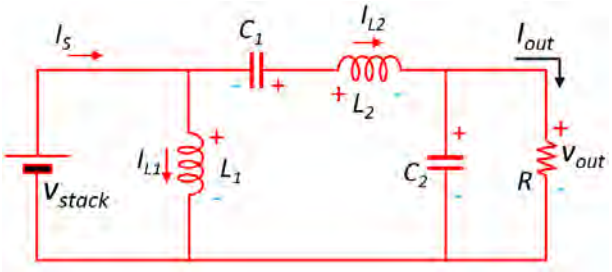

(a) ON state.

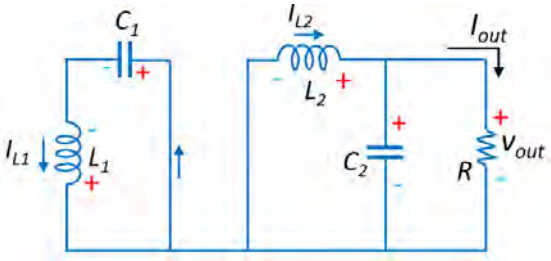

(b) OFF state.

Figure 5.20: Configurations of the Zeta converter circuit.

When the switch is on, the current from the source I_s provides energy to the inductor L_1, whereas the capacitor C_1 is discharged via the inductor L_2, the capacitor C_2, and the load resistor R. When the switch is OFF, the current from the source I_{L1} will split up, whereas the current from the inductor I_{L1} will flow through the switch S_2 (diode). At this time, the energy transfer capacitor C_1 is charged via the input inductor L_1. In the second part of the circuit, the inductor L_2 will provide energy to the capacitor C_2 and to the load resistor R. The main waveforms of current and voltage in the converter are presented in Figure 5.21.

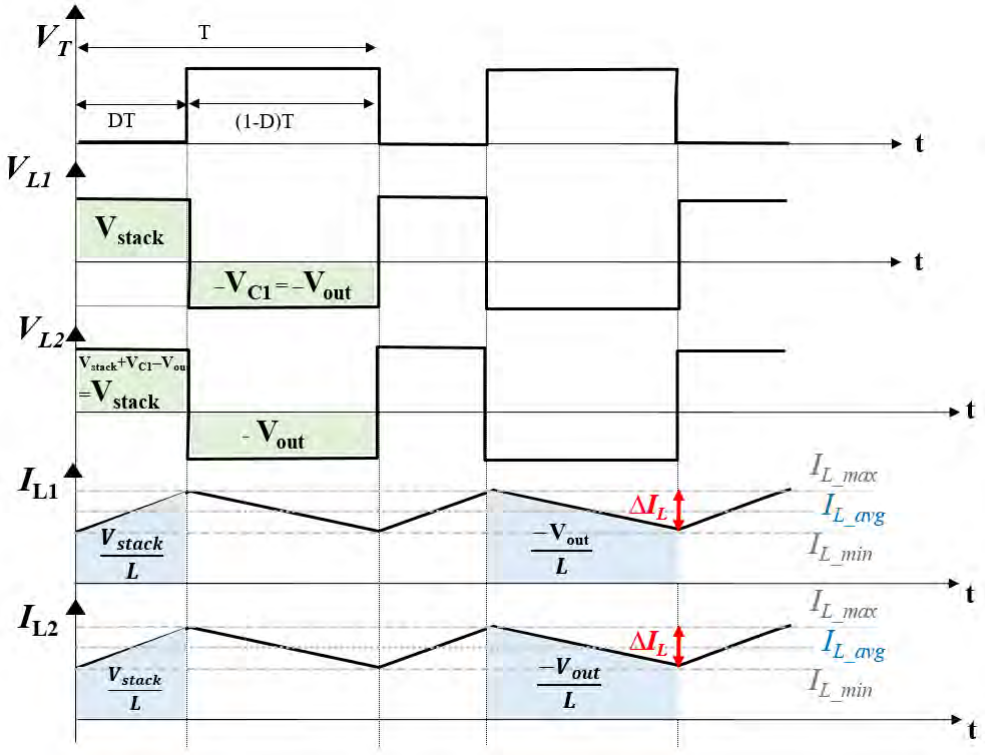

Figure 5.21: Waveforms of different currents and voltages under CCM operation.

5.8. DC-DC Cuk converters

DC-DC Cuk converter is a high step up/down power converter which is used to increase/decrease and regulate an input DC voltage [236–240]. It was discovered by Prof. Slobodan Cuk [241], and it was obtained by sequentially connecting the buck and boost converters. The distinctive aspect of the Cuk converter is the use of a capacitor C_1 for energy transfer [242]. As shown in Figure 5.22, an ideal Cuk converter is consisted of linear (input inductor L_1, energy transfer capacitor C_1, filtering inductor L_2, filtering capacitor C_2, load resistance R) and nonlinear (switching transistor S_1, diode S_2) elements. Since the overage voltage of the inductor L_1 and the inductor L_2 is equal to zero, then the voltage across the energy transfer capacitor C_1 is equal to $V_{stack} + V_{out}$.

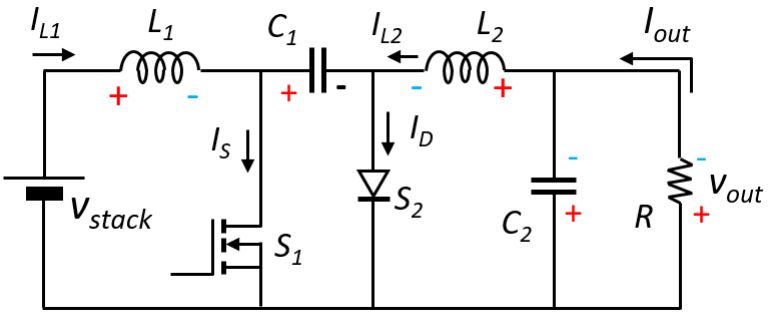

Figure 5.22: Cuk converter circuit.

An important advantage of the Cuk converter topology is the continuous current at both input and output sides; whereas its main disadvantage is the high number of reactive components. The equivalent circuits when the switching element is ON and OFF are respectively presented in Figure 5.23a and Figure 5.23b. When the

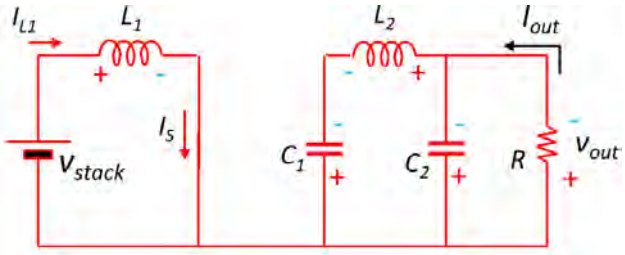

(a) ON state.

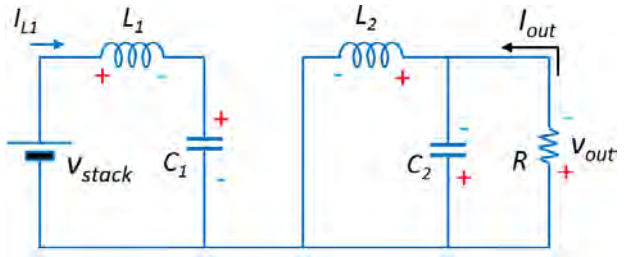

(b) OFF state.

Figure 5.23: Configurations of the Cuk converter circuit.

switch is on, the current from the source I_{L1} provides energy to the inductor L_1. In the second part of the circuit, the capacitor C_1 leads the switch S_2 (diode) to open and it is discharged via the capacitor C_2, load resistor R and inductor L_2. When the switch is OFF, the current from the source I_{L1} will flow through the switch S_2 (diode). At this time, the energy transfer capacitor C_1 is charged via the input inductor L_1, whereas the capacitor C_2 and the inductor L_2 will provide energy to the load resistor R. The main waveforms of current and voltage in the converter are presented in Figure 5.24 [243].

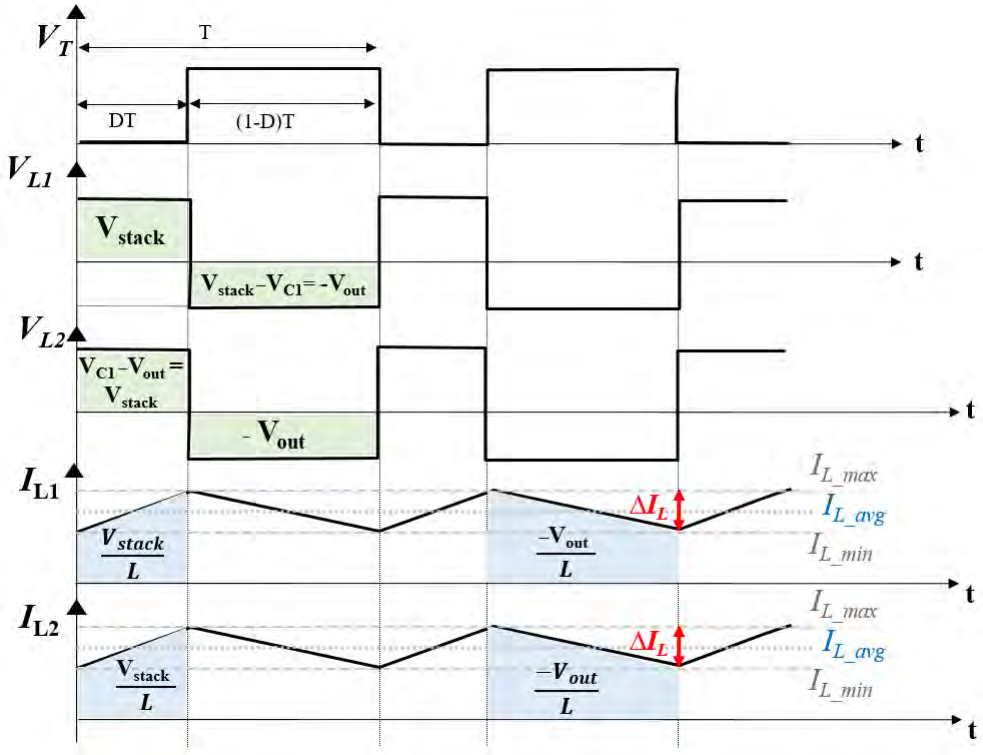

Figure 5.24: Waveforms of different currents and voltages under CCM operation.

5.9. Conclusion

In this chapter, several types of DC-DC converters including buck, boost, buck-boost,SEPIC, Zeta and Cuk, are studied. A comparison among these converters is summarized in Table 5.1. The comparison was done using key design parameters such as type of input and output current, efficiency, and number of components. Each one of these topologies presents advantages and drawbacks. The boost converter is used when the source has low voltage. It characterised by few number of components which reduce its cost as well as resulting in high efficiency. However its pulsed output current still represents an obstacle for many applications. The Zeta and Cuk topologies could replace the boost converter and they provide smooth and continuous output current. However, Zeta and Cuk are characterised by large number of components which leads to increase their cost and lower their efficiency. Moreover, the Cuk provides reversed output polarity. On the other hand, the buck converter is used when the source has low voltage. As the boost converter, the buck is also characterised by few number of components which reduce its cost, leads to simplicity and high efficiency. one drawback of the buck topology is its pulsed input current. Other topologies that can replace the buck converter and overcome this drawback are the SEPIC and the Cuk. However, the SEPIC provides pulsed output current which is another drawback, and the Cuk generates reversed reversed output polarity. Moreover, both of the SEPIC and Cuk needs for twice inductors and a large energy transfer capacitor which leads

to higher cost and lower efficiency. The buck-boost converter is used when the source voltage could be high or low. As the buck and the boost topologies, the buck-boost is characterised by few number of components, simplicity and high efficiency. However, its reversed output voltage polarity as well as its pulsed input and output current are its main drawbacks. The SEPIC, Zeta and the Cuk topologyies can replace the back-boost and they can provide smooth and continuous output current. However, as early explained the main obstacles of these topologies are the cost, the complexity and lower efficiency.

Topology	Type	Input Current	Output Current	Output voltage polarity	DC transfer function $\frac{V_{out}}{V_{in}}$	Number of compo-nents	Efficiency η
Boost	Step up	Continuous	Pulsed	Same	$\frac{1}{1-D}$	4	91%
Buck	Step down	Pulsed	Continuous	Same	D	4	95%
Buck-Boost	Step up/down	Pulsed	Pulsed	Reverse	$-\frac{D}{1-D}$	4	91%
SEPIC	Step up/down	Continuous	Pulsed	Same	$\frac{D}{1-D}$	6	87%
Zeta	Step up/down	Pulsed	Continuous	Same	$\frac{D}{1-D}$	6	87%
Cuk	Step up/down	Continuous	Continuous	Reverse	$-\frac{D}{1-D}$	6	89%

Table 5.1: Comparison of dc-dc power converter

Chapter 6

Description of the experimental system

6.1. Introduction

The experimental study presented in this chapter was developed at the laboratory of Automatic Control and System Engineering (ACSE)/ Universidad del Pais Vasco–Euskal Herriko Uniberstsitatea (UPV/EHU). In the first part, a Heliocentris PEM FC50 stack system with 10 cells which generates an operating voltage between 2.5 and 9 VCC with a current rate of 0-10 A and produce more than 40 W is deeply explained. Then, a boost converter is selected to tackle the low voltage of the fuel cell and provide high level regulated one. The closed loop system including the boost converter, the dSPACE DS1104 and the load are also detailed in this section. Finally, experimental results for the characteristics of the fuel cell as well as the effect of humidity and temperature on the fuel cell efficiency, are discussed.

6.2. PEM fuel cell

The schematic view of the overall experimental test bench system is shown in Figure 6.1. The test bench consists of five main parts: a Heliocentris hy-Expert^{TM} PEMFC Instructor system, a dedicated PC, a DC–DC boost converter, a dSPACE DS1104, and a programmable electronic load.

The technical specifications of the PEMFC Instructor system are enlisted in Table 6.1. The used PEMFC is comprised of a stack of 10 identical cells assembled together. Each fabricated cell has an effective membrane area of 25 cm^2, a thickness equal to $175 \cdot 10^{-6}$ cm, and with platinum loadings of 0.3 mg·Pt/cm^2. According to the manufacturer's specifications, the rated output power of the stack is about 40 W for a rated current of 8 A, and a rated voltage of 5 V. The PEMFC operating voltage ranges from 9 V (no load) to 5 V (Full load). At its maximum current condition, where $I_{max} = 10$ A, the stack can deliver up to 50 W. The PEMFC operates in a temperature range between 15 °C and 50 °C. It is fed directly by pure "dead-end-mode" hydrogen (99.999 *vol* %) and air (oxygen) without prior humidification. Therefore, a pressure regulator is required to feed the PEMFC with the exact rate of hydrogen that is being consumed. Using the H_2 Connection Kits $[1-15]/0.6$ bar (Manometers Ashcraft), hydrogen can be supplied from the supply tank into the

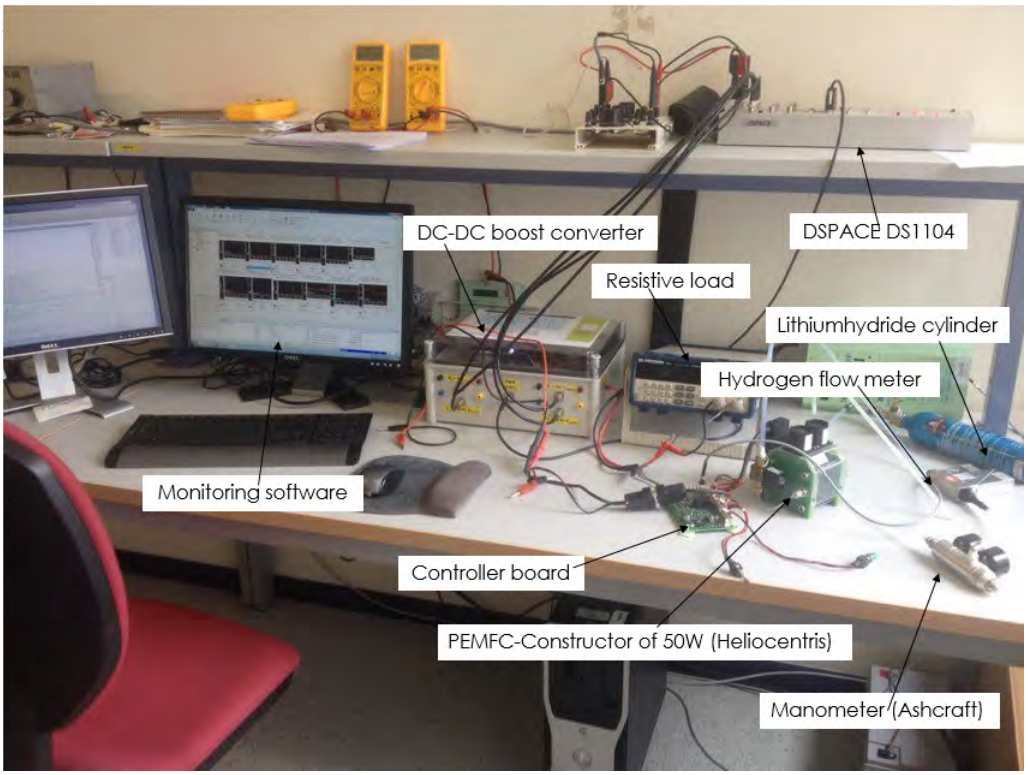

Figure 6.1: Experimental setup.

PEMFC at around 0.6 bar (maximum pressure at which the PEMFC could operate). The hydrogen supply tank used in this work is Lithiumhydride Cylinder Ovonics (LCO), Model: $25G25OB/25G555B$ (Heliocentris). The dimensions of this LCO are 64×305 mm, and it could store 2.391 kg of hydrogen. In order to refill the cylinder, a H_2 Connection Kits $200/[1-15]$ bar is used to supply the hydrogen from the refill tank at approximately 10 bar. The flow rate of hydrogen into the PEMFC is measured using the Bronkhorst Gas Flow Meter (BGFM). This latter operates in a measuring range of [10–1000] sml/min and with a precision of 0.8 % of measured value. The required oxygen that will be used in the electrochemical reactions is supplied to the PEMFC as air. Thus, using the cooling fans which are attached to the stack, air is streamed into the cells at atmospheric pressure. The cooling fans not only serve to provide air for the electrochemical reactions, but they also serve to regulate the PEMFC operating temperature through the convective cooling. Therefore, they result in a reduction in controlling the airflow rate and the stack temperature independently. In addition, the implementation of the oxygen cylinder in such systems can be avoided. The speed of the cooling fans can be either controlled manually by the operator or automatically by an internal controller. If the fan's control software is adjusted in the position "AUTO" mode, the fans will be controlled automatically according to the PEMFC stack power. In other words, the controller sets the desired fan speed in order to ensure sufficient cooling at all times.

Hence, an increase in the PEMFC stack power leads to an increase in the airflow rate (the greater the amount of air is needed for cooling and for the reaction), and so on increasing the fan speed. Additionally, the "AUTO" mode provides enough air in the cathode side in order to decrease as much as possible the mass transport limitations which will result in a reduction in the concentration loss. It should be noted that the airflow used for the convective cooling is significantly more than that used for the electrochemical reactions. Therefore, for systems such as the Heliocentris hy-Expert^{TM} PEMFC Instructor system, excess airflow is extremely important. On the other hand, if the fan's control software is adjusted in a position other than "AUTO" mode, the fans will be controlled directly by the user. Hence, the fans can be operated manually by selecting the percentage of the speed that can be in a range between 0 % and 100 % of the maximum fan speed. According to the technical specifications provided by the Heliocentris hy-Expert^{TM} instructor, at full speed (100 %) of 13,000 rpm, each fan could pump around 276 L/min of airflow. Therefore, the two fans pump around 552 L/min as a maximum amount of airflow that could be supplied to the PEMFC.

A proprietary hy-Expert^{TM} controller board is used for real-time control of the PEMFC system. The controller board represents the distribution center for all data among the PEMFC's complementary instruments including the fans, the H_2 flow meter, the temperature sensor, and the software. It has been developed to provide simple operation, ensure the safety of the PEMFC, as well as to protect the stack from over-loads and short circuits. In addition, it allows to supervise and control the PEMFC system through a dedicated PC using monitoring software provided by Heliocentris. Using an integrated RS232 interface, the software allows for initializing/closing the communications, recording and filing of all the data from the PEMFC auxiliaries and sending power commands during the test, as well as enabling the visualization of all of the operating parameters. Thus, parameters such as the electrical characteristics of the PEMFC (voltage (V) and current (A)), operating temperature (°C), H_2 flow rate (L/min), and fan power (%) can be recorded and graphically drawn on the software interactive screen.

Table 6.1: PEMFC technical data.

Fuel Cell Features		**Electrical features**	
Type	Heliocentris FC-50W w/ 10 cells	Operating Voltage	2.5-9 VDC
Cooling	Cooling fan	Operating Current	0-10 A
Fuel	H_2	Rated power output	40 W
Dimensions	12×10.3×13.5 cm	Max. output power	50 W
Weight	1150 g	Open-circuit voltage	9 VDC

H_2 **Flowmeter**		**15 bar Kit**	
Precision	0.8% of the the quantified value	Inlet pressure	1 -15 bar
Measuring range	10 -1,000 sml/min	Outlet pressure	0.6 bar

Thermal		H_2 **200 bar kit**	
Operating temperature	15-50 ºC	Inlet pressure	200 bar
Max. start temperature	45 ºC	Outlet pressure	1 -15 bar

Fuel		H_2 **Detector**	
Recommended H_2 purity	5.0 (99.999%)	Type of sensor	H_2 4 %
H_2 input pressure	0.4 -8 bar (5.8-11.6 psig)	Measuring principle	3 electrode sensor
H_2 consumption	Max. 700 sml/min (at 0 ºC, 1013 bar)	Range	0 - 4%

6.3. DC-DC boost converter

The DC–DC boost converter used in the test bench was manufactured by TEP-192-Research Group/University of Huelva, Spain. Detailed information about the utilized boost converter is enlisted in Table 6.2. It allows the operator to control the PEMFC system via its metal-oxide-semiconductor field-effect transistor (MOSFET) switching input (20 kHz) which comes directly from the PWM card of the dSPACE. In addition, it is equipped with four sensors: two sensors are used to measure the input and output current, and the others are used to measure the input and output voltage. These sensors are calibrated in order to obtain analog signals between 0 and ±10 V as accepted by the analog-to-digital converter (ADC) block of the dSPACE. In addition, low pass filters were utilized in the measuring units in order to remove the undesired high-frequency noise.

Table 6.2: Technical specifications of the DC–DC boost converter.

Parameter	**Description**
Schottky diode	2xMURF1560 GT, 10 A, 600 V, 15 A/150 °C
Capacitance C_0 and C_1	2xTK Series,1500 µF and 3000 µF
Inductance L	6xPCV-2-564-08 560/6 µH, 7 A, 42 mΩ
I GBT	1xHGT40N60B3, 600 V, 40 A, 1.5 V, 150 °C
Switching frequency	20 KHz
Max. input/output voltage	$V_{in}max$ = 60 V, $V_{out}max$ = 200 V
Max. input/output current	$I_{in}max$ = 20 A, $I_{out}max$ = 20 A

6.4. dSPACE DS1104 real-time controller board

The dSPACE used in this work is DS1104 real-time controller board. It has a MPC8240 processor (PowerPC 603*e* core; 250 MHz CPU), 64-bit floating-point processor, internal cache of 32 MB SDRAM Global memories, slave DSP subsystem DSP/TMS320F240 from Texas Instruments Company (Texas, TIC, United States), 8 MB Flash memories, 8 ADC channels, eight digital-to-analog converter (DAC) channels, and five timer interrupts. The dSPACE is a powerful tool that is able to modify the controller parameters in real time, as well as to monitor the real processes while operating an experiment. Accordingly, using its Real-Time Interface (RTI), it enables the linkage between the hardware system and the MATLAB/Simulink software (R2015a-MATLAB/Simulink 8.5, MathWorks). In detail, the obtained signals from the sensors are linked to the dSPACE via the ADC block and accordingly, they will be read by MATLAB/Simulink using the communication library element $DS1104ADC-CX$. In this work, four channels are used to read the signals from the ADC: $DS1104ADC-C5$ is configured to read V_{stack}, $DS1104ADC-C6$ is configured to read I_{stack}, $DS1104ADC-C7$ is configured to read V_{out}, $DS1104ADC-C8$ is

configured to read I_{out}. As shown in Figure 6.2, the RTI allows the operator to design and implement a digital controller simply by drawing the needed block diagrams (available in the library) on the graphical interface of MATLAB/Simulink.

By compiling the model, the RTI generates and downloads a specific real-time C code for the dSPACE. The standard PWM pulses will be generated using the PWM library block $DS1104SL - DSP - PWM$ and then they will be linked to the MOSFET of the boost converter via the digital-to-analog converter (DAC) block. Meanwhile, the signals came from the channels will be sent to the MATLAB base workspace using "*To workspace*" block. The evolution of each signal will be screened online in the PC using "Controldesk" monitoring software which read the signals data from the workspace.

The system is connected with a BK-Precision-1788B programmable single-output DC power supply, which provides a programmable electronic load with a resistance in the range of 0.1–1000 Ω. The load being made by the Fotronic Corporation Company (Washington, FCC, USA), and it has an operating range between 0 W and 120 W, with a maximum input voltage of 115 V/47 Hz. It can be programmed through PV-1785B-1788 software.

6.5. Results and discussion

The characteristics of Heliocentric hy-Expert^{TM} PEM fuel cell 50 Instructor system are obtained by varying the duty cycle of the boost converter; which will results in a smooth variation of stack current (I_{stack}) from 0.5 to 10A. The current I_{stack} and voltage V_{out} are measured via the laboratory measuring instrument "DT9205A" to validate the theoretical work which already presented in Figure 3.14 and Figure 3.15. It is important to know that, during the last four years, many tests have been done on the stack which occurred a degradation in the cells. This latter caused a decreasing in the fuel cell performances. However, a decreasing in the efficiency is a normal behaviour for any fuel cell and it can not be a big barrier that could prevent the user to study the performance of the fuel cell stack. The experimental polarization curve Current–Voltage (I–V) and Current–Power (I–P) for the Heliocentric hy-Expert^{TM} PEM fuel cell 50 Instructor system is presented in Figure 6.3. The open circuit voltage of the PEM fuel cell stack is in the range of 8–10 V. The drop voltage at the beginning and end of the curves shown in this figure are due to activation and concentration losses, respectively. Actually, the latter does not appear very well due to the integrated controller board which closes the system in order to protect the stack from the damage. The voltage drop in the middle of the curves (which is approximately linear) is due to the ohmic loss in the fuel cell.

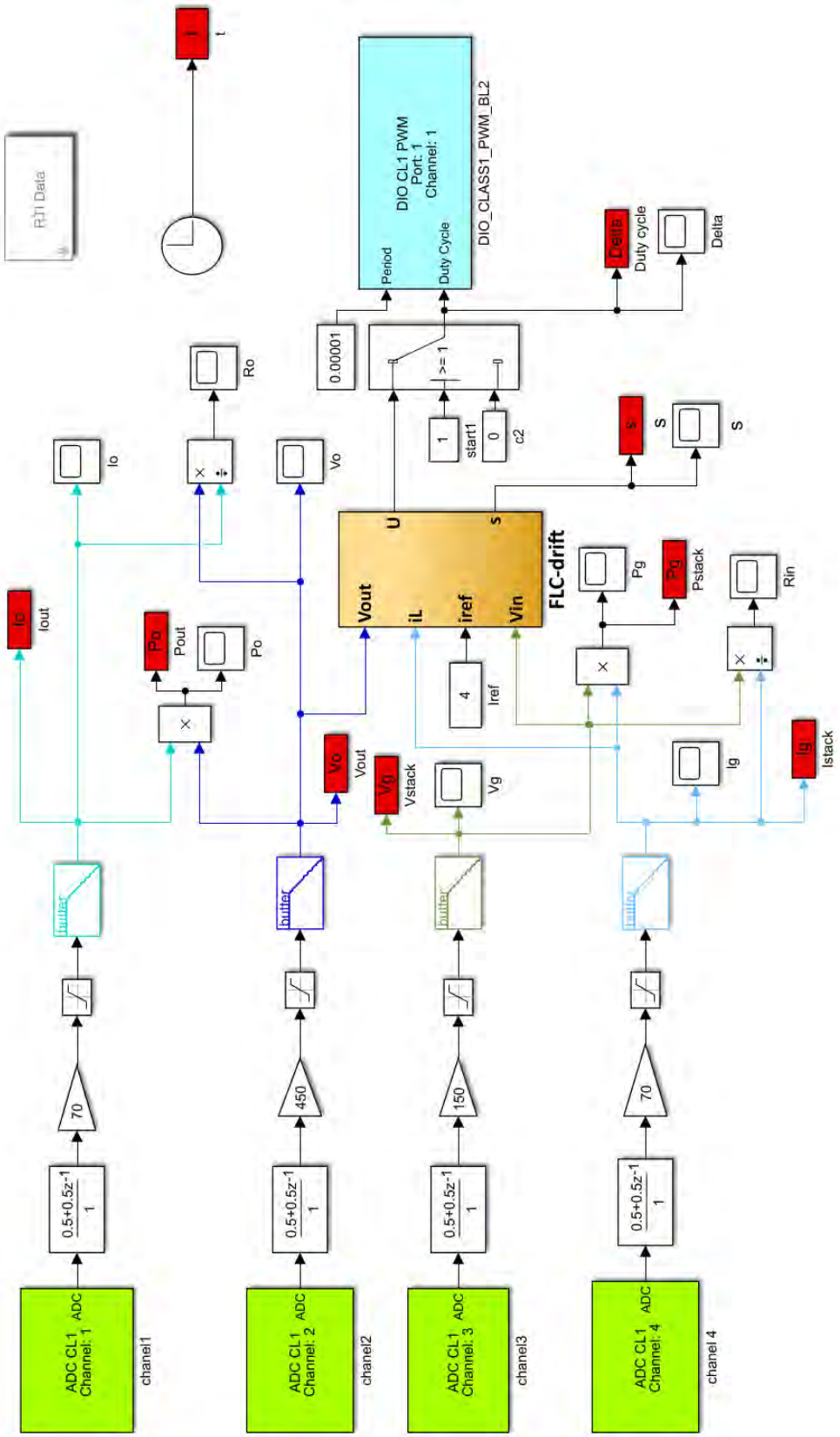

Figure 6.2: Control design in MATLAB/Simulink software.

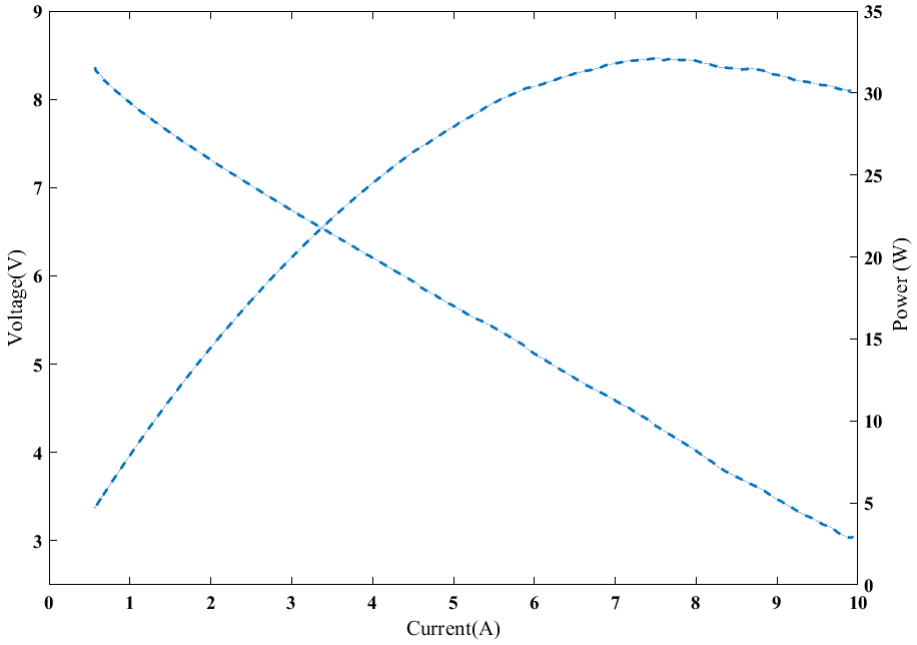

Figure 6.3: Experimental polarization curve I–V and I–P for the Heliocentric hy-Expert^{TM} PEM fuel cell 50 Instructor system.

6.5.1. Comparison Between the Experiment and Simulation Results

The I_{stack}-V_{stack} and I_{stack}-P_{stack} polarization curves of the simulated and real model are presented in Figure 6.4 - Figure 6.9 . According to these figures, it is clear that the predicted model succeeded to provide the same results obtained by the real fuel cell system. It should be noted that the temperature in the experiment curves has an error around $\pm 0.5\,°C$ since it is difficult to make experiments at constant temperatures. One another variable factor that also should be taken into account is the input Hydrogen pressure which is controlled by the manufacture. However, although these two variable factors can differ the predicted results from the real ones, only slight deviations are occurred.

6.5.2. Effect of Temperature and Humidity on the PEM Fuel Cell Stack Performance

The effects of the operation temperature on the polarization curves for a low, medium and high humidification (fans power are set at 10%, 50% and 100%) are presented in Figure 6.4 - Figure 6.9.

At low humidification (Figure 6.4 and Figure 6.5), by varying the temperature from $25\,°C$ to $43\,°C$ the stack performance improves from $T = 25\,°C$ until $T = 31\,°C$ and then deteriorates for temperatures up to $31\,°C$. The improvement of the performance from $T = 25\,°C$ until $T = 31\,°C$ can be explained by the enhancement of

the conductivity of the membrane which leads to reduce the activation loss. However, for temperatures above 31 °C the membrane start to dry due to the lack of water content which leads as a consequence to decrease the performance of the stack.

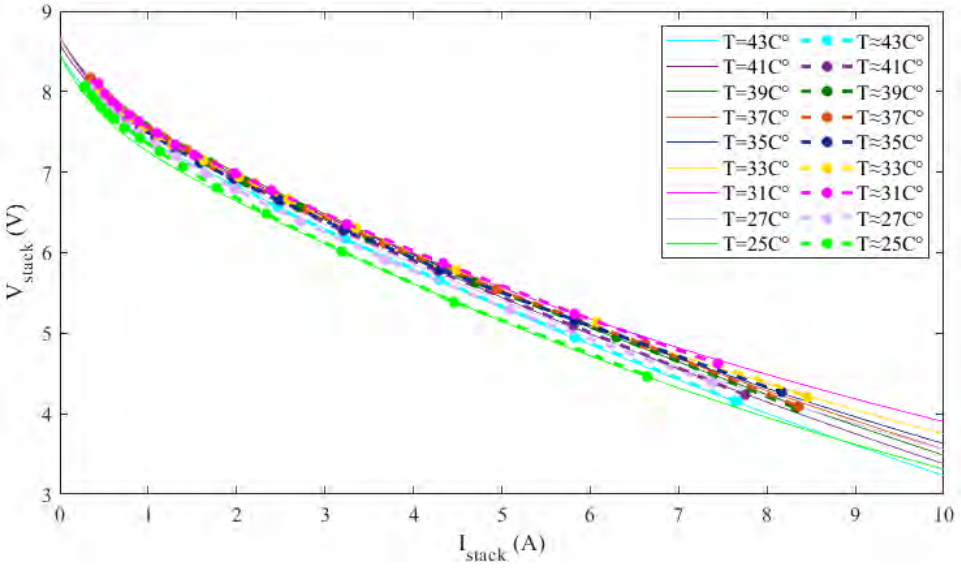

Figure 6.4: Simulation and experiment results (simulation: continuous line; experiment: dashed line); I_{stack}-V_{stack} polarization curves when Fans Power=10%.

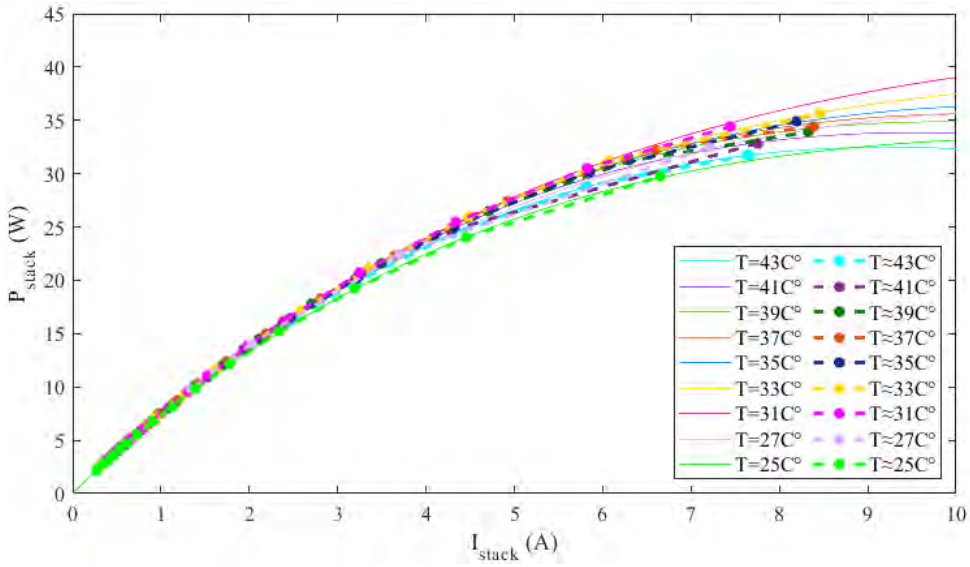

Figure 6.5: Simulation and experiment results (simulation: continuous line; experiment: dashed line); I_{stack}-P_{stack} polarization curves when Fans Power=10%.

At medium humidification (Figure 6.6 and Figure 6.7), the stack performance improves with increasing temperature. However, for higher temperatures only slight improvements are occurred since the membrane requires additional amount of water

content.

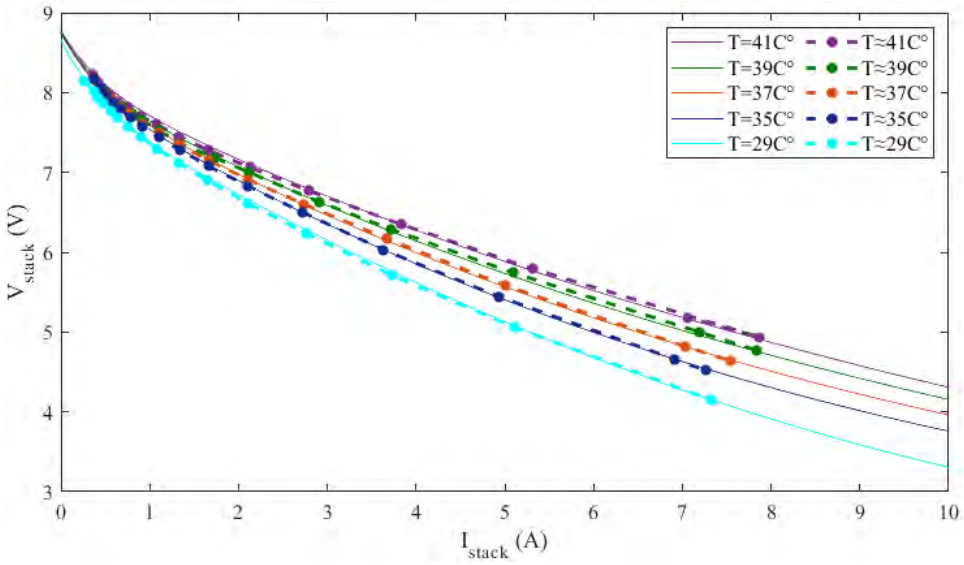

Figure 6.6: Simulation and experiment results (simulation: continuous line; experiment: dashed line); I_{stack}-V_{stack} polarization curves when Fans Power=50%.

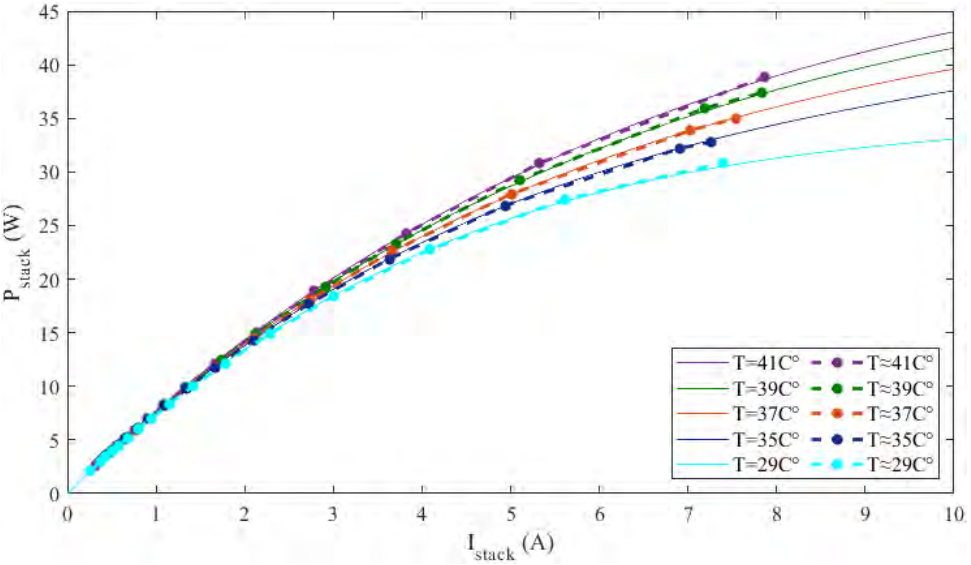

Figure 6.7: Simulation and experiment results (simulation: continuous line; experiment: dashed line); I_{stack}-P_{stack} polarization curves when Fans Power=50%.

Regarding to the last case at which the membrane is 100% humidified (Figure 6.8 and Figure 6.9), the stack performance is largely improved with increasing the temperature from $T = 25\,°C$ until $T = 39\,°C$. It is noticed that even for higher temperatures the stack performance is still improving and this is due to the well humidification provided by the fans. It should be noted that although the high

humidification has a positive effect on the stack performance for higher temperatures, it also has a negative effect for lower temperatures. Hence, according to Figure 6.5 and Figure 6.9 and for a low temperature equal to 25 °C, it is clear that the stack performance for low humidification ($P_{max} = 33W$) is better than the one obtained by high humidification ($P_{max} = 28W$).

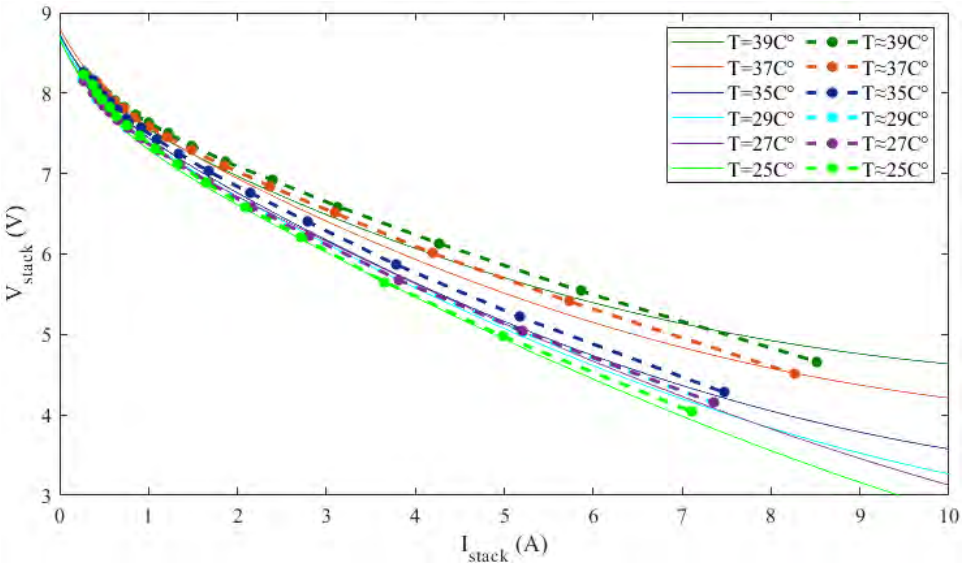

Figure 6.8: Simulation and experiment results (simulation: continuous line; experiment: dashed line); I_{stack}-V_{stack} polarization curves when Fans Power=100%.

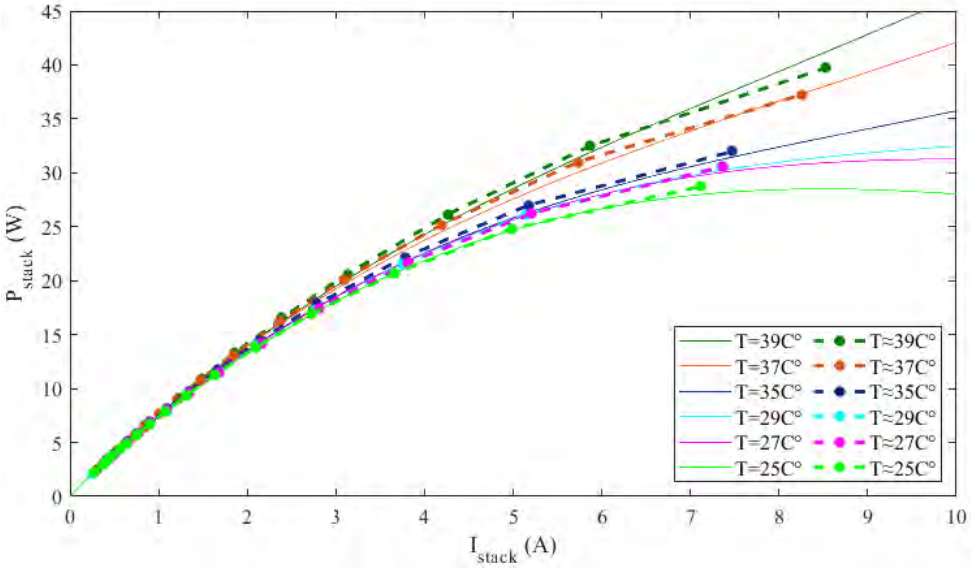

Figure 6.9: Simulation and experiment results (simulation: continuous line; experiment: dashed line); I_{stack}-P_{stack} polarization curves when Fans Power=100%.

6.6. Conclusion

A 50-W PEMFC Instructor system feeding load resistances through step-up DC–DC power converters has been experimentally studied in this work. The hardware system components, including the fuel cell with its auxiliaries, the power converter, the control system and the data acquisition, have been installed and conducted together with the dSPACE 1104 controller board.

The effect of temperature on the PEM fuel cell stack performance was studied for low, medium and high humidification. At low humidification, it was obtained that the performance of the stack improves for low temperatures (from $T = 25\,°C$ until $T = 31\,°C$) and deteriorates for temperatures up to $31\,°C$. At medium and high humidification, it was obtained that the stack performance improves with increasing temperature. However the effect of temperature is clearly pronounced at higher humidification since the increase of temperature results in a large increasing in the stack performance.

Chapter 7

Sliding Mode Control (SMC)

7.1. Introduction

Sliding mode control (SMC) is a nonlinear controller derived from the Variable Structure System (VSS) theory [244]. This last, has been applied to nonlinear systems [245]. The theory of the SMC applied to dc/dc converters can be found in [246]. The need of SMC is to use a high speed switching control to drive the system's state trajectories onto specified surface in the state space. Thus, the technique consists of two modes. The first is the reaching mode in which the trajectory moves towards specified surface from any initial point. This surface known as the switching surface or sliding surface which keep the system's state trajectory along the surface. During this mode, the system response is sensitive to parameter uncertainties and disturbances. The second is the sliding mode in which, the state trajectory sliding to the origin. Thus, once the state trajectory intercepts the sliding surface, it remains on the switching line and sliding along it until reach the origin. During this mode, the system is defined by the equation of the switching surface and thus, it is independent of the system parameters. Therefore, robustness against modeling uncertainties and disturbances can be achieved.

In this chapter, 5 robust controllers based on sliding mode including conventional sliding mode control (CSMC), proportional integral sliding mode control (ISMC), integral terminal sliding mode control (ITSMC), integral fast terminal sliding mode control (IFTSMC) and integral fast terminal SMC combined with quick reaching law (IFTSMC-QRL), are designed and implemented on a commercial PEM fuel cell system. The main innovation of this chapter is the usage of an IFTSMC combined with a QRL in a boost converter for a commercial PEMFC. A valid comparison of the proposed controllers against the conventional SMC is advantageous in order to achieve intriguing progressive results. This is an innovative comparison and implementation since the employment of these controllers in a real boost-converter with PEMFC have never been analysed.

7.2. Stability Proof

To prove the convergence of the sliding mode control, the following tow theorems will be used:

7.2.1. Lyapunov's second method for stability

Theorem 1 *Lyapunov, in his original 1892 work, proposed two methods for demonstrating stability.[1] The first method developed the solution in a series which was then proved convergent within limits. The second method, which is now referred to as the Lyapunov stability criterion or the Direct Method, makes use of a Lyapunov function V(x) which has an analogy to the potential function of classical dynamics. It is introduced as follows: Consider an autonomous (possibly nonlinear) nonlinear dynamical system* $\dot{x} = f(x)$*, having a point of equilibrium at* $x = 0$*.*
If a function $V : \mathbb{R}^n \to \mathbb{R}$ *can be found such that:*

- $V(x) > 0$ *if and only if* $x \neq 0$
- $V(x) = 0$ *if and only if* $x = 0$
- $\dot{V}(x) = \sum_{i=1}^{n} \frac{\partial V}{\partial x_i} f_i(x) = \nabla V \cdot f(x) \leq 0$ *for all values of* $x \neq 0$*.*
  ***Note**: for asymptotic stability,* $\dot{V}(x) < 0$ *for* $x \neq 0$ *is required.*

Then V(x) is called a Lyapunov function and the system is stable in the sense of Lyapunov.

7.2.2. LaSalle's invariance principle

Theorem 2 *LaSalle's invariance principle (also known as Krasovskii-LaSalle principle , Barbashin-Krasovskii-LaSalle principle,[2] or invariance principle,[1]) is a criterion for the asymptotic stability of an autonomous dynamical system.*
Consider the following system: $\dot{x} = f(x)$*, where* x *is the vector of variables, with* $f(0) = 0$
If a function $V : \mathbb{R}^n \to \mathbb{R}$ *can be found such that:*

- $V(x) > 0$ *if and only if* $x \neq 0$
- $V(x) = 0$ *if and only if* $x = 0$
- $\dot{V}(x) \leq 0$ *for all values of* $x \neq 0$*.*
- *if* $\mathcal{I}$ *contains no trajectory of the system except the trivial trajectory* $x(t) = 0$*, for* $t \geq 0$ *(where* $\mathcal{I}$ *is the union of complete trajectories contained entirely in the set* $\{x : \dot{V}(x) = 0\}$*)*

Then the origin is asymptotically stable. Furthermore,

- *If* V *is radially unbounded, i.e.* $V(x) \to \infty, as \|x\| \to \infty$

Then the origin is globally asymptotically stable.

7.2.3. Relation between LaSalle's invariance principle and Lyapunov theory

Lemma 3 *If $\dot{V}(x)$ is negative, the global asymptotic stability of the origin is a consequence of Lyapunov's second theorem. The invariance principle gives a criterion for asymptotic stability in the case when $\dot{V}(x)$ is only non-positive.*

7.3. Conventional Sliding Mode Control (CSMC)

Generally, the control of dc/dc converters is used to regulate the output voltage at a desired level. However, in this work, the controller is used to ensure the actual current to tracks the desired current defined by the user. A first step in the design of a SMC is to choose an adequate sliding variable; in our case, we followed the suggestions that the authors from [244] who defined a suitable expression related on the dynamics of the system and yields the variables to be control at a reference value.

$$s = \left(\frac{d}{dt} + \lambda\right)^{r-1} e \tag{7.1}$$

Where

- r: relative degree of the system.
- λ: a positive constant that associated with the bandwidth of the control to be designed.
- e: is the error between the PEMFC current i_L and the reference current i_{ref} as given in Equation (7.2).

$$e = i_L - i_{ref} \tag{7.2}$$

Hence, the sliding variable can be expressed by equation (7.3).

$$s = \dot{e} + \lambda e \tag{7.3}$$

By using equation (5.41), (7.2) and (7.3), the derivative of the sliding variable can be expressed as equation (7.4).

$$\dot{S}_1 = \frac{V_{out}}{L} u - \frac{V_{out}}{L} + \frac{V_{stack}}{L} + \lambda \cdot e \tag{7.4}$$

The control signal u for the conventional SMC is defined as equation (7.5).

$$u = u_{eq} + u_{eq} \tag{7.5}$$

According to the authors from [60], the equivalent control term can be deduced from the statement $\dot{S}_1 = 0$ [12, 57]. The usage of (7.4) allows to obtain the following expression.

$$u_{eq} = 1 - \frac{V_{stack}}{V_{out}} - \frac{\lambda \cdot e \cdot L}{V_{out}} \tag{7.6}$$

On the other hand, the switching term for this case is defined by the (7.6), based on the references [60].

$$u_{eq} = -k \cdot sign(s) \tag{7.7}$$

Where

- k: is a positive constant, and its choice is very influential because a small value can increase the response time; oppositely, strong oscillations can occur. These effects can excite neglected dynamics (chattering phenomenon), or even deteriorate the hardware [247].

To prove the convergence of the determined control scheme, a positive definite cost function as given in equation (7.8) is designed according to the Lyapunov criterion.

$$V(s) = \frac{1}{2}s^2 \tag{7.8}$$

Where $\dot{V}(s)$ is determined in equation (7.9)

$$\begin{aligned}
\dot{V}(s) &= s\dot{s} \\
&= s\left[\frac{V_{out}}{L}u - \frac{V_{out}}{L} + \frac{V_{stack}}{L} + \lambda \cdot e\right] \\
&= s\left[\frac{V_{out}}{L}(u_{eq} + u_{eq}) - \frac{V_{out}}{L} + \frac{V_{stack}}{L} + \lambda \cdot e\right] \\
&= s\left[\frac{V_{out}}{L}u_{eq} + \frac{V_{out}}{L}u_{eq} - \frac{V_{out}}{L} + \frac{V_{stack}}{L} + \lambda \cdot e\right] \\
&= s\left[\frac{V_{out}}{L}\left(1 - \frac{V_{stack}}{V_{out}} - \frac{\lambda \cdot e \cdot L}{V_{out}}\right) + \frac{V_{out}}{L}\left(-k \cdot sign(s)\right) - \frac{V_{out}}{L} + \frac{V_{stack}}{L} + \lambda \cdot e\right] \\
&= -k \cdot \frac{V_{out}}{L} \cdot s \cdot sign(s) \\
&= -k \cdot \frac{V_{out}}{L} \cdot |s| \\
&\leq 0
\end{aligned} \tag{7.9}$$

Consequently, according to the Lyapunov theory, the system is asymptotically converging to the sliding variable $s = \dot{e} + \lambda e$. Besides, since the sliding variable $s = \dot{e} + \lambda e$ tends to 0, therefore the tracking error (defined by $e = c \cdot e^{-\lambda t}$) tends asymptotically to 0. On he other hand, the convergence trajectory of the sliding mode is presented in Figure 7.1

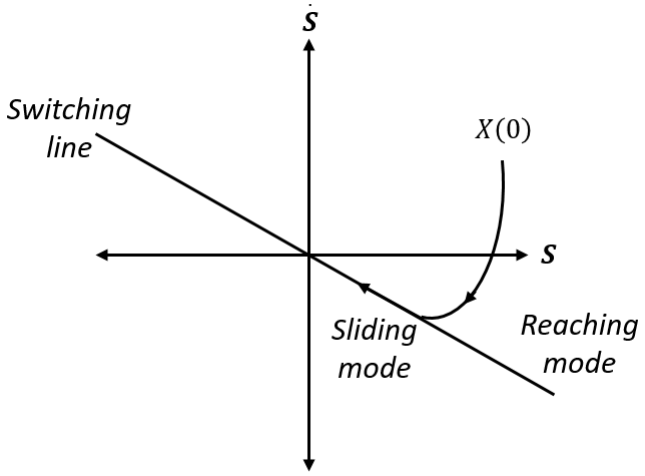

Figure 7.1: Sliding mode control phase trajectory.

Figure 7.2 to Figure 7.5, show the capability of the conventional SMC to stabilise the PEMFC when facing large load variation. In order to simplify and abridge this figure, the following abbreviations “OS", “US", “SSO", “RT" are used respectively instead of “overshoot", “undershoot", “steady-state oscillations", and “response time".

Figure 7.2 presents duty cycle signals delivered by the proposed controller. It is clearly shown that the proposed CSMC effectively force the duty cycle to render the voltage constant with fast response and no drift. It should be noted that the obtained experimental results contain some noise, as it is usual due to the retard of the control signal as well as the parasite signals which came from the system components.

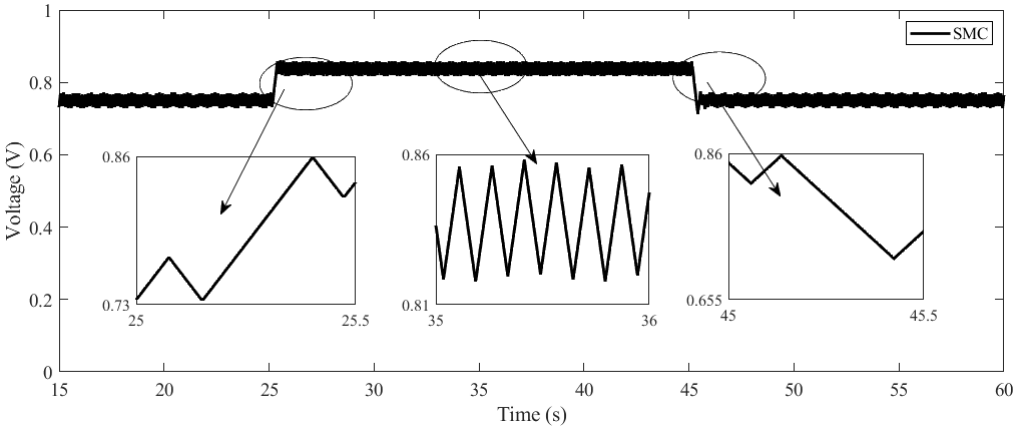

Figure 7.2: Duty cycle signal.

The PEMFC stack current and voltage curves are illustrated in Figure 7.3. These curves explicate the controllers behavior when facing different significant load variation values at $t = 25s$ and $t = 45s$. It is noteworthy that the proposed CSMC appear robustness even for large load variations. Thus, when $t = 25s$, an overshoot voltage

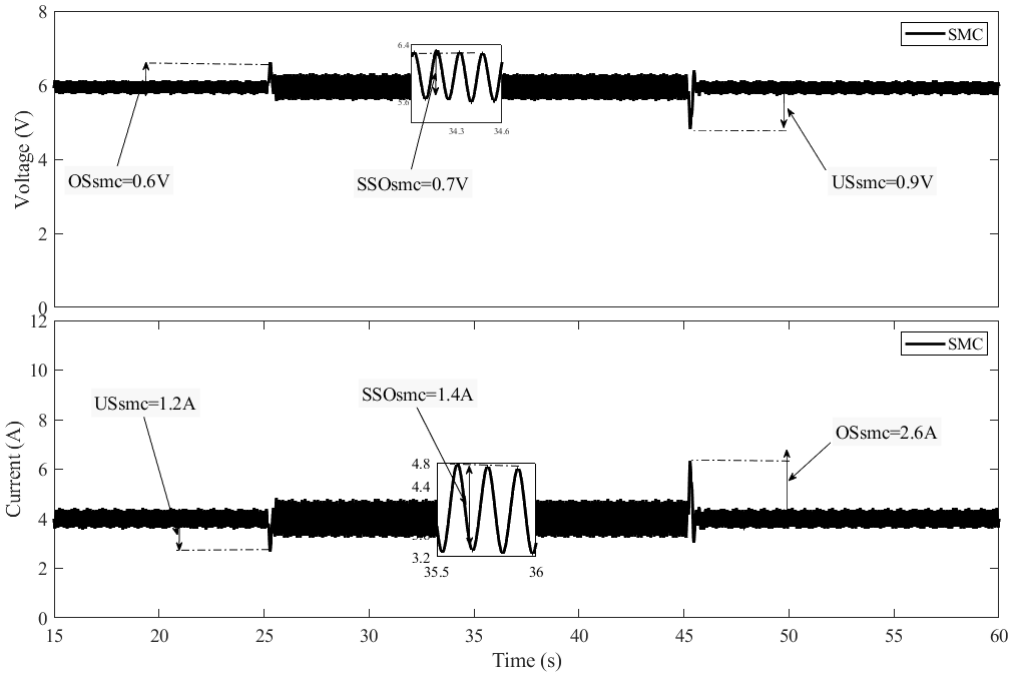

Figure 7.3: PEMFC stack voltage and current.

of $0.6V$ and undershoot current of $1.2A$ are shown by the CSMC, while at $t = 45s$, the controller shows an undershoot voltage of $0.9V$ and an overshoot current of $2.6A$. Nevertheless, these behaviors are only appeared for less than $0.5s$ at first and second load variations. Thereafter, they quickly disappeared by converging to the operating point.

Figure 7.3 also shows that after reaching the steady-state value, the voltage oscillations occurred by using the CSMC is about $0.7V$ which is close to 12% and the current oscillations is about $1.4A$ which represents more than 35%. Therefore, it should be noted that the results are too oscillating, which leads to slight deviations from the functioning power point and this may cause the damage of the PEMFC.

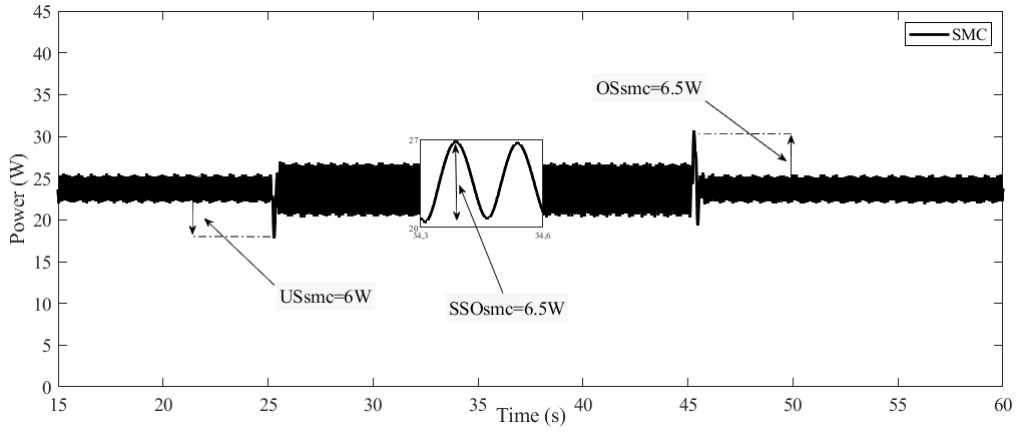

Figure 7.4: PEMFC stack power.

The stack power trajectory of the PEMFC for the CSMC is shown in Figure 7.4. According to this figure, it is clear that the stack power varies in a sinusoidal form, where the magnitude of the power varies from 20.2 to 26.8 W. Therefore, it is clear that the imperfection of CSMC is the chattering phenomenon which occurred around the operating power point (29%). However, high robustness while facing large load variations as well as high converging speed are achieved.

The behavior of the Boost converter outputs under load variation are shown in Figure 7.5. This figure manifests that for a different load values, the proposed controller is rising gradually and smoothly to the desired value. Furthermore, excellent performances such as robustness and low convergence time are attained.

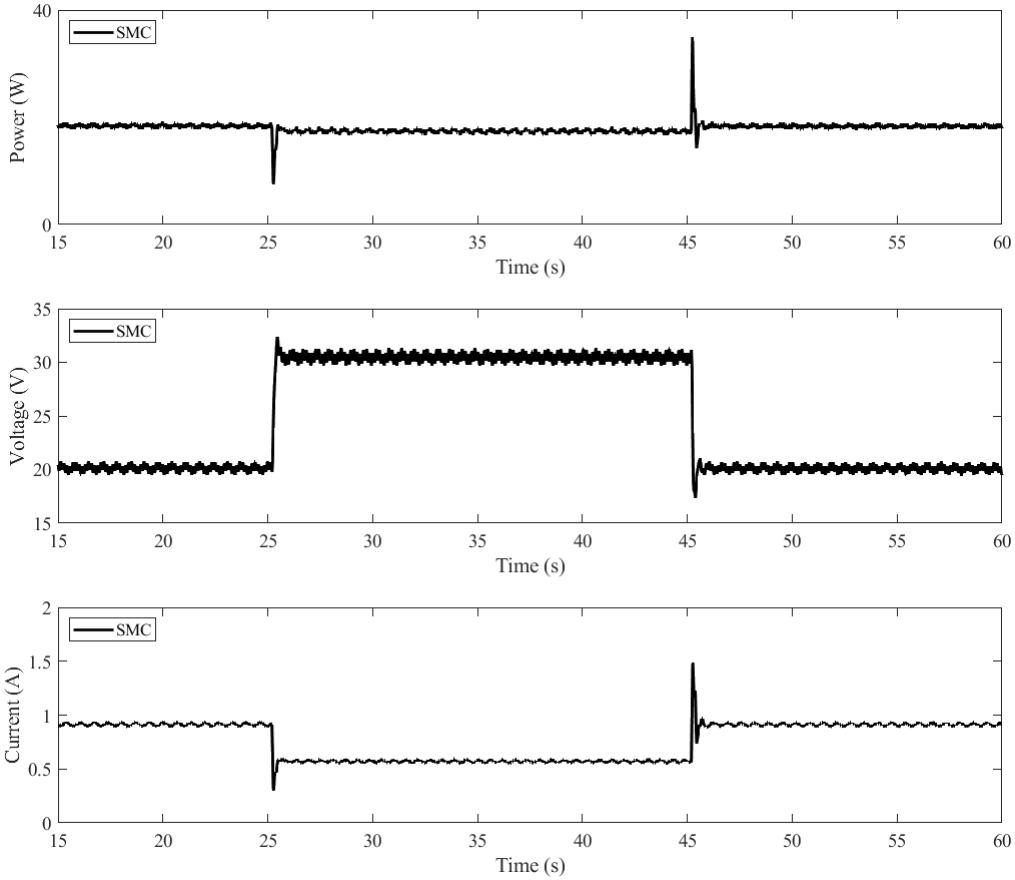

Figure 7.5: Boost converter output power, output voltage, and output current.

7.4. Proportional Integral sliding mode control (PISMC)

Considering the following sliding variable:

$$s = e + \lambda \int e \cdot dt \tag{7.10}$$

Where

- λ is a positive constant.
- e is the error between the PEMFC current i_L and the reference current i_{ref}.

The control law of the first order SMC as given by slotine et al. [244], is expressed as:

$$u = u_{eq} + u_{eq} \tag{7.11}$$

Where

- u_{eq} corresponds to the non-linear component (switching control).
- u_{eq} is the equivalent control yielded from $\dot{s} = 0$.

The switching control that ensuring the convergence of the controlled variable is given in equation (7.12):

$$u_{eq} = -\frac{kL}{x_2} sign(s) \tag{7.12}$$

Where

- k is a positive constant.
- $sign(.)$ is a usual sign function.

The derivative of the sliding variable $\dot{s}$ can be calculated using equation (5.41), (7.2) and (7.10):

$$\dot{s} = \dot{e} + \lambda e = \frac{1}{L}(v - x_2) + \lambda e + \frac{x_2}{L} u \tag{7.13}$$

Therefore, the equivalent control can be determined as equation (7.14):

$$\dot{s} = 0 \Longrightarrow u_{eq} = -\frac{1}{x_2}(v + \lambda L e - x_2) \tag{7.14}$$

The previous obtained control law can be analyzed in terms of the Lyapunov theory of stability. Therefore, to prove the convergence of the determined control scheme, a positive definite cost function as given in equation (7.15) is designed according to the Lyapunov criterion.

$$V_1 = \frac{1}{2} s^2 \tag{7.15}$$

To ensure that the cost function V_1 is converging to zero, its derivative $\dot{V}_1$ must be negative definite. By using equation (7.11), (7.12), (7.13) and (7.14), differentiating equation (7.15) with respect to time yields to:

$$\begin{aligned} \dot{V}_1 &= s\dot{s} \\ &= s\left(\frac{1}{L}(v - x_2) + \lambda e + \frac{x_2}{L}\left(-\frac{kL}{x_2} sign(s) - \frac{1}{x_2}(v + \lambda L e - x_2)\right)\right) \\ &= -sksign(s) \\ &= -k|s| \\ &\leq 0 \end{aligned} \tag{7.16}$$

Consequently, according to the Lyapunov theory, the asymptotic stability is ensured. Besides, by using equation (7.15) and (7.16), the following demonstration can be obtained.

$$\begin{aligned}
\frac{1}{2}\frac{d}{dt}s^2 &= -k\cdot|s| \\
\frac{1}{2}\cdot\int_{t_0}^{t_{reach}}\frac{d}{dt}|s|^2\,dt &= -k\cdot\int_{t_0}^{t_{reach}}|s|\,dt \\
\frac{1}{2}\cdot\int_{t_0}^{t_{reach}}\frac{d}{dt}|s|\,dt &= -k\cdot\int_{t_0}^{t_{reach}}dt \\
|s(t_{reach})|-|s(t_0)| &= -2\cdot k\cdot t\Big|_{t_0}^{t_{reach}} \\
t_{reach} &= \frac{|s(t_0)|}{2\cdot k}
\end{aligned} \tag{7.17}$$

Therefore, the system converges to the sliding variable $s = e + \lambda\int e\cdot dt$ in the finite time $t = t_{reach}$, which implies that $\dot{s} = \dot{e} + \lambda e$ also converges to 0. From the previous equation, the tracking error (defined by $e = c\cdot e^{-\lambda t}$) tends asymptotically to 0.

Figure 7.6 to Figure 7.9 show respectively the duty cycle signal, the PEMFC output signals (voltage, current, and power), and finally the boost converter output signals (voltage, current, and power). These figures show the behaviour of the conventional sliding mode (CSMC) and proportional integral sliding mode (ISMC) to track and maintain the system functioning at an adequate power point. In general, both of the controllers show global stability and satisfactory tracking results so as to keep the system operating at the desired power point. However, it is clearly shown that the ISMC has a high capability to decrease the chattering effect that occurs by the conventional SMC.

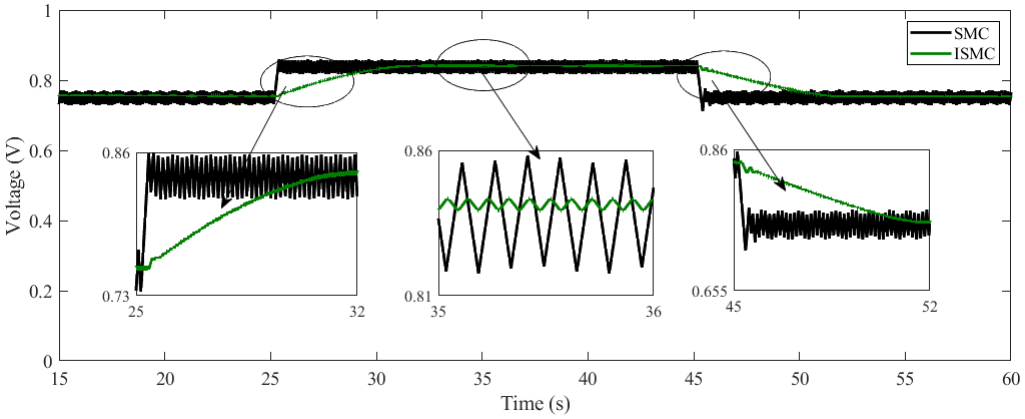

Figure 7.6: Duty cycle signal.

The duty cycle signals generated by the controllers are shown in Figure 7.6. As can be seen from this figure, the controllers effectively control the duty cycle so as to obtain constant current with fast response time and no drift. It is important to note that some noises are occurred in the obtained experimental signals. However, this is

resulting from the effect of time-delay in the control signal, as well as the parasite signals which came from hardware components.

The fuel cell output voltage and current signals are shown in Figure 7.7. This last illustrates the behavior of the CSMC and ISMC when experiencing load variations at t = 25 s and t = 45 s.

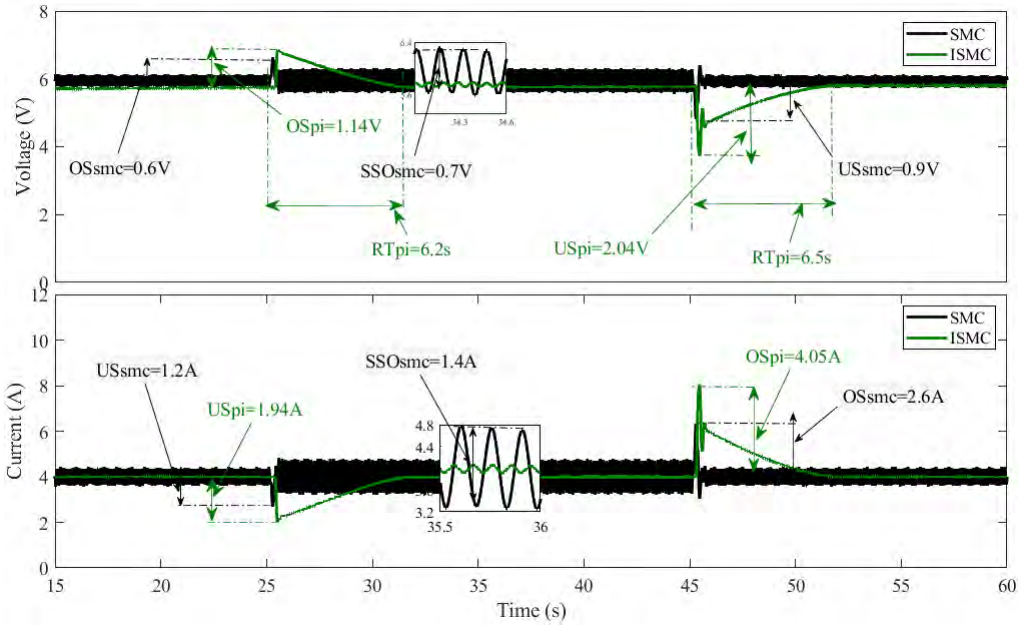

Figure 7.7: PEMFC stack voltage and current.

According to this figure, it is clear that both of the controllers manifest high robustness even when large load variations is accrued (30 Ω). Thus, by varying the load resistance from 20 Ω to 50 Ω and from 50 Ω to 20 Ω, the CSMC manifests an overshoot and undershoot voltage of 0.6 V and 0.9 V, as well as an undershoot and overshoot current of 1.2 A and 2.6 A, respectively. For the same variations, the ISMC manifests an overshoot and undershoot voltage of 1.14 V and 2.04V as well as an undershoot and overshoot current of 1.94A and 4.05A, respectively. Therefore, despite the large load variations, only small overshoots and undershoots are accrued. Regarding the CSMC, these overshoots only appears for a short period of time (response time $\leq$ 1 s), and they swiftly converge to the steady-state value but the chattering phenomenon still its main drawback. However, it is clearly shown that the ISMC could eliminate this drawback. Thus, a reduction of up to 90% of the chattering phenomenon could be attained using the integral SMC.

On the other hand, although the features of the ISMC in the chattering reduction, it should be noted that the slow converging behaviour still an important drawback in comparison with the CSMC. Hence, a response time of 6s is required to converge to steady-state value, which is a considerable time for a nonlinear controller.

The fuel cell output power trajectories are presented in Figure 7.8. According to these trajectories, it is obvious that the adequate power point is attained with swift

speed and stability of the closed-loop system. On the other hand, it is clearly shown that the chattering phenomenon is almost eliminated by using the ISMC. Indeed, the chattering magnitude using the CSMC varies approximately from 20.5 W to 27W, while it only varies from 23.3W to 23.6W using the ISMC. Accordingly, it is proven that the proposed ISMC has succeeded at reducing up to 90% of the chattering effect, which will improve, as a consequence, the fuel cell lifetime. However, the slow convergence of the ISMC still an issue that should be solved.

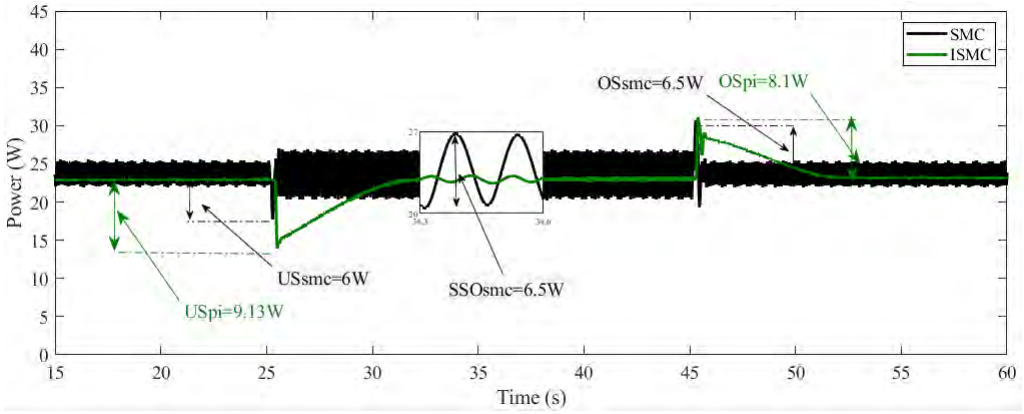

Figure 7.8: PEMFC stack power.

The behaviour of the output power, voltage and current of the DC–DC boost converter under load variations are presented in Figure 7.9. According to this figure, it is clear that, despite the heavy loading conditions, both of controllers manifests gradual and smooth movement to the desired voltage at which the system will operate at the desired power point.

Based on these results, it is clearly manifested that this experimental work has demonstrated the capability of the ISMC to reduce the chattering effect, while attaining high robustness .

7.5. Integral Terminal Sliding Mode Control (ITSMC)

An integral terminal sliding variable s is proposed as the following mathematical expression [151]

$$s = e + \lambda \left(\int e \, dt \right)^{p/q} \tag{7.18}$$

Where

- e is the error.
- λ is a positive constant ($\lambda > 0$).
- p and q are odd numbers and they should satisfy the relation $1 < p/q < 2$.

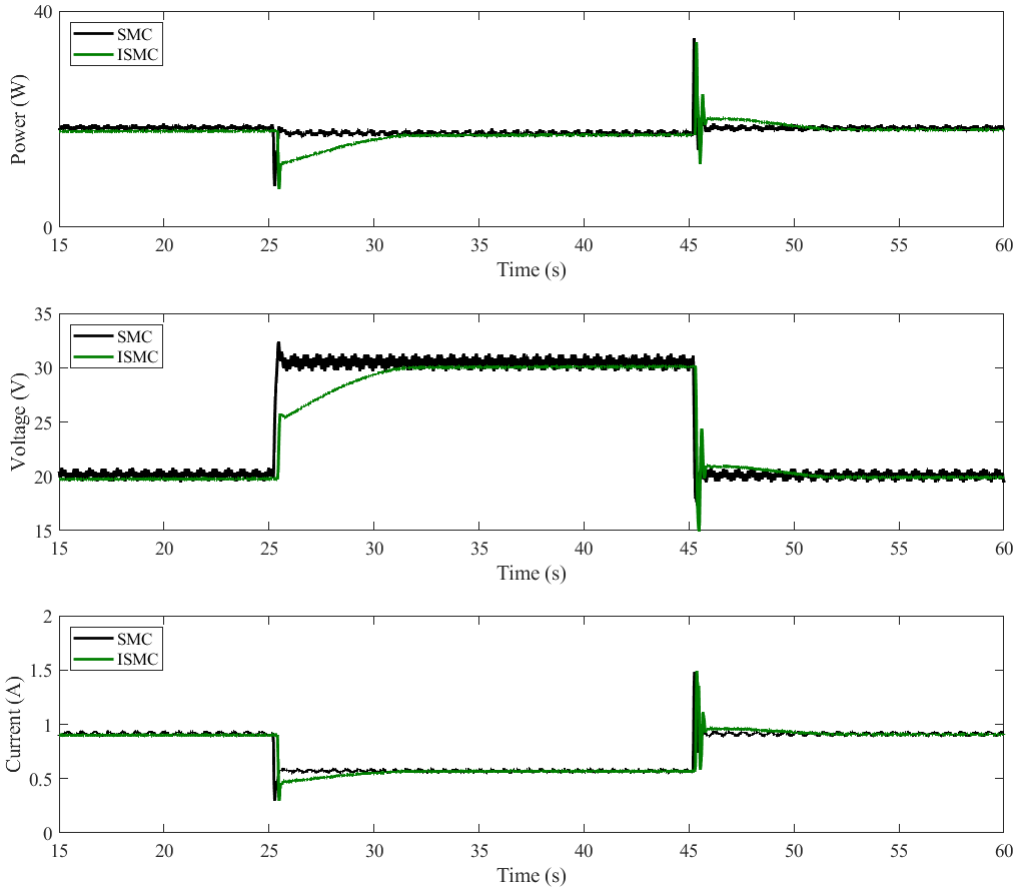

Figure 7.9: Boost converter output power, output voltage, and output current.

The derivation of Equation (7.18) leads to the following Equation (7.19).

$$\dot{s} = \dot{e} + \lambda \left(\frac{p}{q}\right) \cdot e \cdot \left(\int e\, dt\right)^{p/q-1} \tag{7.19}$$

Since the current reference is constant, therefore the derivative of the error is defined as $\dot{e} = \dot{I}_L$. Thus, s is declared as:

$$\dot{s} = \frac{V_{out}}{L} u - \frac{V_{out}}{L} + \frac{V_{stack}}{L} + \lambda \left(\frac{p}{q}\right) \cdot e \cdot \left(\int e\, dt\right)^{p/q-1} \tag{7.20}$$

The embodiment of the control law through means of an ITSMC is yields to the following expression:

$$u = u_{eq} + u_{eq} \tag{7.21}$$

The equivalent term u_{eq} is gathered by $s = 0$ and it is gleaned as follows:

$$u_{eq} = 1 - \frac{V_{stack}}{V_{out}} - \frac{\lambda\, e\, L}{V_{out}} \left(\frac{p}{q}\right) \cdot \left(\int e\, dt\right)^{p/q-1} \tag{7.22}$$

The switching control that belongs to the ITSMC approach is given in the following

equation.

$$u_{eq} = -k \cdot sign(s) \tag{7.23}$$

To prove the convergence of the determined control scheme, a positive definite cost function as given in equation (7.24) is designed according to the Lyapunov criterion.

$$V(s) = \frac{1}{2}s^2 \tag{7.24}$$

Where $\dot{V}(s)$ is determined in equation (7.25)

$$\begin{aligned}
\dot{V}(s) &= s\dot{s} \\
&= s\left[\dot{e} + \lambda\left(\frac{p}{q}\right) \cdot e \cdot \left(\int_0^t e\,dt\right)^{p/q-1}\right] \\
&= s\left[u\frac{V_{out}}{L} - \frac{V_{out}}{L} + \frac{V_{stack}}{L} + \lambda\left(\frac{p}{q}\right) \cdot e \cdot \left(\int_0^t e\,dt\right)^{p/q-1}\right] \\
&= s\left[(u_{eq} + u_{eq})\frac{V_{out}}{L} - \frac{V_{out}}{L} + \frac{V_{stack}}{L} + \lambda\left(\frac{p}{q}\right) \cdot e \cdot \left(\int_0^t e\,dt\right)^{p/q-1}\right] \\
&= s\left[\frac{V_{out}}{L}\left(1 - \frac{V_{stack}}{V_{out}} - \frac{\lambda\, e\, L}{V_{out}}\left(\frac{p}{q}\right) \cdot \left(\int_0^t e\,dt\right)^{p/q-1} + \frac{V_{out}}{L}\left(-k \cdot sign(s)\right)\right)\right] \\
&\quad + s\left[-\frac{V_{out}}{L} + \frac{V_{stack}}{L} + \lambda\, e\left(\frac{p}{q}\right) \cdot \left(\int_0^t e\,dt\right)^{p/q-1}\right] \\
&= -k \cdot \frac{V_{out}}{L} \cdot s \cdot sign(s) \\
&= -k \cdot \frac{V_{out}}{L} \cdot |s| \\
&\leq 0
\end{aligned} \tag{7.25}$$

Consequently, according to the Lyapunov theory, the asymptotic stability is ensured. Besides, since the surface $s = e + \lambda\,(\int e\,dt)^{p/q}$ tends to 0, therefore the tracking error e tends to 0.

Figure 7.10 to Figure 7.13, show the capability of the integral terminal sliding mode ITSMC to maintain the robustness of conventional SMC while reducing the undesirable chattering phenomenon. Figure 7.10 presents the duty cycle signals delivered by the CSMC and ITSMC. It is clearly shown that both of SMC and ITSMC effectively force the duty cycle to render the voltage constant with fast response and no drift. As explained before, some noise are occurred at the signals which is a usual behaviour due to the time delay of the control signal as well as the parasite signals which came from the system components.

The PEMFC stack voltage and current curves are illustrated in Figure 7.11 respectively. These curves explicate the controllers behavior when facing different significant load variation values at $t = 25s$ and $t = 45s$. It is noteworthy that each

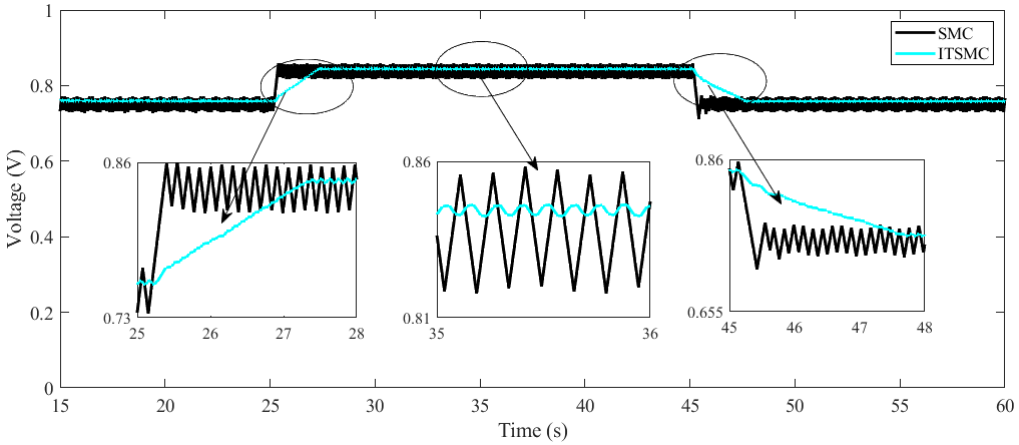

Figure 7.10: Duty cycle signal.

of ITSMC and the classical SMC show robustness even for large load variations. Thus, when $t = 25s$, an overshoot voltage of $0.6V$ and undershoot current of $1.2A$ are shown by the CSMC, while the ITSMC shows an overshoot voltage of $1.16V$ and an undershoot current of $1.88A$. At $t = 45s$, the CSMC shows an undershoot voltage of $0.9V$ and an overshoot current of $2.6A$, while an undershoot voltage of $2.05V$ and overshoot current of $3.71A$ are shown by the ITSMC. Nevertheless, these behaviors are only appeared for less than $1s$ for the case of the CSMC and for less than $2.2s$ for the case of the ITSMC. Thereafter, they quickly disappeared by converging to the operating point. Figure 7.11 also show that after reaching the steady-state value, the voltage oscillations occurred by using the SMC is close to 11% and the current oscillations is more than 35%. Therefore, it should be noted that the results are too oscillating, which leads to slight deviations from the functioning power point and this may cause the damage of the PEMFC. On the other hand, the voltage oscillations using ITSMC is about 1.3% and the current oscillations is about 1.5%. These relatively slight variations are in the acceptable range of the fuel cell operation. Therefore, using the ITSMC, healthy operational is achieved even under large load disturbance.

The stack power trajectories of the PEMFC for the CSMC and ITSMC are shown in Figure 7.12. According to this figure, it is clear that using the ITSMC, the operating desired zone is achieved with high accuracy and global system stability. In addition, it is noticeable that the stack power varies in a sinusoidal form. With the conventional SMC, the magnitude of the power varies from 20.2 to 26.8 W while it varies only from 23.1 to 23.45 W using the ITSMC controller. Therefore, it is clear that the imperfection of CSMC is the chattering phenomenon which occurred around the operating power point. However, the ITSMC track the optimal power with great precision and very low power fluctuations (les than 2%) which increase as a consequence the efficiency of the operating power point. Accordingly, the ITSMC scheme has performed successfully for set-point tracking and a chattering reduction

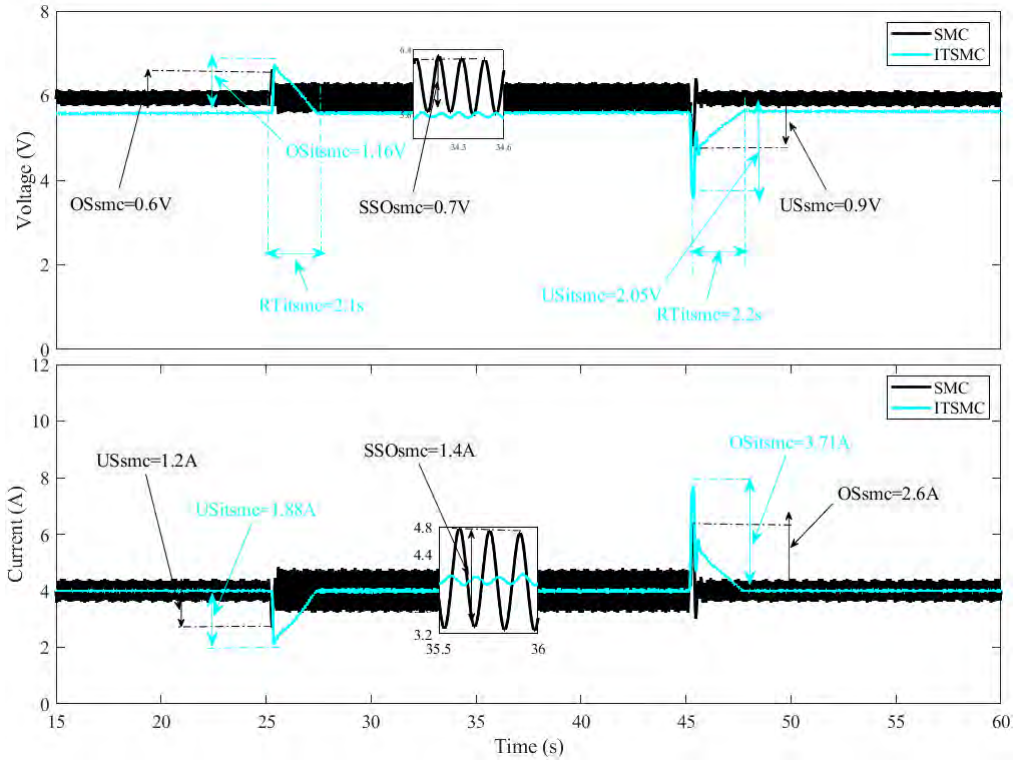

Figure 7.11: PEMFC stack voltage and current.

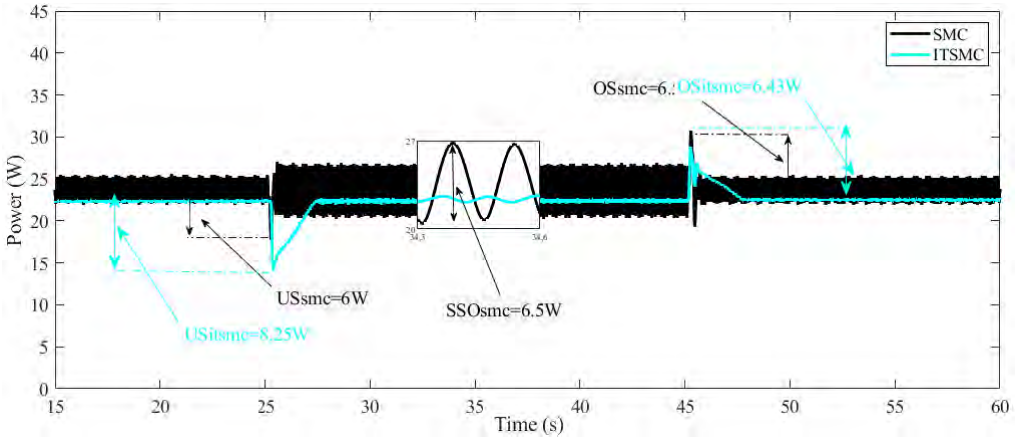

Figure 7.12: PEMFC stack power.

of 82.7% is achieved.

The behavior of the Boost converter outputs under load variation are shown in Figure 7.13 . This figure manifests that for a different load values, the ITSMC is rising gradually and smoothly to the desired value. Furthermore, excellent performances such as great precision, high efficiency, robustness, acceptable response time, and good dynamic behavior are attained.

Based on the above results, the capability of ITSMC to counteract the chattering phenomenon while achieving high performances and good dynamic behavior, are

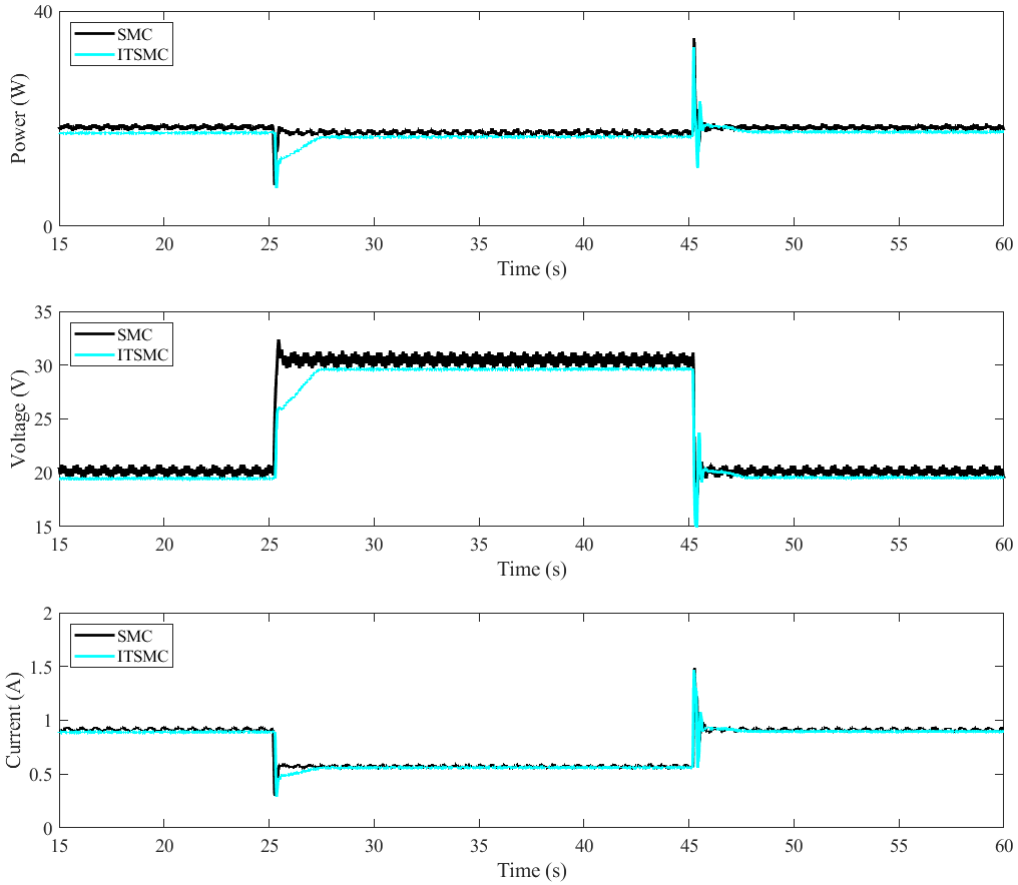

Figure 7.13: Boost converter output power, output voltage, and output current.

clearly proven.

7.6. Integral Fast Terminal Sliding Mode Control (IFTSMC)

IFTSMC is a new type of terminal sliding mode control which was invented by the scientist Venkataraman and Gulati [248] in the Jet Propulsion Laboratory. It is a nonlinear and a robust control based on the concept of the conventional TSMC and through a development of SMC. The command law u of the IFTSMC consists of two terms, a discontinuous term u_{eq} that remains the system on the sliding surface, and an equivalent term u_{eq} that brings the system to the sliding surface [244]. The total command law can be expressed as Equation (7.26).

$$u = u_{eq} + u_{eq} \tag{7.26}$$

The discontinuous term u_{eq} is defined in Equation (7.27). [249].

$$u_{eq} = -\frac{L}{V_{out}} \cdot k \cdot sign(s) \tag{7.27}$$

Where

- k is a positive constant.
- sign(s) is the signum function.

The equivalent term u_{eq} is obtained by setting a sliding variable s and is finally achieved by establishing $\dot{s} = 0$ [244]. The sliding variable is proposed as Equation (7.28) [250–252].

$$s = e + \alpha \int_0^t e.dt + \lambda \left(\int_0^t e.dt \right)^{p/q} \tag{7.28}$$

Where

- e is the error.
- α is a positive constant ($\alpha > 0$).
- λ is a positive constant ($\lambda > 0$).
- p and q are two positive constants that satisfy the following condition: $1 < p/q < 2$

The time derivative of the sliding variable can be expressed as in Equation (7.29).

$$\dot{s} = \dot{e} + \alpha \cdot e + \lambda \left(\frac{p}{q} \right) \cdot e \cdot \left(\int_0^t e.dt \right)^{\frac{p-q}{q}} \tag{7.29}$$

Also, the error expression was already defined in the Equation (7.2). As the reference current is constant, therefore, a derivative expression can be obtained from (5.41) which results in the following Equation (7.30).

$$\dot{e} = -\frac{(1-d)}{L} i_L + \frac{1}{L} \cdot V_{in} \tag{7.30}$$

Thus, through a combination of Equation (7.29), with the latter Equation (7.30), a complete expression of the derivative of the sliding variable is gathered in the following Equation (7.31).

$$\begin{aligned} \dot{s} = & \quad -\frac{(1-d)}{L}.V_{out} + \frac{1}{L}.V_{in} + \alpha \cdot e + \lambda \left(\frac{p}{q} \right) \cdot e \cdot \left(\int_0^t e.dt \right)^{\frac{p-q}{q}} \\ \dot{s} = & \quad \frac{u}{L}.V_{out} - \frac{1}{L}.V_{out} + \alpha \cdot e + \frac{1}{L}.V_{in} + \lambda \left(\frac{p}{q} \right) \cdot e \cdot \left(\int_0^t e.dt \right)^{\frac{p-q}{q}} \end{aligned} \tag{7.31}$$

Finally, stating that that $\dot{s} = 0$, the equivalent term of the control law is achieved as in Equation (7.32).

$$u_{eq} = 1 - \frac{V_{in}}{V_{out}} - \frac{\alpha \cdot e \cdot L}{V_{out}} - \frac{\lambda.e.L}{V_{out}} \left(\frac{p}{q}\right) \cdot \left(\int_0^t e.dt\right)^{\frac{p-q}{q}} \tag{7.32}$$

To prove the stability of the PEMFC system, a positive definite Lyapunov candidate function is chosen as the Equation (7.15). Thus, the derivative of the latter expression is established in the next expression such that $\dot{s}$ from (7.31) is replaced as follows.

$$\begin{aligned} \dot{V}(s) &= s\dot{s} \\ &= s\left(\frac{u}{L}.V_{out} - \frac{1}{L}.V_{out} + \frac{1}{L}.V_{in} + \alpha \cdot e + \lambda \left(\frac{p}{q}\right) \cdot e \cdot \left(\int_0^t e.dt\right)^{\frac{p-q}{q}}\right) \end{aligned} \tag{7.33}$$

The replacement of the control term u with the Equations (7.26), (7.27) and (7.32), yields to the following expression. Further mathematical development as follows, accomplishes with the Lyapunov stability proof since $\dot{V}(s)$ is concluded to be less or equal to zero.

$$\begin{aligned} \dot{V}(s) &= s\left(\frac{(u_{eq} + u_{eq})}{L}.V_{out} - \frac{1}{L}.V_{out} + \frac{1}{L}.V_{in} + \alpha \cdot e + \lambda \left(\frac{p}{q}\right) \cdot e \cdot \left(\int_0^t e.dt\right)^{\frac{p-q}{q}}\right) \\ &= s\left(\frac{V_{out}}{L}\left[1 - \frac{V_{in}}{V_{out}} - \frac{\alpha \cdot e \cdot L}{V_{out}} - \frac{\lambda.e.L}{V_{out}} \left(\frac{p}{q}\right) \cdot \left(\int_0^t e.dt\right)^{\frac{p-q}{q}} - \frac{L}{V_{out}}.k.sign(s)\right]\right) \\ &\quad + s\left(-\frac{1}{L}.V_{out} + \frac{1}{L}.V_{in} + \alpha \cdot e + \lambda \left(\frac{p}{q}\right) \cdot e \cdot \left(\int_0^t e.dt\right)^{\frac{p-q}{q}}\right) \\ &= -k \cdot s \cdot sign(s) \\ &= -k \cdot |s| \\ &\leq 0 \end{aligned} \tag{7.34}$$

Consequently, according to the Lyapunov theory, the asymptotic stability is ensured. Besides, since the sliding variable $s = e + \alpha \int_0^t e.dt + \lambda \left(\int_0^t e.dt\right)^{p/q}$ tends to 0, therefore the tracking error e tends to 0.

Figure 7.14 to Figure 7.17 show respectively the duty cycle signal, the PEMFC output signals (voltage, current, and power), and finally the boost converter output signals (voltage, current, and power). These figures express the behaviour of the integral fast terminal sliding mode control (IFTSMC) to track and maintain the system functioning at an adequate power point. According to these figures and as a general note, it is clear tht both of the controllers show global stability while keeping the system operating at the desired power point. However, it is clearly shown that the IFTSMC has a high capability to decrease the chattering effect that occurs by the SMC.

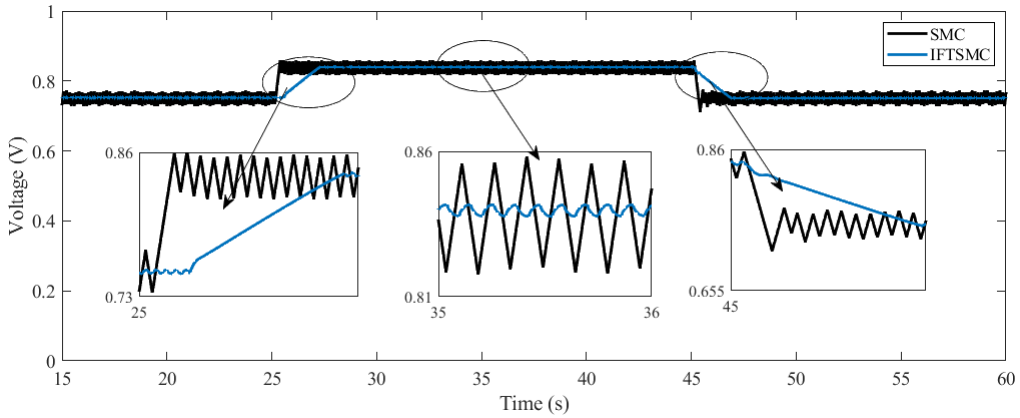

Figure 7.14: Duty cycle signal.

The duty cycle signals generated by the CSMC and IFTSMC are shown in Figure 7.14. As can be seen from this figure, high chattering reduction is clearly achieved using the proposed IFTSMC while providing fast and robust response.

The fuel cell output voltage and current signals are shown in Figure 7.15. This last illustrates the behavior of the CSMC and IFTSMC when experiencing load variations at t = 25 s and t = 45 s. According to this figure, it is clear that both of the controllers manifest high robustness even when large load variations is accrued (30 Ω). Thus, by varying the load resistance from 20 Ω to 50 Ω and from 50 Ω to 20 Ω, the CSMC manifests an overshoot and undershoot voltage of 0.6 V and 0.9 V, as well as an undershoot and overshoot current of 1.2 A and 2.6 A, respectively. For the same variations, the IFTSMC manifests an overshoot and undershoot voltage of 1.06 V and 1.95 V as well as an undershoot and overshoot current of 1.9 A and 4 A, respectively. Therefore, despite the large load variations, only small overshoots are accrued. In addition, these overshoots only appear for a short period of time (response time $\leq$ 2 s), and they swiftly converge to the steady-state value.

Figure 7.15 also shows that the fuel cell output DC voltage oscillations using IFTSMC is only about 1.4% and the oscillations of the output current is less than 2%. Therefore, compared to the CSMC (which has an oscillation voltage of 11% and oscillation current of 35%), high accuracy, robustness, and good dynamic behavior are obtained even with large load variations.

The fuel cell output power trajectories are presented in Figure 7.16. According to these trajectories, it is obvious that the adequate power point is attained with swift speed and stability of the closed-loop system. On the other hand, it is clearly shown that the chattering phenomenon is almost eliminated by using the IFTSMC. Indeed, the chattering magnitude using the conventional SMC varies approximately from 20.5 W to 27 W, while it only varies from 23.2 W to 23.6 W using the IFTSMC. Accordingly, it is proven that the proposed IFTSMC has succeeded at reducing up to more than 90% of the chattering effect, which will improve, as a consequence, the dynamic behaviour of the PEMFC system.

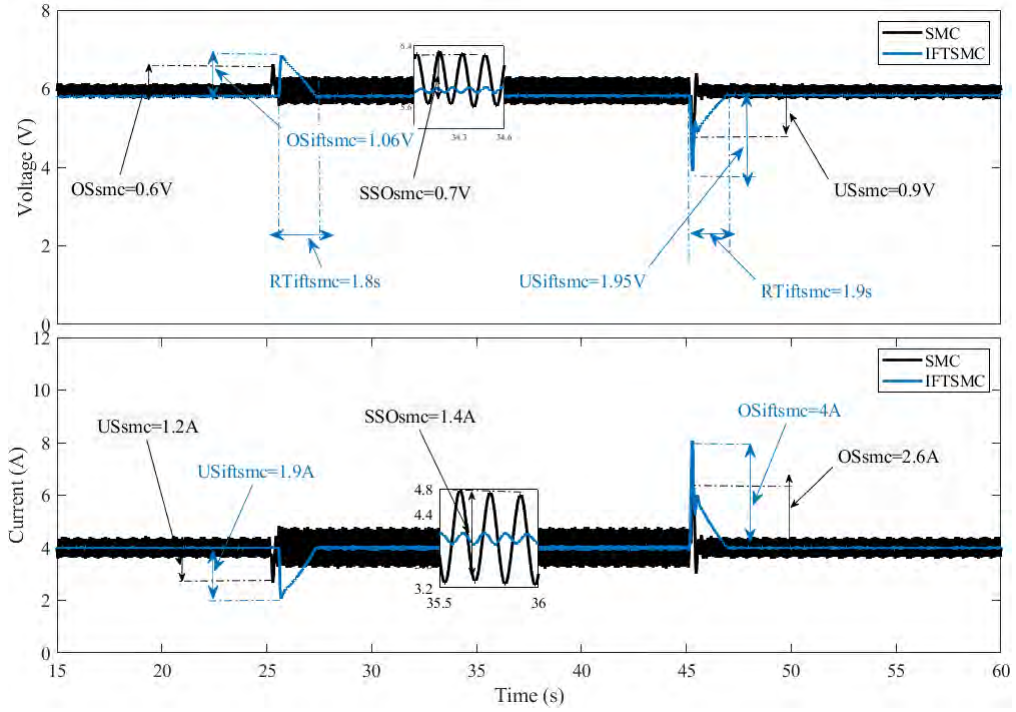

Figure 7.15: PEMFC stack voltage and current.

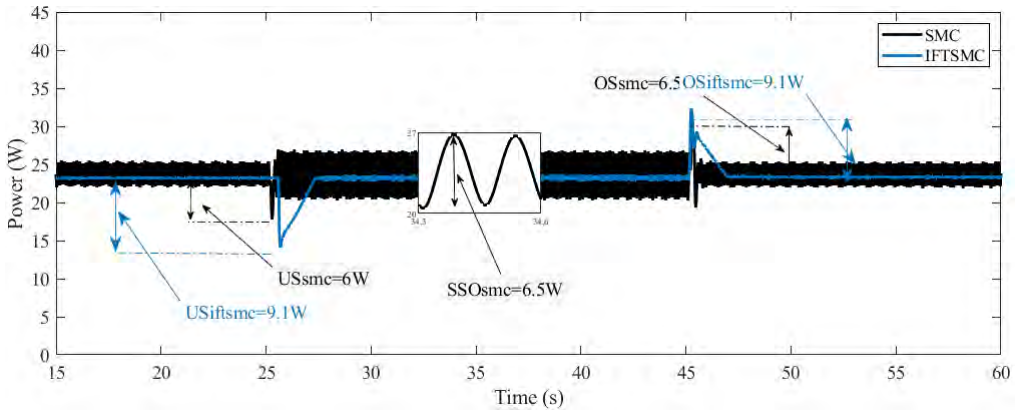

Figure 7.16: PEMFC stack power.

The behaviour of the output voltage, current, and power of the DC–DC boost converter under load variations are presented in Figure 7.17. According to this figure, it is clear that, despite the heavy loading conditions, the IFTSMC manifests gradual and smooth movement to the desired voltage at which the system will work in the adequate power point. Moreover, high performances such as low response time (less than 2 s), robustness, great precision, as well as excellent dynamic behavior are achieved.

Based on these results, it is clearly manifested that this experimental work have demonstrated the capability of the IFTSMC to reduce the chattering effect, while attaining high performances.

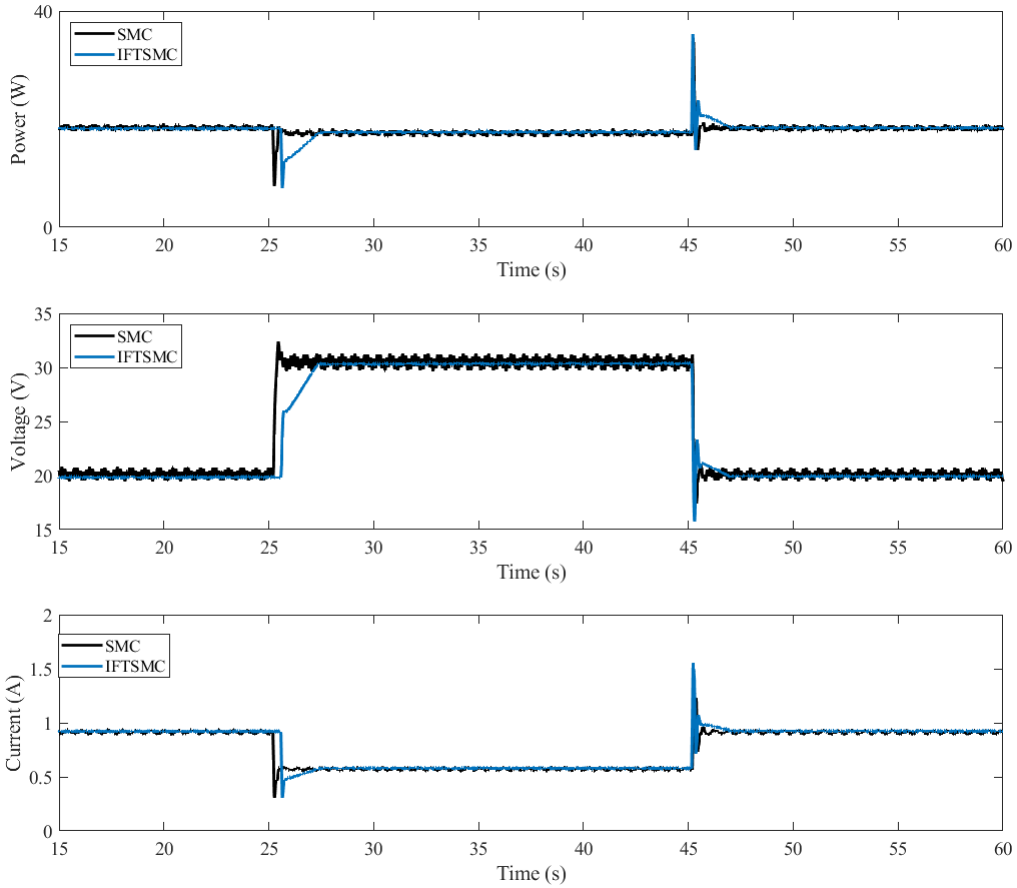

Figure 7.17: Boost converter output power, output voltage, and output current.

7.7. Integral Fast Terminal SMC combined with Quick Reaching Law (IFTSMC-QRL)

Similarly as previous presented, the control composition is obtained and differentiated within the following expression with its sub-indexes that correspond to the IFTSMC-QRL.

$$u = u_{eq} + u_{eq} \tag{7.35}$$

The equivalent term u_{eq} is retrieved through $s = 0$ and it is reached as follows:

$$u_{eq} = 1 - \frac{V_{in}}{V_{out}} - \frac{\alpha \cdot e \cdot L}{V_{out}} - \frac{\lambda.e.L}{V_{out}} \left(\frac{p}{q}\right) \cdot \left(\int_0^t e.dt\right)^{\frac{p-q}{q}} \tag{7.36}$$

In regards to the switching term u_{eq}, the expression is similar to the mentioned sliding controllers but, the proportional constant is now replaced with a variable which is also known the QRL.

$$u_{eq} = -\psi \cdot sign(s) \tag{7.37}$$

$$\psi = -\left[k_1\left(b^{|s|}-1\right) + k_2|s|^a + (D+\eta)\right] \tag{7.38}$$

The aim of the QRL is to improve the performance of the designed control; this comprises a similarity within the fast power reaching law and the double power reaching law which behaviour takes into account that the approach speed is reduced when the states are near the sliding surface so that not only enhance the rate convergence but also the chattering is reduced [253].

The parameters given in Equation (7.38) should adhere to the following conditions:

- $b > 1$.
- $\eta > 0$.
- $|s|^a > 1$.
- $k_{1,2} > 0$.
- The disturbance boundary $D > 0$.

The stability proof of the IFTSMC-QRL is also retrieved in the same way as the preceding sections.

$$\begin{aligned}
\dot{V(S_3)} &= s\dot{s} \\
&= s\left(\frac{u}{L}.V_{out} - \frac{1}{L}.V_{out} + \frac{1}{L}.V_{in} + \alpha\cdot e + \lambda\left(\frac{p}{q}\right)\cdot e\cdot\left(\int_0^t e.dt\right)^{p/q-1}\right) \\
&= s\left(\frac{(u_{eq}+u_{eq})}{L}.V_{out} - \frac{1}{L}.V_{out} + \frac{1}{L}.V_{in} + \alpha\cdot e + \lambda\left(\frac{p}{q}\right)\cdot e\cdot\left(\int_0^t e.dt\right)^{p/q-1}\right) \\
&= s\left(\frac{V_{out}}{L}\left[1 - \frac{V_{in}}{V_{out}} - \frac{\alpha\cdot e\cdot L}{V_{out}} - \frac{\lambda.e.L}{V_{out}}\left(\frac{p}{q}\right)\cdot\left(\int_0^t e.dt\right)^{p/q-1} - k.sign(s)\right]\right) \\
&\quad + s\left(-\frac{1}{L}.V_{out} + \frac{1}{L}.V_{in} + \alpha\cdot e + \lambda\left(\frac{p}{q}\right)\cdot e\cdot\left(\int_0^t e.dt\right)^{p/q-1}\right) \\
&= -\psi\cdot\frac{V_{out}}{L}\cdot s\cdot sign(s) \\
&= -\psi\cdot\frac{V_{out}}{L}\cdot|s| \\
&\leq 0
\end{aligned} \tag{7.39}$$

Consequently, according to the Lyapunov theory, the asymptotic stability is ensured. Besides, since the sliding variable $s = e + \alpha\int_0^t e.dt + \lambda\left(\int_0^t e.dt\right)^{p/q}$ tends to 0, therefore the tracking error e tends to 0.

Figure 7.18 to Figure 7.21 show respectively the duty cycle signal, the PEMFC output signals (voltage, current, and power), and finally the boost converter output signals (voltage, current, and power). Despite the sharp variations of the load resistance, it is clearly shown that both of controllers succeeded to converge the

signals to the desired values; which will guarantee as a result the stability of the system.

The duty cycle signals generated by both CSMC and IFTSMC-QRL are presented in Figure 7.18. According to this figure, it is clearly shown that the proposed IFTSMC generates fast response in comparison with the previous methods. Hence, it takes only less than 1.5s to reach the equilibrium point while while providing an accurate response.

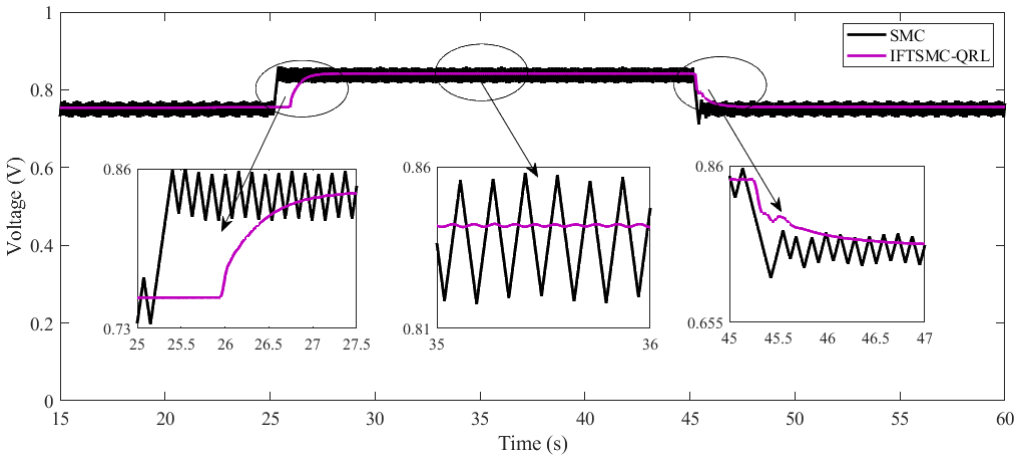

Figure 7.18: Duty cycle signal.

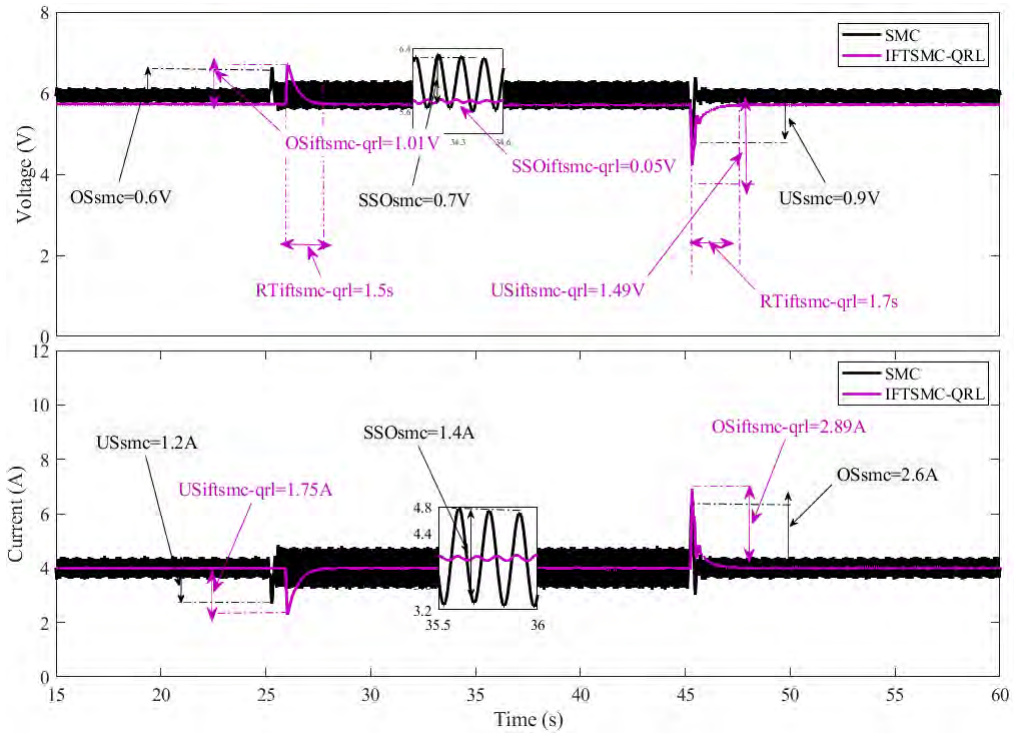

Figure 7.19: PEMFC stack voltage and current.

The electric outputs of the FC-50W stack, under the application of CSMC and

IFTSMC-QRL, are presented in Figure 7.19 and Figure 7.20; where the three graphs shows, respectively, the stack voltage, stack current and stack power. At $t = 25$ s, by applying load variation from 20 Ω to 50 Ω, the CSMC shows an overshoot of 0.6V in voltage, an undershoot of 1.2A in current, and an undershoot of 6W in power; while the proposed IFTSMC-QRL shows an overshoot of 1.01V in voltage, an undershoot of 1.75A in current, and an undershoot of 7.69 W in power. On the other hand, at $t = 45$ s, by applying load variation from 50 Ω to 20 Ω, the CSMC shows an undershoot of 0.9V in voltage, an overshoot of 2.6 A in current, and an overshoot of 6.5W in power; while the proposed IFTSMC-QRL shows an undershoot of 1.49V in voltage, an overshoot of 2.89A in current, and an overshoot of 6.66W in power. According to these results, it is clear that both of CSMC and IFTSMC-QRL have almost the same performance in term of overshoots and undershoots; where the proposed IFTSMC-QRL has an improvement of 94% in the chattering reduction over the CSMC. Hence, it is clearly shown that the feature of the proposed IFTSMC-QRL appears in its high capability to counteract the chattering phenomenon while converging the system to the reference value with high speed (1.5s). Thus, in spite

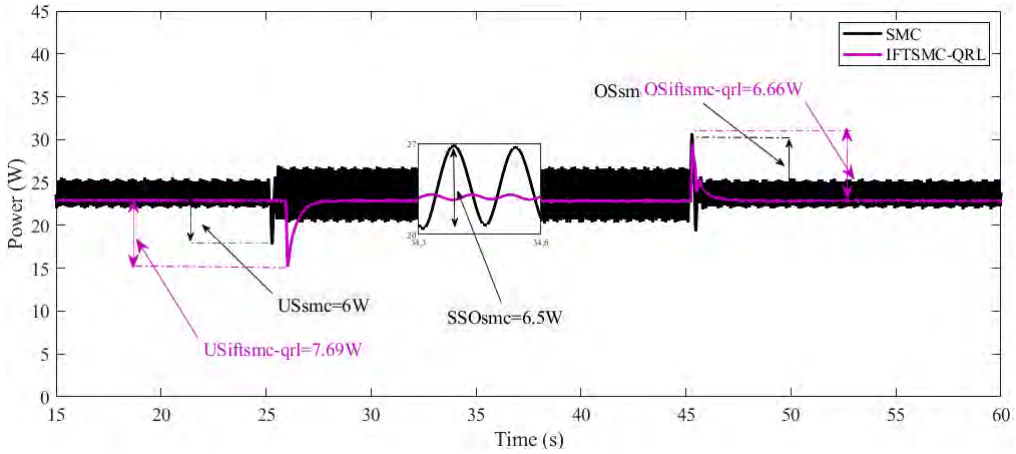

Figure 7.20: PEMFC stack power.

of the large load resistance variations, excellent performances such as high efficiency, robustness, low response time, and good dynamic behavior are attained.

Figure 7.21 shows the output signals behaviour of the step-up DC-DC converter. According to this figure, gradual and smooth movements to the correspondent voltage value are obtained.

Based on these results, although the CSMC still has slight better convergence speed, the proposed IFTSMC-QRL has provided excellent results in terms of chattering reduction, high tracking accuracy, high convergence speed (in comparison with the previous methods) and high robustness when facing unexpected external disturbance.

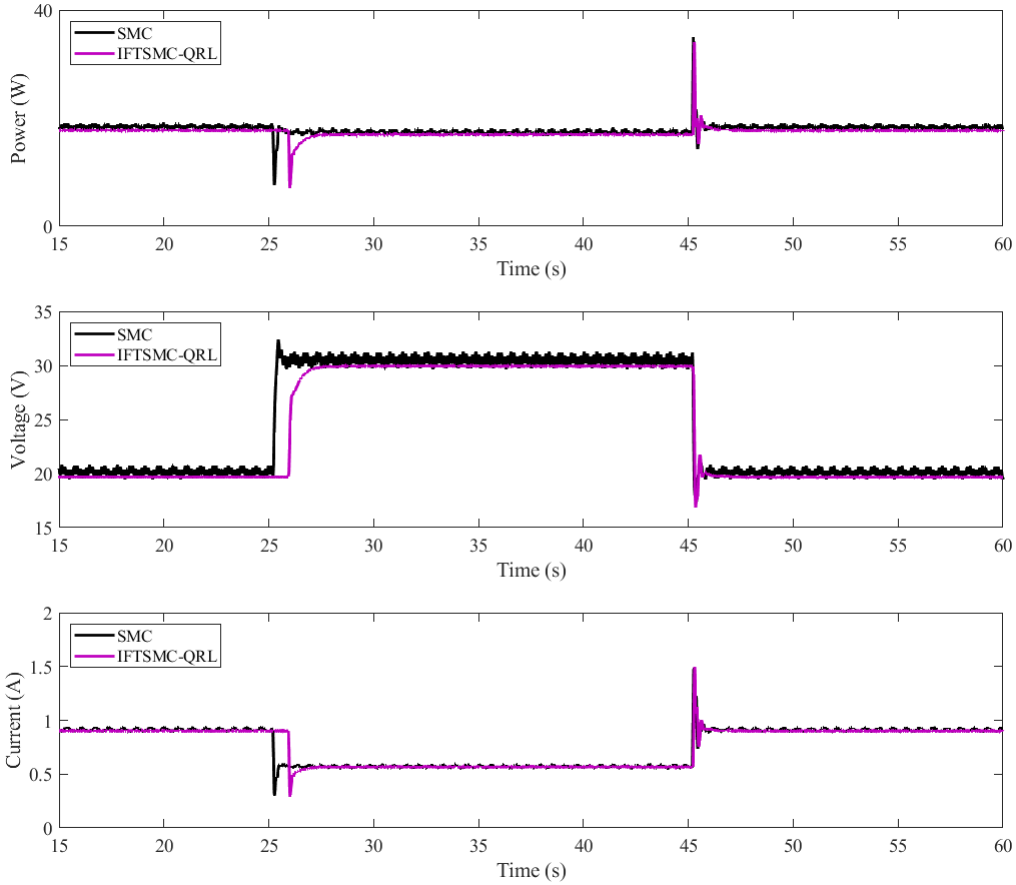

Figure 7.21: Boost converter output power, output voltage, and output current.

7.8. Performance Metrics Used

To achieve the best performance, the gains of the controller were obtained through the minimization of the integral of the absolute error (IAE), which is given in Equation (7.40). This helps to adjust the controller parameters through a decrement in the tracking error in real-time.

$$IAE = \sum_{i=1}^{N} |e_i| \Delta t \tag{7.40}$$

Where

- e_i is the tracking error.
- N is an observation data length time for the calculation.

Since the main objective is the tracking performance enhancement, not only was the IAE calculated but other types of metrics were also used to gather accurate results. These were the root-mean-square-error (RMSE) and the relative root-mean-square

(RRMSE), which are reflected in Equations (7.41) and (7.42), respectively.

$$RMSE = \sqrt{\frac{1}{N}\sum_{i=1}^{N}(e_i)^2} \tag{7.41}$$

$$RRMSE = \sqrt{\sum_{i=1}^{N}(e_i)^2 / \sum_{i=1}^{N}(r_i)} \times 100\% \tag{7.42}$$

Where

- r_i is the reference along the i-th sample.

7.9. Conclusion

In this chapter, an innovative structure for current reference following was defined and implemented in a PEMFC. Robust controllers like conventional sliding mode control (CSMC), proportional integral sliding mode control (ISMC), integral terminal sliding mode control (ITSMC), integral fast terminal sliding mode control (IFTSMC) and integral fast terminal SMC combined with quick reaching law (IFTSMC-QRL), were also implemented and contrasted with the novel design to highlight the features that could define the effectiveness of each in different scenarios such as constant and dynamic change following.

An assembled test rig with a commercial PEMFC from Heliocentris with a boost converter were used to evaluate each structure in a dSPACE DS1102. The PEMFC can be controlled through a PWM signal generator that belongs to the converter, and this was managed by a proper designed controller. The reference was established as two load changes at 25 s and 45 s where in the first one, the resistance shifted from 20 Ω to 50 Ω and in the second step regressed to 20 Ω.

The experimental results showed that during the dynamic changes, the five proposed techniques have shown high robustness against variations of the load resistance. The performance of these algorithms are summarised in Table 7.1. As it is clearly shown, the IFTSMC-QRL has the superior performance in terms of accuracy (steady state oscillation) over the other algorithms. Moreover, it shows faster response and better robustness over the ISMC, ITSMC, and IFTSMC. On the other hand, although the conventional SMC provides higher robustness over the terminal sliding modes, its chattering effect is still one of its drawbacks.

Table 7.1: Performance of the proposed SMC algorithms.

Controller	**Overshoot**	**Undershoot**	**Response Time**	**Steady State Oscillation**
CSMC	6.5W	6W	0.2s	6.5W
ISMC	8.1W	9.13W	6.2s	0.7W
ITSMC	6.43W	8.25W	2.1s	0.35W
IFTSMC	9.1W	9.1W	1.8s	0.4W
IFTSMC-QRL	6.66W	7.69W	1.5s	0.25W

Chapter 8

High order sliding mode (HOSM)

8.1. Introduction

High order sliding mode (HOSM) control is a nonlinear controller introduced by Emel'Yanov et al. [254], aiming to attain a finite time on the sliding set of order r. This type of control belongs to the theory of systems with variable structure. Its main advantage over other control tools is that it provides a prompt response, robustness, stability in undetermined environments and low computation is required [255]. This technique gathers a control law that changes the dynamics of a system based on a sliding surface that ensures the convergence [254].

HOSM has the same features of traditional SMC such as system robustness and finite-time convergence. Moreover, it has an intrinsic capability to overcome the drawback of SMC by reducing the ripples (called "chattering phenomenon" in control literature [256–259]) even the existence of disturbances and model uncertainties. These features lead to an improvement in the fuel cell performance and lifetime while guaranteeing the global system stability.

Like the SMC, the control law of HOSM is composed of two parts, equivalent and switching control. The equivalent control u_{eq} is a continuous function proposed by slotine in [244]. u_{eq} was developed to drive the system without considering its uncertainties and external disturbance, and it can be obtained by zeroing $\dot{s}$ ($\dot{s} = 0$). The switching control u_{sw} is a discontinuous function which contains the switching element. The main purpose of this function is to ensure the convergence of the overall system by keeping it moving onto the sliding surface. Moreover, it guarantees the robustness against uncertainties and external disturbances.

In this chapter, HOSM based on twisting algorithm (TA), super twisting algorithm (STA), prescribed convergence law algorithm (PCL), quasi-continuous algorithm (QCA) and finally drift algorithm (DA) are designed to drive the boost converter in order to improve the power quality and to remain the fuel cell functioning at an adequate power point.

8.2. Twisting algorithm (TA)

Twisting algorithm is one of the most popular schemes among the second order SMC. It has been utilized to reduce the chattering in relative degree one system via the inclusion of an integrator in the equation of the controlled variable [260]. The main feature of this control scheme is its capability to maintain the robustness of conventional SMC while reducing the undesirable chattering phenomenon.
Considering the following uncertain second-order system:

$$\begin{cases} \dot{y}_1 = y_2 \\ \dot{y}_2 = \varphi(x,t) + \gamma(x,t)\nu \end{cases} \tag{8.1}$$

Where

- ν represents the control derivative $\nu = \dot{u}$.
- y_1 and y_2 are local coordinates and they respectively represents s and $\dot{s}$.
- $\varphi(x,t)$ and $\gamma(x,t)$ are smooth functions and they are determined in Equation (8.4).

The parameter u in (8.3) is used as a state variable, where, $\dot{u}$ represents the discontinuous control which drives the sliding variable s in the second order sliding surface S^2. In this way, chattering is eliminated. Differentiating equation (8.2) with respect to time yields to equation (8.3):

$$\dot{s} = \dot{e} + \lambda e = \frac{1}{L}(v - x_2) + \lambda e + \frac{x_2}{L}u \tag{8.2}$$

$$\begin{aligned} \dot{y}_2 &= \ddot{s} \\ &= \frac{1}{L}(\dot{v} - \dot{x}_2) + \lambda\dot{e} + \frac{1}{L}(\dot{x}_2 \cdot u + x_2 \cdot \dot{u}) \\ &= \frac{1}{L}(\dot{v} - \dot{x}_2) + \lambda\left(\frac{1}{L}(v - x_2) + \frac{1}{L}x_2 \cdot u\right) + \frac{1}{L}(\dot{x}_2 \cdot u + x_2 \cdot \dot{u}) \\ &= \frac{1}{L}[(u-1)\dot{x}_2 + \dot{v} + \lambda(u-1)x_2 + \lambda v] + \frac{1}{L}x_2 \cdot \dot{u} \\ &= \frac{1}{L}[(u-1)\dot{x}_2 + \dot{v} + \lambda(u-1)x_2 + \lambda v] + \frac{1}{L}x_2 \cdot \nu \end{aligned} \tag{8.3}$$

Therefore, φ and γ can be given as equation (8.4).

$$\begin{cases} \varphi = \frac{1}{L}[(u-1)\dot{x}_2 + \dot{v} + \lambda(u-1)x_2 + \lambda v] \\ \gamma = \frac{1}{L}x_2 \end{cases} \tag{8.4}$$

The control objective is to guarantee that the tracking error e is converging to zero. ν is commuting at every axis crossing, which necessitates the presence of a sign

function of the derived sliding variable in the control signal. Therefore, the dynamic control law ν_{sw} using twisting algorithm can be given as: [260]

$$\nu_{sw} = -\frac{k_1 L}{x_2}(s + k_2 \cdot sign(\dot{s})) \tag{8.5}$$

Where

- k_1 and k_2 are two positive constants.

By annulling $\dot{y}_2$, the equivalent control ν_{eq} can be expressed as:

$$\nu_{eq} = -\frac{\varphi}{\gamma} = -\frac{1}{x_2}\left[(u-1)\dot{x}_2 + \dot{v} + \lambda(u-1)x_2 + \lambda v\right] \tag{8.6}$$

The overall control law is then defined in equation (8.7).

$$\nu = \nu_{eq} + \nu_{sw} \tag{8.7}$$

In order to prove the convergence of the determined control scheme, a positive definite cost function as given in equation (8.8) is designed according to the Lyapunov criterion.

$$V = \frac{1}{2}k_1 s^2 + \frac{1}{2}\dot{s}^2 \tag{8.8}$$

To ensure that the cost function V is converging to zero in finite time, its derivative $\dot{V}$ must be asymptotic stable. By using equation (8.1), (8.3), (8.19), (8.5), (8.6) and (8.7), differentiating equation (8.8) with respect to time yields to:

$$\begin{aligned}
\dot{V} &= k_1 s\dot{s} + \dot{s}\ddot{s} \\
&= k_1 s\dot{s} + \dot{s}(\varphi + \gamma\nu) \\
&= \dot{s}\left(k_1 s + \frac{1}{L}\left[(u-1)\dot{x}_2 + \dot{v} + \lambda(u-1)x_2 + \lambda v\right] + \frac{1}{L}x_2\nu\right) \\
&= \dot{s}\left(k_1 s + \frac{1}{L}\left[(u-1)\dot{x}_2 + \dot{v} + \lambda(u-1)x_2 + \lambda v\right]\right) + \\
&\quad \dot{s}\frac{x_2}{L}\left(-\frac{k_1 L}{x_2}(s + k_2 sign(\dot{s})) - \frac{1}{x_2}\left[(u-1)\dot{x}_2 + \dot{v} + \lambda(u-1)x_2 + \lambda v\right]\right) \\
&= -\dot{s}k_1 k_2 sign(\dot{s}) \\
&= -|\dot{s}|k_1 k_2 \\
&\leq 0
\end{aligned} \tag{8.9}$$

Consequently, according to the Lyapunov theory and LaSalle's invariance principle, the asymptotic stability is ensured. Besides, since the derivative of the sliding variable $\dot{s} = \dot{e} + \lambda e$ tends to 0, therefore the tracking error e tends to 0.

Note: In the above case, LaSalle's invariance principle is required to prove the asymptotic stability because when $\dot{V}(s, \dot{s}) = 0$ implies that $\dot{s} = 0$, but s could be different to 0.

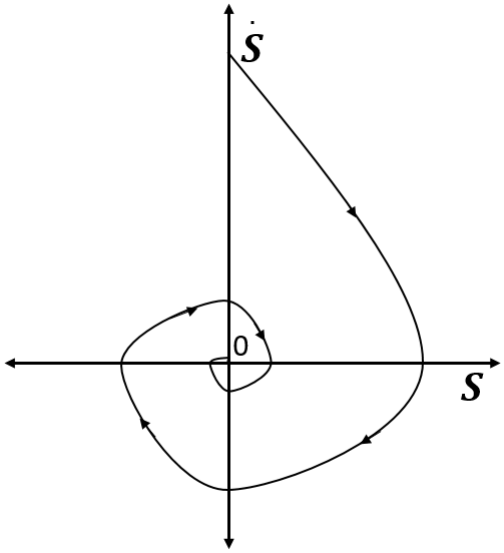

Figure 8.1: Twisting algorithm phase trajectory.

The convergence trajectory of the twisting algorithm is presented in Figure 8.1

Figure 8.2 to Figure 8.6, show the capability of HOSM-TA to maintain the robustness of conventional SMC while reducing the undesirable chattering phenomenon. Figure 8.2 presents duty cycle signals delivered by SMC and HOSM-TA. It is clearly shown that both of SMC and HOSM-TA effectively force the duty cycle to render the voltage constant with fast response and no drift. It should be noted that the obtained experimental results contain some noise, as it is usual due to the retard of the control signal as well as the parasite signals which came from the system components.

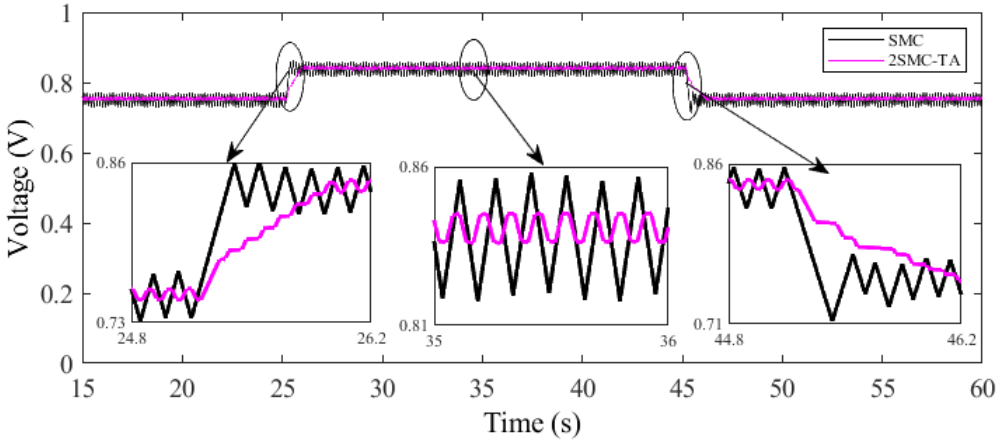

Figure 8.2: Duty cycle signal.

The PEMFC stack current and voltage curves are illustrated in Figure 8.3 and Figure 8.4 respectively. These curves explicate the controllers behavior when facing different significant load variation values at $t = 25s$ and $t = 45s$. It is noteworthy

that each of HOSM-TA and classical SMC appear robustness even for large load variations. Thus, when $t = 25s$, an overshoot voltage of $0.5V$ and undershoot current of $1.2A$ are shown by the SMC, while the HOSM-TA shows an overshoot voltage of $0.8V$ and an undershoot current of $1.8A$. At $t = 45s$, the SMC shows an undershoot voltage of $0.7V$ and an overshoot current of $2.6A$, while an undershoot voltage of $1.5V$ and overshoot current of $3.9A$ are shown by the HOSM-TA. Nevertheless, these behaviors are only appeared for $1s$ and $1.2s$ at first and second load variations respectively. Thereafter, they quickly disappeared by converging to the operating point. Figure 8.3 and Figure 8.4 also show that after reaching the steady-state

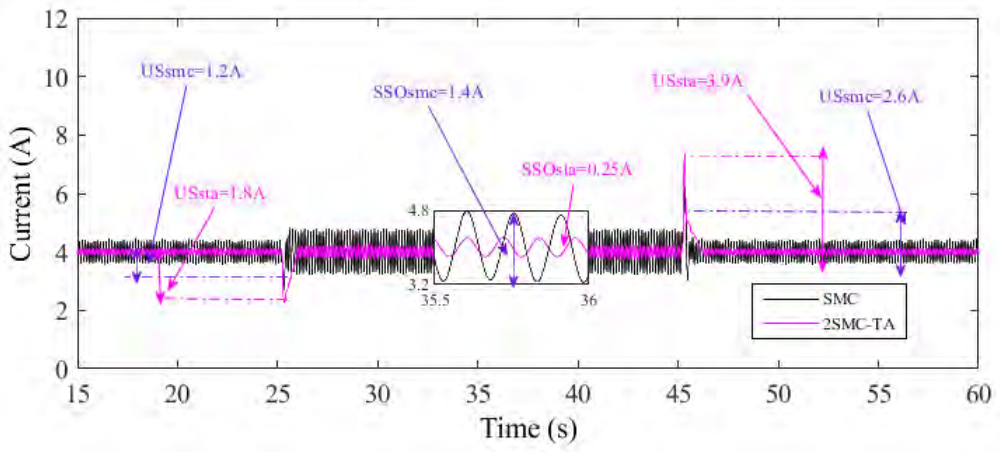

Figure 8.3: PEMFC stack current.

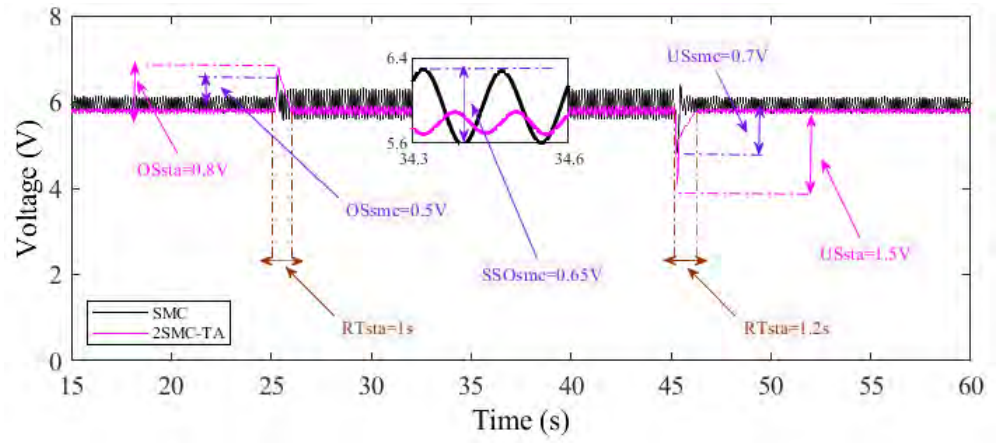

Figure 8.4: PEMFC stack voltage.

value, the voltage oscillations occurred by using the SMC is close to 11% and the current oscillations is more than 35%. Therefore, it should be noted that the results are too oscillating, which leads to slight deviations from the functioning power point and this may cause the damage of the PEMFC. On the other hand, the voltage oscillations using HOSM-TA is about 4% and the current oscillations is about 6%.

These relatively slight variations are in the acceptable range of the fuel cell operation. Therefore, using the HOSM-TA, healthy operational is achieved even under large load disturbance.

The stack power trajectories of the PEMFC for SMC and HOSM-TA are shown in Figure 8.5 According to this figure, it is clear that using the HOSM-TA, the operating desired zone is achieved fleetly with high accuracy and global system stability. In addition, it is noticeable that the stack power varies in a sinusoidal form. With the traditional SMC, the magnitude of the power varies from 20.2 to 26.8 W while it varies only from 23.1 to 24.4 W using the HOSM-TA controller. Therefore, it is clear that the imperfection of traditional SMC is the chattering phenomenon which occurred around the operating power point (29%). However, the HOSM-TA track the optimal power with great precision and very low power fluctuations (5%) which increase as a consequence the efficiency of the operating power point. Accordingly, the HOSM-TA

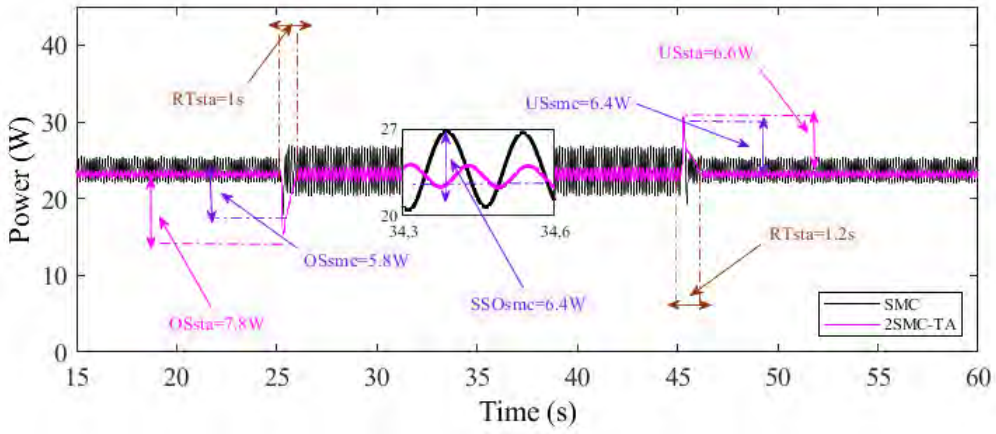

Figure 8.5: PEMFC stack power.

scheme has performed successfully for setpoint tracking and a chattering reduction of 82.7% is achieved.

The behavior of the Boost converter outputs under load variation are shown in Figure 8.6 . This figure manifests that for a differnet load values, the HOSM-TA is rising gradually and smoothly to the desired value. Furthermore, excellent performances such as great precision, high efficiency, robustness, low response time, and good dynamic behavior are attained.

Based on the above results, the capability of HOSM-TA to counteract the chattering phenomenon while achieving high performances and good dynamic behavior, are clearly proven.

8.3. Super twisting algorithm (STA)

Super-twisting algorithm (STA) is one of the most powerful 2-order continuous SMC, which ensures all fundamental properties of its traditional 1-order together

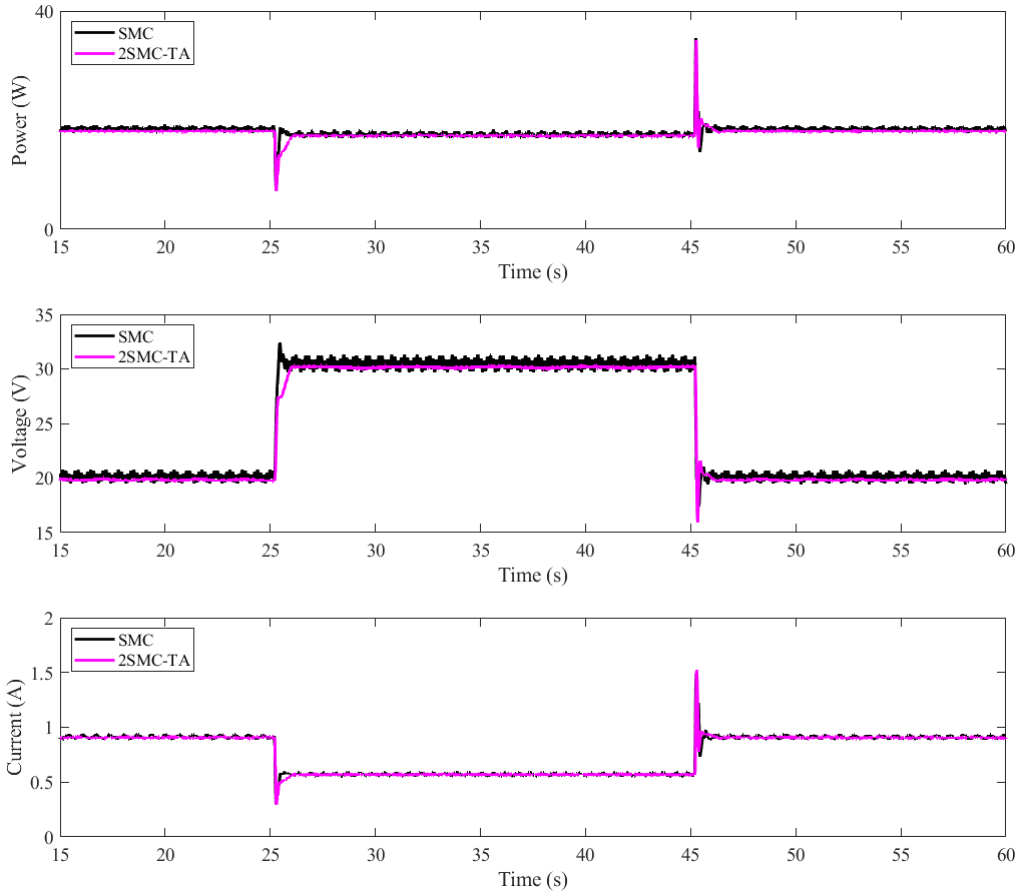

Figure 8.6: Boost converter output power, output voltage, and output current.

with chattering reduction [261]. In other words, it is not only robust against system uncertainties and external disturbances, but also has the ability to track the system with high accuracy. It was proposed in 1993 by Professor Levant for systems with a relative degree equal to 1 [260]. Unlike other 2-order SMC algorithms, STA requires only the knowledge of the sliding variable and it does not need any information about its time derivative. This leads to make it a relatively straightforward control law, and, therefore, it is one of the most preferable algorithms for a wide range of applications. In this work, the STA has been applied to drive the converter with the purpose of keeping the PEMFC operating at an efficient power point. The control solution directly tackles the stack current through a STA to generate the control signal $u(t)$ for the switch S after treating the sliding mode variable $s(x)$ (namely, the error between the reference current I_{ref} and the measured inductor current I). Since STA belongs to the 2-order sliding mode approach, therefore the control signal $u(t)$ can be written as:

$$u = u_{eq} + u_{sw}. \tag{8.10}$$

The switching control u_{sw} is designed based on STA as given in Equation 8.11 [262].

It is composed of two parts: a discontinuous part u_1 and a continuous part u_2:

$$u_{sw} = u_1 + u_2, \tag{8.11}$$

$$u_1 = -k_1.|S|^{1/2}.sign(s), \tag{8.12}$$

$$\dot{u}_2 = -k_2.sign(s), \tag{8.13}$$

where

- k_1 and k_2 are designed parameters. They can be obtained using the sufficient conditions that are required to ensure the convergence [262]:

$$\begin{cases} k_2 > \frac{\Phi}{\Gamma_m}, \\ k_1 > \sqrt{\frac{2}{\Gamma_m^2}.\frac{(\Gamma_m.k_2+\Phi)^2}{(\Gamma_m.k_2-\Phi)}}. \end{cases} \tag{8.14}$$

Accordingly, the overall command law of the STA can be obtained as given in Equation (19). On the other hand, the implementation of this command law in MATLAB/Simulink^{TM} is clearly presented in Figure 8.7:

$$u = \frac{V_{out} - V_{stack}}{L} - k_1|S|^{0.5}sign(S) - \int k_2.sign(S)dt. \tag{8.15}$$

Trajectories on the 2-sliding plane are characterized by bending around the origin. Thus, as shown in Figure 8.8, they perform an infinite number of rotations while converging to the origin.

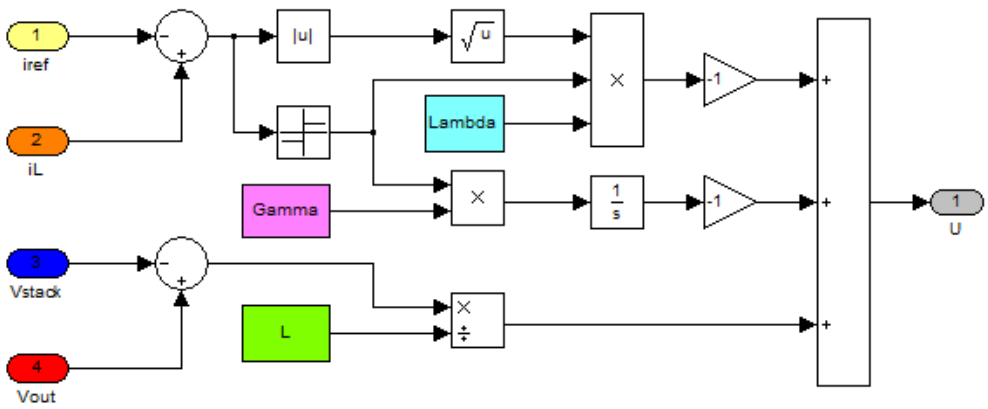

Figure 8.7: The synoptic diagram of the super-twisting algorithm.

In order to find out the performance of super twisting algorithm (STA) and its features over traditional 1-order SMC, load variation from 20 Ω to 50 Ω is applied at t = 25 s and from 50 Ω to 20 Ω is applied at t = 45 s.

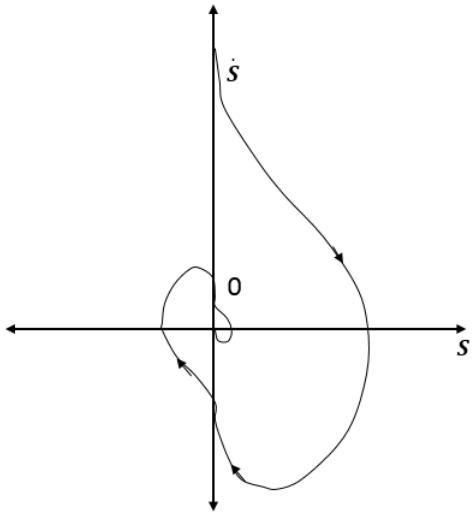

Figure 8.8: Super-twisting algorithm phase trajectory.

Figures 8.9–8.12 show respectively the duty cycle signal, the PEMFC output signals (voltage, current, and power), and finally the boost converter output signals (voltage, current, and power). These figures show the behaviour of the SMC and STA to track and maintain the system functioning at an adequate power point. In general, both of the controllers show global stability and satisfactory tracking results so as to keep the system operating at the desired power point. However, it is clearly shown that the STA has a high capability to decrease the chattering effect that occurs by the SMC.

The duty cycle signals generated by the controllers are shown in Figure 8.9. As can be seen from this figure, the controllers effectively control the duty cycle so as to obtain constant current with fast response time and no drift. It is important to note that some noises are occurred in the obtained experimental signals. However, this is resulting from the effect of time-delay in the control signal, as well as the parasite signals which came from hardware components.

The fuel cell output voltage and current signals are shown in Figure 8.10. This last illustrates the behavior of the SMC and STA when experiencing load variations at t = 25 s and t = 45 s. According to this figure, it is clear that both of the controllers manifest high robustness even when large load variations is accrued (30 Ω). Thus, by varying the load resistance from 20 Ω to 50 Ω and from 50 Ω to 20 Ω, the SMC manifests an overshoot and undershoot voltage of 0.6 V and 0.9 V, as well as an undershoot and overshoot current of 1.2 A and 2.6 A, respectively. For the same variations, the STA manifests an overshoot and undershoot voltage of 0.9 V and 1.6 V as well as an undershoot and overshoot current of 1.8 A and 3.9 A, respectively. Therefore, despite the large load variations, only small overshoots are accrued. In addition, these overshoots only appear for a short period of time (response time $\leq$ 1 s), and they swiftly converge to the steady-state value. Figure 8.10 also shows that,

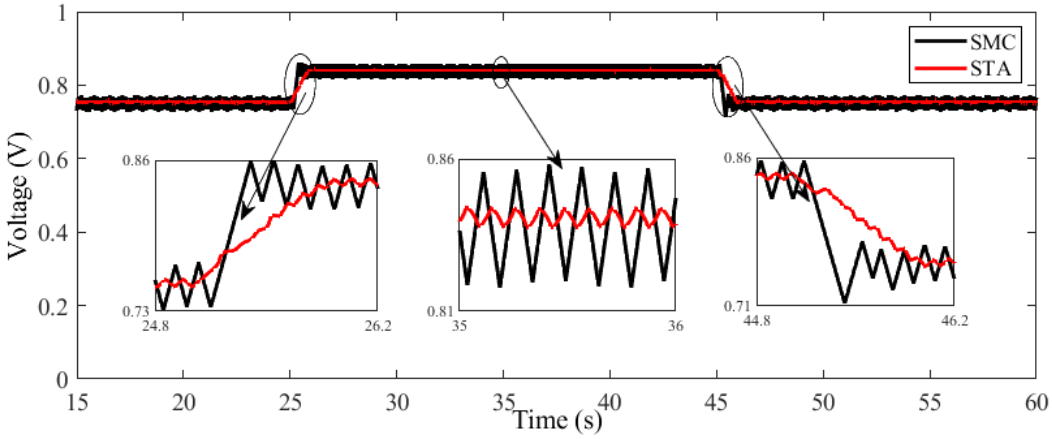

Figure 8.9: Duty cycle signal.

using SMC, the fuel cell output DC voltage oscillations can reach about 12% while the oscillations of the output current is over 35%. These oscillations introduce small deviations from the operating point and especially they may even cause irreversible damage to the fuel cell. On the other side, the fuel cell output DC voltage oscillations using STA is only about 0.26% and the oscillations of the output current is less than 7%. Therefore, compared to the SMC, high accuracy, robustness, and good dynamic behavior are obtained even with large load variations.

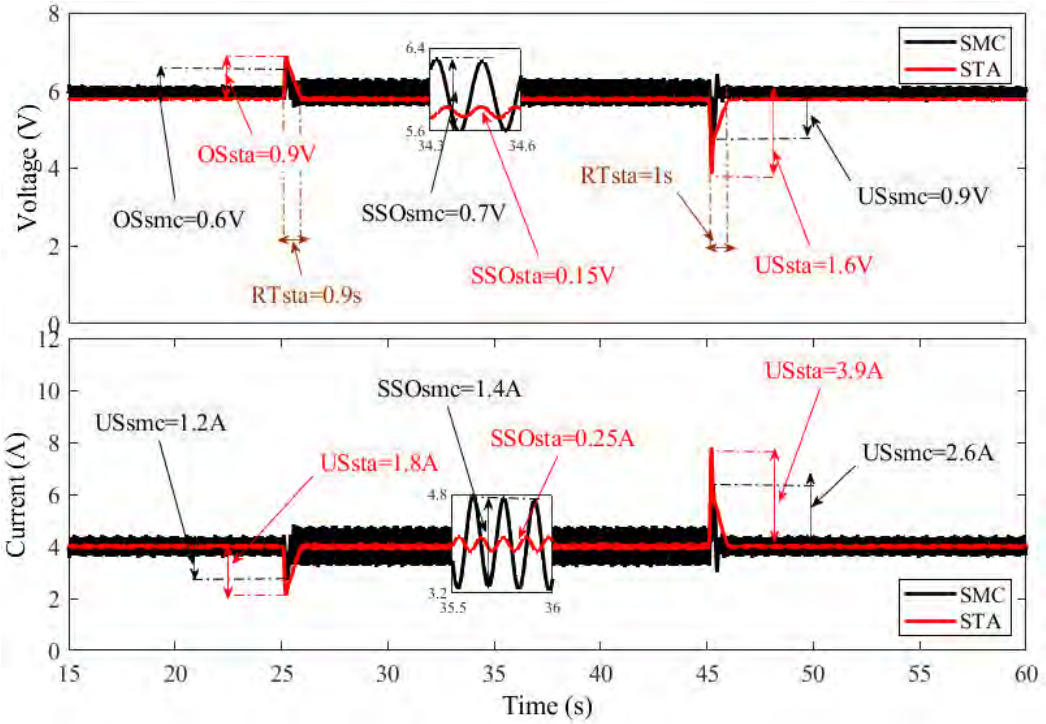

Figure 8.10: PEMFC stack voltage and current.

The fuel cell output power trajectories are presented in Figure 8.11. According to

these trajectories, it is obvious that the adequate power point is attained with swift speed and stability of the closed-loop system. On the other hand, it is clearly shown that the chattering phenomenon is almost eliminated by using the STA. Indeed, the chattering magnitude using the SMC varies approximately from 20.5 W to 27 W, while it only varies from 23.3 W to 23.9 W using the STA. Accordingly, it is proven that the proposed STA has succeeded at reducing about 91% of the chattering effect, which will improve, as a consequence, the fuel cell lifetime.

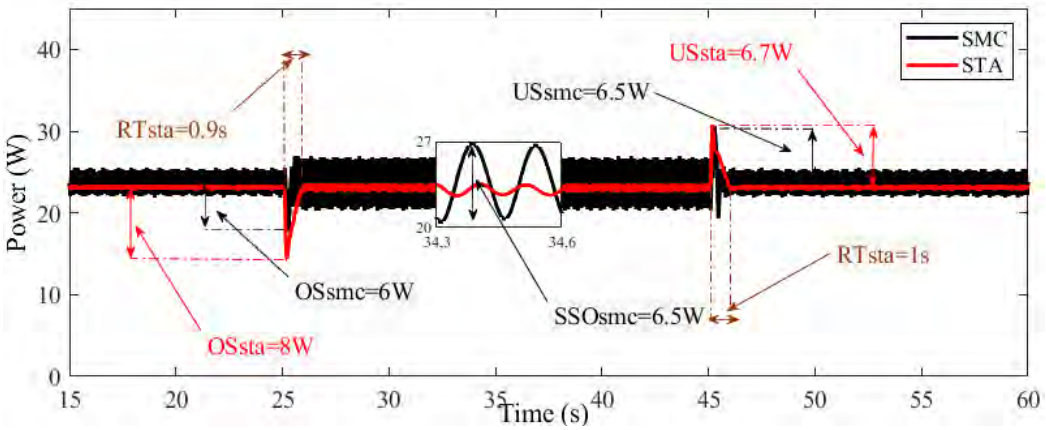

Figure 8.11: PEMFC stack power.

The behaviour of the output voltage, current, and power of the DC–DC boost converter under load variations are presented in Figure 8.12. According to this figure, it is clear that, despite the heavy loading conditions, the STA manifests gradual and smooth movement to the desired voltage at which the system will work in the adequate power point. Moreover, high performances such as low response time (less than 1 s), robustness, great precision, as well as excellent dynamic behavior are achieved.

Based on these results, it is clearly manifested that this experimental work have demonstrated the capability of the STA to reduce the chattering effect, while attaining high performances.

8.4. Prescribed convergence law algorithm (PCL)

The sliding surface of the PCL algorithm could be written as Equation (8.16):

$$s = e + \lambda \int e \cdot dt \tag{8.16}$$

Where

- λ is a positive constant ($\lambda > 0$).
- e is the error ($e = x_1 - x_{1mpp}$).

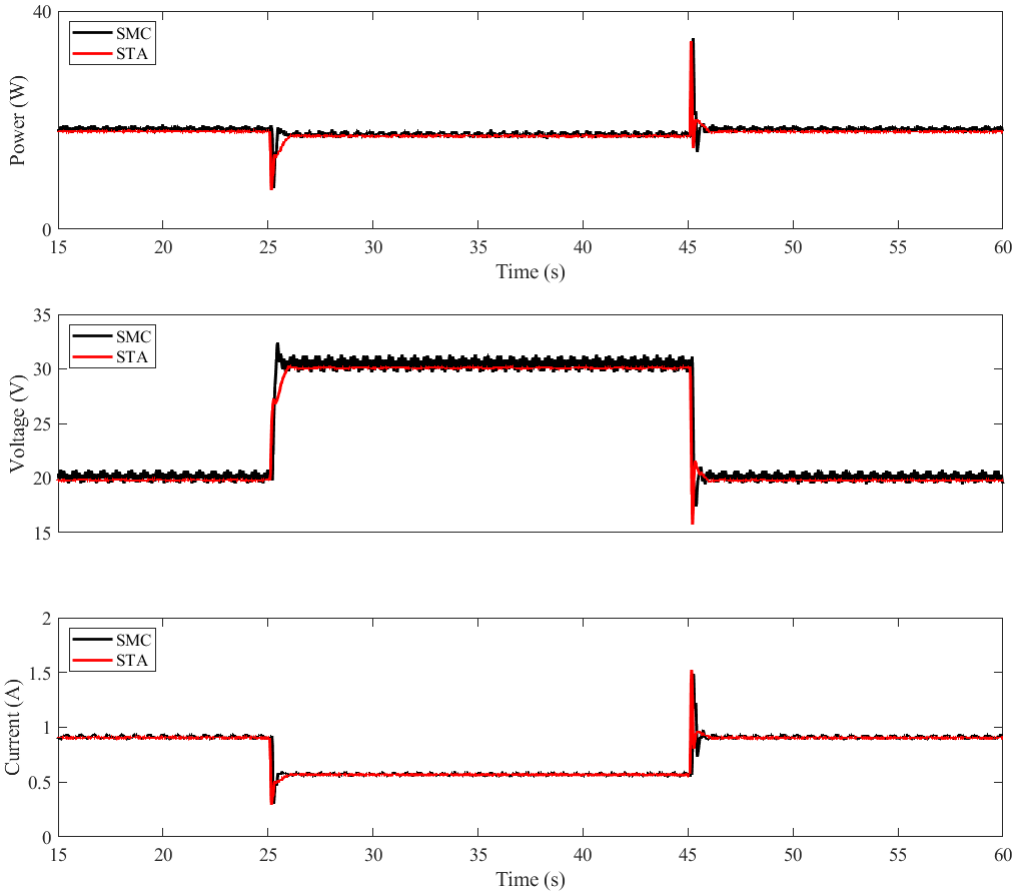

Figure 8.12: Boost converter output power, output voltage, and output current.

Based on the state-space model given in Equation (5.41), an uncertain second-order system could be written as Equation (8.17):

$$\begin{cases} \dot{z}_1 = y_2 \\ \dot{z}_2 = \chi(x,t) + \phi(x,t) \cdot \sigma \end{cases} \tag{8.17}$$

Where

- $z_1 = s$.
- $z_2 = \dot{s}$.
- σ is the derivative of the control u.

Using Equation (8.17), $\chi(x,t)$ and $\phi(x,t)$ can be determined as Equation (8.18) and (8.19).

$$\chi = \frac{1}{L}\left[(u-1)\dot{x}_2 + \dot{V}_{stack} + \lambda(u-1)x_2 + \lambda \cdot V_{stack}\right] \tag{8.18}$$

$$\phi = \frac{1}{L}x_2 \tag{8.19}$$

Assuming that χ and ϕ are bounded as:

$$|\chi| \leq \chi_d, 0 < \phi_{min} \leq \phi \leq \phi_{max}. \tag{8.20}$$

Where

- χ_d, ϕ_{min} and ϕ_{max} are positive scalars.

The general formulation of the HO-PCL control scheme is given by Equation (8.21) [247]:

$$\sigma = -k_1 \cdot sign(z_2 - g_c(z_1)) \tag{8.21}$$

Where

- $g_c(z_1)$ is a continuous smooth function defined as:

$$g_c(z_1) = -k_2 \cdot |z_1|^{1/2} \cdot sign(z_1) \tag{8.22}$$

- k_1 and k_2 are two positive designed parameters. They should be determined according to the sufficient condition given in Equation (8.23) so as to guarantee the convergence in finite time to the sliding variable [247]:

$$k_1 \cdot \phi_{min} - \chi_d > \frac{k_2^2}{2} \tag{8.23}$$

The implementation of the HO-PCL command law in MATLAB/Simulink is shown in Figure 8.13. Whereas the convergence trajectory of the continuous function $g_c(z_1)$ is presented in Figure 8.14

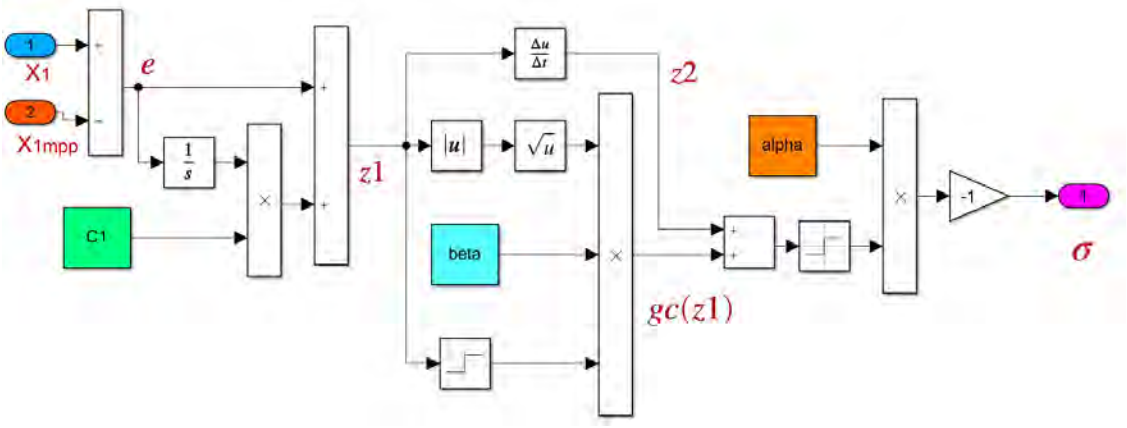

Figure 8.13: Synoptic diagram of HO-PCL algorithm.

The performance of the FC50 under the use of the proposed PCL algorithm is presented in Figure 8.15 to Figure 8.18. These figures shows respectively the waveforms of the duty cycle signal, stack voltage, stack current, stack power, and fianlly

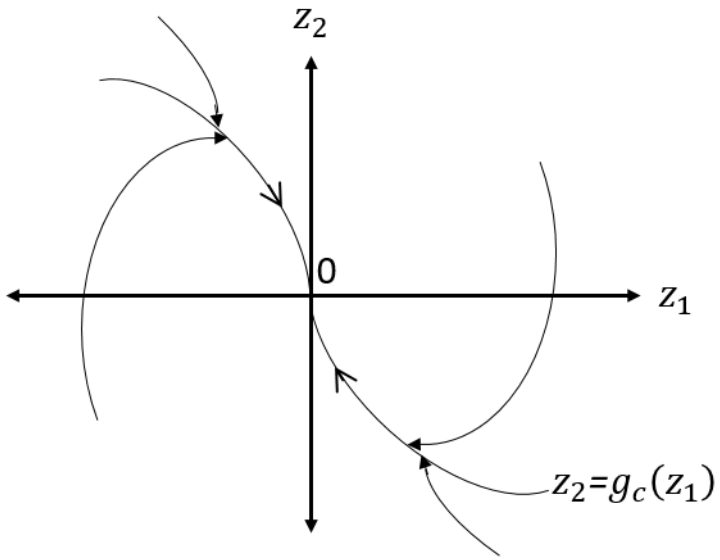

Figure 8.14: Phase trajectories of HO-PCL algorithm.

the DC-DC output power. Aiming to find out the behavior of the PCL against the unexpected disturbances, variation of 30 Ω in the load resistance is applied at t=25s and t=45s. These variations are done using the programmable electronic load (PEL) that commuting between 20 Ω and 50 Ω. Although these sharp variations, it is clearly shown in these figures that the proposed PCL shows robustness against external unexpected disturbances.

Figure 8.15 presents the duty cycle signals delivered by SMC and PCL. It is clearly shown that both of SMC and PCL effectively force the duty cycle to render an adequate value so as to obtain constant current with fast response and no drift.

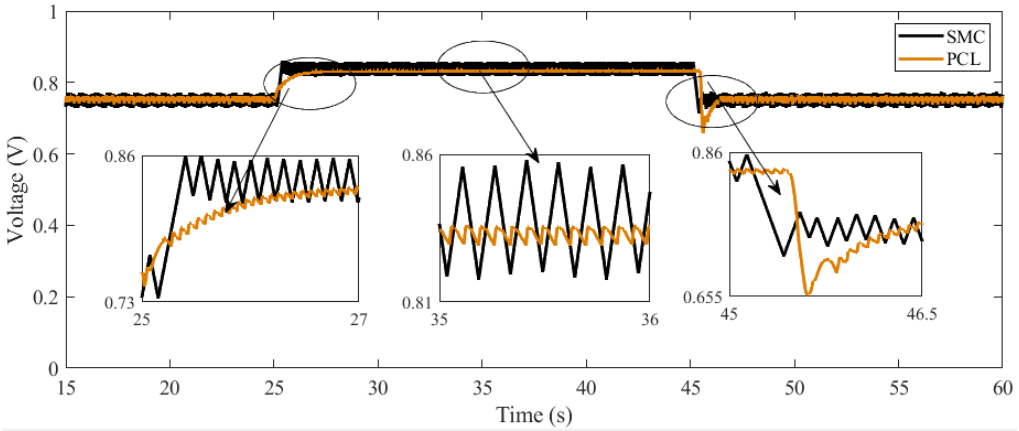

Figure 8.15: Duty cycle signal.

The PEMFC stack voltage and current curves are illustrated in Figure 8.16. These curves explicate the controllers behavior when facing different significant load

variation values at $t = 25s$ and $t = 45s$. It is noteworthy that each of PCL and classical SMC appear robustness even for large load variations. Thus, when $t = 25s$, an overshoot voltage of $0.6V$ and undershoot current of $1.2A$ are shown by the SMC, while the PCL shows an overshoot voltage of $1.04V$ and an undershoot current of $1.8A$. At $t = 45s$, the SMC shows an undershoot voltage of $0.9V$ and an overshoot current of $2.6A$, while an undershoot and overshoot voltage of $1.1V$ and $0.78V$, and, an overshoot and undershoot current of $2.25A$ and $1.4A$ are shown by the PCL. Nevertheless, these behaviors are only appeared for less than $1.8s$ at first and second load variations. Thereafter, they quickly disappeared by converging to the operating point. Figure 8.16 also show that after reaching the steady-state value, a chattering reduction of 93% can be attained using the proposed PCL algorithm. However, in spite of these features, the PCL shows one drawback which is the lack of precision. Hence, it is clearly noticed that for high resistance load (between t=25s and t=45s), an error of $0.11A$ is occurred using the proposed PCL algorithm.

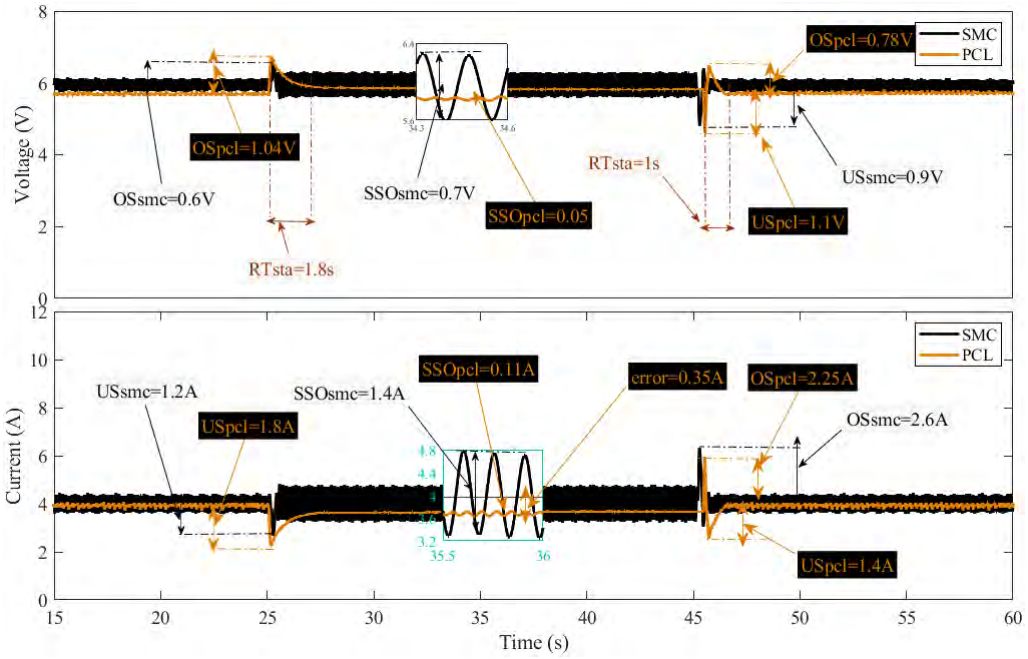

Figure 8.16: PEMFC stack voltage and current.

The stack power trajectories of the PEMFC for SMC and PCL are shown in Figure 8.17. According to this figure, it is clear that using the PCA, the adequate power point is achieved fleetly with high accuracy and global system stability. In addition, it is noticeable that with the traditional SMC, the magnitude of the power 6.5 W while it is only 0.6 W using the proposed PCL algorithm. Therefore, it is clear that PCL track the optimal power with great precision and very low power fluctuations (2.6%) which increase as a consequence the efficiency of the operating power point. Accordingly, the PCL scheme has performed successfully for set-point tracking and a chattering reduction of 93% is achieved.

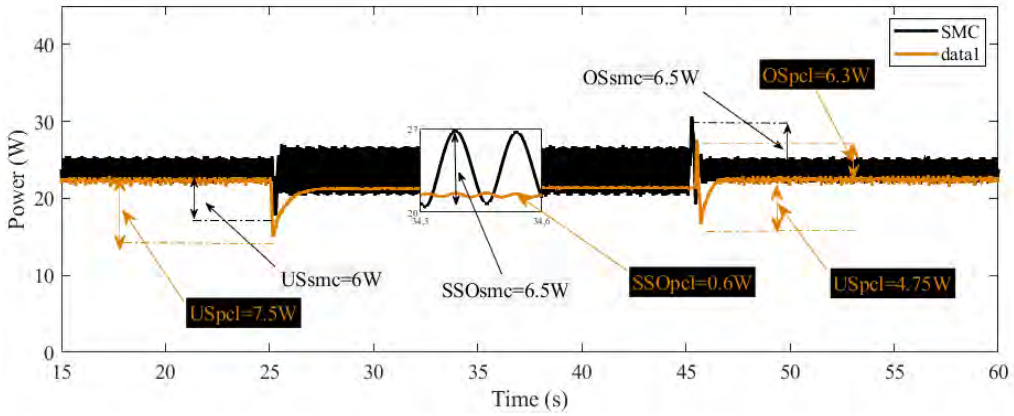

Figure 8.17: PEMFC stack power.

The behavior of the Boost converter outputs under load variation are shown in Figure 8.18. This figure manifests that for a different load values, the PCL is rising gradually and smoothly to the desired value. Furthermore, although the lack of precision for large load resistance, excellent performances such as high efficiency, robustness, low response time, and good dynamic behavior are attained.

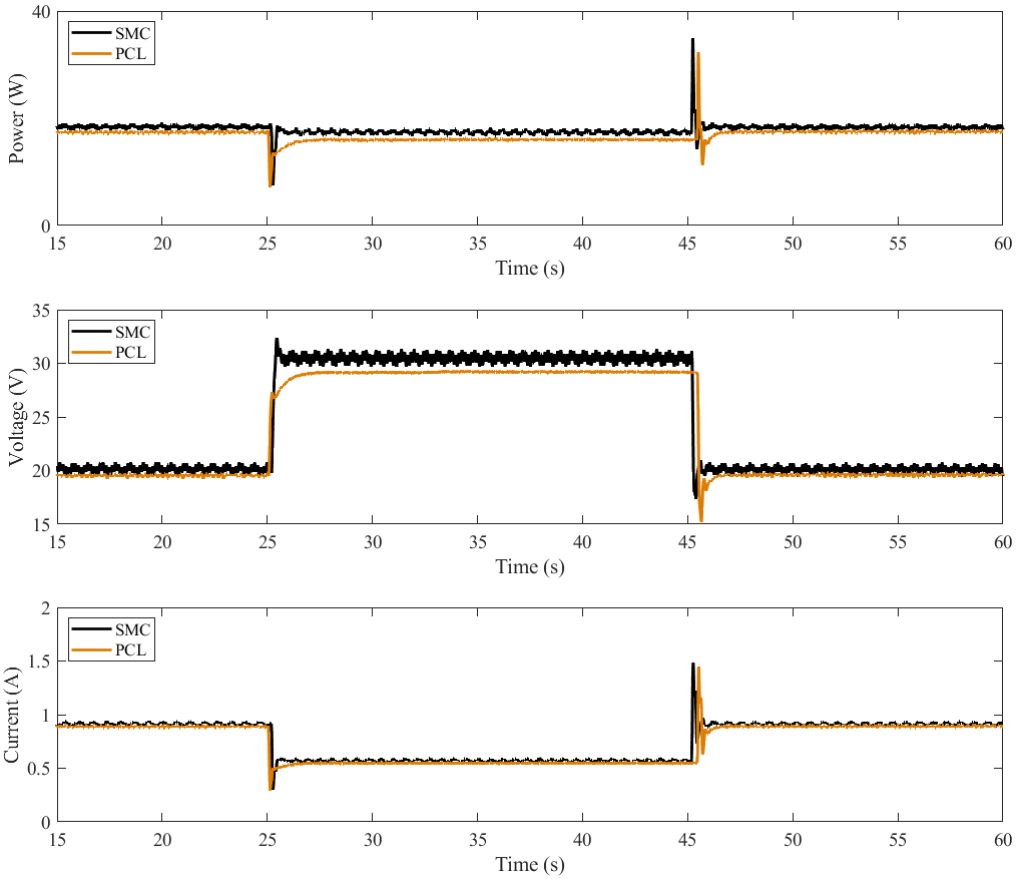

Figure 8.18: Boost converter output power, output voltage, and output current.

8.5. Quasi-continuous algorithm (QCA)

The higher-order sliding mode has recently been developed by [263] according to the principle of homogeneity [264]. This type of control belongs to the theory of systems with variable structure. It ensures the convergence of the state towards the origin in finite time. In this work, the QC-HOSM has been applied to drive the step-up converter to hold the PEMFC at an optimal power point, and ensuring of reducing the chattering phenomenon and prolong the PEMFC lifetime. In order to design the controller, we consider the nonlinear system described by equation (8.24):

$$\dot{x} = f(t,x) + g(t,x)u \tag{8.24}$$

Where

- $f(t,x)$ and $g(t,x)$ are nonlinear functions.
- u is a discontinuous and bounded signal depending on the state x and time t.

The sliding variable can be written as equation (8.25):

$$s = e + \lambda \int_0^t e dt \tag{8.25}$$

Where

- e is the the tracking error.
- λ is a positive constant.

Using equation (5.41), (7.2), and (8.25), the derivative of the sliding variable can be expressed as equation (8.26):

$$\dot{s} = \frac{1}{L}(V_{stack} - x_2) + \lambda e + \frac{x_2}{L}u \tag{8.26}$$

To design the QC-HOSM, the uncertain second-order system should be written as equation (8.27)

$$\ddot{s} = \psi(x,t) + \phi(x,t)\nu \tag{8.27}$$

Where

- $\nu = \dot{u}$ is the control signal.
- $\psi(x,t)$ and $\phi(x,t)$ are smooth functions and they were determined by equation (8.4).

The control signal ν is the sum of two components, the equivalent component, and the discontinuous component. It can be written as equation (8.28):

$$\nu = \nu_{eq} + \nu_{sw} \tag{8.28}$$

Where, ν_{eq} is the equivalent control proposed by [244]. It is deduced from the relation of ($\ddot{s} = 0$). Therefore, the equivalent control can be expressed as equation (8.29):

$$\nu_{eq} = -\frac{\psi}{\phi} = -\frac{1}{x_2} \cdot [(u-1)\dot{x_2} + \dot{V_{stack}} + \lambda(u-1)x_2 + \lambda V_{stack}] \tag{8.29}$$

ν_{sw} is the switching control. Its key aim is to ensure the stability and the convergence by holding the system on the sliding surface. In this work, we propose the switching control as equation (8.30):

$$\nu_{sw} = -k\frac{\dot{s} + |s|^{1/2} sign(\dot{s})}{|\dot{s}| + |s|^{1/2}} \tag{8.30}$$

In order to prove the stability, the following Lyapunov function is proposed: $V_s = \frac{1}{2}\dot{s}^2$. The time derivative of this function is calculated in equation (8.31).

$$\begin{aligned}
\dot{V_s} &= \dot{s}\ddot{s} \\
&= \dot{s}(\psi + \phi\nu) \\
&= \dot{s}\left(\frac{1}{L}\left[(u-1)\dot{x_2} + \dot{V_{stack}} + \lambda(u-1)x_2 + \lambda V_{stack}\right] + \frac{1}{L}x_2\nu\right) \\
&= \dot{s}\left(\frac{1}{L}\left[(u-1)\dot{x_2} + \dot{V_{stack}} + \lambda(u-1)x_2 + \lambda V_{stack}\right]\right) + \\
&\quad \dot{s}\frac{x_2}{L}\left(-\frac{1}{x_2}\left[(u-1)\dot{x_2} + \dot{V_{stack}} + \lambda(u-1)x_2 + \lambda V_{stack}\right] - \frac{kL}{x_2} \cdot \frac{\dot{s} + |s|^{1/2} sign(\dot{s})}{|\dot{s}| + |s|^{1/2}}\right) \\
&= -k \cdot \dot{s} \cdot \frac{\dot{s} + |s|^{1/2} sign(\dot{s})}{|\dot{s}| + |s|^{1/2}} \\
&= -k \cdot \dot{s} \cdot sign(\dot{s}) \cdot \frac{\dot{s} \cdot sign(\dot{s}) + |s|^{1/2}}{|\dot{s}| + |s|^{1/2}} \\
&= -k \cdot |\dot{s}| \cdot \frac{|\dot{s}| + |s|^{1/2}}{|\dot{s}| + |s|^{1/2}} \\
&= -k \cdot |\dot{s}| \\
&\leq 0
\end{aligned} \tag{8.31}$$

Consequently, according to the Lyapunov theory the asymptotic stability is ensured. Besides, since the sliding variable $s = e + \lambda \int_0^t e.dt$ tends to 0, which implies that $\dot{s} = \dot{e} + \lambda e$ also converges to 0, therefore the tracking error e tends to 0.

Figure 8.19 to Figure 8.22 show the capability of the quasi-continuous algorithm to maintain the robustness of conventional SMC while reducing the undesirable chattering phenomenon. Figure 8.19 shows the duty cycle signal for both algorithms. It is noticed that both of the algorithms show a soft and smooth rise to the desired reference value. However, it is clearly shown that the proposed QC algorithm effectively overcome the drawbacks of the conventional first SMC by reducing its chattering phenomenon.

Figure 8.20 shows the FC50 current and voltage signals. The effectiveness of

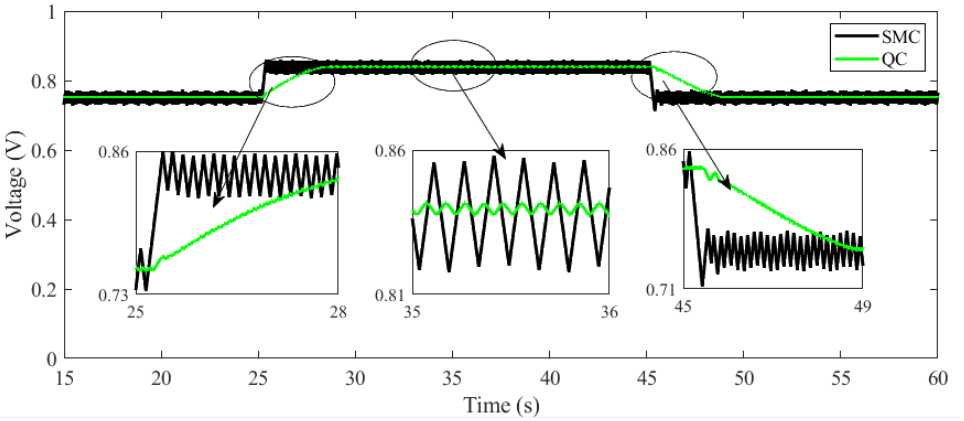

Figure 8.19: Duty cycle signal.

both algorithms when experiencing significant changes in load resistance is clearly demonstrated at $t = 25s$ and $t = 45s$. Hence, at the instant $t = 25s$, the SMC shows an undershoot current of $1.2A$, and an overshoot voltage of $0.6V$. For the instant $t = 45s$, an overshoot current of $2.6A$, and an undershoot voltage of $0.9V$. On the other hand, at the instant $t = 25s$, the QC algorithm shows an undershoot current of $1.9A$, and an overshoot voltage of $1V$. For the instant $t = 45s$, an overshoot current of $4.3A$, and an undershoot voltage of $1.7V$. However, these undershoot and overshoots are appeared only for short duration and then, they converge to the reference value. Thus, at the instant $t = 25s$, the response time of the QC is only $2.7s$, while at $t = 45s$ it is $3.4s$. Therefore, high robustness against load variations is achieved using both algorithms. The effectiveness of the proposed QC over the conventional SMC appears in its capability to reduce the oscillations. Hence, chattering reduction of 93% could be attained.

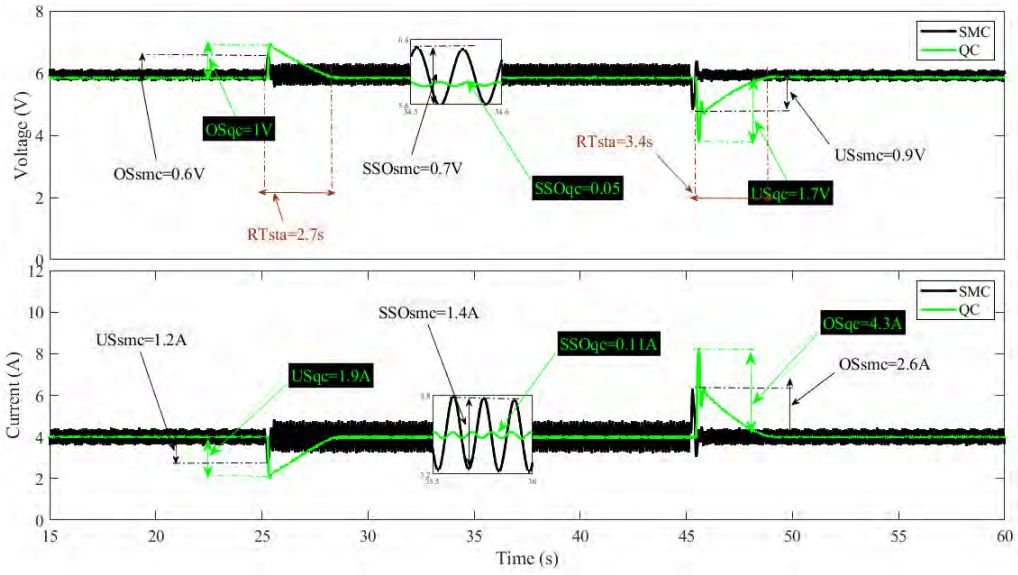

Figure 8.20: PEMFC stack voltage and current.

Figure 8.21 shows the trajectory of the generated power. It is obvious that the adequate power point is achieved with high robustness and global stability of the closed-loop system. The chattering magnitude using the conventional SMC is $6.5W$ while it is only about $0.6W$ using the proposed QC algorithm. It is therefore proven

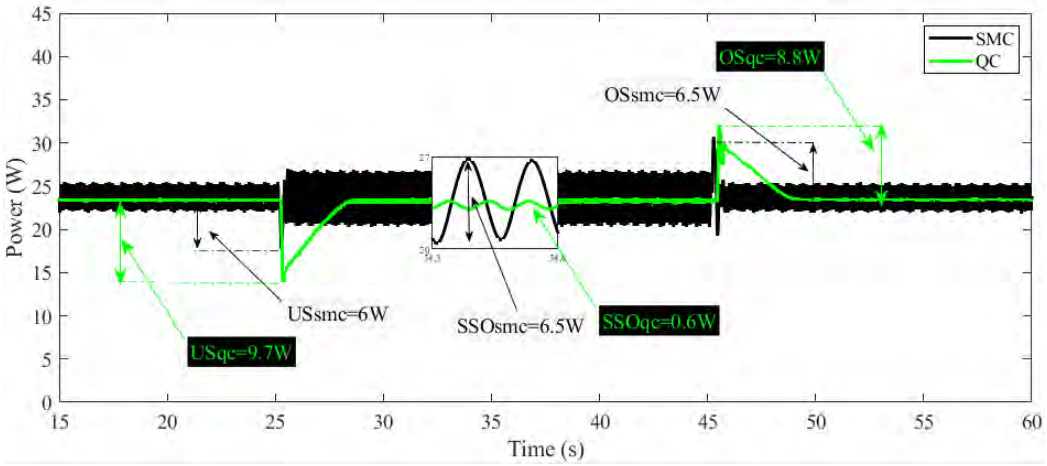

Figure 8.21: PEMFC stack power.

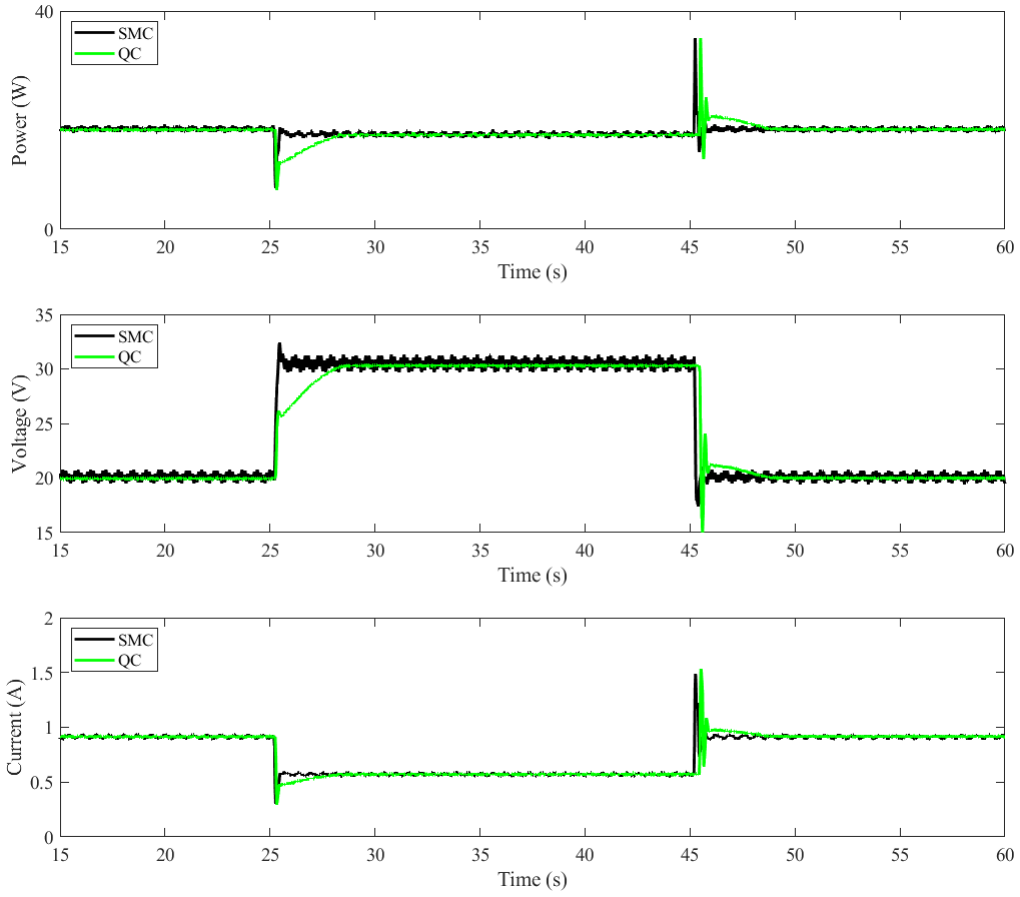

Figure 8.22: Boost converter output power, output voltage, and output current.

that the proposed algorithm succeeded in decreasing the chattering effect, which will improve as a consequence the fuel cell efficiency, lifetime, and the dynamic system behaviour.

Figure 8.22 shows the behaviour of the step-up DC-DC converter outputs. According to this figure, despite of facing sharp resistance variation, the QC shows gradual and smooth movements to the desired voltage at which the system runs in the adequate power point. Furthermore, high performances such as low response-time, great robustness, high precision, as well as outstanding dynamic behaviour, are achieved.

According to these results, it is noticed that the SMC and QC show good behaviour against load resistance variations. However, it is clearly seen that the advantage of the QC is its effectiveness to reduce the unwanted oscillation (chattering effect) with significant value. Thus, a chattering reduction of 93%, which will increase as a consequence, the accuracy and the overall system efficiency, is obtained.

8.6. Drift algorithm (DA)

The idea of the algorithm is to drive the trajectory of the 2^{th} sliding mode $s = 0$ while keeping the derivative of the sliding variable $\dot{s}$ relatively small, that is to cause $drift$ towards the origin along axis z_1. When using the DA, the phase trajectories on the 2^{th} sliding plane are characterised by loops with constant sign of the sliding variable z_1 (Figure 8.23).

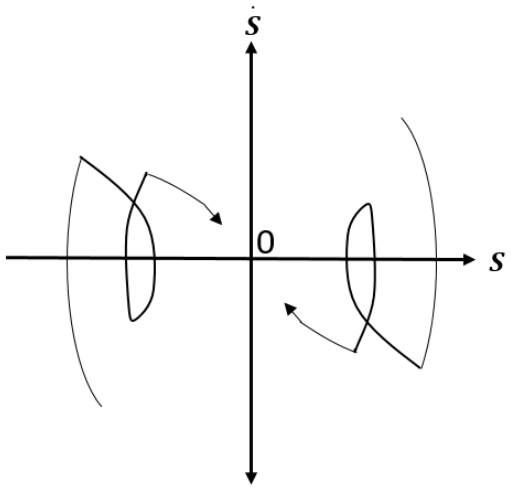

Figure 8.23: Drift algorithm phase trajectory.

Considering the sliding variable given in Equation (8.16) and the uncertain second-order system given in Equation (8.17), the general formulation of the DA can be

defined by the control law given in (8.32) [260, 265, 266]

$$\dot{u} = \begin{cases} -u & if \quad |u| > 1 \\ -k_1 \cdot sign(\Delta z_1) & if \quad z_1 \Delta z_1 \leq 0; |u| \leq 1 \\ -k_2 \cdot sign(\Delta z_1) & if \quad z_1 \Delta z_1 > 0; |u| \leq 1 \end{cases} \tag{8.32}$$

Where k_1 and k_2 are two positive constants such that $k_1 < k_2$ and $\frac{k_2}{k_1}$ is sufficiently large, $\Delta z_1 = z_1(t) - z_1(t-\tau)$, and τ is the sampling period.

The range of the duty cycle supplied to the boost converter is between 0 and 1. Therefore, (8.32) can be simplified as (8.33)

$$\dot{u} = \begin{cases} -k_1 \cdot sign(\Delta z_1) & if \quad z_1 \Delta z_1 \leq 0; |u| \leq 1 \\ -k_2 \cdot sign(\Delta z_1) & if \quad z_1 \Delta z_1 > 0; |u| \leq 1 \end{cases} \tag{8.33}$$

In order to prove the stability, the following Lyapunov function is proposed: $V_s = \frac{1}{2} z_2^2$. The time derivative of this function has two equations: (8.35) and (8.37).

- Case 1: $z_1 \Delta z_1 \leq 0$

$$\begin{aligned} \dot{V}_s &= z_2 \dot{z_2} \\ &= z_2(\chi(x,t) + \phi(x,t)) \\ &= z_2 \left(\frac{1}{L} \left[(u-1)\dot{x}_2 + \dot{V_{stack}} + \lambda(u-1)x_2 + \lambda V_{stack} \right] + \frac{1}{L} x_2 \nu \right) \\ &= z_2 \left(\frac{1}{L} \left[(u-1)\dot{x}_2 + \dot{V_{stack}} + \lambda(u-1)x_2 + \lambda V_{stack} \right] \right) + \\ &\quad z_2 \frac{x_2}{L} \left(-k_1 \cdot sign(\Delta z_1) - \frac{1}{x_2} \left[(u-1)\dot{x}_2 + \dot{V_{stack}} + \lambda(u-1)x_2 + \lambda V_{stack} \right] \right) \\ &= -k_1 z_2 \frac{x_2}{L} \cdot sign(\Delta z_1) \end{aligned} \tag{8.34}$$

Since $\tau \to 0$, z_2 has the same sign of Δz_1, therefore z_2 could be substituted by $\frac{\Delta z_1}{\tau}$. Consequently, (8.34) can be expressed as (8.35).

$$\begin{aligned} \dot{V}_s &= -k_1 \Delta z_1 \frac{x_2}{L\tau} \cdot sign(\Delta z_1) \\ &= -k_1 \frac{x_2}{L\tau} \cdot |\Delta z_1| \\ &= -k_1 \frac{x_2}{L} \cdot |z_2| \\ &\leq 0 \end{aligned} \tag{8.35}$$

Consequently, according to the Lyapunov theory, the asymptotic stability is ensured. Besides, since the sliding variable $s = e + \lambda \int_0^t e.dt$ tends to 0, which implies that $\dot{s} = \dot{e} + \lambda e$ also converges to 0, therefore the tracking error e tends to 0.

$V_s \geq 0$ and $\dot{V}_s \leq 0$, therefore, according to the Lyapunov theory, the stability is ensured for $z_1 \Delta z_1 \leq 0$.

- Case 2: $z_1 \Delta z_1 > 0$

$$\begin{aligned}
\dot{V_s} &= z_2 \dot{z_2} \\
&= z_2(\chi(x,t) + \phi(x,t)) \\
&= z_2 \left(\frac{1}{L} \left[(u-1)\dot{x}_2 + \dot{V_{stack}} + \lambda(u-1)x_2 + \lambda V_{stack} \right] + \frac{1}{L} x_2 \nu \right) \\
&= z_2 \left(\frac{1}{L} \left[(u-1)\dot{x}_2 + \dot{V_{stack}} + \lambda(u-1)x_2 + \lambda V_{stack} \right] \right) + \\
&\quad z_2 \frac{x_2}{L} \left(-k_2 \cdot sign(\Delta z_1) - \frac{1}{x_2} \left[(u-1)\dot{x}_2 + \dot{V_{stack}} + \lambda(u-1)x_2 + \lambda V_{stack} \right] \right) \\
&= -k_2 z_2 \frac{x_2}{L} \cdot sign(\Delta z_1) \qquad (8.36)
\end{aligned}$$

Since $\tau \to 0$, z_2 has the same sign of Δz_1, therefore z_2 could be substituted by $\frac{\Delta z_1}{\tau}$. Consequently, (8.36) can be expressed as (8.37).

$$\begin{aligned}
\dot{V_s} &= -k_2 \Delta z_1 \frac{x_2}{L\tau} \cdot sign(\Delta z_1) \\
&= -k_2 \frac{x_2}{L\tau} \cdot |\Delta z_1| \\
&= -k_2 \frac{x_2}{L} \cdot |z_2| \\
&\leq 0 \qquad (8.37)
\end{aligned}$$

$V_s \geq 0$ and $\dot{V}_s \leq 0$, therefore, according to the Lyapunov theory, the stability is ensured for $z_1 \Delta z_1 > 0$.

Since the stability is ensured for both $z_1 \Delta z_1 \leq 0$ and $z_1 \Delta z_1 > 0$, then the system is stable.

The performance of the fuel cell under the use of the DA is presented in Figure 8.24 to Figure 8.27. These figures shows respectively the wave-forms of the duty cycle signal, stack voltage, stack current, stack power, and finally the DC-DC output power.

Figure 8.24 presents the duty cycle signals delivered by SMC and DA. It is clearly shown that both of SMC and DA effectively force the duty cycle to render an adequate value so as to obtain constant current with fast response and no drift.

The waveforms of the stack voltage V_{stack} and current I_{stack} are presented in Figure 8.25. The stack power P_{stack} is shown in Figure 8.26; whereas the boost converter output signals (current, voltage and power) are exhibited in Figure 8.27. According to these graphs, it is clear that both of SMC and DA have succeeded to drive the the PEMFC operating at an adequate power point even when experiencing large load variation. However, although the SMC track the reference, high fluctuations are occurred during the operating process. Regarding to the overshoots and undershoots, the SMC shows an undershoot current of 1.2A, an overshoot voltage of 0.6V and an undershoot power of 6W for the first load variation; an overshoot current of 2.6A, an undershoot voltage of 0.9V and an overshoot power of 6.5W for the second load

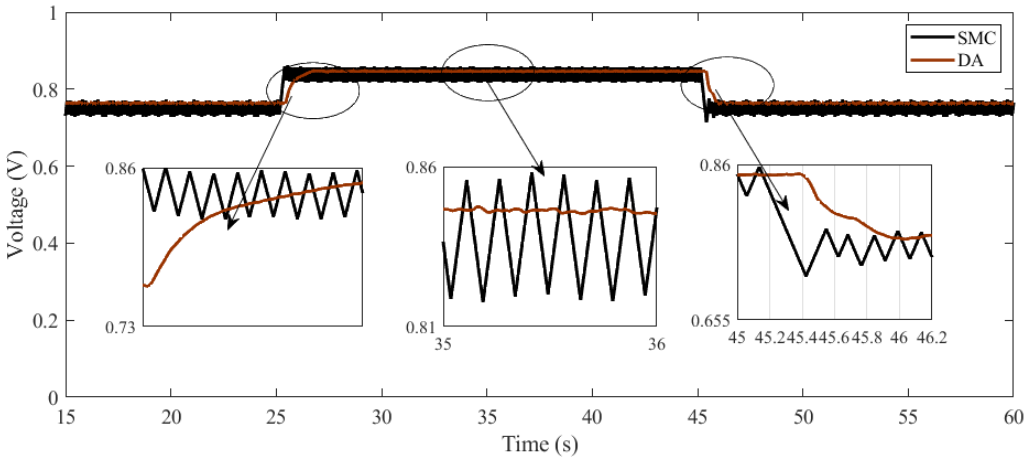

Figure 8.24: Duty cycle signal.

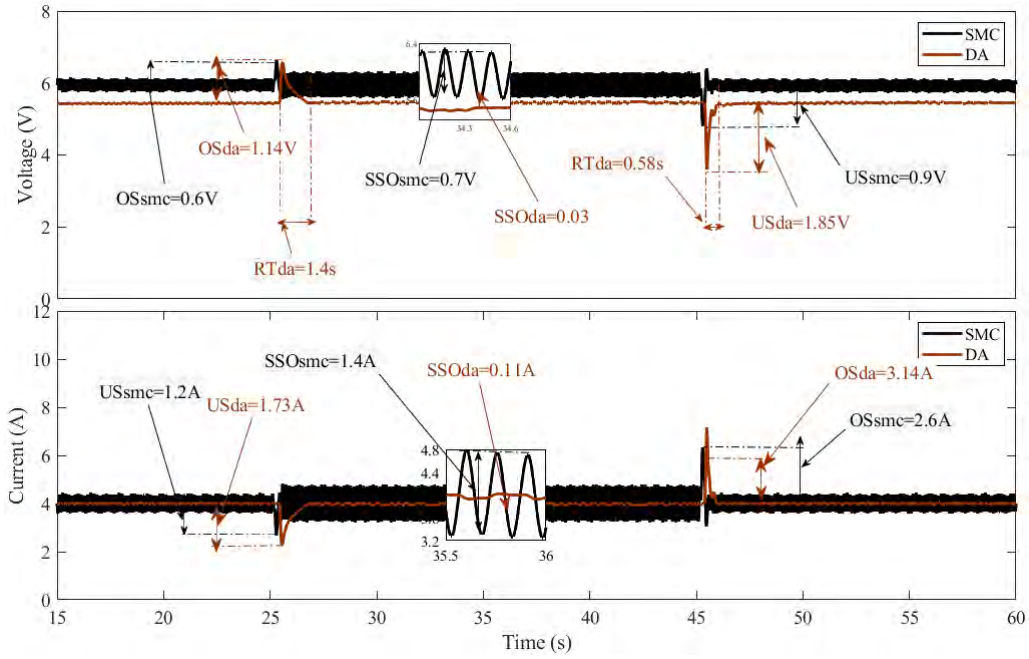

Figure 8.25: PEMFC stack voltage and current.

variation. On the other hand, the application of the DA performs an undershoot current of 1.73A, an overshoot voltage of 1.14V and an undershoot power of 6.9W for the first load variation; an overshoot current of 3.14A, an undershoot voltage of 1.85V and an overshoot power of 5.02W for the second load variation. It should be noted that both experiments are made at different temperature since it is difficult to keep the fuel cell operating at a constant temperature. Since the stack current is forced via the controllers to follow the reference then the temperature effect of each experiment on the stack performance is appeared in the stack voltage and power.

The effectiveness of the proposed DA over the conventional SMC appears in its capability to reduce the oscillations. Hence, it is clear that the DA provides better

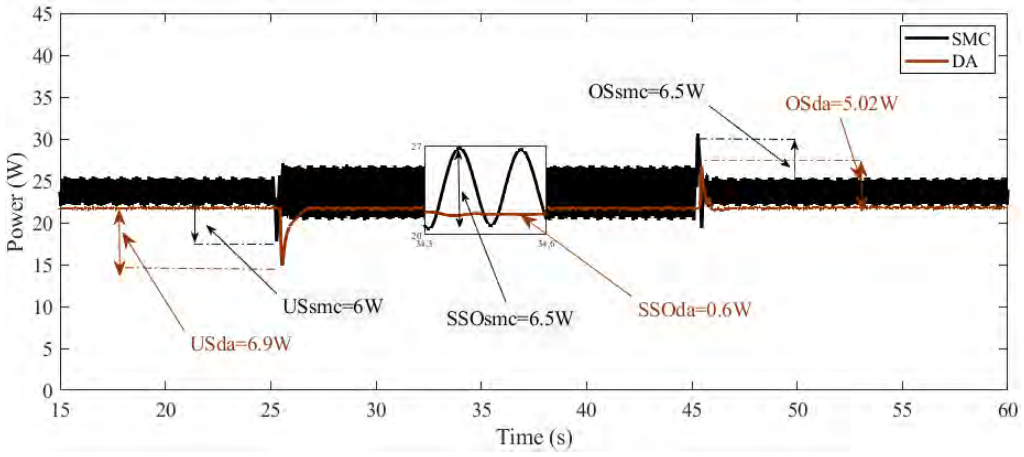

Figure 8.26: PEMFC stack power.

results in terms of accuracy since it reduces the amplitude of ripples from 1.1A to less than 0.11A. Therefore, although the SMC shows slight lower overshoots in comparison with the DA, this latter provides significant higher performance in terms of chattering reduction which can obtain around 93%.

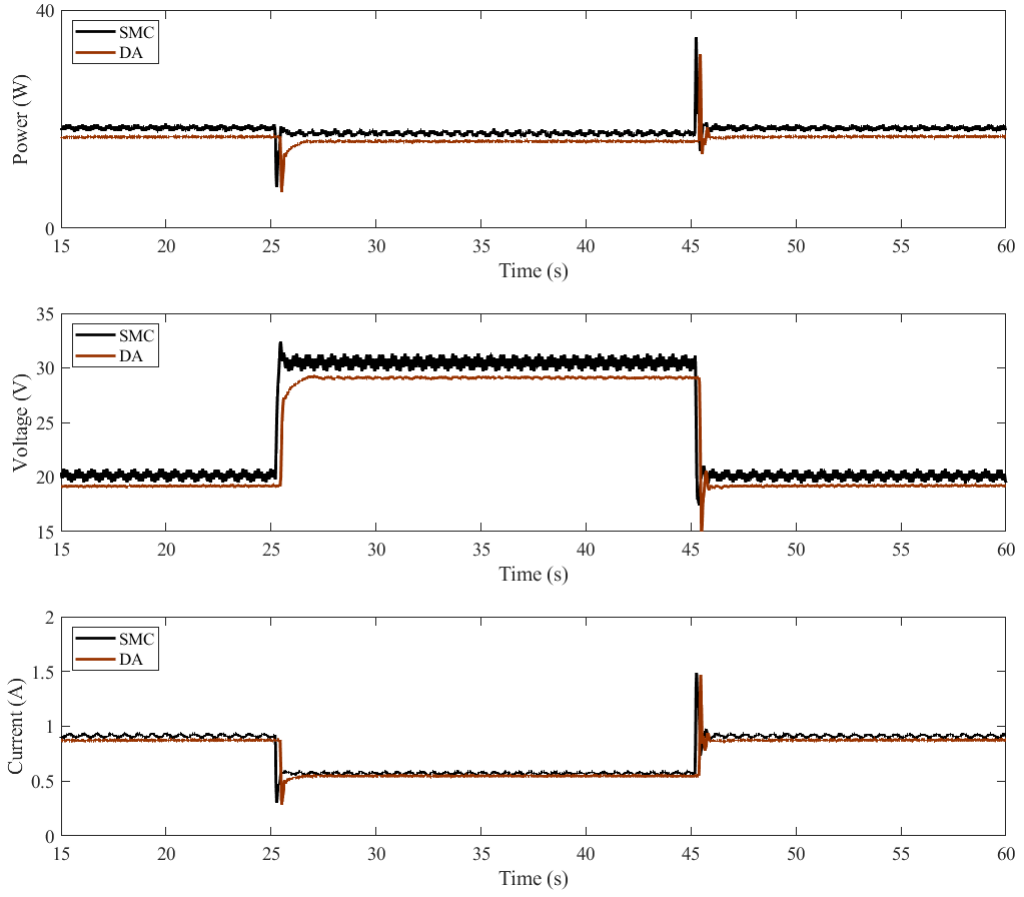

Figure 8.27: Boost converter output power, output voltage, and output current.

The behavior of the Boost converter outputs under load variation are shown in Figure 8.27. This figure manifests that for a different load values, the DA is rising gradually and smoothly to the desired value. Furthermore, although the lack of precision for large load resistance, excellent performances such as high efficiency, robustness, low response time, and good dynamic behavior are attained

8.7. Conclusion

In this chapter, five types of high order sliding mode control including twisting algorithm (TA), super twisting algorithm (STA), prescribed convergence law algorithm (PCL), quasi-continuous algorithm (QCA) and drift algorithm (DA) have been designed and implemented for a Heliocentris commercial PEMFC; where the goal is to reduce the chattering phenomenon of the conventional sliding mode (that has been designed in the previous chapter), and obtain a robust and an accurate response. To test the robustness of these types, two load changes at 25 s and 45 s were used. Regarding the first change, the resistance is shifted from 20 Ω to 50 Ω, where in the second change it regressed to 20 Ω.

The experimental results showed that during the dynamic changes, the five proposed techniques have shown high capability to reduce the chattering phenomenon while providing high robustness against variations of the load resistance. The performance of the proposed algorithms that presented in this chapter are summarised in Table 8.1. As it is clearly shown, the DA has the superior performance in terms of accuracy and robustness over the TA, PCL, QCA and STA; while this latter has the lowest response time over the rest of algorithms.

Table 8.1: Performance of the proposed high order SMC algorithms.

Controller	**Overshoot**	**Undershoot**	**Response Time**	**Steady State Oscillation**
CSMC	6.5W	6W	0.2s	6.5W
TA	6.6W	7.8W	1s	0.8W
STA	6.7W	8W	0.9s	0.7W
PCL	6.3W	7.5W	1.8s	0.6W
QCA	8.8W	9.7W	2.7s	0.7W
DA	5.02W	6.9W	1.4s	0.4W

Chapter 9

Alternative control methods for PEM fuel cell system

9.1. Introduction

Linear controllers can be a suitable initial option to control the fuel cell through the DC–DC converter. Hence, a typical first and classic approach like the proportional–integral (PI) is designed in this chapter. On the other hand, nonlinear strategies design can improve the effectiveness, specially when a real-time controller is embedded. Fuzzy-logic controller (FLC) represents a non-linear strategy which its construction is based on the designer expertise within the system and traduced through if-then causal rules in fuzzy sets. FLC is known for its simplicity and robustness which are the main advantages when it is employed in complex models [70]. Due to their significant benefits, predictive control methods also have attracted the intention of many researches and they have been implemented in a wide range of applications, including power converters, actuator faults, pharmaceuticals industry, chemical processes, and induction motors [80–91]. Another nonlinear controller is back-stepping (BSTP) which is a Lyapunov-based design that intents to split the whole feedback-system into sub-systems with the aim of developing a controller that considers the sub-parts [118]. Therefore, the mechanics of this approach through a Lyapunov-design can ensure the stability of the entire close-loop system.

9.2. Proportional integral (PI) Control

Proportional–Integral controller (PI) is a control loop feedback system that attempts as much as possible to continuously calculate the difference between the desired and actual (measured) outputs. The control function of the PI controller is given in Equation 9.1, while its synoptic diagram is shown in Figure 9.1. Where $e(t)$ is the error, K_p and K_i are respectively the proportional and integral coefficient terms.

$$s = K_p e(t) + K_i \int e(t)dt \tag{9.1}$$

Although the PI controller is commonly used in a wide range of applications,

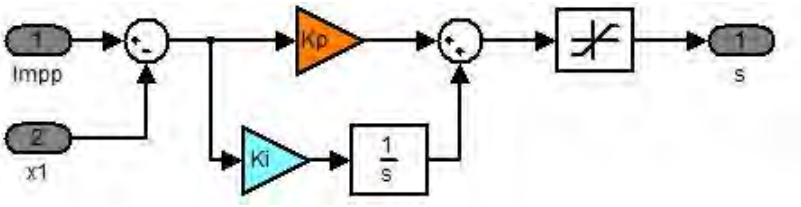

Figure 9.1: Synoptic Diagram of PI Controller.

several drawbacks such as the difficulties of finding out the constants K_p and K_i are causing a big issue [267–270]. Moreover, its sensibility dealing with the load variations has caused researchers to look for another controllers which can provide robustness against load variations. In this paper, the method used for determining the values of K_p and K_i is known as "Ziegler–Nichols tuning method". This last, was found and developed by J. G. Ziegler and N. B. Nichols. It is an online method which is usually used when there is a lack of knowledge of the model parameters [271]. In order to apply this method, three main steps should be accomplished.

1. The first step is to switch off the integral and derivative gains ($K_i = 0$ and $K_d = 0$).

2. The second step is to increase the k_p gain from a low/zero value until the first sustained oscillation occurs (Figure 9.2). The reached gain at the sustained oscillation is noted as a critical value k_{cr}, while the period of these oscillations is measured as P_{cr}.

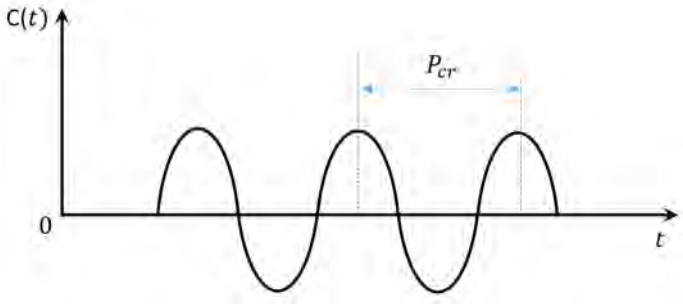

Figure 9.2: Sustained oscillation with a period P_{cr}.

3. Finally, taking into account the type of the used controller, K_p and K_i can be calculated using the formula given in Table 2.

The performances of the PEMFC stack and the boost converter, under the use of the PI controller are presented in Figures 9.3, 9.4, 9.5 and 9.6.

Figure 9.3 exposes the performance of the duty cycle signal in the first and second load change. As it can be seen in this figure, the duty cycle of the SMC shows several chattering behaviour in the steady reference following. Since the duty cycle is the control action, certainly it will reflect this phenomenon in the input and output

Table 9.1: Ziegler–Nichols Tuning Rules.

Type of Controller	K_p	$T_i = K_p/K_i$	$T_d = K_d/K_p$
P	$k_{cr}/2$	∞	0
PI	$k_{cr}/2.2$	$P_{cr}/1.2$	0
PID	$k_{cr}/1.7$	$P_{cr}/2$	$P_{cr}/8$

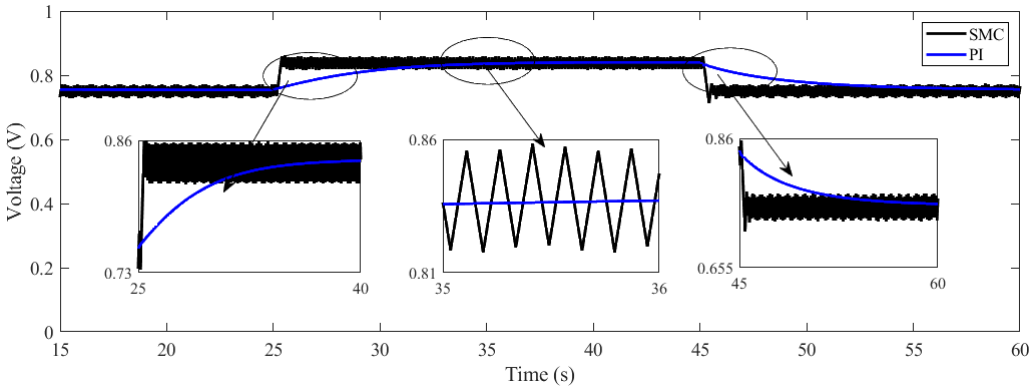

Figure 9.3: Duty cycle signal.

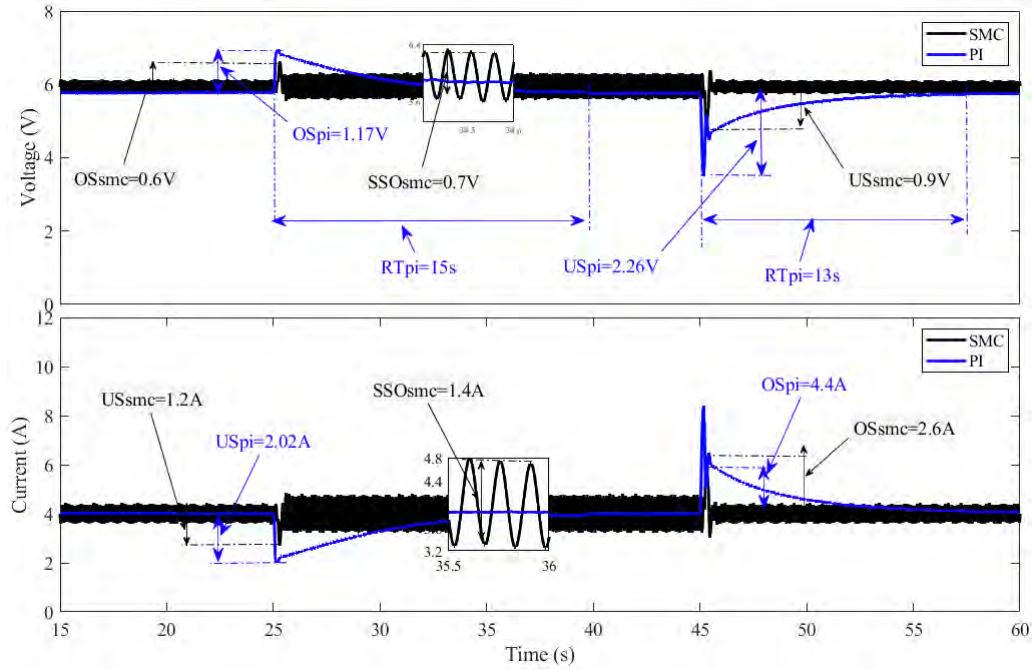

Figure 9.4: PEMFC stack voltage and current.

electrical measures of the boost converter. On the other hand, the duty cycle signal of the PI controller indicates a smooth and gradual rise to the desired operating point. However, one drawback of the PI controller is its slow response time since it takes around 15 s for the first load change and around 13 s for the second load change.

Figure 9.4 shows the PEMFC generated voltage and current where the robustness can be reflected in the overshoot and undershoot measured in the first load rise. In comparison to the SMC (which performance was the highest one in this step), the PI overshoot and undershoot were 1.17 V and 2.02 V respectively for voltage and current, which entails a difference of 0.57 V and 0.82 A when compared with the SMC. A similar trend was observed in the second load change where the SMC still had a better demeanour than the PI since it showed same improved features as the voltage undershoot and current overshoot decreased from 2.26 V and 4.4 A to 0.9 V 2.6 A respectively.

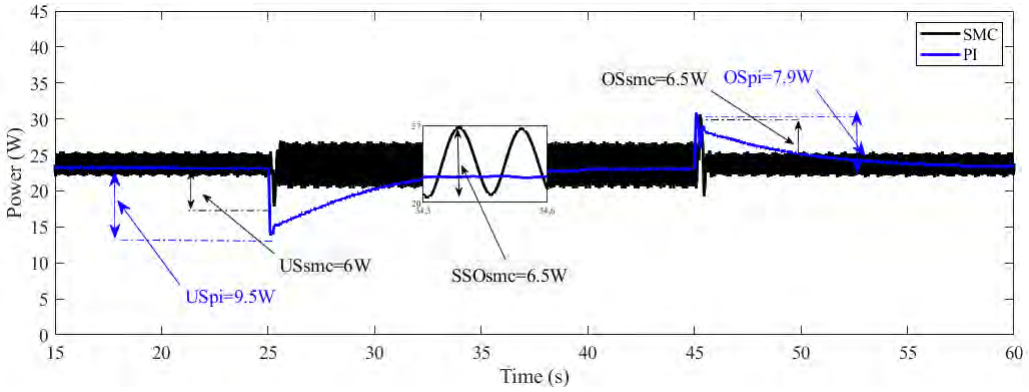

Figure 9.5: PEMFC stack power.

The stack power signal is displayed in figure 9.5. This latter presents a slight similarity within each structure, the SMC accomplished an undershoot of 6 W and and an overshoot of 6.5 W respectively for the first and second load variations, whereas the PI got a further difference with 3.5 W and 1.4 W. Regarding the response time for each stack analyzed variable, certainly the SMC is faster than the PI as the integral reduces the speed; however, a reduction in the response time of the PI could be achieved but this will lead to turn off the stack since the current overshoot will increase to limit current of the PEMFC.

Last description takes into account Figure 9.6 which represents the analysis of the boost converter signals (P_{out}, V_{out} and I_{out}) when the load increases to 50 Ω at t= 25 s and shifts back to 20 Ω at 45 s.

9.3. Fuzzy Logic Control (FLC)

An improved procedure from the last presented architecture is a type-1 fuzzy interference, which is a non-linear controller that operates better than a conventional PID, especially for severe nonlinearities [272]. The input to the controller consists of the error and its derivative which are multiplied by the factors K_e and K_d; this results in the variables E and ΔE, which represent error and its change normalized in the range of [-1 1]. The constant K_b is intended to increase the output of the FLC based on an incremental control action (Figure 9.7).

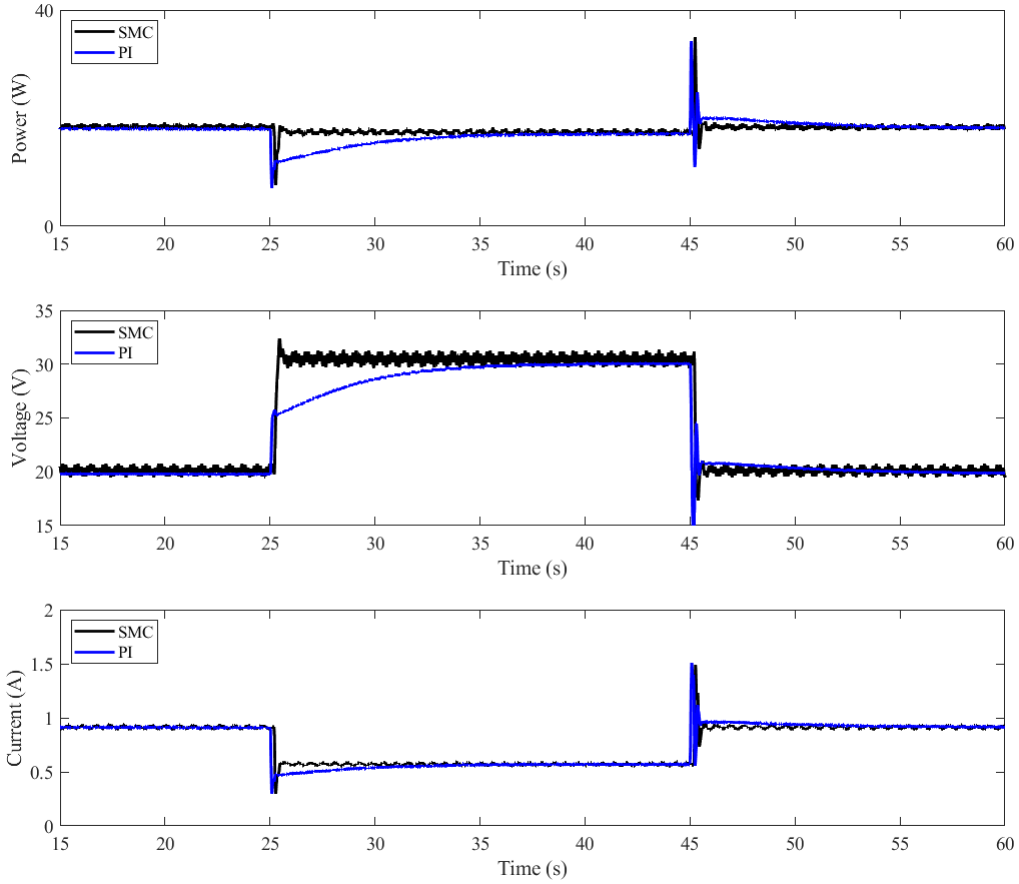

Figure 9.6: Boost converter output power, output voltage, and output current.

The structure of the rules was configured as the Equation 9.2: where ΔU is the output of the fuzzy block, G_m is the corresponding crisp set in which m goes from 1 to the total number of rules used; k and l cover the range of membership functions that corresponds to E and ΔE, respectively. The fuzzification process entails triangular overlapped membership functions related to each normalized input. In this research, the membership functions for the inputs were uniformly discretized in terms of negative big (NB), negative medium (NM), negative small (NS), zero (Z), positive small (PS), positive medium (PM) and positive big (PB); these values were defined as -1, -0.66, -0.33, 0, 0.33, 0.66 and 1, respectively. Therefore, 25 fuzzy rules were adapted where its defuzzification mechanism was configured in constants discretized uniformly in the range of [-1 1].

$$R_m: \ \textit{If } E = B_{1k} \textit{ and } \Delta E = B_{2l} \Rightarrow \Delta U = G_m \tag{9.2}$$

The performance of the PEMFC stack under the use of the FLC is presented from Figure 9.8 to Figure 9.11. These figures shows respectively the wave-forms of the duty cycle signal, stack voltage, stack current, stack power, and finally the DC-DC output signals.

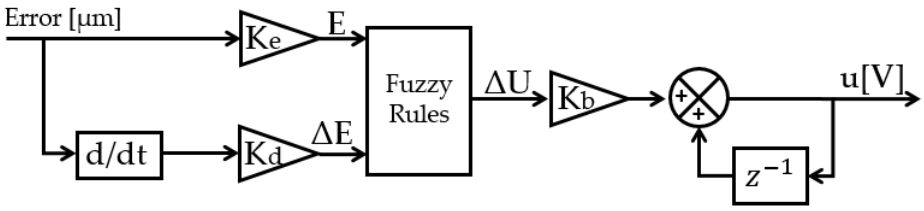

Figure 9.7: Type 1 fuzzy logic control structure.

E \ ΔE	NB	NS	Z	PS	PB
NB	NB	NM	NM	NS	Z
NS	NM	NM	NS	Z	Z
Z	NM	NS	Z	PS	PM
PS	Z	Z	PS	PM	PM
PB	Z	PS	PM	PM	PB

Table 9.2: FLC linguistic rules.

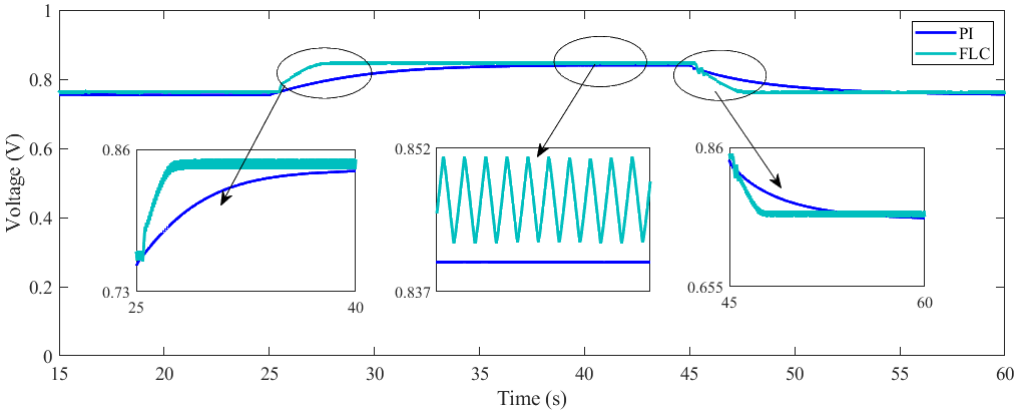

Figure 9.8: Duty cycle signal.

Figure 9.8 exposes the performance of the duty cycle signal in the first and second load change. As it can be seen in this figure, the duty cycle of the FLC shows several chattering behaviour in the steady reference following. Since the duty cycle is the control action, certainly it will reflect this phenomenon in the input and output electrical measures of the boost converter. On the other hand, the duty cycle signal of the PI controller indicates a smooth and gradual rise to the desired operating point. However, one drawback of the PI controller is its slow response time since it takes around 15 s for the first load change and around 13 s for the second load change.

Figure 9.9 shows the PEMFC generated voltage and current where the robustness can be reflected in the overshoot and undershoot measured in the first load rise. In comparison to the PI controller, the FLC overshoot and undershoot were 1.03 V and 1.72 A respectively for voltage and current, which entails a difference of 0.14 V and

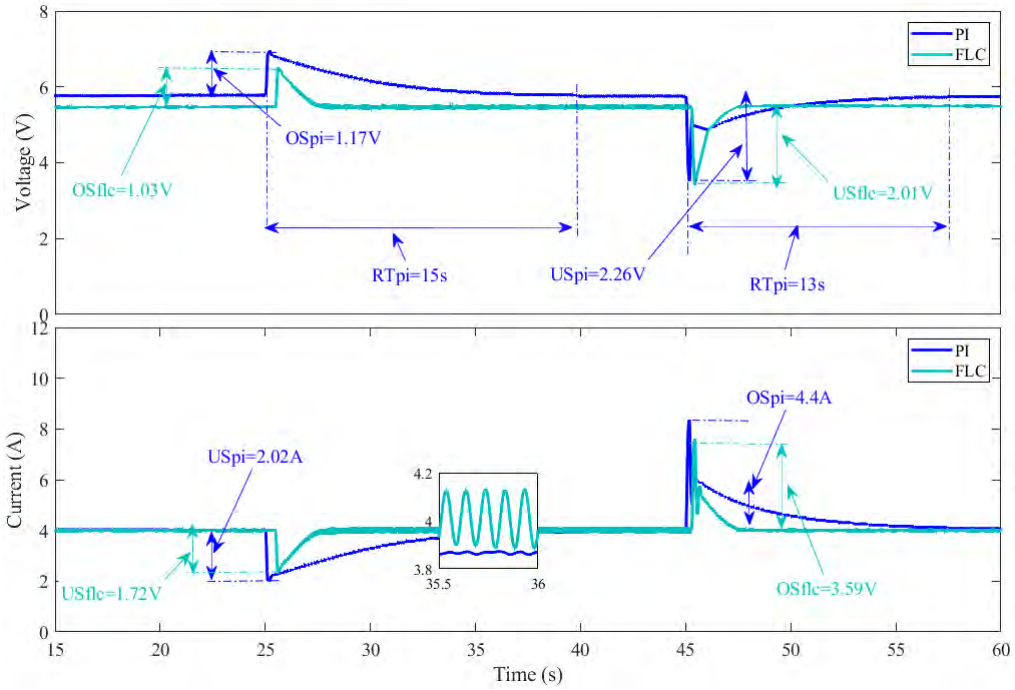

Figure 9.9: PEMFC stack voltage and current.

0.3 A when compared with the conventional PI. A similar trend was observed in the second load change where the FLC still had a better demeanour than the PI since it showed same improved features as the voltage undershoot and current overshoot decreased from 2.26 V and 4.4 A to 2.01 V and 3.59 A respectively.

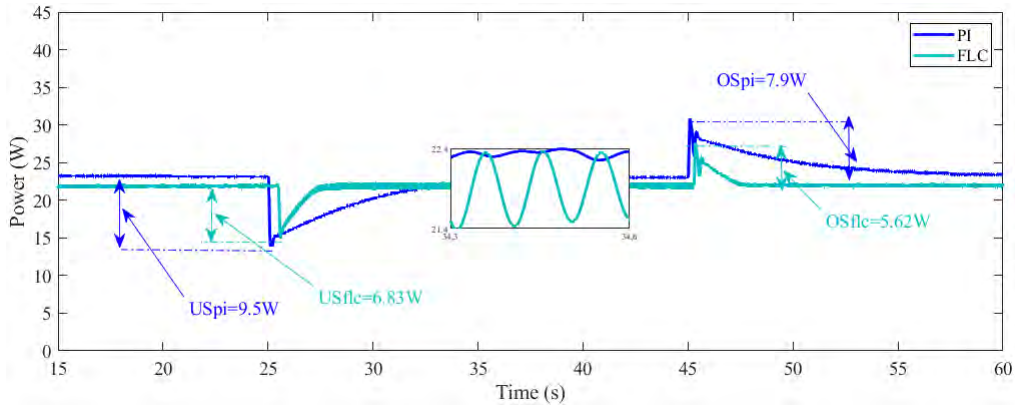

Figure 9.10: PEMFC stack power.

Figure 9.10 shows the trajectory of the generated power. It is obvious that, using the FLC, the desired operating power point is achieved with high robustness and global stability of the closed-loop system . The chattering magnitude using the FLC is around 0.9 W, while it is only around 0.1 W when using the conventional PI controller. However, the drawback of this latter is it lack of robustness when facing load variation since it takes around 15 s to reach the desired operating power point.

Figure 9.11 shows the output signals behaviour of the step-up DC-DC converter. According to this figure, gradual and smooth movements to the desired value are obtained. However, in spite of the chattering phenomenon which is caused by the FLC during the steady state, its robustness to converge the system in a short times which will results in a high tracking accuracy, is an important advantage over the conventional PI.

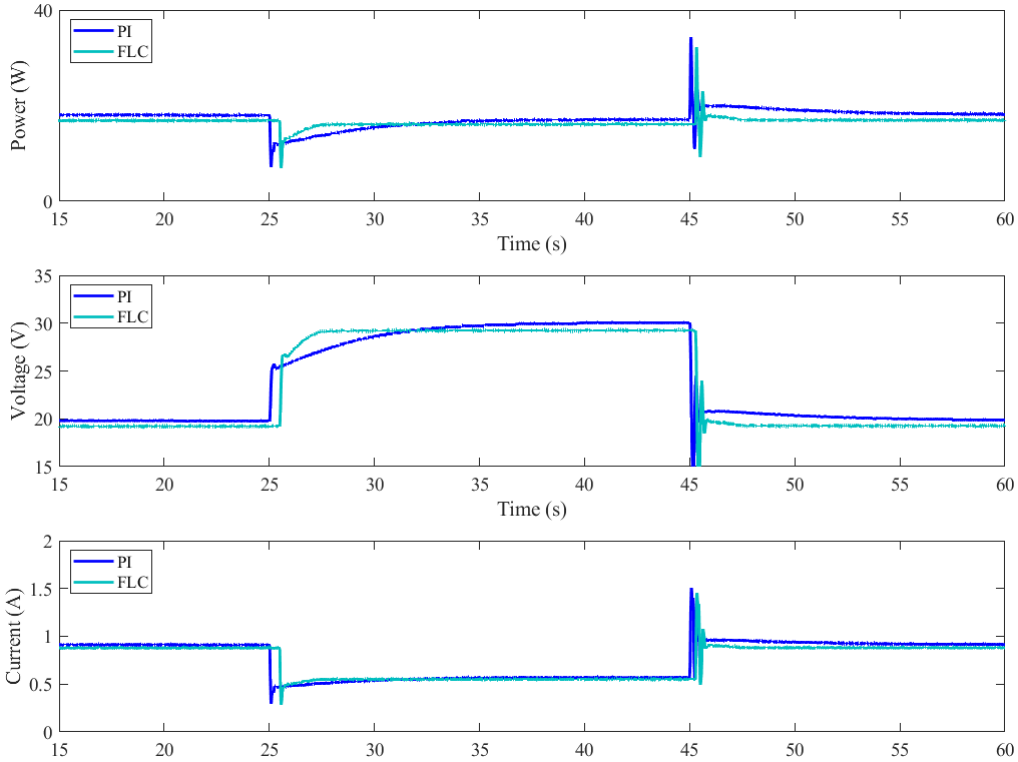

Figure 9.11: Boost converter output power, output voltage, and output current.

9.4. Model predictive control (MPC)

The main feature of the model predictive control (MPC) is its capability to predict the future behavior of the desired control variables [273]. In other words, it is an optimization technique that computes the next control action by minimizing the cost function which is the deference between the predicted variable and the specified reference. The MPC is also characterized by a straight forward implementation, it has no issue with the stability, and the quality of the response is depending on the control design. In MPC, the future predicted state path is called the prediction horizon. This latter is the number of samples T_s over which a prediction of the plant states/outputs is evaluated. According to Figure 9.12, the future values of output variables at the samples $k+1$, $k+2$.. are predicted using the dynamic model of the process ($X(k)$) and current measurements. Besides, according to this figure, it is

noticed that the control actions are based on both future predictions and current measurements. The manipulated control variables $u(k)$, at the $k-th$ sampling time are computed such that the objective function J is minimized. These control variables will be implemented as a control signal to the process.

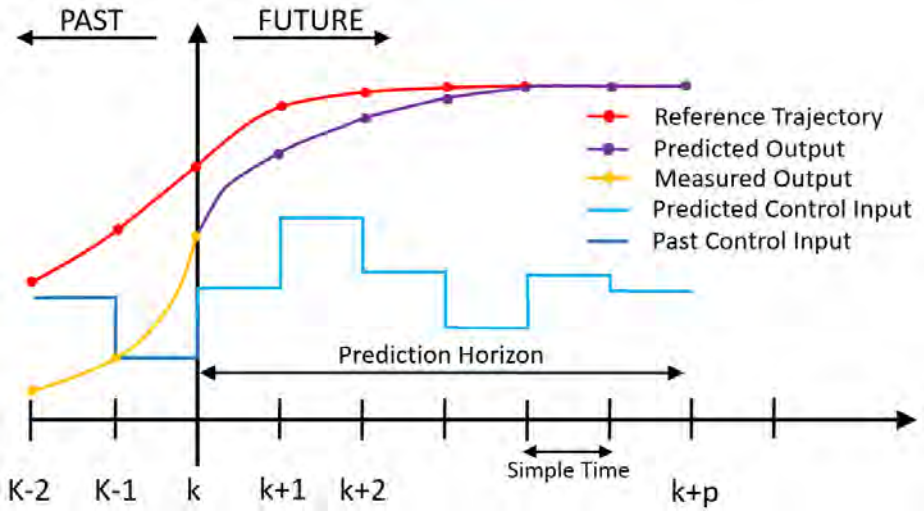

Figure 9.12: Basic concept for Model Predictive Control MPC.

Figure 9.13 illustrates the general scheme of the MPC approach for power electronics converters [273], where $X(k)$ are the measured variables which used in the model to compute the predictions $X(k+1)$ of the controlled variables. The model used for the prediction is a discrete time state-space model which can provide predictive capability for the MPC controller [274]. The design of the MPC control for high step-up power electronic converter (boost converter) can be done using the following steps [273]:

- Modeling the power converter and determining its state-space model.
- Obtaining the discrete time state-space model that allows the prediction of the future behaviour.
- Defining the cost function J that represents the desired behaviour of the system.
- Determining the MPC control law that minimizes the cost function J.

According to [275–277], and by using the sampling time T_s, the discretized equations of the boost converter can be given as Equations (9.3) and (9.4) for the open switch case, and (9.5), (9.6) for the close switch case.

Open switch:

$$I_L(k+1) = I_L(k) - \frac{T_s}{L}V_{out}(k) + \frac{T_s}{L}V_{stack}(k) \tag{9.3}$$

$$V_{out}(k+1) = V_{out}(k) - \frac{T_s}{RC}V_{out}(k) + \frac{T_s}{C}I_L(k) \tag{9.4}$$

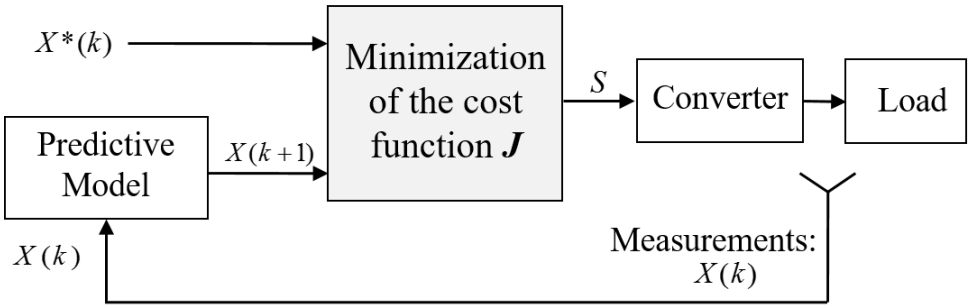

Figure 9.13: MPC general scheme for power electronics converters

Closed switch:

$$I_L(k+1) = I_L(k) + \frac{T_s}{L} V_{stack}(k) \tag{9.5}$$

$$V_{out}(k+1) = V_{out}(k) - \frac{T_s}{RC} V_{out}(k) \tag{9.6}$$

Using the discretized Equations given in (9.3), (9.4), (9.5), and (9.6), or by using the the forward Euler approximation [278] given in Equation (9.7), the discrete-time state-space model of the boost converter can be written as Equations (9.8):

$$x(k+1) = (I + T_s A)x(k) + T_s B d(k) \tag{9.7}$$

$$\begin{bmatrix} I_L(k+1) \\ V_{out}(k+1) \end{bmatrix} = \begin{bmatrix} 1 & -(1-D(k))\frac{T_s}{L} \\ (1-D(k))\frac{T_s}{C} & 1-\frac{T_s}{RC} \end{bmatrix} \begin{bmatrix} I_L(k) \\ V_{out}(k) \end{bmatrix} + \begin{bmatrix} \frac{T_s}{L} \\ 0 \end{bmatrix} V_{stack}(k) \tag{9.8}$$

The control objective is to make the stack current $I_L(k)$ close as much as possible to the reference current $I_{ref}(k)$. This could be obtained by minimizing the cost function J which is is defined as the error between the predicted value and the desired reference value. The expression of the cost function can be written as Equation (9.9). Hence, if the used prediction horizon is equal to one $h = 1$, then, once the value of the controlled variables are obtained at the next sample time and for both switching states, $s = 0$ and $s = 1$, the cost function J will be evaluated. The block scheme of the proposed MPC technique is shown in Figure 9.14.

$$J_{s=n}^{n=0,1} = |I_{L,s=n(k+1)} - I_{ref}| \tag{9.9}$$

By evaluating the cost function J for both states, it selects the one at which the next predicted value is closer to the value of the desired reference current i_{ref}. It should be noted that the MPC approach has the capability to predict the next n-samples of the prediction horizon, which means that the cost function at the future n-step can be calculated. The discrete-time system that provides the n-samples of the future

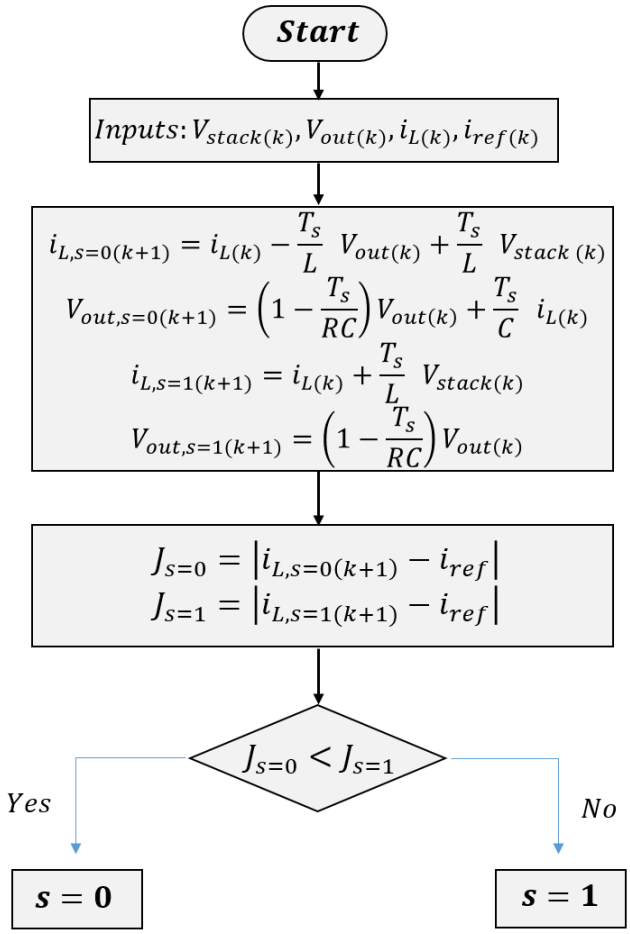

Figure 9.14: Block scheme of the proposed MPC technique.

prediction horizon can be written as Equations (9.10) and (9.11).

$$I_L(k+n+1) = I_L(k+n) - (1 - D(k+n))\frac{T_s}{L}V_{out}(k+n) + \frac{T_s}{L}V_{stack}(k+n) \quad (9.10)$$

$$V_{out}(k+n+1) = (1 - D(k+n))\frac{T_s}{C}I_L(k+n) + (1 - \frac{T_s}{RC})V_{out}(k+n) \quad (9.11)$$

In this work, a MPC with prediction horizon equal to two $h = 2$ is used. To this end, the calculation of the controlled variable I_L at time t_{k+2} is necessary. However, this could be an easy task by using Equations (9.10) and (9.11). The process of the proposed MPC technique with a prediction horizon $h = 2$ is depicted in Figure 9.15. According to this figure, to calculate the value of predicted controlled variable $I_{L(k+2)}$, the calculation of the system variables at time t_{k+1} is required.

Figure 9.16 illustrates the operating principle of the proposed MPC technique. Hence, by observing the system behaviour for the future two-step horizon and by evaluating the cost function at each step, it will be possible to select the best switching

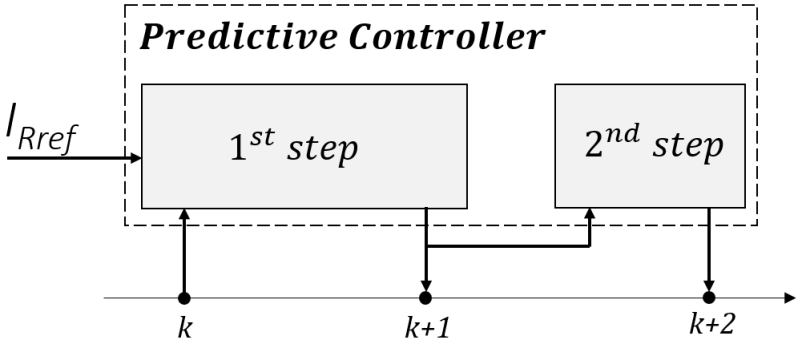

Figure 9.15: Schematic diagram of the proposed MPC process with a 2-step prediction horizon

state at which the cost function has the lowest value. The whole possible sets of switching states that could be evaluated for $h = 2$ are given in Equation (9.12).

$$\begin{cases} S_{(k+1)} = 0 \quad and \quad S_{(k+2)} = 0 \\ S_{(k+1)} = 0 \quad and \quad S_{(k+2)} = 1 \\ S_{(k+1)} = 1 \quad and \quad S_{(k+2)} = 0 \\ S_{(k+1)} = 1 \quad and \quad S_{(k+2)} = 1 \end{cases} \tag{9.12}$$

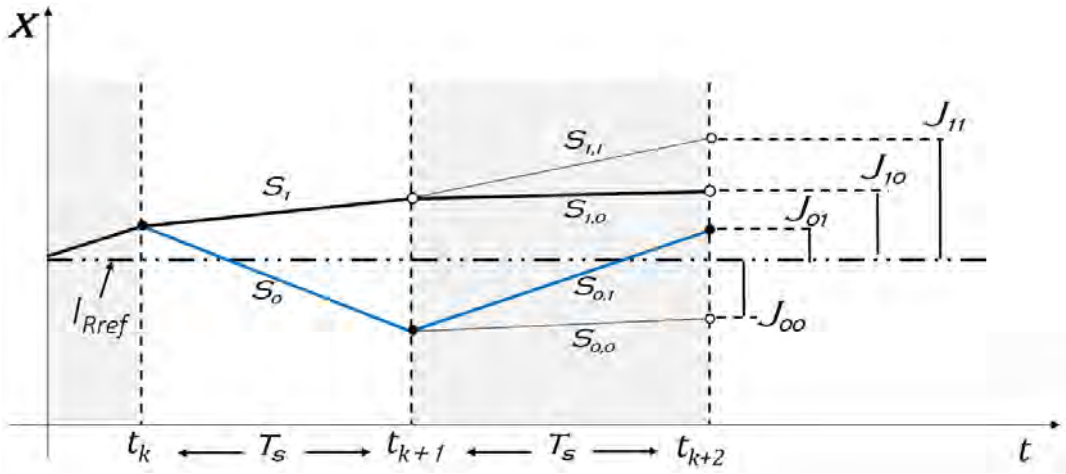

Figure 9.16: Schematic diagram of the proposed MPC operating principle.

It should be noted that there are two strategies that could be used to calculate the predicted state $X(k+2)$. The first one is to evaluate the cost function at each step (sampling time). For instance, by taking the example presented in Figure 9.16 where the performed switching actions are indicated with the black bold line; at first, when the sampling time is t_k, the controller has to choose between S_1 and S_0, where

the choice is based on the most preferred switching condition that leads to minimize the cost function J. Since S_1 is selected in this example, then, it means that the predicted controlled variable $I_{L,s=1(k+1)}$ that corresponds to S_1 is the closest to the desired reference I_{ref}. Following the same criterion for the two-step horizon at which the sampling time is t_{k+1}, the controller will decide between S_{11} and S_{10}. Since S_{10} is selected, then, the cost function J_{10} is performed and considered as the cost function of the previous step at the sampling time t_{k+1}. However, although the simplicity of this strategy, it may fall in a local lower cost function since the cost functions J_{01} and J_{11} that respectively corresponding to the switching states S_{01} and S_{11} were not evaluated. The second strategy is to evaluate the cost functions of the whole sets of switching states that given in Equation (9.12) and finally the lowest cost function is performed. The performed switching actions using this method are indicated with the blue bold line. The main feature of this method is its capability to calculate the global lower cost function for two-step horizon. Therefore, a new cost function for the two-step prediction horizon is defined in Equation (9.13). This letter is composed of the error at the sampling time t_{k+1} plus the error at the sampling time t_{k+2}.

$$J_{s=m}^{n=0,1\&m=0,1} = |I_{L,s=m(k+2)} - I_{ref}| + J_{s=n} \tag{9.13}$$

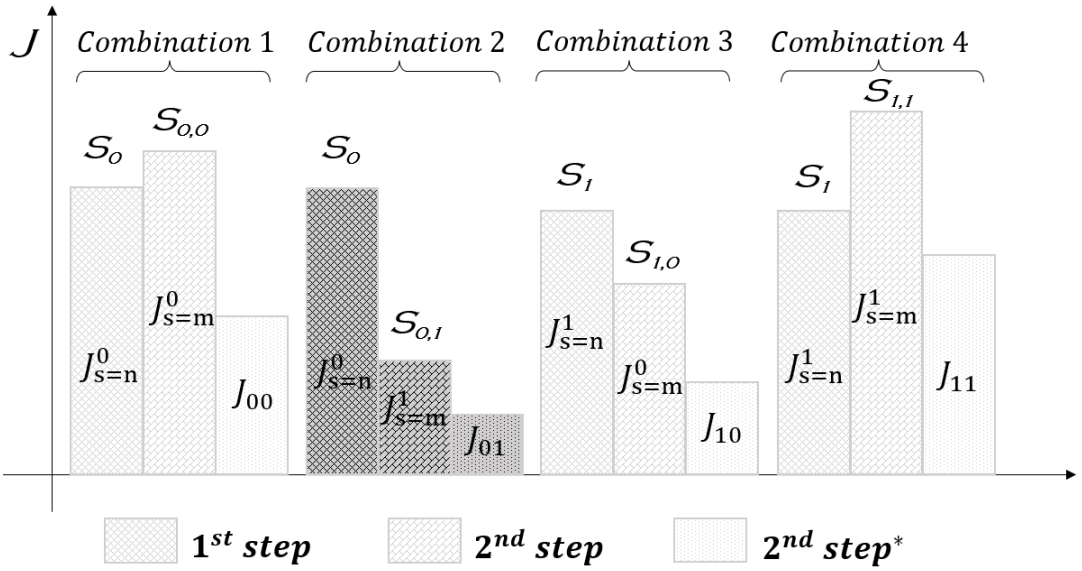

Figure 9.17: Schematic diagram of the switching condition combinations for the 2-step horizon.

The evaluation of the four cost functions J_{00}, J_{01}, J_{10} and J_{11}, for the 2-step horizon is presented in Figure 9.17. The combination with the lower cost function value for the 2-step prediction horizon is represented by the the black color, where faded colors were used for the combinations with higher cost functions value. According to these combinations, if the first method of prediction is used then the preferred

cost function belongs to the combination 3 since $S_1 < S_0$ and $S_{10} < S_{11}$. If only the evaluation of the cost function for the 1-step is considered (Equation (9.9)), then, the preferred cost function belongs to the combination 3 or 4 since $S_1 < S_0$. If only the evaluation of the cost function for the 2-step is considered ($J_{s=m}^{m=0,1}$), then, the preferred cost function belongs to the combination 2 since S_{01} lower than S_{00}, S_{10} and S_{11}. However, although this evaluation gives the same result with the proposed method for the example presented in Figure 9.17, it may not be the most appropriate for other examples. Therefore, a combined cost function involving the two steps, as defined in Equation (9.13), can provide the best switching condition for tracking the desired reference.

Figure 9.18 shows the duty cycle signal for both PI and MPC algorithms. It is noticed that both of the algorithms show a soft and smooth rise to the desired reference value. However, it is clearly shown that the proposed MPC algorithm is characterised by a high convergence speed in comparison with the conventional PI.

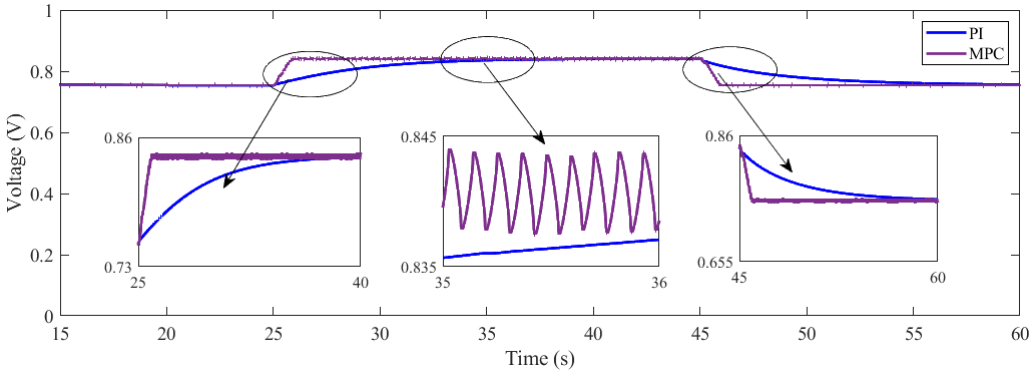

Figure 9.18: Duty cycle signal.

Figure 9.19 and Figure 9.10 shows the stack current, voltage and power signals. The performances of both algorithms when experiencing significant changes in load resistance is clearly demonstrated at t=25 s and t=45 s. Hence, at the instant t=25 s, the PI shows an undershoot current of 2.02 A, an overshoot voltage of 1.17 V and an undershoot power of 9.5 W. For the instant t=45s, an overshoot current of 4.4 A, an undershoot voltage of 2.26 V and an overshoot power of 7.9 W.

On the other hand, at the instant t=25 s, the MPC algorithm shows an undershoot current of 1.9 A, an overshoot voltage of 1.09 V and an undershoot power of 9.3 W. For the instant t=45 s, an overshoot current of 3.87 A, an undershoot voltage of 1.9 V, and an overshoot power of 7.75 W. However, these undershoot and overshoots of the MPC are appeared only for short duration and then, the signals converge to the desired value. Thus, at both times of load variations, the response time of the MPC is less than 2 s. Therefore, high robustness against load variations is achieved using the MPC algorithm. The chattering magnitude of the MPC is around 0.124 V, 024 A, and 0.9 W respectively for voltage, current and power.

Figure 9.21 shows the behaviour of the step-up DC-DC converter output power,

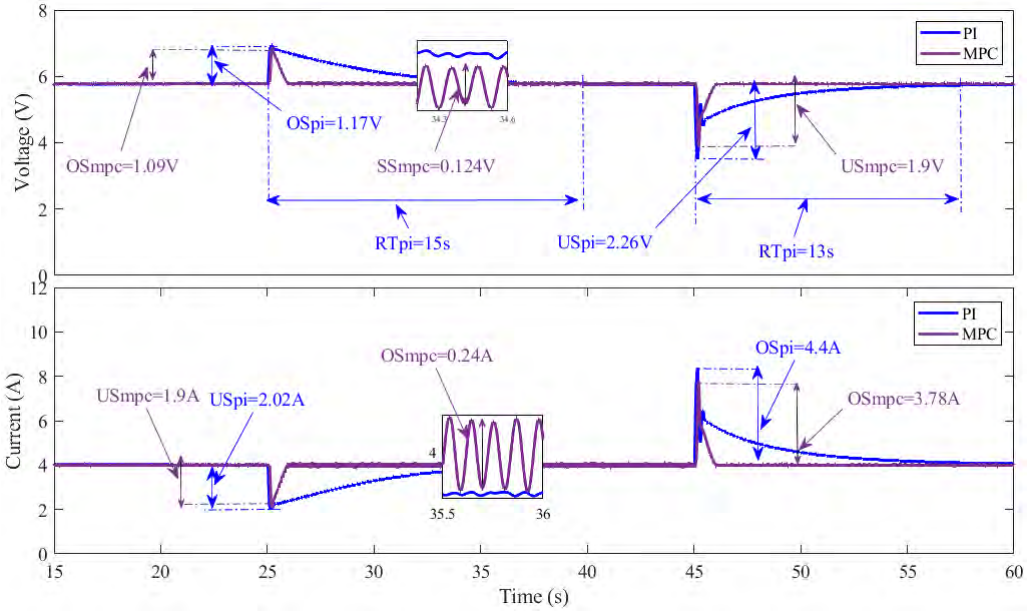

Figure 9.19: PEMFC stack voltage and current.

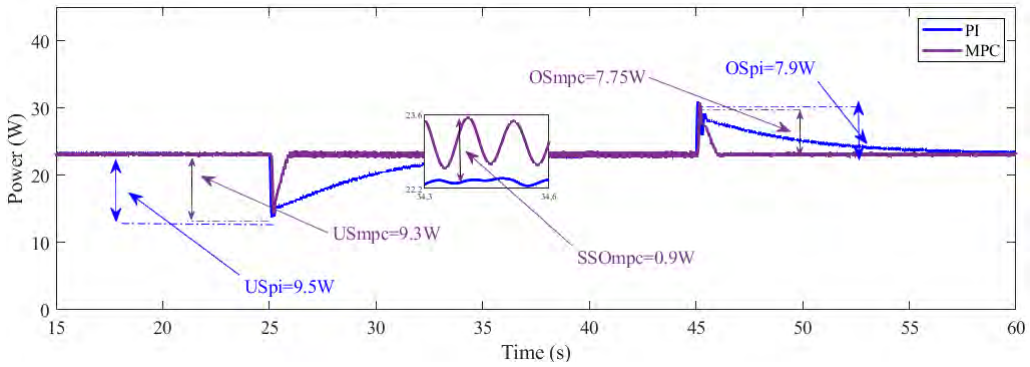

Figure 9.20: PEMFC stack power.

output voltage, and output current, while facing load resistance variation at t= 25 s and t= 45 s. It should be noted that the two experiments of PI and MPC were done in different temperature conditions which results in slight difference in the results.

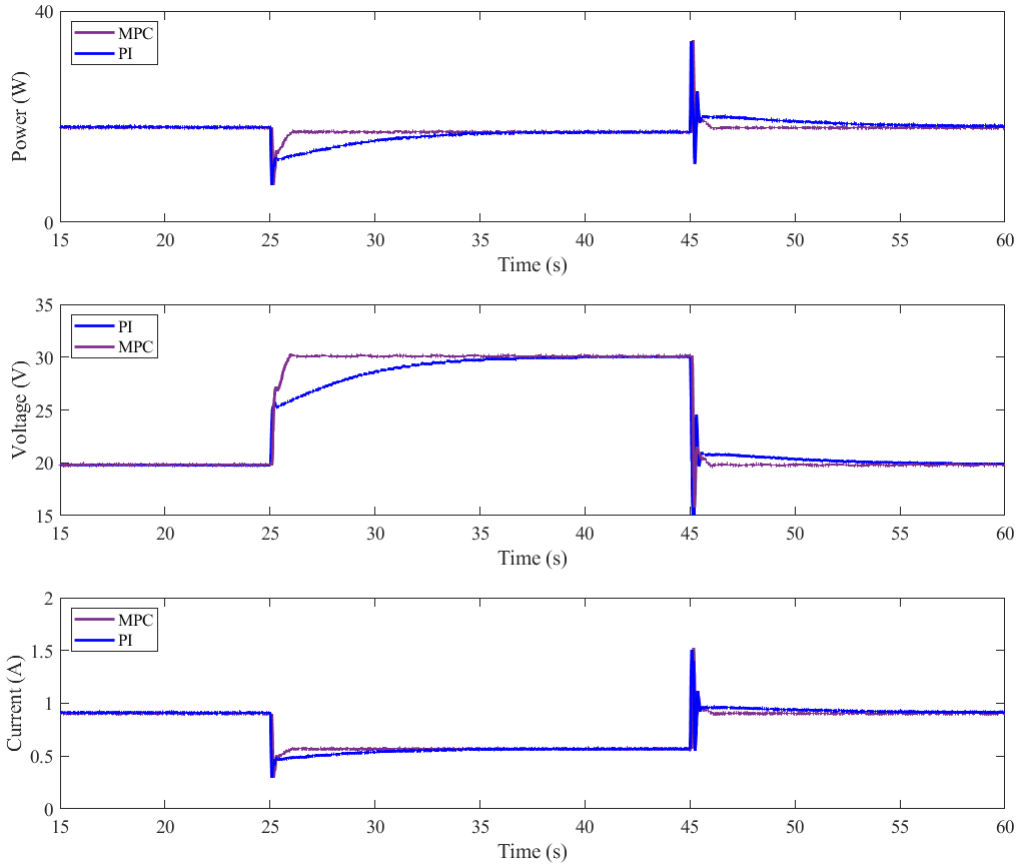

Figure 9.21: Boost converter output power, output voltage, and output current..

9.5. Back-stepping control (BSC)

Back-stepping technique is a recursive design methodology developed in 1990 by P. V. Kokotovic and his coauthors for designing stabilizing controls. It becomes one of the most important robust algorithms due to its ability to control chaos and its flexibility in the construction of control law. Recently, it has been commonly used in numerous applications especially for nonlinear uncertain systems (e.g., PEMFC power systems) [121–126, 279–284]. The back-stepping approach is designed as follows:

- **Step 1.** First, we define the tracking current error as

$$e_1 = x_1 - I_{mpp}. \tag{9.14}$$

In order to achieve the tracking objective, it is needed to enforce e_1 to vanish. Therefore, the dynamics of e_1 must be clearly defined. By placing Equation (5.41) into Equation (9.14), the time derivative of e_1 can be written as

$$\dot{e_1} = -(1 - u_1)\frac{x_2}{L} + \frac{V_{Stack}}{L} - \dot{I}_{ref} \tag{9.15}$$

where the quantity $\frac{x_2}{L}$ is a virtual variable. In order to stabilize the virtual error e_1, a Lyapunov function V_1 is considered:

$$V_1 = \frac{1}{2}e_1^2. \tag{9.16}$$

Using the equations mentioned above, the time derivative of V_1 can be represented as

$$\dot{V}_1 = e_1\dot{e}_1 = e_1\left(-(1-u_1)\frac{x_2}{L} + \frac{V_{Stack}}{L} - \dot{I}_{ref}\right). \tag{9.17}$$

Equation (9.17) shows that e_1 can be adjusted to zero ($e_1 = 0$) if $\frac{x_2}{L} = \gamma_1$, where the stabilizing function γ_1 is defined by Equation (9.18):

$$\gamma_1 = \frac{1}{1-u_1}\left(b_1e_1 + \frac{V_{Stack}}{L} - \dot{I}_{ref}\right) \tag{9.18}$$

where b_1 is a positive constant parameter. Since $\frac{x_2}{L}$ is a virtual variable and not the actual input of the controller, then a second tracking error variable e_2 is given by Equation (9.19):

$$e_2 = \frac{x_2}{L} - \gamma_1. \tag{9.19}$$

Using Equations (9.15) and (9.18), Equation (9.19) can be written as

$$\dot{e}_1 = -b_1e_1 - (1-u_1)e_2. \tag{9.20}$$

Therefore, the Lyapunov function given in Equation (9.17) can also be rewritten as

$$\dot{V}_1 = -b_1e_1^2 - (1-u_1)e_1e_2. \tag{9.21}$$

- **Step 2.** The aim of this step is to enforce the errors (e_1, e_2) to vanish. For this reason, first of all, the dynamics of e_2 must be determined. Using Equations (9.18) and (9.20), the time-derivative of e_2 can be obtained as

$$\dot{e}_2 = -\frac{\dot{u_1}}{1-u_1}\gamma_1 + \Psi \tag{9.22}$$

where

$$\Psi = \frac{1}{1-u_1}\left(b_1^2e_1 + (1-u_1)b_1e_2 - \frac{\dot{V}_{Stack}}{L} + \dot{I}_{ref}\right) + \frac{1}{L}\left(\frac{1-u_1}{C}x_1 - \frac{x_2}{RC}\right) \tag{9.23}$$

In order to obtain a stabilizing control law u_1 for the whole system, the following Lyapunov function candidate is proposed:

$$V = V_1 + \frac{1}{2}e_2^2 = \frac{1}{2}e_1^2 + \frac{1}{2}e_2^2. \tag{9.24}$$

The time derivative of the above Lyapunov function is obtained by combining Equations (9.21) and (9.22):

$$\dot{V} = \dot{V}_1 + e_2\dot{e}_2 \tag{9.25}$$

$$= -b_1 e_1^2 + e_2\left(\dot{e}_2 - (1-u_1)e_1\right). \tag{9.26}$$

It can be easily determined that the global asymptotic stability of the equilibrium $(e_1, e_2) = (0, 0)$ is achieved only if the time derivative of the error variable e_2 is chosen as

$$\dot{e}_2 = -b_2 e_2 + (1-u_1)e_1 \tag{9.27}$$

where b_2 is a positive design parameter. Finally, by combining Equations (9.22) and (9.27), the following control law can be obtained:

$$\dot{u_1} = \frac{1-u_1}{\gamma_1}\left(b_2 e_2 - (1-u_1)e_1 + \Psi\right). \tag{9.28}$$

Using the above equations, the implementation of the back-stepping algorithm in the *Matlab–Simulink*^{TM} environment is presented by Figure 9.22.

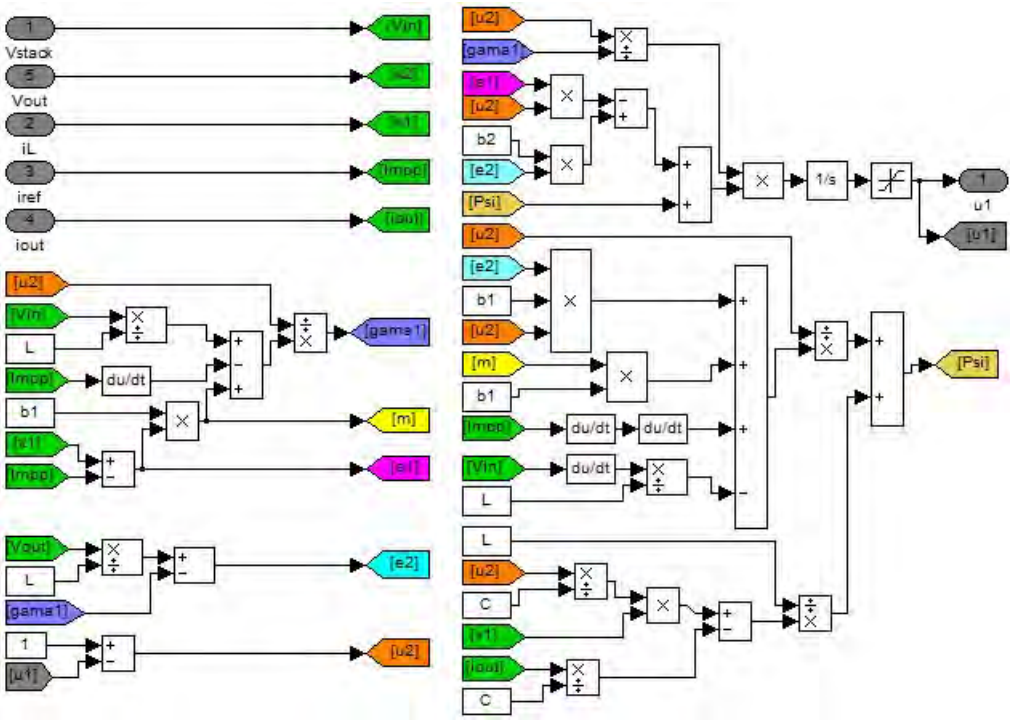

Figure 9.22: Synoptic diagram of the back-stepping algorithm.

Figures from 9.23 to 9.25 show respectively the duty cycle signal, the PEMFC output signals (voltage, current, and power), and finally the boost converter output signals (voltage, current, and power). These figures show the behaviour of the back-stepping and PI algorithms to track the desired reference current. In general,

both of the controllers show global stability and satisfactory tracking results so as to keep the system operating at the desired value. However, it is clearly shown that the back-stepping algorithm has a high capability to decrease the response time from 15 s to 7.5 s which represents a reduction of 50 %, when facing sharp load resistance variation at t=25 s and t=45 s.

The duty cycle signals generated by the controllers are shown in Figure 9.23. As can be seen from this figure, the controllers effectively control the duty cycle so as to obtain constant current with global system stability. It is important to note that, one advantage of the back-stepping over the previous studied algorithm is its robustness while providing smooth response with almost zero chattering.

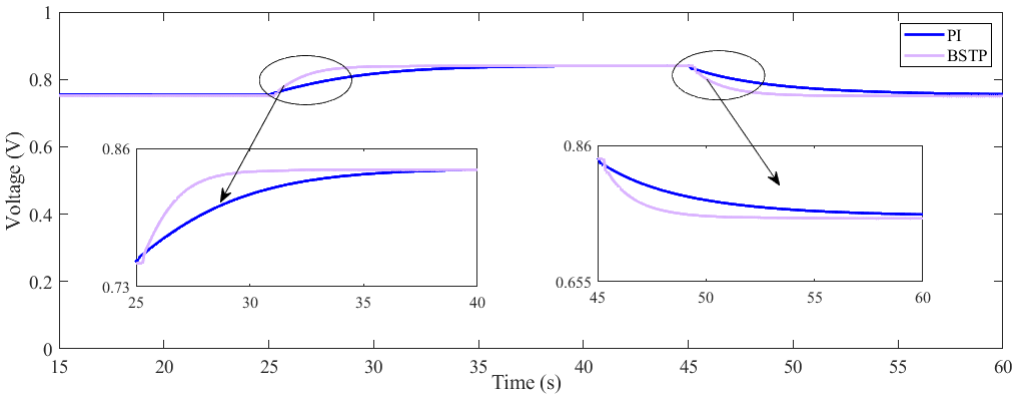

Figure 9.23: Duty cycle signal.

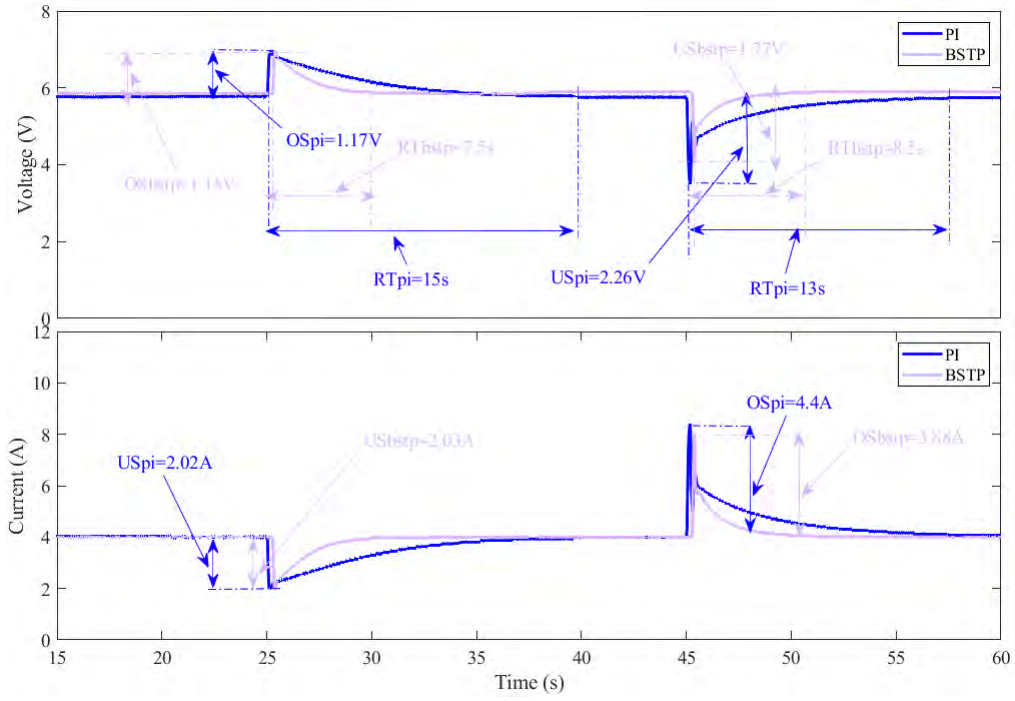

Figure 9.24: PEMFC stack voltage and current.

The behaviour of the fuel cell output voltage and current signals when facing load resistance change is shown in Figure 9.24. According to this figure, it is clear that both of the controllers manifest almost zero ripples in the steady-state response zone. However, the advantage of the back-stepping over the conventional PI is its high robustness. Hence, by varying the load resistance from 20 Ω to 50 Ω and from 50 Ω to 20 Ω, the back-stepping manifests an improved overshoot and undershoot voltage of 0.02 V and 0.049 V. Moreover, when using the back-stepping, the signals swiftly converge to the steady-state value with an improvement of 50 % when comparing to PI scheme.

The fuel cell output power trajectories are presented in Figure 9.25. According to these latter, it is obvious that using the back-stepping, the desired operating power point is attained with swift speed and stability of the closed-loop system. Besides, smooth response with almost zero steady-state ripples is obtained. It should be noted that although the overshoot and undershoot voltage of the back-stepping were better than the PI's one, the power overshoot and undershoot shown in in Figure 9.25 displays opposite results. However, it is clearly proven that the back-stepping has succeeded at reducing about 50 % of the convergence time when comparing to the conventional PI.

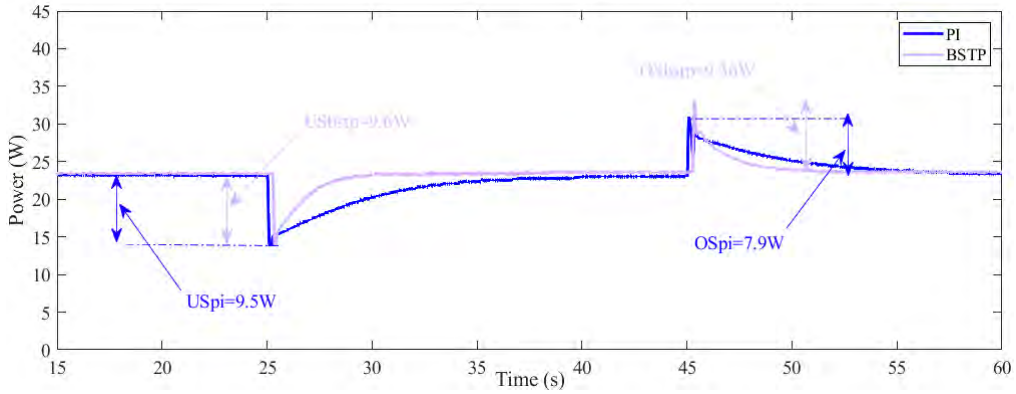

Figure 9.25: PEMFC stack power.

9.6. Conclusions

In this chapter, five alternative algorithms including proportional integral (PI), fuzzy logic control (FLC), module predictive control (MPC) and back-stepping control (BSC) have been designed and implemented for a Heliocentris commercial PEMF; where the goal is to obtain fast, robust and an accurate response. To test the robustness of these types, two load changes at 25 s and 45 s where in the first one, the resistance shifted from 20 Ω to 50 Ω and in the second step regressed to 20 Ω, were used.

Results presented in this chapter have shown that when comparing to the conventional PI controller, the proposed techniques have shown high capability to reduce

the response time while providing high robustness against variations of the load resistance. The performance of the proposed algorithms that presented in this chapter are summarised in Table 9.3.

As it is shown, the advantages and drawbacks are varied from one algorithm to another. In terms of overshoots and undershoots, the FLC shows the highest performance but the response time and the steady state oscillation are not the best when comparing to other algorithms.

The performance of the MPC are quite near to the the FLC one. It has better convergence speed but the overshoots and undershoots are higher.

Regarding the BSC, it has the best results in terms of steady state oscillation since it shows the lowest value with the PI controller over the rest of algorithms. However, in spite of reducing the response time of the PI by 50 %, this value still higher when comparing to the other algorithms.

Table 9.3: Performance of the proposed high order SMC algorithms.

Controller	**Overshoot**	**Undershoot**	**Response Time**	**Steady State Oscillation**
PI	7.9W	9.5W	15s	0.2W
FLC	5.62W	6.83W	3s	0.9W
MPC	7.75W	9.3W	1.2s	0.9W
BSC	9.36W	9.6W	7.5s	0.2W

Chapter 10

Application of maximum power point tracking algorithms (MPPT) for real systems

10.1. Introduction

In the literature, a great number of classical MPPT methods have been reported [285–313]. However, the commonly used are: fractional short or open-circuit (FSC, FOC) [285, 286], perturb and Observe (P&O) [287, 288], voltage and current based MPPT [289], incremental conductance (Inc-Cond) [290], extremum seeking control (ESC) [291–294], proportional-integral-derivative (PID) [295], linear quadratic regulator (LQR) [296], sliding mode control (SMC) [297–301], current sweep (CS) [302], fuzzy logic control (FLC) [303–309]. Each method of these existing algorithms characterized by its complexity in hardware implementation, convergence speed, sensors required, sensed parameters and cost.

This chapter presents a real time application of different MPPT methods including P&O, INC, SMC, FLC, MPC and high order sliding mode control based prescribed convergence law (HOSMC-PCL). This latter was used for a commercial fuel cell system FC-42 Evaluation Kit 360W, where the other algorithms were applied for a commercial PV system PEIMAR SG340P.

10.2. Hardware Description

10.2.1. Fuel cell system

The experimental system presented in Figure 10.1 consist of: FC-42 Evaluation Kit 360W, FC-42 Control unit, DC/DC converter, slide adjustable power resistor, programmable DC power supplies (BK Precision 1788), MicroLabBox dSPACE DS1202, and a host computer.

The FC-42 Evaluation Kit is a system that operates fuel cell stacks. It provides reliable and easy operation for FC-42/HLC stack series module which manufactured by Schunk Bahn industry. The technical data of this system are shown in Table 10.1. The FC-42/HLC stack is composed of 42 cells supplied by hydrogen and cooled

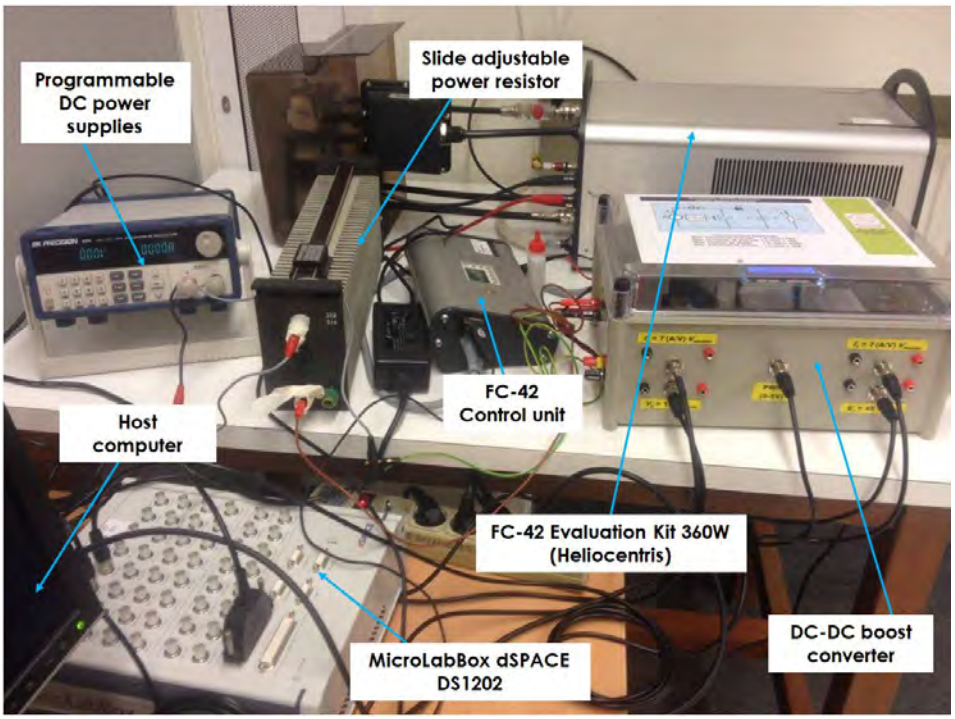

Figure 10.1: Experimental setup.

with water. It delivers 360 W as a rated power with current 15 A and voltage 24 V. The FC-42 360 W Evaluation Kit is equipped with complex hydrogen and air supply system, cooling system, as well as protection and regulation system. The main role of the protection system is allowing low range variations in quantities of temperature and supplied air. One of the most important factors which influence the stack effectiveness is moistening the membrane. This latter is required for assuring the conductivity of protons in the membrane and prevent the dryness. On the other hand, high humidity results in water condensation in the membrane surface which leads to limit the bonding between oxygen and hydrogen. However, proper moistening could be done by supplying an adequate amount of air via the cathode side. Since the supplied air is dependent on the stack temperature, then, a proper setting of temperature leads to proper moistening which will result in an increase in the overall stack efficiency. To obtain proper humidity of supplied air (RH $\approx 95\%$), it must go through the cooling tank, where a properly moistened is realized. Hydrogen inlet pressure P_1 is supplied at the anode side with a constant level ($P_1 \approx 28$ kPa). The outlet of the anode is kept closed using a valve. This latter opens periodically in pulses so as to perform the purging of the anode. Regulation and protection systems also have the role of avoiding the destruction of the stack by preventing the exceeding values of temperature, current, and voltage. Thus, at cooling water temperatures more than 55 °C, voltages below 20 V, and currents above 35 A, the disconnection of the load is done automatically.

Table 10.1: Technical data of the FC-42 Evaluation Kit.

General properties		**Electrical properties**	
Type	FC-42/HLC (42 cells)	Operating voltage	20–45 V
Cooling	Liquid (drinking water)	Open-circuit voltage	36–42 V
Fuel	Hydrogen H_2	Nominal stack voltage	24 V
Service life	$>$ 1500 h	Booster voltage	12 V (11–14 V)
W$\times$ D$\times$ H (mm)	168$\times$230 $\times$115	Operating current	0–30 A
Total weight	17.1 kg	Nominal stack current	15 A
Starting time	2 min	Nominal stack power	360 W
Noise	Max 65 dB	Power consumption	70W
Thermal properties		**Fuel properties**	
Max. temperature of the surface	60 °C	H_2 inlet pressure P_1	1–11 bar
Exhaust air temperature	10–60 °C	H_2 operating pressure P_2	50–360 mbar
Ambient temperature	10–30 °C	Purity of H_2	99.99%
Coolant temperature	10–57 °C	H_2 Consumption	0–4 l/min
Cooling capacity	400 W @ 25 °C	Air volume flow rate	65 l/ min
Coolant volume flow rate	240 l /h	Air pressure	400 mbar
Coolant pressure	320 mbar	Excess air	1.50–4.00

The FC-42 360 W Evaluation Kit is also equipped with measuring and control system as shown in Figure 10.2. It is used to determine the following quantities:

- Stack current (with an accuracy of 0.8 A)
- Stack voltage (with an accuracy of 0.1 A)
- Stack power (calculated)
- Cooling temperature T_1 (with an accuracy of 0.7 °C)
- Exhaust air temperature T_2 (with an accuracy of 0.7 °C)
- hydrogen inlet pressure P_1
- hydrogen operating pressure P_2
- Excess air (calculated)

It should be noted that the authors also have used external devices for current and voltage measurements so as to avoid the low accuracy of the measuring system.

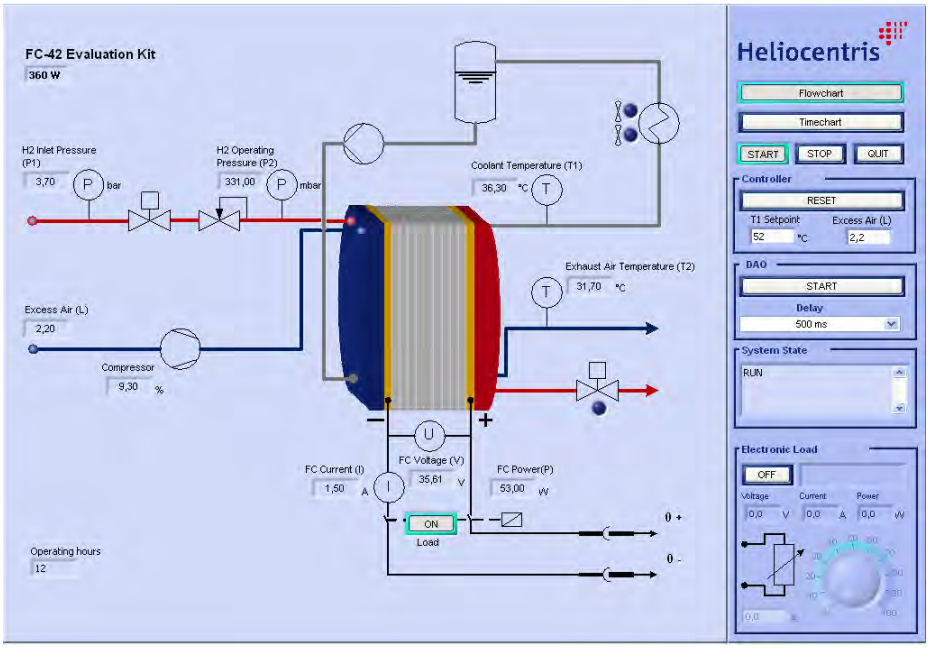

Figure 10.2: PEM fuel cell measuring system.

The host computer has an important role in the experimental system. It organizes and exchanges the data between the software (simulink, controldesk..)and the hardware (dSPACE, FC-42 Control unit..). The characteristics of the host computer used in the experiments are as follows; operating system: windows 10; processor: Intel$^{(R)}$ Core^{TM} i7 CPU; RAM:16 GB; Hard disk space: 500 GB; ports: 6 free USB

ports; graphical user interface with resolution of 1920×1200 pixels; and I/O boards interface for physical interactions with the DS1202.

The dSpace used in this experiment is MicroLabBox dSPACE-DS1202. It is a new laboratory's compact system that offers excellent performance and versatility. It helps the user to turn the theoretical concepts into reality, as well as it enables the user to setup the experiments quickly and easily. MicroLabBox has more than 100 channels with different I/O types which make it a versatile development system that could be utilized in many fields such as development areas and mechatronic applications. Besides, it has a dual-core processor with 2 GHz and a programmable FPGA which allow the user to test even exceedingly fast control loops. It is supported by Real-Time Interface (RTI) and ControlDesk software packages so as to enable the linkage with the Simulink$^{(R)}$ and ConrolDesk software. The integration of the MicroLabBos with the host computer and the power converter is shown in Figure 10.3. Once the Simulink model is compiled, the RTI sends the generated C code to the

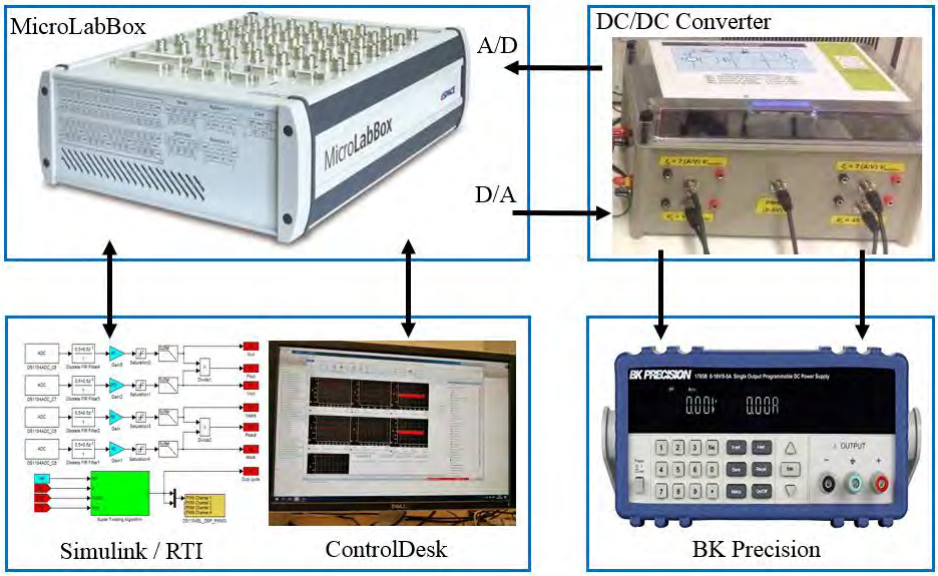

Figure 10.3: System implementation.

MicroLabBox. This latter will convert this code to PWM pulses and they will be sent to the power converter so as to track the desired operating power point. The power converter signals are supplied to the MicroLabBox via its analog-to-digital converter (ADC), and they will be linked with the Simulink model using the RTI library. The evolution of all the obtained signals are recorded and visualized online using the Controldesk monitoring software. This latter has the ability to measure and adjust all the model parameters at run time. Besides, it provides different graphical tools which help the user to obtain clear results. Therefore, the observation and evaluation of the parameters changes can be easily done at run time.

The experimental power and potential Vs current characteristic curves of the

FC-42 Evaluation Kit are shown in Figure 10.4. According to this figure, it is clear that the potential characteristic curves validate the theoretical results which already presented in Figure 3.14 and Figure 3.15. Besides, it is notable that the performances of the FC-42 are enhanced by boosting the operating temperature from 42 °C to 45 °C, while they are dropped for temperatures above than 53 °C . The increase of the performances could be explicated by the rise in membrane conductivity and the exchange current density which leads as a consequence to reduce the activation losses. However, for higher temperatures, the conductivity of the membrane reduces because of the diminishing of the relative humidity in the cell membrane. It is also observed from the characteristic curves that the appearance of the activation and the concentration zones is inconspicuous and this is due to the measurement sensitivity at low and high currents.

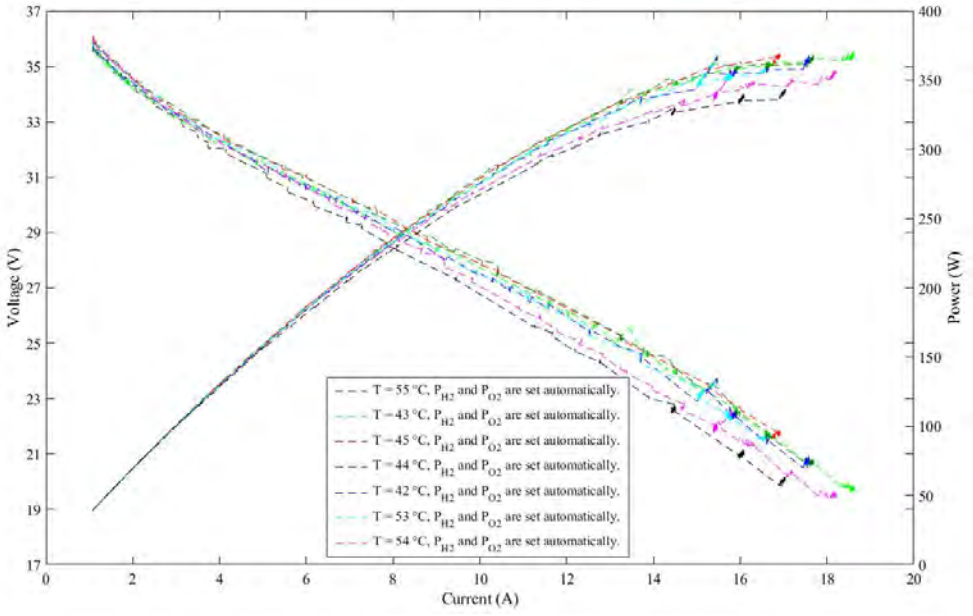

Figure 10.4: Experimental power and potential Vs current characteristic curves of the FC-42 Evaluation Kit.

10.2.2. PV system

The Figure 10.5 shows the workflow through the hardware involved in the experiments. The PV module used is a PEIMAR SG340P made of polycrystalline silicon which represents a suitable versatility and efficiency. These are commonly employed in commercial, residential and industrial installations. Since the structure design was focused in the lightness and robustness it has high stiffness and feasible installation. Extra technical information of this devices is detailed in the Table 10.2.

The temperature and irradiation were measured with a silicon external sensor from the manufacturer Ingenieurbüro Si-V-10TC-T, which is reliable for PV variables

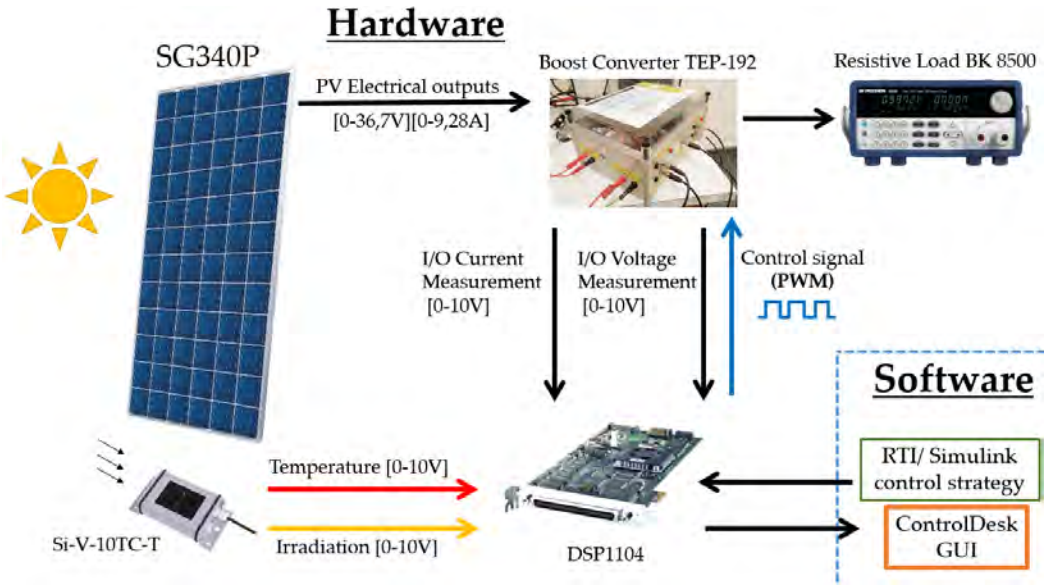

Figure 10.5: Software-hardware workflow diagram.

Table 10.2: Peimar SG340P Specifications

Properties	Values	Units
Dimensions	156x156	mm
Maximum power	340	W
Open circuit voltage	45.2	V
Max power voltage	36.7	V
Max power current	9.28	A
Number of cells in series	6	unit
Number of cells in parallel	12	units
I_{sc}	9.9	A

related monitoring. This module is made of a monocrystalline silicon solar cell that is connected to a shunt. Also it is capable to compensate the measurements since it has an active temperature compensator through a sensor that is laminated to the back surface of the module. As a consequence of this action, it provides a temperature lecture for additional information. Both measured signals are transmitted as voltage variations in the range of 0-10V. Further concerning details are provided in the Table 10.3.

Table 10.3: Ingenieurbüro Si-V-10TC-T Specifications

Properties	Values	Units
Voltage supply	12 to 28	VDC
Irradiance measurement range	Up to 1500	W/m^2
Temperature measurement range	-40 to 90	ºC

The characteristics curves shown in Figure 10.6 were obtained by a considerable value of resistance linked to the PV system; this value was decreased gradually while the data were being recorded. Simultaneously, the environment temperature and irradiation were gathered, which varied, respectively, between 14.6 °C and 36.6 °C and from 64 W/m^2 to 808 W/m^2.

Figure 10.6a indicates the relation between the voltage and the current where three sections are distinguished and were labeled in the research conducted by the authors of [314]. The first is called the *current source part*, where this feature tends to stay constant; the second one, known as *the knee* of the I-V curve, is the section where the MPP is achieved; and finally, the *voltage source part* is where the current–voltage is linearly related. Along the current source section, this tends to stay almost constant between 0 V and 35 V. However, this section is highly dependent on the irradiation, which, ideally, lean these curves upwards, whereas the temperature shifts in a horizontal movement [315]. The knee and the voltage source part are mostly conditioned by the temperature, which moves the curves to the right hand side of the graph [316].

Figure 10.6b shows the voltage–power curve where, in this case, the irradiation leans the curves upwards and the slope of the initial linear behaviour ascends. Nevertheless, the temperature influences a diagonal drive of the curves. Therefore, this means that the irradiation moves the MPP on a vertical axis, whereas the temperature moves the curves on an slanted axis.

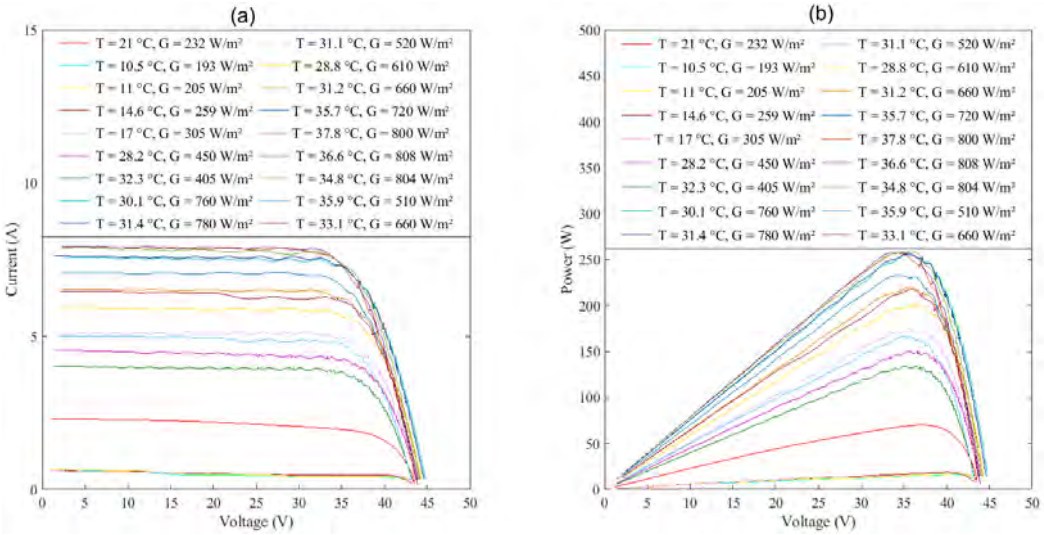

Figure 10.6: PV panel characteristic curves, where: (**a**) voltage-current; (**b**) voltage–power.

10.3. Perturb and observation P&O Algorithm

This algorithm is based on an intentional and periodical perturbation on the control command with a following observation and evaluation of the system output [317].

Applied to PV systems, the perturbation is generated through a change in the voltage $V_{pv}(k)$ and current $I_{pv}(k)$, such that the power of the PV is measured. This implies that the slope $\Delta P/\Delta V$ can be calculated, which helps with knowing whether the MPP is achieved, as Figure 10.8 shows.

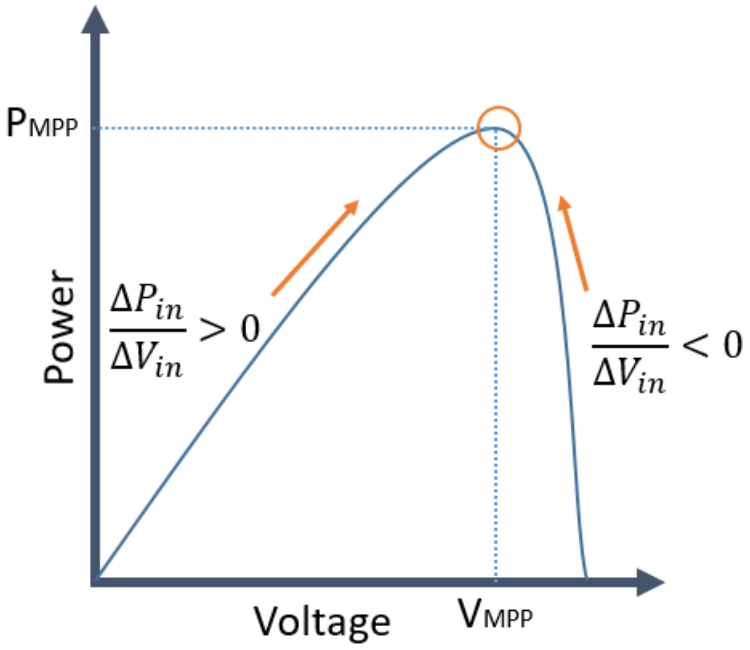

Figure 10.7: Power–Voltage curve with the P&O mechanism to reach the MPP.

Based on the previous description and on the detailed logic of Figure 10.8, the knowledge of $P_{pv}(k)$ and $V_{pv}(k)$ and its delay in $k-1$ allows for the calculation of the slope. Therefore, if the latter mentioned value is positive, the duty cycle d will increase such that the algorithm output $u = d + \delta d$ and aims to reach the MPP; on the contrary, when the position is at the right side of the MPP, the control signal decreases through $u = d + \delta d$.

An interesting example of simulated implementation of P&O was carried out by Murtaza et al. [318], where they used this algorithm for a two-stage coordinated PV system. Despite that this study lacks of experimental results, the authors showed that it is also effective in distributed systems. Another case where experiments were involved in a PV system, had shown that conventional P&O techniques are very sensitive to step size (which is related to the disadvantages of this method) [319].

The results of the P&O tracking method applied for the SG340P panel are presented in Figure 10.9 and Figure 10.10, where the irradiation, temperature, load resistance, duty cycle and current signal are respectively displayed from (a) to (e) in Figure 10.9; while the PV voltage signal, PV power, boost converter current, voltage and power, are respectively unveiled from (a) to (e) in Figure 10.10. A resistance load change was configured with a period of 120s Figure 10.9(c) shows. The amplitude was

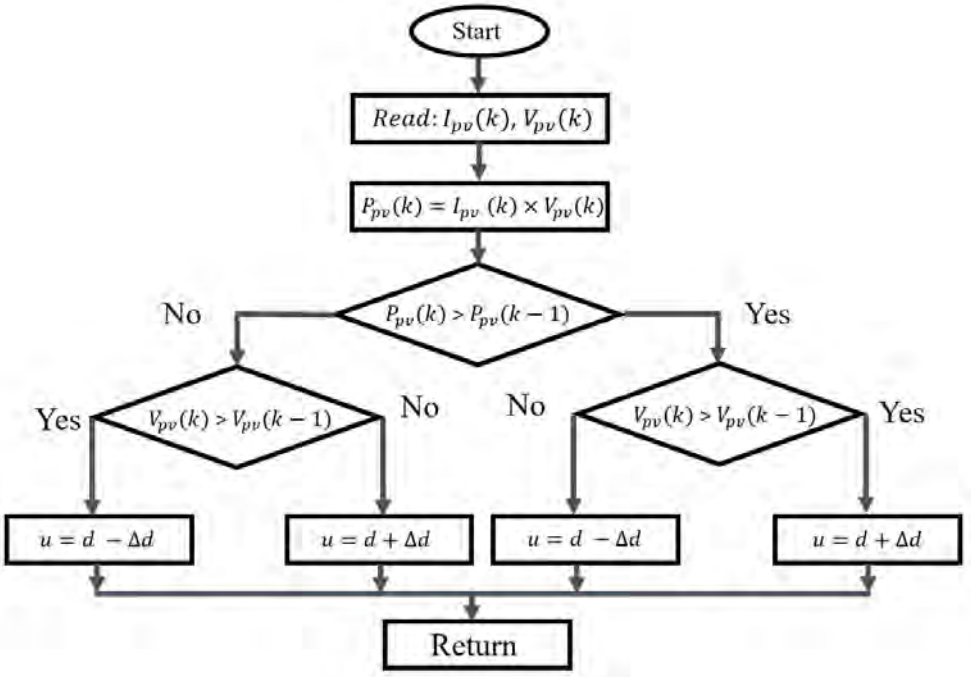

Figure 10.8: Flowchart of P&O algorithm.

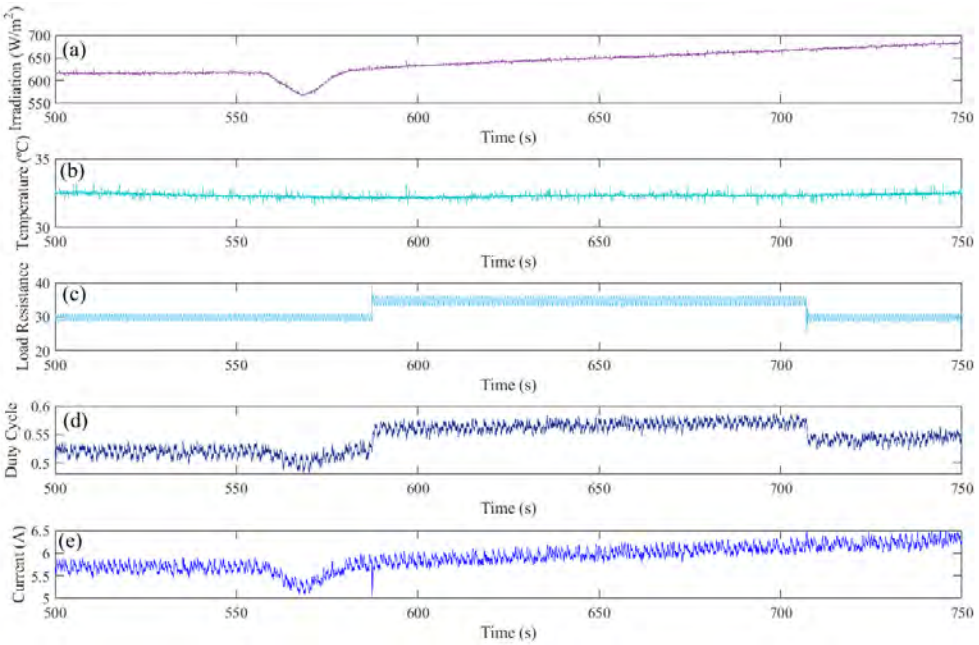

Figure 10.9: MPPT based on P&O: (**a**) Irradiation (W/m^2); (**b**) Temperature (°C); (**c**) Load resistance (V_{out}/I_{out}); (**d**) Duty cycle; (**e**) PV current.

configured in a square change from 30 Ω to 35 Ω that stayed constant for a certain time. Later, during the decrease, the change was from 35 Ω to 30 Ω. The schedule was configured with the aim of testing the algorithm performance at unexpected and

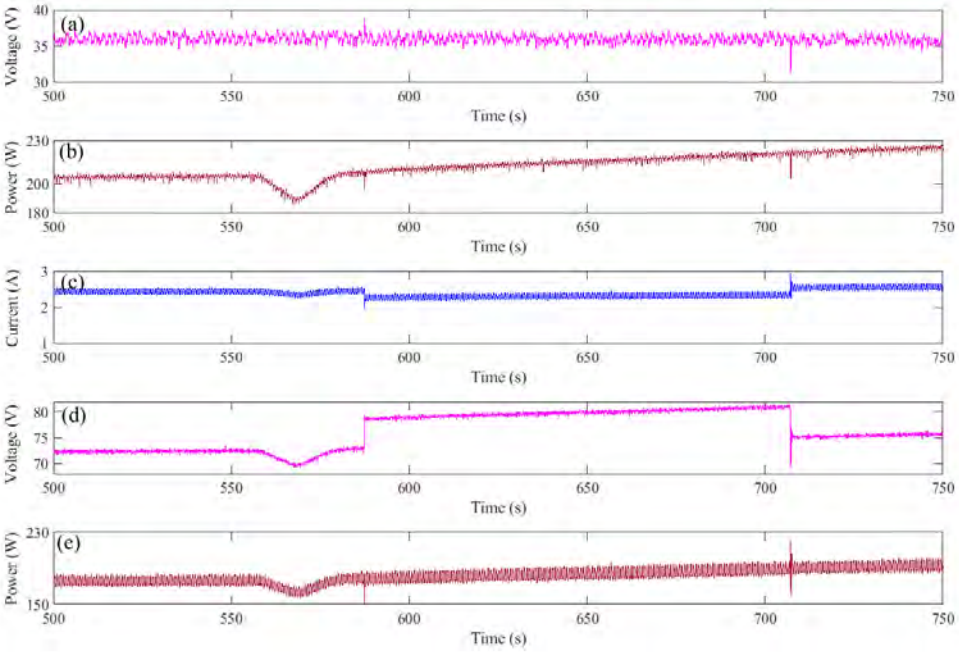

Figure 10.10: MPPT based on P&O: (**a**) PV voltage; (**b**) PV power; (**c**) Boost converter output current; (**d**) Boost converter output voltage; (**e**) Boost converter output power.

complex disturbances. Several other unexpected effects such as sudden variation of the sun irradiation, which is resulting from the transitory cloud, are presented in Figure 10.9 as well. This variation directly affects the PV performance as can be seen at $t = 570s$ of Figure 10.9(e) and Figure 10.10(b), (d) and (e).

Figure 10.9 and Figure 10.10 also reveals the behaviour of the P&O when facing unexpected load variation. Hence, it is clearly that the controller shows robustness for both load variations. However, chattering phenomenon with an amplitude of 0.3 A is also noticed in Figure 10.9(e). This implies that some amount of the extracted power will be lost. Regarding to the performance of the boost converter, it is noticed that the output power (shown in Figure 10.10(e)) was reduced in comparison with the PV extracted power (displayed in Figure 10.10(b)). Actually, this is a usual behaviour since the converter was designed to deliver higher power, which implies that it will not be efficient at low power operation.

10.4. Reference current estimator for tracking the MPP of a FC-42 Evaluation Kit

The reference current estimator (RCE) has the objective of researching the highest power point provided by the fuel cell. The corresponding current of this maximum power point is taken by the controller as a reference current and it generates the adequate command signal so as to drive the power converter device. In order to

determine I_{mpp} which will be used as a reference current (I_{ref}), the performance of the fuel cell at different operating conditions must be studied. In any fuel cell, variation in temperature, oxygen, or hydrogen has an influence in its performances. However, the fuel cell used in this work is FC-42 Evaluation Kit 360W, and is equipped with an internal control system which provides the required quantities of hydrogen and air (oxygen) for each operating condition. In other words, variations in the ambient temperature will automatically results in variation in supplied hydrogen and air. Therefore, to study the performance of the fuel cell at different operating conditions, experiment tests are occurred at several temperature values as presented in figure 10.11. The MPP bold red curve depicted in this figure is constructed using Matlab Curve Fitting Toolbox™ (CFT) which provides functions and applications for fitting curves and surfaces to data. The CFT bolsters non-parametric modeling techniques like smoothing, splines, and interpolation. It also provides optimized solver parameters so as to improve the quality of the fit. In order to construct the MPP curve, the following steps should be performed:

- Gather the data of P_{max} and I_{max} for each P-I polarization curve in two vectors and load this data at the MATLAB command line. The experimental data obtained from the FC-42 Evaluation Kit is enlisted in Table 10.4.

Table 10.4: Data of P_{max} and I_{max}

$\boldsymbol{P_{max}}$	363	362.6	367.2	361	336	357.8	346
$\boldsymbol{I_{max}}$	16.89	16.88	16.92	16.86	16.77	16.83	16.80

.

- Execute CFT by entering the function “sftool" or “cftool" in the Command Window.

- Select I_{max} as X data, and P_{max} as Y data so as to import the database. The CFT will create a default interpolation to fit the loaded data.

- Using the fit category drop-down list (Interpolant, Polynomial, Fourier, Gaussian, Weibull..), select various types and try to find the best curve by comparing the graphical and numerical fit results including fitted coefficients and the goodness of fit (GOF). Regarding to the latter mentioned, it includes the sum of squared due to error (SSE), the R-square, the adjusted R-square and the root mean squared error (RMSE); these metrics are tools that contribute to find the best curve that fits the data, for instance, a small SSE indicates a good fitting.

- Export the best fit to the Matlab workspace.

In this work, many tests were performed in order to achieve excellent statistics of the GOF. Hence, the MPP fitting curve constructed using the CFT is presented in

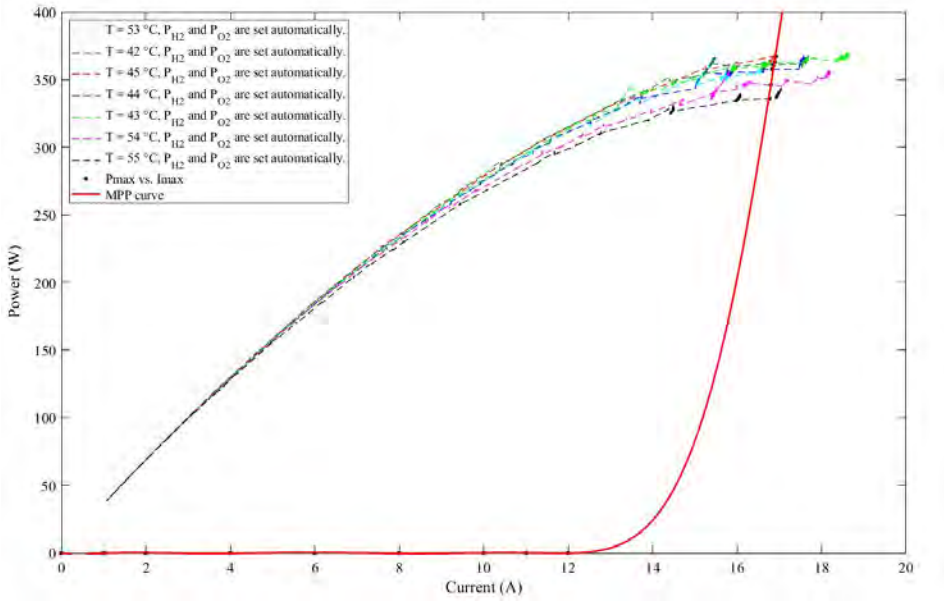

Figure 10.11: P-I polarization curves at different operating temperatures.

Equation (10.1).

$$f(x) = P_1 * x^9 + P_2 * x^8 + P_3 * x^7 + P_4 * x^6 + P_5 * x^5 + P_6 * x^4 + P_7 * x^3 + P_8 * x^2 + P_9 * x + P_{10} \tag{10.1}$$

Were the coefficients P_i (i=1..10) and the goodness of the function are given in Table 10.5.

Table 10.5: Goodness and coefficient parameters of the fitting function.

Goodness of the fit				
SSE: $6873e^{-2}$	R-square: $9998e^{-4}$	Adjusted R-square: $9996e^{-4}$		RMSE: $3708e^{-3}$
Coefficients with 95% confidence bounds				
$P_1 = -1514e^{-9}$	$P_2 = 1034e^{-7}$	$P_3 = -2898e^{-6}$	$P_4 = 433e^{-4}$	$P_5 = -3741e^{-4}$
$P_6 = 1887e^{-3}$	$P_7 = -5321e^{-3}$	$P_8 = 7463e^{-3}$	$P_9 = -3863e^{-3}$	$P_{10} = 2661e^{-5}$

Figure 10.12 explains the operation of the RCE. Thus, by occurring several projections on MPPT curve (red curve), the PEMFC will be brought from the operating power point to the desired point at which the stack will deliver its maximum power. In other words, assuming that the stack is operating at P_{01} with an operating current I_{01}. The tracking control will force P_{01} to be projected onto the MPPT curve which results in changing its operating current from I_{01} to I_{02} and as a consequence, the operating power point will be P_{02}. The same process is occurred with P_{02} and P_{03} and many other power operating points until the stack achieves the point at which the MPPT curve crossed the P vs I curve. This intersection point is called the

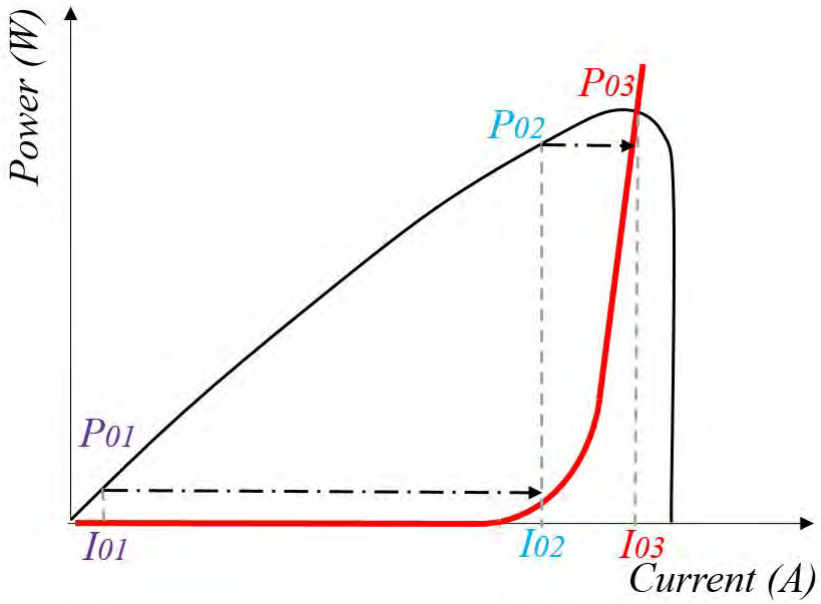

Figure 10.12: Principle of the RCE.

MPP and its current "I_{mpp}" is used as a reference current for the control algorithm. Any algorithm of the previous studied ones can be used to drive the actual current to the desired I_{mpp}. However, in this work we used the high order sliding mode based prescribed converge law (HO-PCL) which is already designed previously.

The performances of the FC-42 under the use of the proposed MPPT control method are presented in Figure 10.13. It shows respectively the waveforms of stack current, stack voltage, and stack power. It should be noticed that the noise occurred in the obtained signals is due to the impact of the control signal time-delay. The noise also could be resulting from the parasite signals that come from the hardware system components. Therefore, according to these results, it is clearly demonstrated that the proposed control method succeeded to extract the maximum power from the fuel cell. Thus, by running the fuel cell for up to more than 200 seconds, the MPP can be extracted for temperature variation in a range of [42-55 °C]. Before starting the control process and aiming to find out the influence of the temperature on the MPPT control method, the fuel cell was heated manually until 54 °C using the FC-40 control unit which shown in Figure 10.1. Then, by applying the controller, the FC-42 power could reach about 375W as shown in Figure 10.13.C. However, with temperature variations, this amount decreases until 355W or less. This validates that the proposed control method tracks the MPP curve which already presented in Figure 10.11.

On the other hand, aiming to find out the behavior of the HO-PCL against the unexpected disturbances, variation of 20 Ω in the load resistance is applied each 25s. These variations, as shown in Figure 10.14.A, are done using the programmable

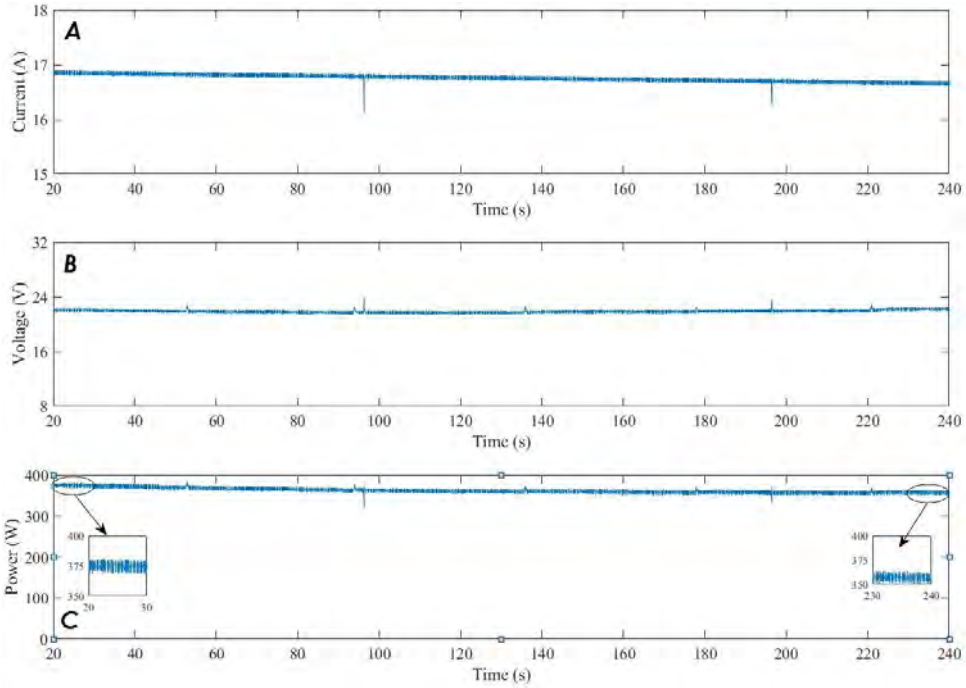

Figure 10.13: Control results: (**A**) stack current; (**B**) stack voltage; (**C**) stack power;

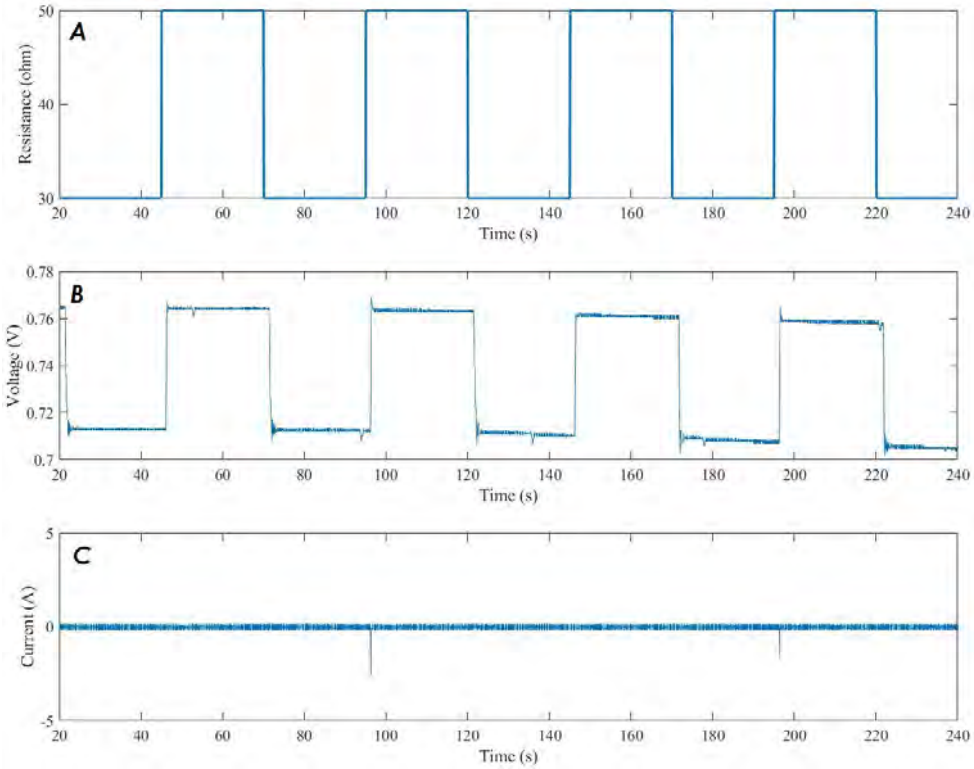

Figure 10.14: Control results: (**A**) load variations; (**B**) duty cycle ; (**C**) error signal;

electronic load (PEL) that commuting between 30 Ω and 50 Ω. Although these sharp variations, it is clearly shown in Figure 10.13, Figure 10.14.B, Figure 10.14.C, and Figure 10.15, that the proposed HO-PCL shows robustness against external unexpected disturbances. Thus, soft signals with high accuracy and with small overshoots are obtained. Besides, a smooth and fast rise to the desired value also can be seen in Figure 10.15.A and Figure 10.15.B. Consequently, high tracking performance with good dynamic behavior and global system stability are obtained.

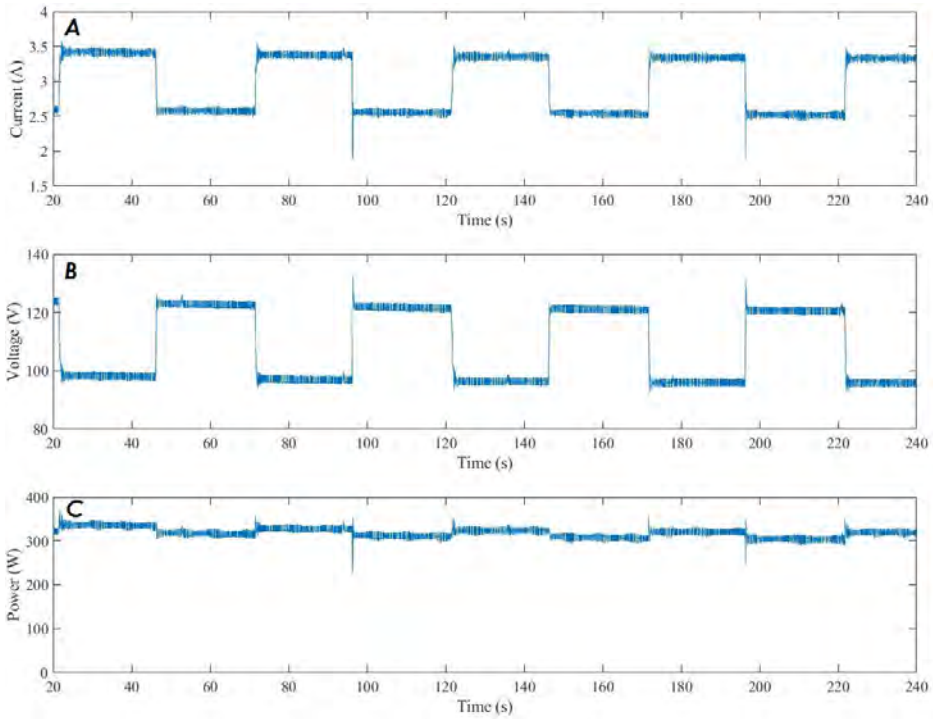

Figure 10.15: Control results: (**A**) the converter output current; (**B**) the converter output voltage; (**C**) the converter output power;

10.5. Reference voltage estimator for tracking the MPP of a PV SG340P module

In this case, a RVE was developed by highlighting the MPP points from 790 curves like those in Figure 10.6b, which varied with the radiation, and then a surface $V_{ref\_MPP} = f(P, T)$ was constructed. This function was attained with the Matlab Curve Fitting Toolbox since it employs an optimized solver to achieve suitable parameters that could reach the best fit quality for curves and surfaces. The framework provided a polynomial surface represented by Equation (10.2); these parameters were obtained through an optimization of performance metrics to acquire a suitable goodness of fitting (GOF); these are the sum of squared errors (SSE), R-square, adjusted R-square and root mean square of the errors (RMSE).

Table 10.6 provides the obtained metric values, which are appropriate because the SSE and the RMSE should be minimum whereas the R-square and its adjusted version should be near the unit [320–322]. Furthermore, the coefficients of Equation (10.2) are also exhibited with 95% confidence bounds. The representation of the surface is shown in Figure 10.16 based on voltage, power and temperature.

$$f(x,y) = p_{00} + p_{10} \cdot x + p_{01} \cdot y + p_{20} \cdot x^2 + p_{11} \cdot x \cdot y + p_{30} \cdot x^3 + p_{21} \cdot x^2 \cdot y. \quad (10.2)$$

Table 10.6: Goodness and coefficient parameters of the fitting function.

Goodness of the fit			
SSE: 107.7	R-square: 0.97	Adjusted R-square: 0.97	RMSE: 0.36
Coefficients with 95% confidence bounds			
$P_{00} = 38.18$	$P_{10} = 0.067$	$P_{20} = -0.00057$	$P_{30} = 1.389^{-6}$
$P_{01} = -0.088$	$P_{11} = -7.207^{-5}$	$P_{21} = -7.86^{-7}$	

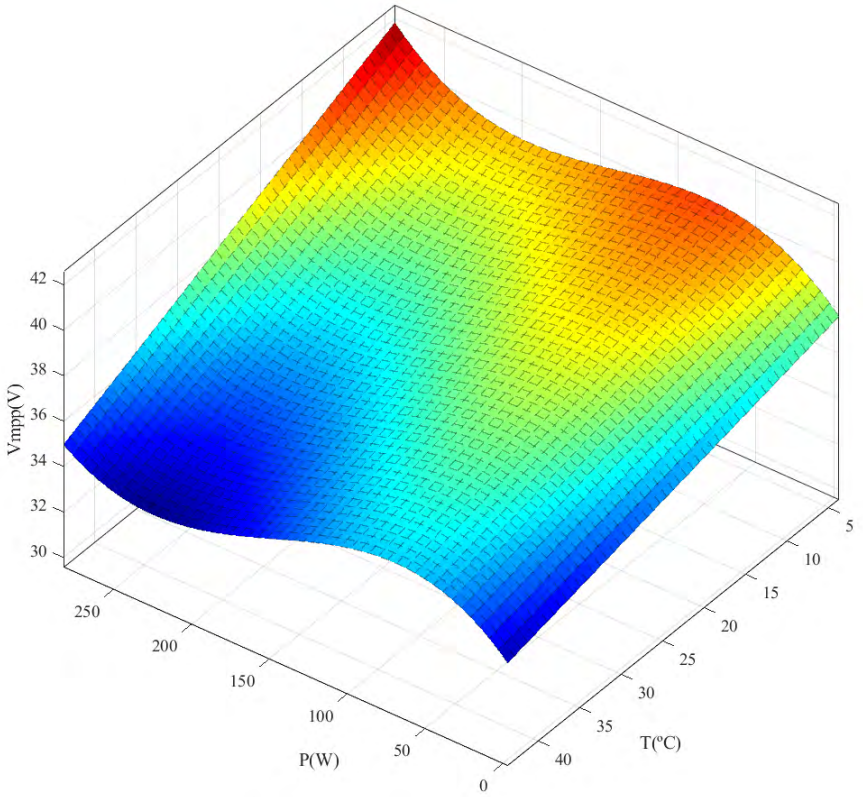

Figure 10.16: Reference voltage representation.

To verify the performance of the designed and explained RVE, two experiments were conducted in different conditions, the outcomes of which are shown in Figures 10.17 and 10.18. For each figure, (d) is the output of the RVE, whereas the data of (b) and (e) are the inputs. Based on both figures, the values of temperature and the

irradiation match with each curve where the MPP voltage is around 36 V and 32 V, respectively, for each condition; this is verified with the obtained results where the voltages are around the mentioned values. Surely, these are inconstant as the power fluctuates as well as being mainly affected by the irradiation and temperature; this effect is seen as a correlation between sub-figures (a) and (e).

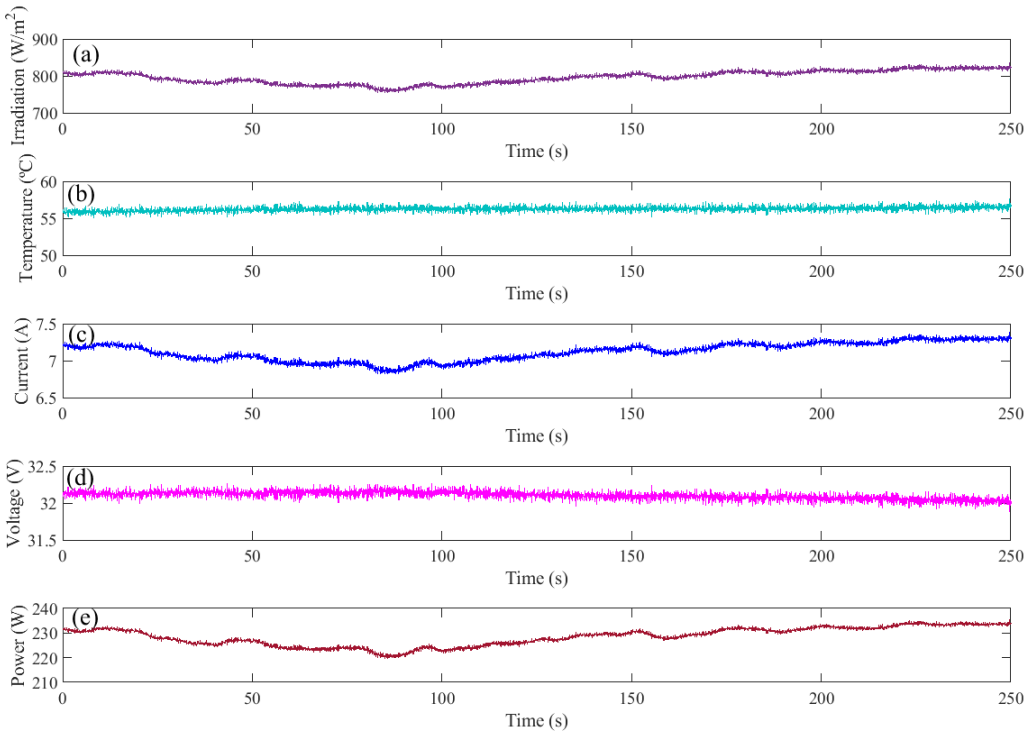

Figure 10.17: RVE experiment used for the SMC: (**a**) Irradiation (W/m^2); (**b**) Temperature (°C); (**c**) PV current; (**d**) PV voltage; (**e**); (**f**) PV power.

10.5.1. SMC based RVE

The results of the MPPT tracking method based on a combination of SMC and RVE are presented in Figure 10.19 and Figure 10.20. Certainly, the irradiation and temperature are different to the previous weather condition since the experiment was performed in diverse surroundings. The load resistance variation values which exhibited in Figure 10.19(a) were set the same as the previous P&O experiment. One advantage of the SMC is its implementation simplicity since it does not need high human skills.

With regards to the PV controlled outputs which presented in Figure 10.19(b), Figure 10.19(c) and Figure 10.19(d), the first feature that can be highlighted over the P&O algorithm is the chattering reduction. This is clearly visible in Figure 10.19(c) where the amplitude is almost 1 V and it is almost 2 V with the case of the P&O algorithm. This phenomenon cutback is also clearly presented in the duty cycle signal which is depicted in Figure 10.20(a), where the reduction is up to 70 % in comparison

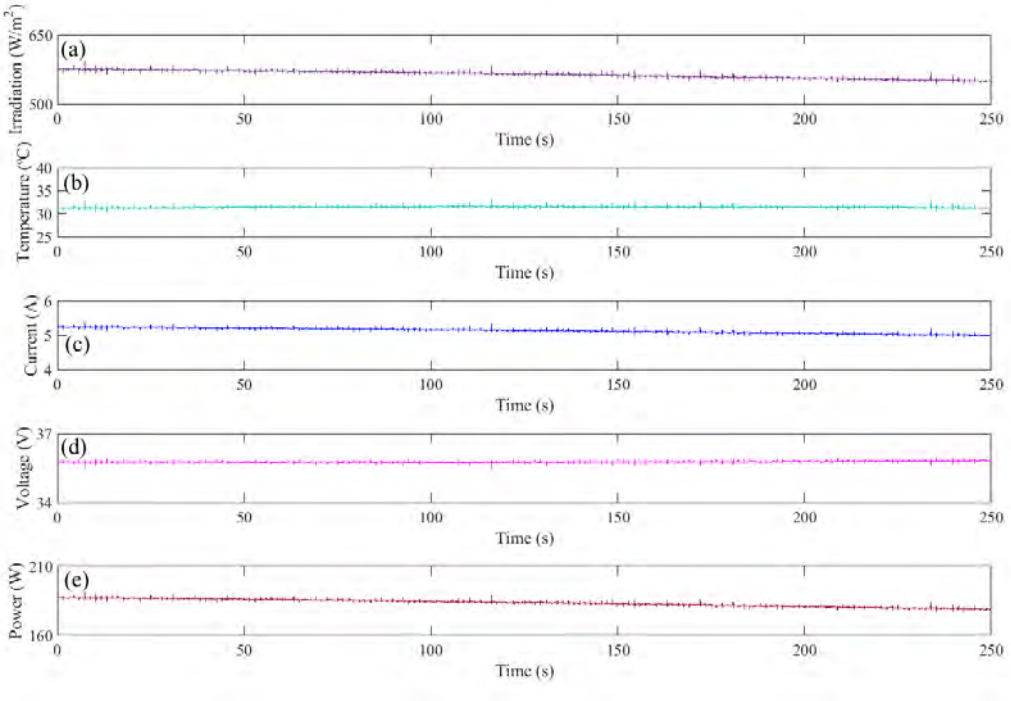

Figure 10.18: RVE experiment used for the FLC: (**a**) Irradiation (W/m^2); (**b**) Temperature (°C); (**c**) PV current; (**d**) PV voltage; (**e**); (**f**) PV power.

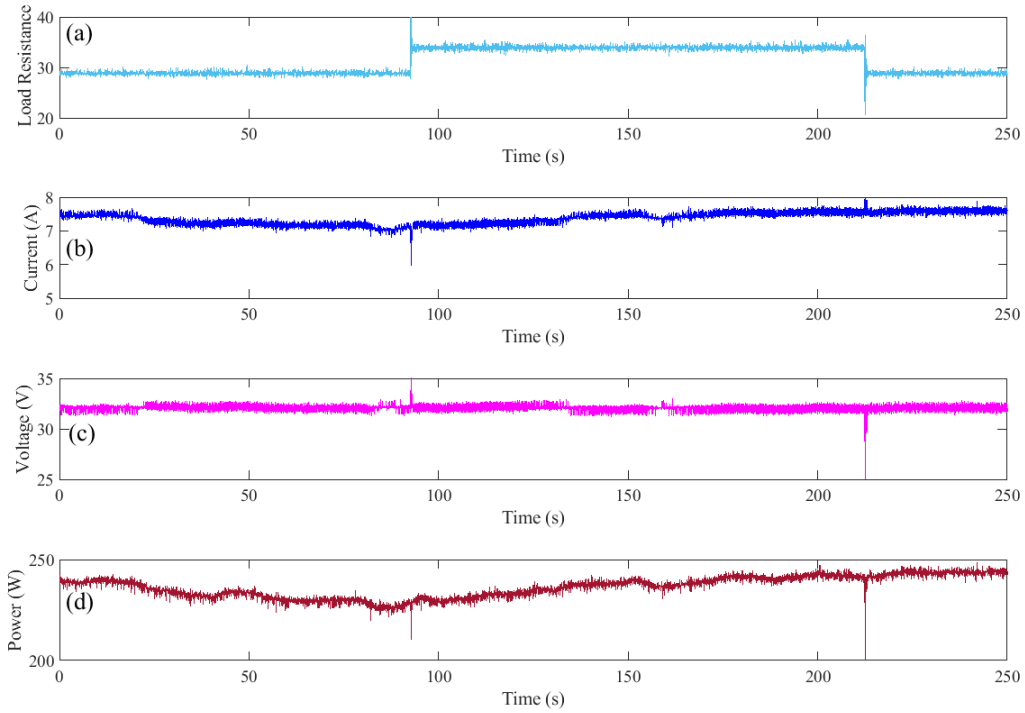

Figure 10.19: MPPT based on RVE and SMC: (**a**) Load Resistance (V_{out}/I_{out}); (**b**) PV current; (**c**) PV voltage; (**d**) PV power.

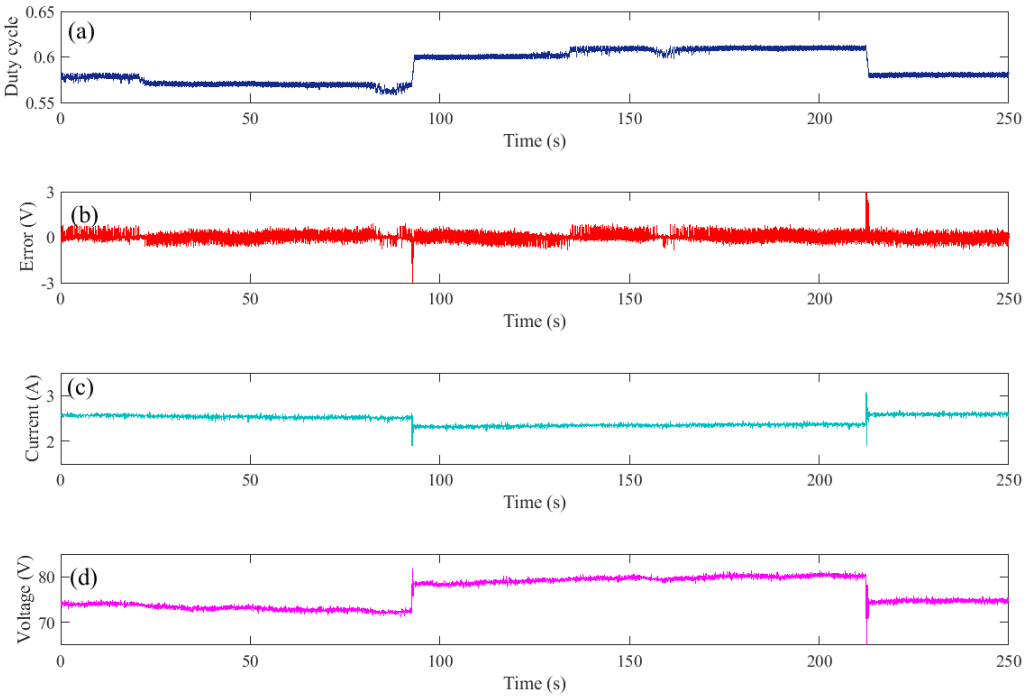

Figure 10.20: MPPT based on RVE and SMC: (**a**) Duty cycle; (**b**) Error; (**c**) Boost converter output current (I_{out}); (**d**) Boost converter output voltage (V_{out}).

with the the duty cycle signal of the P&O which presented in Figure 10.9(d). In reality, the SMC shows less chattering than the presented amplitudes because part of these amplitudes came from the chattering in the reference that generated by the RVE model. Another feature that should be highlighted is the robustness of the SMC. This latter faces the sharp load variations with high robustness since it forces the controlled signal to converge to the desired values with less than 1 s. Finally, it is important to mention that the SMC designed in this work is an error-based controller whereas the P&O is perturbation-based. The acquired error values of the SMC algorithm are displayed in Figure 10.20(b), where the chattering amplitude of this scheme still its main drawback.

10.5.2. FLC based RVE

The results of the implementation of FLC and RVE for MPPT are presented in Figure 10.21 and Figure 10.22. The atmospheric conditions (irradiation and temperature) that supplied the RVE model are reflected in Figure 10.18(a) and Figure 10.18(b). The predicted MPP current I_{mpp}, MPPT voltage V_{mpp} and the maximum power P_{max} are, respectively, displayed in Figure 10.18(c), Figure 10.18(d) and Figure 10.18(e).

The performance of the FLC for tracking the I_{mpp}, generated by the RVE model, is exhibited in Figure 10.21 and Figure 10.22. Initially, in comparison with the previous

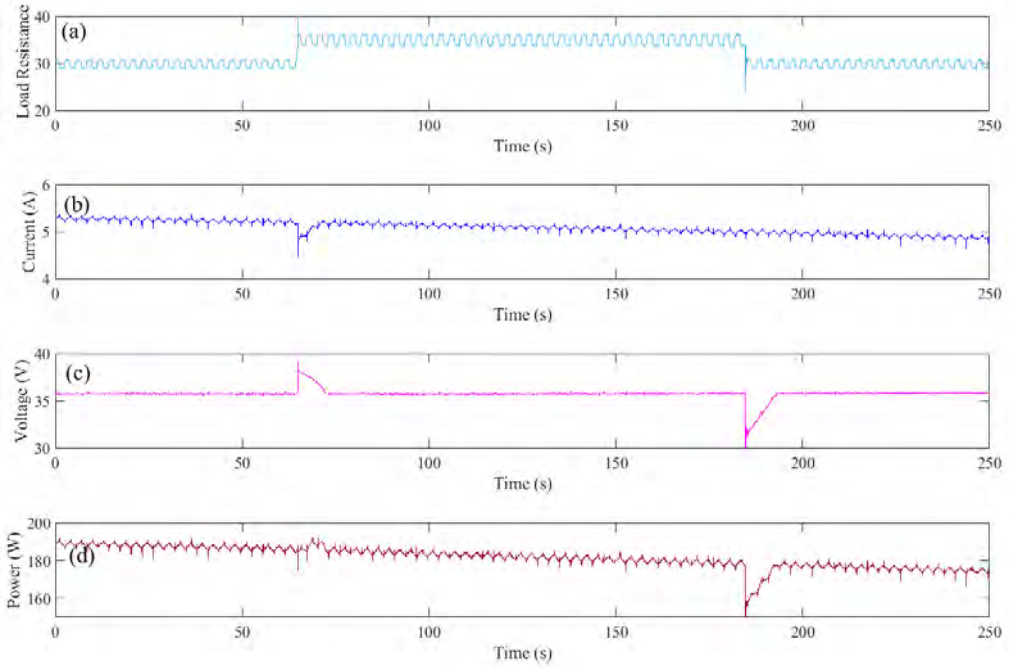

Figure 10.21: MPPT based on RVE and FLC: (**a**) Load Resistance (V_{out}/I_{out}); (**b**) PV current; (**c**) PV voltage; (**d**) PV power.

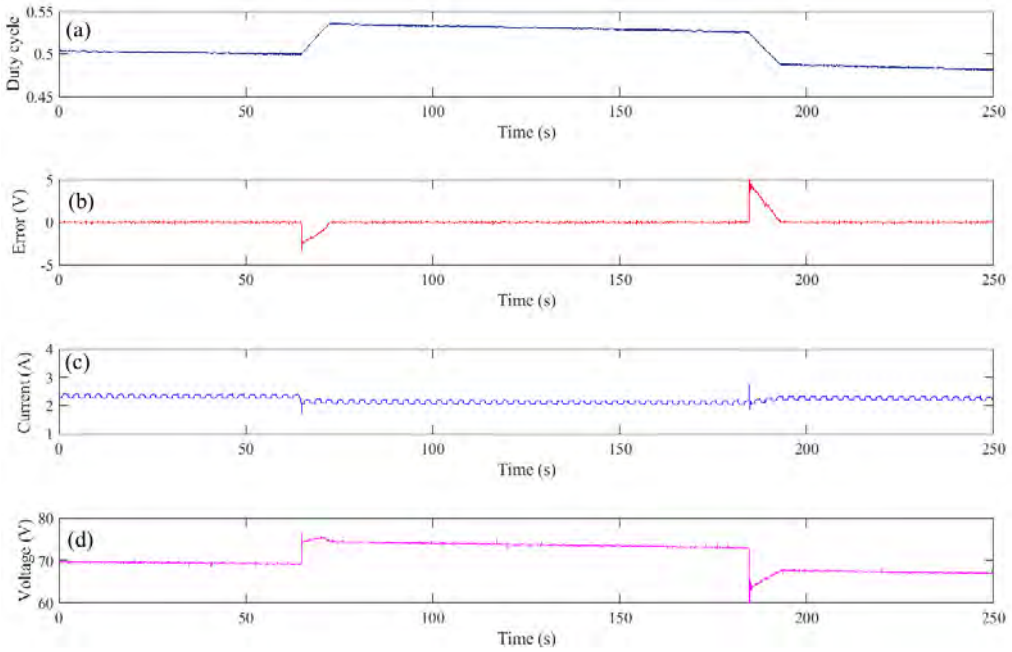

Figure 10.22: MPPT based on RNN and FLC: (**a**) Duty cycle; (**b**) Error; (**c**) Boost converter output current (I_{out}); (**d**) Boost converter output voltage (V_{out}).

MPP tracking controllers, FLC performs better in terms of chattering reduction since the current ripple amplitude is less than 0.1 A as displayed in Figure 10.21(b). This is also clearly presented in the voltage signal of Figure 10.21(c) which is almost vanished in comparison with the chattering voltage of the previous controllers. The ripples that appears in the load resistance of Figure 10.21(a) are consequence of an electrical relation of the output current and voltage (Figure 10.22(c) and Figure 10.22(d)) since the programmable resistance lacks direct measurement. One disadvantage of the FLC found in the experiments when compared to the previous tracking controllers was its lack of robustness when facing sharp load variations. Hence, for both increasing and decreasing the load resistance, it takes around 10 s to reach the desired tracking value.

10.6. Recurrent neural networks (RNN) for tracking the MPP

The implementation of the MPPT based RNN is shown in Figure 10.23. A MicroLabBox dSPACE DS1202 also was used for the acquisition and control signal generation. This device has various channels for the communication with the host PC and the converter. The configuration of these channels can be made via its real-time-interface libraries. Additional equipment such as the irradiation and temperature sensors, as well as the ControlDesk software for the visualisation, were also used in the experiments.

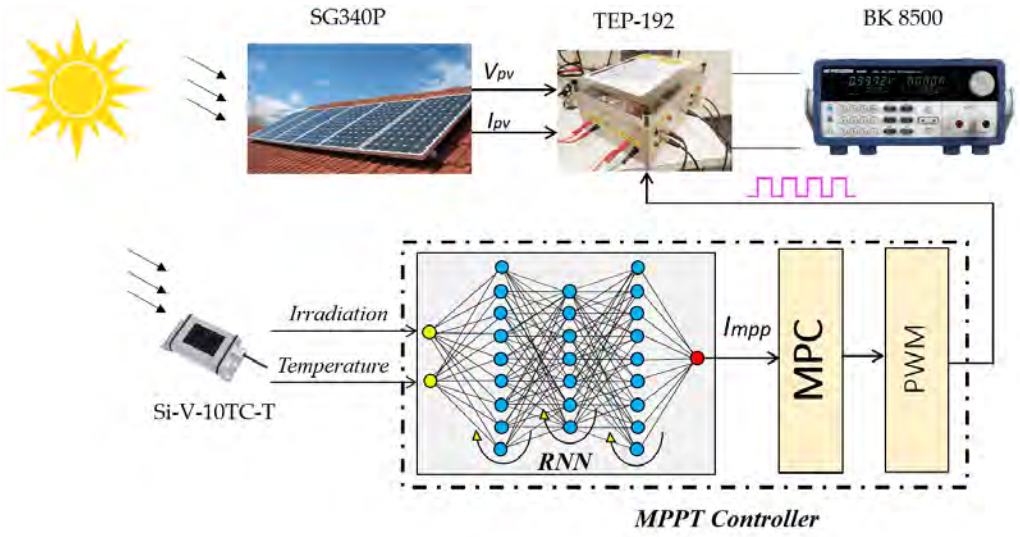

Figure 10.23: Implementation architecture of the MPPT controller.

The RNN is a class of artificial neural networks that uses information from the previous iteration to ameliorate the performance of the NN in current and future inputs. In comparison with other networks, it can be said that RNN is unique because is the only network that contains a hidden state (memory) and loops. This

structure allows the RNN to store past information in the hidden state and operate on sequences. In other words, it gets part of its output as an input for the next time step. These features are well suited for solving different problems with sequential data of varying length. Different RNN architectures such as, fully recurrent (FRNN), long short-term memory (LSTM), gated recurrent units (GRUs), etc., have been introduced in the last decades. Due to its simplicity, RNN configuration have been used in many filtering and modeling applications. The hidden layer and the output of the RNN can be calculated using Equation (10.3).

$$h_t = \sigma_h(W_h x_t + U_h h_{t-1} + b_h) \tag{10.3}$$

$$y_t = \sigma_y(W_y h_t + b_y) \tag{10.4}$$

Where x_t, h_t, y_t, are respectively, the input vector, the hidden layer vector, and the output vector; W, U, and b, are parameter matrices and vector; σ_h and σ_y are activation functions, respectively, given in Equation (10.5) and (10.6) .

$$\sigma_h(x) = \frac{2}{1 + e^{-2x}} - 1 \tag{10.5}$$

$$\sigma_y(x) = x \tag{10.6}$$

To train the RNN model, we selected the temperature and irradiation as two input feature vectors while the output is the reference current vector I_{mpp} that corresponds to the ongoing of the MPP. The dataset used in this work contains 796 normalized samples where 70% was used for the training, 15% for the validation and 15% for the test. Different training algorithms were checked so as to obtain an accurate model. Finally, we set the configuration of the LRN with the following parameters: training algorithm = Levenberg-Marquardt (LM), learning rate = 0.1, hidden layers = 2, neurons = 41, maximum epochs = 5000. The training performance was measured using mean square error (MSE, defined in Equation (10.7)), where the error is the difference between the predicted output and the the target, and N is the number of training data. The predicted output, the target and the error are presented in Figure 10.24.

$$MSE = \frac{1}{N}\sum_{i=0}^{N}(e_i)^2 \tag{10.7}$$

The performance of the trained model can be analysed using the regression values presented in Figure 10.25; where R represents the output-target relationship, which is ranged between 0 and 1 (0: low accuracy, 1: ideal accuracy). According to Figure 10.25, it is clear that the obtained RNN model is characterised by high prediction accuracy since the R values for training, validation and test are, respectively equal to 0.99566, 0.99521 and 0.9936.

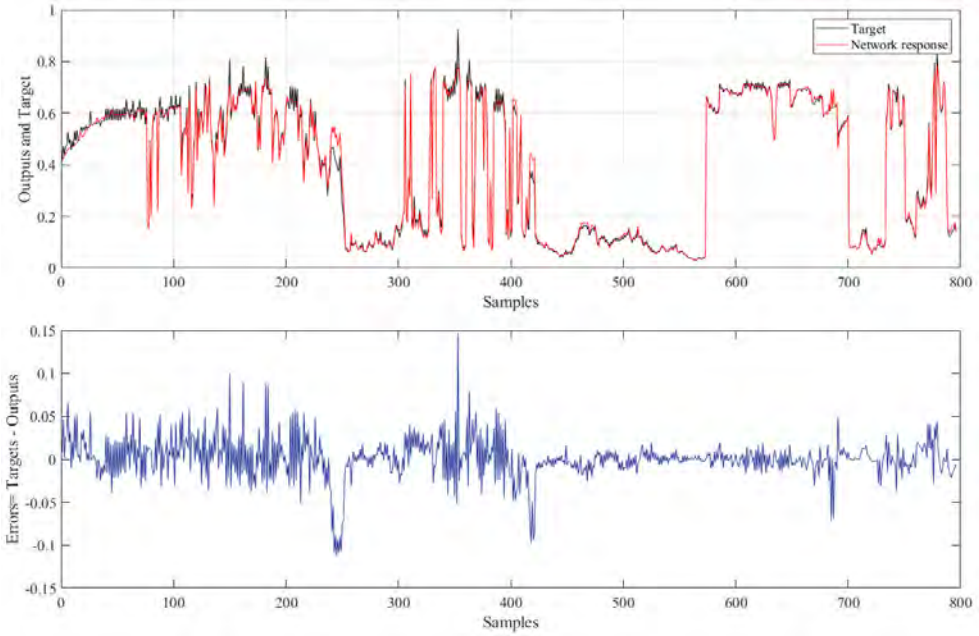

Figure 10.24: Predicted outputs results.

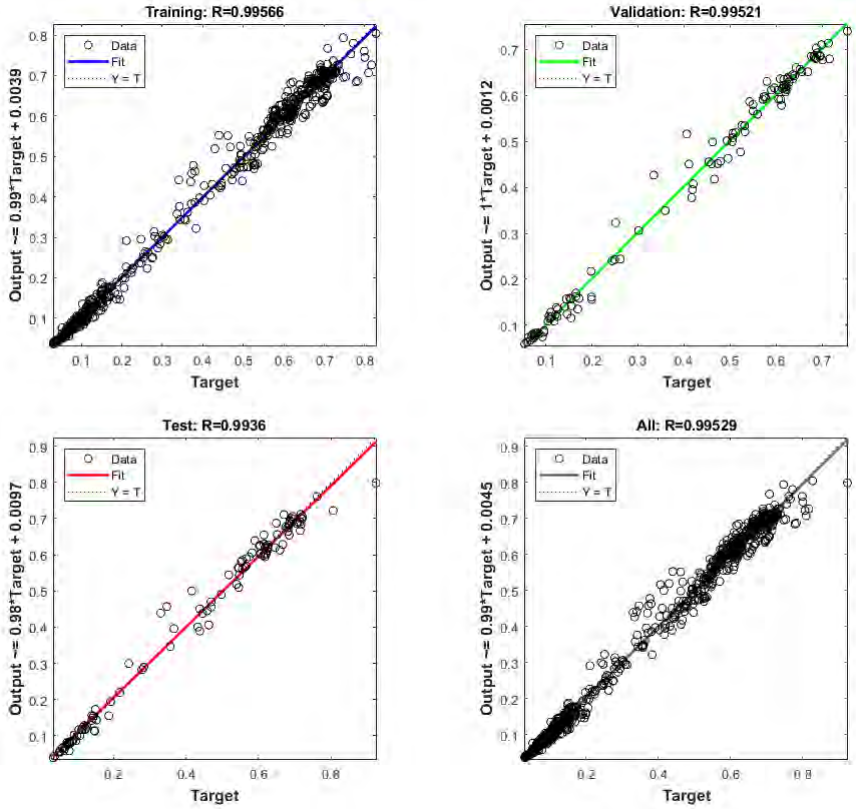

Figure 10.25: Performance analysis of the predicted LRN model.

The characteristics of the current corresponds to the MPP for each temperature and irradiation, that are plotted in Figure 10.26. According to this figure, it is

noticeable that the highest currents (yellow area) are found at high irradiation and low temperature, a reduction in the current can be occurred via an increase in temperature or via a decrease in irradiation. Besides, the results from this figure show that the current is hardly affected by the irradiation in comparison with the temperature. Hence, for a constant irradiation and by increasing the temperature from 0 °C to 50 °C, the current of the maximum power is decreased around 2 A. On the other hand, for a constant temperature and by decreasing the irradiation from 900 W/m^2 to 100 W/m^2, the current of the maximum power is decreased around 7 A.

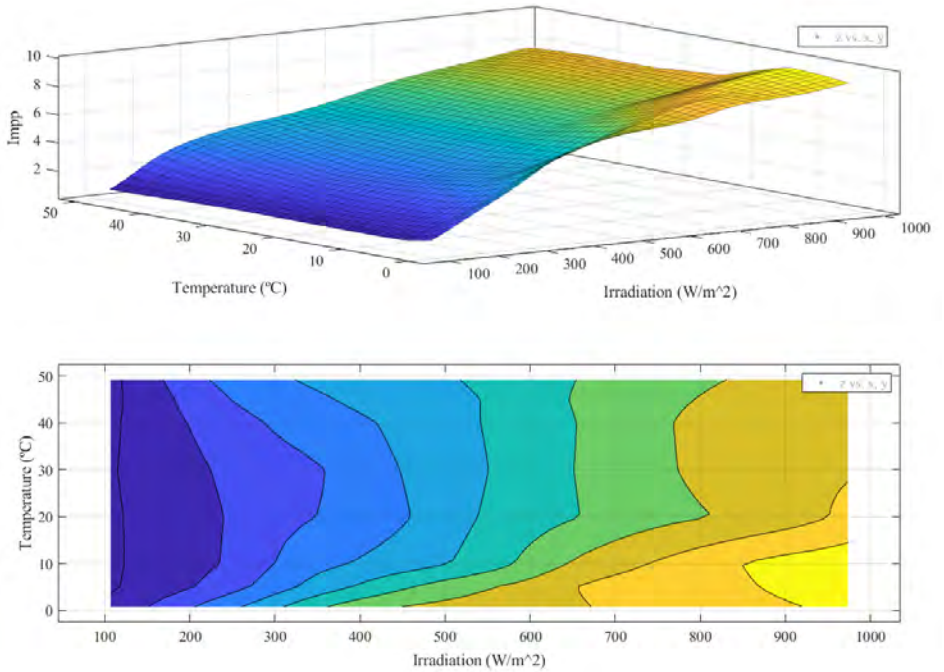

Figure 10.26: *Irradiation − Temperature − Current* characteristic surface of the MPP.

The results of the MPC tracking method are presented in Figure 10.27, Figure 10.28 and Figure 10.29. Figure 10.27 exhibits the irradiation, temperature, predicted current, voltage and power that corresponding to the MPP, while the performance of the MPC for tracking the I_{mpp} are exhibited in Figure 10.28 and Figure 10.29. Despite that the experiments of the MPC was conducted under wide variation of irradiation, Figures 10.27 proves the effectiveness of the RNN model to track I_{mpp}. Hence, it is clearly presented in Figure 10.27(c) that the predicted current fluctuates in the same way as the irradiation signal (displayed in Figure 10.27(a)). Moreover, the characteristic of the predicted power shown in Figure 10.27(d) is equivalent with the characteristic of the MPP previously shown in Figure 10.6. For instance, at $t = 50\ s$, the values extracted from Figure 10.27 for irradiation, temperature, current, voltage and power, are almost equal to the MPP characteristic values of the orange curve of Figure 10.6.

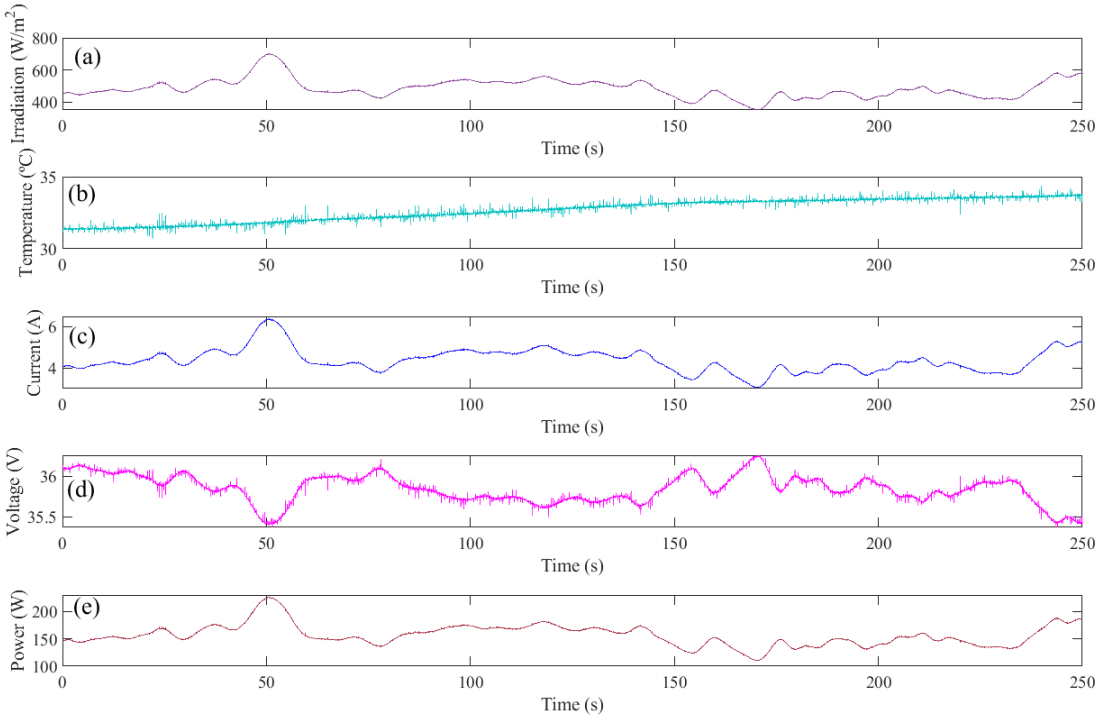

Figure 10.27: MPPT based on RNN and MPC: (**a**) Irradiation (W/m^2); (**b**) Temperature (°C); (**c**) PV current; (**d**) PV voltage; (**e**); (**f**) PV power.

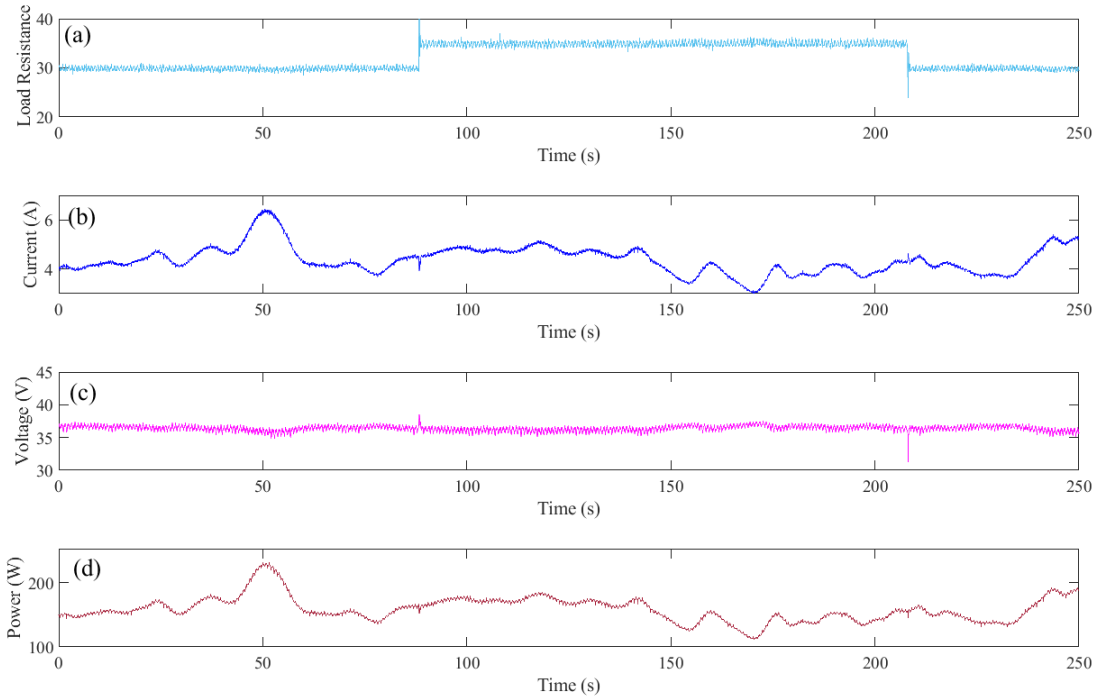

Figure 10.28: MPPT based on RNN and MPC: (**a**) Load Resistance (V_{out}/I_{out}); (**b**) PV current; (**c**) PV voltage; (**d**) PV power.

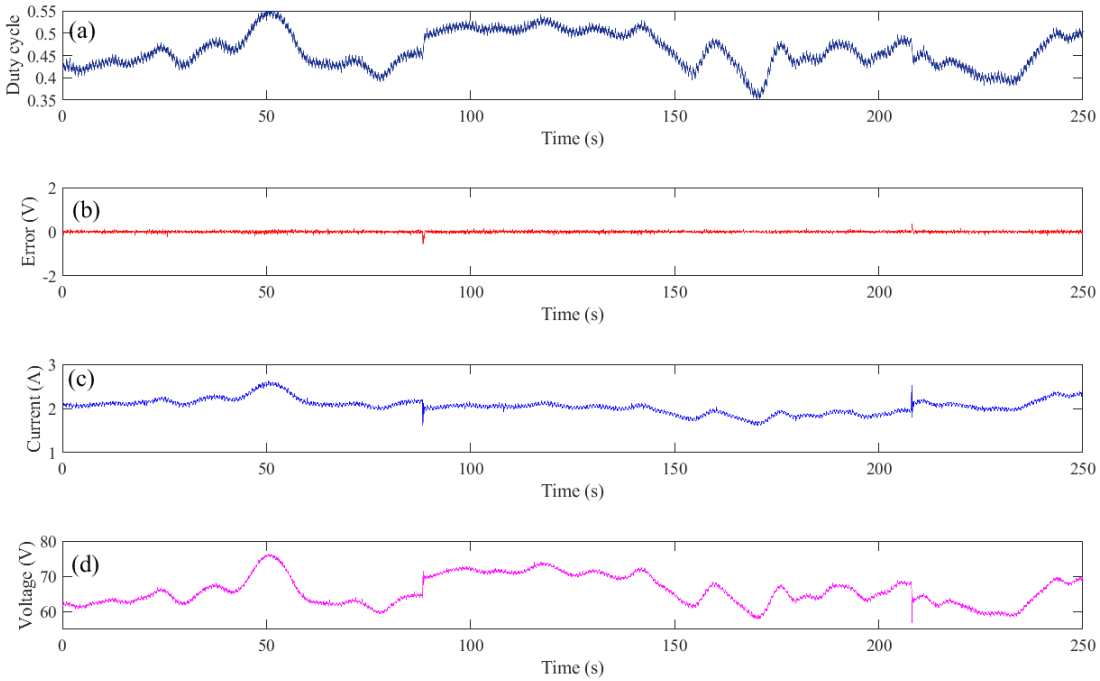

Figure 10.29: MPPT based on RNN and MPC: (**a**) Duty cycle; (**b**) Error; (**c**) Boost converter output current (I_{out}); (**d**) Boost converter output voltage (V_{out}).

10.7. Conclusion

This chapter presented an analysis of a real PEMFC and PV systems, the objective of which was to track the MPP for performance improvement. Because the variation of the inputs, such as stack temperature, PV temperature and radiation, non-linearities were reflected within the surroundings.

For the case of the PV system, four controllers were designed and tested. The tests were carried with variable load to check each controller capabilities. The P&O algorithm, commonly used in MPPT, was chosen and implemented despite exhibiting several problems that were pinpointed, such as falling in a local MPP, which is linked to chattering, which in turn leads to an increase of the energy consumption of the system. As a consequence, if the amplitude is sufficiently large (like in the experiments), over–undershoots due to external resistance changes are faded. In a second step, an SMC was embedded with the proposed RVE, where the overshoots were fairly visible and the chattering amplitude was three times lower in comparison to that of P&O. However, to improve the chattering reduction, an advanced FLC type-1 was developed and embedded, which produced a significant improvement in comparison to P&O and FLC. The chattering of the controlled voltage decreased by several orders of magnitude and, as a consequence, over–undershoots were unveiled. The contrast in terms of the error with SMC showed that the FLC has a slower correction, although the ripple amplitude is reduced significantly. The last tested

controller was MPC which was embedded with the proposed RNN. In this sense, the results showed outstanding performance in resemblance to the former structures. With a simple configuration that could avoid the computational saturation of the hardware, the outcomes displayed high accuracy and robustness.

For the case of the PEM fuel cell, a high order sliding mode based RCE was designed and tested on a FC-42 Evaluation Kit 360W. The obtained results have proven the success of the proposed method in extracting the maximum power from the FC-42 with high tracking performance. Robustness, high tracking accuracy, good dynamic behavior, and global system stability are obtained even under large load variation.

Finally, since the MPPT methods are significantly important for clean energy sources such as PEIMAR SG340 and Heliocentric FC-42 Evaluation Kit, this chapter may pave the way for more progressing and sophisticated research on this topic.

Chapter 11

Conclusions and future perspectives

11.1. Conclusions and contributions

The main achievements and conclusions reached in this thesis are summarized below:

The thesis starts with reviewing the state of the art of controllers applied for PEM fuel cell systems. The review was mainly divided into two parts including the linear and nonlinear controllers. The features and drawbacks of each of these two types also has been briefly illustrated.

As a second step, The proton exchange membrane fuel cell system has been studied in depth. Subjects like the basics, advantages, drawbacks etc., have been clearly explained. After these explanations, the fuel cell was meddled based on mathematical equations. Two parts were studied, the static and the dynamic model. It was found that suffer from three main loses which are the activation, ohmic and concentration loss. The first mentioned is due to the reaction kinetics at the electrode of the PEMFC and its amount is important at low current densities. The second loss is derived from the impedance of the membrane and the resistance of the construction materials such the collecting plates and the carbon electrodes. The third loss is occurred due to the propagation of ions through the electrolyte membrane which leads to the lack of reactants mass transfer at the electrode. However, these losses can be reduced by selecting an appropriate operating power point.

By studying the efficiency of the fuel cell 50W which constructed by Heliocentric, it was found that the operating power point that keeps the fuel cell working at its maximum efficiency is the the power point at which the stack current between 1 and 2A. On the other hand, the effect of temperature and hydrogen on the fuel cell efficiency are studied based on the mathematical model and it has been proven that the efficiency can improve by increasing the cell temperature and input fuel

To obtain high accurate model, artificial neural networks ANNs have been used for modeling the fuel cell. Due to the several input variations of the PEMFC, such as stack temperature, humidity and oxygen, which results in nonlinearities and high model complexity, extensive tests with various ANN parameters were required to predict an efficient model. Since the ANN model requires a large data-set, an efficient automatic method was designed to simplify and facilitate the data collection. This

was obtained by generating a triangular signal which varies the duty cycle of the power converter that was inserted between the stack and the load. An experimental data-set composed of 20,512 samples over a wide operating range (different operating current, temperature and fan power) of a commercial stack was recorded and saved for the training process.

Different structures of feed-forward neural network perceptron with backpropagation learning rule were tested to predict the performance of the Heliocentric FC50 fuel cell system. A comparison study including various ANN parameters such as the training algorithm, the number of hidden layers and the number of neurons at each layer was made to obtain the highest accurate model. Finally, an accurate model composed of 3 hidden layers and 90 neurons trained by BR algorithm was used for a comparison study with the real results.

The next step of the thesis was focused on studying the power converter since it is required for the experimental system. Hence, one chapter was focused on the power converter where the most used types including buck, boost, buck-boost,SEPIC, Zeta and Cuk, were introduced and studied mathematically. A comparison was done using key design parameters such as type of input and output current, efficiency, and number of components. It was found that each type of the studied topologies presents advantages and drawbacks. The boost converter is used when the source has low voltage. It characterised by few number of components which reduce its cost as well as resulting in high efficiency. However its pulsed output current still represents an obstacle for many applications. The Zeta and Cuk topologies could replace the boost converter and they provide smooth and continuous output current. However, Zeta and Cuk are characterised by large number of components which leads to increase their cost and lower their efficiency. Moreover, the Cuk provides reversed output polarity. On the other hand, the buck converter is used when the source has low voltage. As the boost converter, the buck is also characterised by few number of components which reduce its cost, leads to simplicity and high efficiency. one drawback of the buck topology is its pulsed input current. Other topologies that can replace the buck converter and overcome this drawback are the SEPIC and the Cuk. However, the SEPIC provides pulsed output current which is another drawback, and the Cuk generates reversed reversed output polarity. Moreover, both of the SEPIC and Cuk needs for twice inductors and a large energy transfer capacitor which leads to higher cost and lower efficiency. The buck-boost converter is used when the source voltage could be high or low. As the buck and the boost topologies, the buck-boost is characterised by few number of components, simplicity and high efficiency. However, its reversed output voltage polarity as well as its pulsed input and output current are its main drawbacks. The SEPIC, Zeta and the Cuk topologyies can replace the back-boost and they can provide smooth and continuous output current. However, as early explained the main obstacles of these topologies are the cost, the complexity and lower efficiency.

To study the performance of the PEMFC, An experimental 50-W PEMFC Instruc-

tor system feeding load resistances through step-up DC–DC power converters has been used in this research. The effect of temperature on the PEM fuel cell stack performance was studied for for both, simulation and experimental work, and for low, medium and high humidification. At low humidification, it was obtained that the performance of the stack improves for low temperatures (from $T = 25\,°C$ until $T = 31\,°C$) and deteriorates for temperatures up to $31\,°C$. At medium and high humidification, it was obtained that the stack performance improves with increasing temperature. However the effect of temperature is clearly pronounced at higher humidification since the increase of temperature results in a large increasing in the stack performance.

The second part of this thesis was focused in the control methods that can be used for tracking improvements in a fuel cell system. Robust sliding mode controllers like conventional sliding mode control (CSMC), proportional integral sliding mode control (ISMC), integral terminal sliding mode control (ITSMC), integral fast terminal sliding mode control (IFTSMC) and integral fast terminal SMC combined with quick reaching law (IFTSMC-QRL), were used as a first attempt to improve the tracking performance. These algorithms were implemented and contrasted with novel designs to highlight the features that could define the effectiveness of each in different scenarios such as constant and dynamic change following. An assembled test rig with a commercial PEMFC from Heliocentric with a boost converter were used to evaluate each structure in a dSpace DS1102. The PEMFC can be controlled through a PWM signal generator that belongs to the converter, and this was managed by a proper designed controller. To test the performance of the controllers, the reference was established as two load changes at 25 s and 45 s where in the first one, the resistance shifted from 20 Ω to 50 Ω and in the second step regressed to 20 Ω. The experimental results showed that during the dynamic changes, the five proposed techniques have shown high robustness against variations of the load resistance. It was found that the IFTSMC-QRL has the superior performance in terms of accuracy (steady state oscillation) over the other algorithms. Moreover, it shows faster response and better robustness over the ISMC, ITSMC, and IFTSMC. On the other hand, although the conventional SMC provides higher robustness over the terminal sliding modes, its chattering effect is still one of its drawbacks.

High order sliding mode controllers also have been used in this thesis since thy keeps the same advantages of the conventional SMC while they reduces its main drawbacks which is the chattering phenomenon. Hence, five types of high order sliding mode control including twisting algorithm (TA), super twisting algorithm (STA), prescribed convergence law algorithm (PCL), quasi-continuous algorithm (QCA) and drift algorithm (DA) have been designed and implemented for a Heliocentric commercial PEMF. The same load variations as with the conventional SMC were used. The experimental results showed that during the dynamic changes, the five proposed techniques have shown high capability to reduce the chattering phenomenon while providing high robustness against variations of the load resistance. It was

found that the DA has the superior performance in terms of accuracy and robustness over the TA, PCL, QCA and STA; while this latter has the lowest response time over the rest of algorithms.

Alternative algorithms like proportional integral (PI), fuzzy logic control (FLC), module predictive control (MPC) and back-stepping control (BSC) also have been designed and implemented for the Heliocentric commercial PEMF. It was found that when comparing to the conventional PI controller, the other techniques have shown high capability to reduce the response time while providing high robustness against variations of the load resistance. However, the advantages and drawbacks are varied from one algorithm to another. In terms of overshoots and undershoots, the FLC showed the highest performance but the response time and the steady state oscillation are not the best when comparing to other algorithms. The performance of the MPC are quite near to the the FLC one. It has better convergence speed but the overshoots and undershoots are higher. Regarding the BSC, it has the best results in terms of steady state oscillation since it shows the lowest value with the PI controller over the rest of algorithms. However, in spite of reducing the response time of the PI by 50 %, this value still higher when comparing to the other algorithms.

Finally, the thesis ends with different maximum power point tracking methods applied on PEM fuel cell and PV system. Novel MPPT techniques such as reference voltage estimator, reference current estimator and recurrent neural networks were designed and implemented in real time. For the PV case, and under the weather conditions available during experiments and available hardware, it was shown that MPC under a simple settle, can provide the best results in comparison with P&O, FLC, and SMC. Regarding the case of PEM fuel cell, the obtained results of the HO-PCL based RCE have proven the success of the proposed method in extracting the maximum power from the FC-42 with high tracking performance.

11.2. Future perspectives

After the contribution made in this thesis, the following are proposed as future perspectives of work:

- Analyze other types of neural networks, with special attention to the new paradigms, to analyze if they could have a better behavior.
- Develop new models that allow predicting the fuel cell electrical characteristics when the input hydrogen is not controlled by the manufacture.
- Analyse and study the effect of the hydrogen on the performance of the membrane.
- Within the section of sliding mode control, an optimised SMC based neural networks or fuzzy logic can be performed.

- Within the section of high order SMC, third order sliding mode can be a good option to obtain high performance in terms of chattering reduction.
- Although their high computational resources, intelligent techniques are very encouraged as alternatives control methods.
- The application of the studied algorithms in a complete hybrid system also can be expected.

Chapter 12

Conclusiones y perspectivas de futuro

12.1. Conclusiones y aportes

Los principales logros y conclusiones alcanzados en esta tesis se resumen a continuación:

La tesis comienza con la revisión del estado del arte de los controladores aplicados a los sistemas de pilas de combustible PEM. La revisión se dividió principalmente en dos partes, incluidos los controladores lineales y no lineales. Las características y desventajas de cada uno de estos dos tipos también se han ilustrado brevemente.

Como segundo paso, se ha estudiado en profundidad el sistema de pila de combustible de membrana de intercambio de protones. Temas como los conceptos básicos, ventajas, inconvenientes, etc., se han explicado claramente. Después de estas explicaciones, la celda de combustible se modelizó en base a ecuaciones matemáticas. Se estudiaron dos partes, el modelo estático y el dinámico. Se encontró que sufren tres pérdidas principales que son pérdida de activación, óhmica y de concentración. La primera mencionada se debe a la cinética de reacción en el electrodo de la PEMFC y su cantidad es importante a bajas densidades de corriente. La segunda pérdida se deriva de la impedancia de la membrana y la resistencia de los materiales de construcción, como las placas colectoras y los electrodos de carbón. La tercera pérdida se produce debido a la propagación de iones a través de la membrana del electrolito, lo que conduce a la falta de transferencia de masa de los reactivos en el electrodo. Sin embargo, estas pérdidas se pueden reducir seleccionando un punto de alimentación operativo adecuado.

Al estudiar la eficiencia de la pila de combustible de 50 W construida por Heliocentris, se descubrió que el punto de potencia operativo que mantiene la pila de combustible funcionando con su máxima eficiencia es el punto de potencia en el que la corriente de pila está entre 1 y 2 A. Por otro lado, se ha estudiado el efecto de la temperatura y el hidrógeno en la eficiencia de la celda de combustible con base en el modelo matemático y se ha probado que la eficiencia puede mejorar aumentando la temperatura de la celda y el combustible de entrada.

Para obtener un modelo de alta precisión, se han utilizado redes neuronales artificiales ANN para modelar la celda de combustible. Debido a las diversas variaciones de entrada del PEMFC, como la temperatura , la humedad y el oxígeno,

lo que da como resultado no linealidades y una alta complejidad del modelo, se requirieron pruebas exhaustivas con varios parámetros ANN para predecir un modelo adecuado. Dado que el modelo ANN requiere un gran conjunto de datos, se diseñó un método automático para simplificar y facilitar la recopilación de datos de forma eficiente. Esto se obtuvo generando una señal triangular que varía el ciclo de trabajo del convertidor de potencia que se insertó entre la pila y la carga. Se registró y guardó para el proceso de entrenamiento un conjunto de datos experimentales compuesto por 20.512 muestras en un amplio rango operativo (diferentes corrientes operativas, temperatura y potencia del ventilador) de una pila comercial.

Se probaron diferentes estructuras de perceptrón de red neuronal de avance con regla de aprendizaje de retropropagación para predecir el rendimiento del sistema de la celda de combustible Heliocentric FC50. Se realizó un estudio de comparación que incluyó varios parámetros ANN, como el algoritmo de entrenamiento, la cantidad de capas ocultas y la cantidad de neuronas en cada capa para obtener el modelo más preciso. Finalmente, se utilizó un modelo preciso compuesto por 3 capas ocultas y 90 neuronas entrenadas por el algoritmo BR para un estudio de comparación con los resultados reales.

El siguiente paso de la tesis se centró en estudiar el convertidor de potencia que se requiere para el sistema experimental. Por lo tanto, un capítulo se centró en el convertidor de potencia donde se introdujeron y estudiaron matemáticamente los tipos más utilizados, incluidos buck, boost, buck-boost, SEPIC, Zeta y Cuk. Se realizó una comparación utilizando parámetros clave de diseño, como el tipo de corriente de entrada y salida, la eficiencia y la cantidad de componentes. Se encontró que cada tipo de topología estudiada presenta ventajas e inconvenientes. El convertidor elevador se usa cuando la fuente tiene bajo voltaje. Se caracteriza por un número reducido de componentes que reducen su costo además de resultar en una alta eficiencia. Sin embargo, su corriente de salida pulsada todavía representa un obstáculo para muchas aplicaciones. Las topologías Zeta y Cuk podrían reemplazar el convertidor elevador y proporcionan una corriente de salida suave y continua. Sin embargo, Zeta y Cuk se caracterizan por tener una gran cantidad de componentes, lo que conduce a un aumento de su costo y a una disminución de su eficiencia. Además, el Cuk proporciona polaridad de salida invertida. Por otro lado, el convertidor reductor se usa cuando la fuente tiene bajo voltaje. Como convertidor boost, el buck también se caracteriza por unos pocos componentes que reducen su costo, conducen a la simplicidad y alta eficiencia. un inconveniente de la topología reductora es su corriente de entrada pulsada. Otras topologías que pueden sustituir al convertidor reductor y superar este inconveniente son el SEPIC y el Cuk. Sin embargo, el SEPIC proporciona corriente de salida pulsada, que es otro inconveniente, y el Cuk genera una polaridad de salida invertida. Además, tanto SEPIC como Cuk necesitan el doble de inductores y un gran condensador de transferencia de energía, lo que conduce a un mayor costo y una menor eficiencia. El convertidor reductor-elevador se usa cuando el voltaje de la fuente puede ser alto o bajo. Al igual que las topologías buck y boost, la buck-boost

se caracteriza por un número reducido de componentes, simplicidad y alta eficiencia. Sin embargo, su polaridad de voltaje de salida invertida, así como su corriente de entrada y salida pulsada, son sus principales inconvenientes. Las topologías SEPIC, Zeta y Cuk pueden reemplazar el buck-boost y pueden proporcionar una corriente de salida suave y continua. Sin embargo, como se explicó anteriormente, los principales obstáculos de estas topologías son el costo, la complejidad y la menor eficiencia.

Para estudiar el rendimiento del PEMFC, en esta investigación se ha utilizado un sistema de Instructor PEMFC experimental de 50 W que alimenta resistencias de carga a través de convertidores de potencia CC-CC elevadores. Se estudió el efecto de la temperatura en el rendimiento de la pila de celdas de combustible PEM tanto para simulación como para trabajo experimental, y para humidificación baja, media y alta. A baja humidificación se obtuvo que el desempeño de la pila de combustible mejora para bajas temperaturas (desde T=25 °C hasta T=31 °C) y se deteriora para temperaturas de hasta 31 °C. A media y alta humidificación se obtuvo que el rendimiento de la pila mejora con el aumento de la temperatura. Sin embargo, el efecto de la temperatura es claramente pronunciado a mayor humidificación ya que el aumento de la temperatura da como resultado un gran aumento en el rendimiento de la pila de combustible.

La segunda parte de esta tesis se centró en los métodos de control que se pueden utilizar para realizar un buen seguimiento en un sistema de pila de combustible. Controladores de modo deslizante robustos como control de modo deslizante convencional (CSMC), control de modo deslizante integral proporcional (ISMC), control de modo deslizante de terminal integral (ITSMC), control de modo deslizante de terminal rápido integral (IFTSMC) y SMC de terminal rápido integral combinado con ley de alcance rápido (IFTSMC-QRL), se utilizaron como un primer intento de mejorar el rendimiento del seguimiento. Estos algoritmos se implementaron y contrastaron con diseños novedosos para resaltar las características que podrían definir la efectividad de cada uno en diferentes escenarios, como el seguimiento de cambios constantes y dinámicos. Se utilizó un equipo de prueba ensamblado con un PEMFC comercial de Heliocentric con un convertidor elevador junto a un sistema de control en tiempo real dSPACE DS1102. El PEMFC se puede controlar a través de una señal PWM que alimenta al convertidor, y está señal PWM se genera en el dSPACE DS1102 mediante una estrategia de control adecuada. . Para probar el desempeño de los controladores, la referencia se establecieron dos cambios de carga a los 25 s y 45 s, donde en el primero, la resistencia pasó de 20 Ohm a 50 Ohm y en el segundo paso retrocedió a 20 Ohm. Los resultados experimentales mostraron que durante los cambios dinámicos, las cinco técnicas propuestas han mostrado alta robustez frente a variaciones de la resistencia de carga. Se encontró que el IFTSMC-QRL tiene un rendimiento superior en términos de precisión (oscilación de estado estable) sobre los otros algoritmos. Además, muestra una respuesta más rápida y una mejor robustez sobre ISMC, ITSMC e IFTSMC. Por otro lado, aunque el SMC convencional proporciona una mayor robustez sobre los modos deslizantes del terminal, su efecto

de oscilación sigue siendo uno de sus inconvenientes.

Los controladores de modo deslizante de alto orden también se han utilizado en esta tesis ya que mantienen las mismas ventajas del SMC convencional mientras reducen su principal inconveniente, que es el fenómeno de oscilación. Por lo tanto, se han diseñado e implementado cinco tipos de controles deslizantes de alto orden, incluido el algoritmo twisting (TA), el algoritmo de súper twisting (STA), el algoritmo de ley de convergencia prescrita (PCL), el algoritmo cuasi continuo (QCA) y el algoritmo drift (DA). Se utilizaron las mismas variaciones de carga que con el SMC convencional. Los resultados experimentales mostraron que durante los cambios dinámicos, las cinco técnicas propuestas han demostrado una gran capacidad para reducir el fenómeno de oscilación al tiempo que proporcionan una gran robustez frente a las variaciones de la resistencia de carga. Se encontró que el DA tiene un rendimiento superior en términos de precisión y robustez sobre el TA, PCL, QCA y STA; mientras que este último tiene el tiempo de respuesta más bajo sobre el resto de algoritmos.

También se han diseñado e implementado algoritmos alternativos como proporcional-integral (PI), control de lógica difusa (FLC), control predictivo (MPC) y control backstepping (BSC) para la PEMFC. Se encontró que, en comparación con el controlador PI convencional, las otras técnicas han demostrado una gran capacidad para reducir el tiempo de respuesta, al tiempo que proporcionan una gran robustez frente a las variaciones de la resistencia de carga. Sin embargo, las ventajas y desventajas varían de un algoritmo a otro. En términos de sobreimpulsos y subimpulsos, el FLC mostró el rendimiento más alto, pero el tiempo de respuesta y la oscilación de estado estable no son los mejores en comparación con otros algoritmos. El rendimiento del MPC está bastante cerca del FLC. Tiene una mejor velocidad de convergencia, pero los sobreimpulsos y los subimpulsos son mayores. En cuanto al BSC, es el que mejores resultados tiene en términos de oscilación en estado estacionario ya que muestra el valor más bajo con el controlador PI sobre el resto de algoritmos. Sin embargo, a pesar de reducir el tiempo de respuesta del PI en un 50 %, este valor aún es mayor al compararlo con los demás algoritmos.

Finalmente, en esta tesis también se proponen diferentes métodos de seguimiento del punto de máxima potencia aplicados a celdas de combustible PEM y a sistemas fotovoltaicos. Se diseñaron e implementaron en los sistemas experimentales métodos MPPT modernos y avanzados, como el estimador de voltaje de referencia (RVE), el estimador de corriente de referencia (RCE) y las redes neuronales recurrentes (RNN). Para el caso de PV, y bajo las condiciones climáticas disponibles durante los experimentos y el hardware disponible, se demostró que MPC empleando una predicción de un paso es capaz de proporcionar los mejores resultados en comparación con P&O, FLC y SMC. En cuanto al caso de la pila de combustible PEM, los resultados obtenidos del RCE basado en HO-PCL han demostrado el éxito del método propuesto para extraer la máxima potencia del FC-42 con un alto rendimiento de seguimiento.

12.2. Perspectivas de futuro

Tras el aporte realizado en esta tesis, se proponen como futuras perspectivas de trabajo las siguientes:

Analizar otro tipo de redes neuronales, con especial atención a los nuevos paradigmas, para analizar si podrían tener un mejor comportamiento.

Desarrollar nuevos modelos que permitan predecir las características eléctricas de las pilas de combustible cuando el hidrógeno de entrada no está controlado por el fabricante.

Analizar y estudiar el efecto del hidrógeno en el rendimiento de la membrana.

Dentro de la sección de control de modo deslizante, se pueden realizar redes neuronales basadas en SMC optimizadas o lógica difusa. Dentro del apartado de SMC de alto orden, el modo deslizante de tercer orden puede ser una buena opción para obtener un alto rendimiento en términos de reducción de vibraciones.

Por otro lado, a pesar de sus altas necesidades computacionales, las técnicas inteligentes son muy recomendadas como métodos alternativos de control.

También se podría validar la aplicación de los algoritmos estudiados en un sistema híbrido completo.

Bibliography

[1] Irene Romero-Fiances, Emilio Muñoz-Cerón, Rafael Espinoza-Paredes, Gustavo Nofuentes, and Juan de la Casa. Analysis of the performance of various pv module technologies in peru. *Energies*, 12(1):186, 2019.

[2] Alberto Bocca, Luca Bergamasco, Matteo Fasano, Lorenzo Bottaccioli, Eliodoro Chiavazzo, Alberto Macii, and Pietro Asinari. Multiple-regression method for fast estimation of solar irradiation and photovoltaic energy potentials over europe and africa. *Energies*, 11(12):3477, 2018.

[3] Milad Zeraatpisheh, Reza Arababadi, and Mohsen Saffari Pour. Economic analysis for residential solar pv systems based on different demand charge tariffs. *Energies*, 11(12):3271, 2018.

[4] Erik Möllerström. Wind turbines from the swedish wind energy program and the subsequent commercialization attempts–a historical review. *Energies*, 12(4):690, 2019.

[5] Mazhar Hussain Baloch, Dahaman Ishak, Sohaib Tahir Chaudary, Baqir Ali, Ali Asghar Memon, Touqeer Ahmed Jumani, et al. Wind power integration: An experimental investigation for powering local communities. *Energies*, 12(4):1–24, 2019.

[6] Clare Raynard Magoon Jr. *Creation and the Big Bang: How God Created Matter from Nothing*. WestBow Press, 2018.

[7] Aidan M. Smith and Andrew B. Ross. Production of bio-coal, bio-methane and fertilizer from seaweed via hydrothermal carbonisation. *Algal Research*, 16:1–11, 2016.

[8] Omar Guerra, Joshua Eichman, J. Kurtz, and Bri-Mathias Hodge. Cost competitiveness of electrolytic hydrogen. *Joule*, 3, 07 2019.

[9] DC Choudhury and David W Kraft. Big bang nucleosynthesis and the missing hydrogen mass in the universe. In *AIP Conference Proceedings*, volume 698, pages 345–348. American Institute of Physics, 2004.

[10] J.M. Andújar and F. Segura. Fuel cells: History and updating. a walk along two centuries. *Renewable and Sustainable Energy Reviews*, 13(9):2309–2322, 2009.

[11] Jonathan Ho, Ewe-Chai Saw, Louis Lu, and John Liu. Technological barriers and research trends in fuel cell technologies: A citation network analysis. *Technological Forecasting and Social Change*, 82:66–79, 02 2014.

[12] E. Weidner, R. Ortiz Cebolla, and J. Davies. Global deployment of large capacity stationary fuel cells. *JRC Technical Reports*, 2019.

[13] Tabbi Wilberforce, Oluwatosin Ijaodola, Emmanuel Ogungbemi, Zaki El Hassan, James Thompson, and Abdul G. Olabi. Effect of bipolar plate materials on performance of fuel cells. In *Reference Module in Materials Science and Materials Engineering*. Elsevier, 2018.

[14] Rony Escobar Yonoff, Guillermo Valencia Ochoa, Yulineth Cardenas-Escorcia, Jorge Iván Silva-Ortega, and Lourdes Meriño-Stand. Research trends in proton exchange membrane fuel cells during 2008–2018: A bibliometric analysis. *Heliyon*, 5(5):e01724, 2019.

[15] Ahmad Mayyas and Margaret Mann. Emerging manufacturing technologies for fuel cells and electrolyzers. *Procedia Manufacturing*, 33:508–515, 2019. Sustainable Manufacturing for Global Circular Economy: Proceedings of the 16th Global Conference on Sustainable Manufacturing.

[16] Phatiphat Thounthong, Pongsiri Mungporn, Serge Pierfederici, Damien Guilbert, and Nicu Bizon. Adaptive control of fuel cell converter based on a new hamiltonian energy function for stabilizing the dc bus in dc microgrid applications. *Mathematics*, 8(11):2035, 2020.

[17] Nicu Bizon and Phatiphat Thounthong. A simple and safe strategy for improving the fuel economy of a fuel cell vehicle. *Mathematics*, 9(6):604, 2021.

[18] Nicu Bizon and Phatiphat Thounthong. Energy efficiency and fuel economy of a fuel cell/renewable energy sources hybrid power system with the load-following control of the fueling regulators. *Mathematics*, 8(2):151, 2020.

[19] Milad Bahrami, Jean-Philippe Martin, Gaël Maranzana, Serge Pierfederici, Mathieu Weber, Farid Meibody-Tabar, and Majid Zandi. Multi-stack lifetime improvement through adapted power electronic architecture in a fuel cell hybrid system. *Mathematics*, 8(5):739, 2020.

[20] Asma Charaabi, Oscar Barambones, Abdelaziz Zaidi, and Nadia Zanzouri. A novel two stage controller for a dc-dc boost converter to harvest maximum energy from the pv power generation. In *Actuators*, volume 9, page 29. Multidisciplinary Digital Publishing Institute, 2020.

[21] Alberto Boschetto, Luana Bottini, Girolamo Costanza, and Maria Elisa Tata. Shape memory activated self-deployable solar sails: small-scale prototypes man-

ufacturing and planarity analysis by 3d laser scanner. In *Actuators*, volume 8, page 38. Multidisciplinary Digital Publishing Institute, 2019.

[22] Suzana Lampreia, Valter Vairinhos, Victor Lobo, and José Requeijo. A statistical state analysis of a marine gas turbine. In *Actuators*, volume 8, page 54. Multidisciplinary Digital Publishing Institute, 2019.

[23] Dominika Matuszewska, Marta Kuta, and Piotr Olczak. Techno-economic assessment of mobilized thermal energy storage system using geothermal source in polish conditions. *Energies*, 13(13):3404, 2020.

[24] Carlos Alberto Vargas and Hector Andres Tinoco. Electrical performance of a piezo-inductive device for energy harvesting with low-frequency vibrations. In *Actuators*, volume 8, page 55. Multidisciplinary Digital Publishing Institute, 2019.

[25] Rodrigo Ai, Luciana LS Monteiro, Paulo Cesar Monteiro, Pedro MCL Pacheco, Marcelo A Savi, et al. Piezoelectric vibration-based energy harvesting enhancement exploiting nonsmoothness. In *Actuators*, volume 8, page 25. Multidisciplinary Digital Publishing Institute, 2019.

[26] Wei Wei, Qiang Li, Fangchao Xu, Xiaoyou Zhang, Junjie Jin, Jiaqi Jin, and Feng Sun. Research on an electromagnetic actuator for vibration suppression and energy regeneration. In *Actuators*, volume 9, page 42. Multidisciplinary Digital Publishing Institute, 2020.

[27] Noureddine Boukrich, Mohamed Derbeli, Maissa Farhat, and Lassaad Sbita. Smart auto-tuned regulators in electric vehicule pmsm drives. In *Green Energy Conversion Systems (GECS), 2017 International Conference on*, pages 1–5. IEEE, 2017.

[28] Mohammed Yousri Silaa, Mohamed Derbeli, Oscar Barambones, and Ali Cheknane. Design and implementation of high order sliding mode control for pemfc power system. *Energies*, 13(17):4317, 2020.

[29] Slah Yaacoubi, Peter McKeon, Weina Ke, Nico F Declercq, and Fethi Dahmene. Towards an ultrasonic guided wave procedure for health monitoring of composite vessels: Application to hydrogen-powered aircraft. *Materials*, 10(9):1097, 2017.

[30] Al-Attar Ali Mohamed, Shimaa Ali, Salem Alkhalaf, Tomonobu Senjyu, and Ashraf M Hemeida. Optimal allocation of hybrid renewable energy system by multi-objective water cycle algorithm. *Sustainability*, 11(23):6550, 2019.

[31] Ibrahem E Atawi, Ahmed M Kassem, and Sherif A Zaid. Modeling, management, and control of an autonomous wind/fuel cell micro-grid system. *Processes*, 7(2):85, 2019.

[32] Tabbi Wilberforce, Abed Alaswad, A Palumbo, Michele Dassisti, and Abdul-Ghani Olabi. Advances in stationary and portable fuel cell applications. *International journal of hydrogen energy*, 41(37):16509–16522, 2016.

[33] Sofia Boulmrharj, Mohammed Khaidar, Mohamed Bakhouya, Radouane Ouladsine, Mostapha Siniti, and Khalid Zine-dine. Performance assessment of a hybrid system with hydrogen storage and fuel cell for cogeneration in buildings. *Sustainability*, 12(12):4832, 2020.

[34] Patrick S Bass, Lin Zhang, Maobing Tu, and ZhongYang Cheng. Enhancement of biodegradable poly (ethylene oxide) ionic–polymer metallic composite actuators with nanocrystalline cellulose fillers. In *Actuators*, volume 7, page 72. Multidisciplinary Digital Publishing Institute, 2018.

[35] Byung Chul Kweon, Joo Seong Sohn, Youngjae Ryu, and Sung Woon Cha. Energy harvesting of ionic polymer-metal composites based on microcellular foamed nafion in aqueous environment. In *Actuators*, volume 9, page 71. Multidisciplinary Digital Publishing Institute, 2020.

[36] Li Fang, Li Di, and Yang Ru. A dynamic model of pem fuel cell stack system for real time simulation. In *2009 Asia-Pacific Power and Energy Engineering Conference*, pages 1–5, 2009.

[37] A. Saadi, M. Becherif, A. Aboubou, and M.Y. Ayad. Comparison of proton exchange membrane fuel cell static models. *Renewable Energy*, 56:64–71, 2013. The International Conference on Renewable Energy: Generation and Applications.

[38] J. C. Amphlett, R. M. Baumert, R. F. Mann, B. A. Peppley, P. R. Roberge, and T. J. Harris. Performance modeling of the ballard mark IV solid polymer electrolyte fuel cell: I . mechanistic model development. *Journal of The Electrochemical Society*, 142(1):1–8, jan 1995.

[39] Mohsen Kandidayeni, Alvaro Macias, Loïc Boulon, and João Pedro F. Trovão. Online modeling of a fuel cell system for an energy management strategy design. *Energies*, 13(14), 2020.

[40] Larminie JE and Andrew Dicks. Fuel cell system explained. 03 2013.

[41] Junbom Kim, Seong-Min Lee, Supramaniam Srinivasan, and Charles Chamberlin. Modeling of proton exchange membrane fuel cell performance with an empirical equation. *Journal of The Electrochemical Society*, 142:2670–2674, 08 1995.

[42] P.R. Pathapati, X. Xue, and J. Tang. A new dynamic model for predicting transient phenomena in a pem fuel cell system. *Renewable Energy*, 30(1):1–22, 2005.

[43] Sharjeel Ansari, Mustafa Khalid, Khurram Kamal, Tahir Abdul Hussain Ratlamwala, Ghulam Hussain, and Mohammed Alkahtani. Modeling and simulation of a proton exchange membrane fuel cell alongside a waste heat recovery system based on the organic rankine cycle in matlab/simulink environment. *Sustainability*, 13:1218, 01 2021.

[44] Gómer Abel Rubio and Wilton Edixon Agila. A fuzzy model to manage water in polymer electrolyte membrane fuel cells. *Processes*, 9(6), 2021.

[45] Bijan Moaveni, Fatemeh Rashidi Fathabadi, and Ali Molavi. Fuzzy control system design for wheel slip prevention and tracking of desired speed profile in electric trains. *Asian Journal of Control*, pages 1–13, 11 2020.

[46] Cristian Napole, Oscar Barambones, Isidro Calvo, Mohamed Derbeli, Mohammed Silaa, and Javier Velasco. Advances in tracking control for piezoelectric actuators using fuzzy logic and hammerstein-wiener compensation. *Mathematics*, 8, 11 2020.

[47] Ying Tian, Qiang Zou, and Jin Han. Data-driven fault diagnosis for automotive pemfc systems based on the steady-state identification. *Energies*, 14(7), 2021.

[48] Jianli Shao, Xin Liu, and Wenqing He. Kernel based data-adaptive support vector machines for multi-class classification. *Mathematics*, 9(9), 2021.

[49] Mohamed Derbeli, Cristian Napole, and Oscar Barambones. Machine learning approach for modeling and control of a commercial heliocentris fc50 pem fuel cell system. *Mathematics*, 9(17):2068, 2021.

[50] Fereshteh Salimi Nanadegani, Ebrahim Nemati Lay, Alfredo Iranzo, J. Antonio Salva, and Bengt Sunden. On neural network modeling to maximize the power output of pemfcs. *Electrochimica Acta*, 348:136345, 2020.

[51] Wafa Torki and Mohamed Derbeli. Modeling and control of a stand-alone pemfc for ac load-pmsm application. In *Green Energy Conversion Systems (GECS), 2017 International Conference on*, pages 1–6. IEEE, 2017.

[52] Mohamed Derbeli, Imen Mrad, Lassaad Sbita, and Oscar Barambones. Pem fuel cell efficiency boosting—robust mpp tracking. In *Renewable Energy Congress (IREC), 2018 9th International*, pages 1–5. IEEE, 2018.

[53] Chun-Liang Lin, Hao-Che Hung, and Jia-Cheng Li. Active control of regenerative brake for electric vehicles. In *Actuators*, volume 7, page 84. Multidisciplinary Digital Publishing Institute, 2018.

[54] En-Ping Chen, Jiangfeng Cheng, Jia-Hung Tu, and Chun-Liang Lin. Sensorless driving/braking control for electric vehicles. In *Actuators*, volume 9, page 22. Multidisciplinary Digital Publishing Institute, 2020.

[55] Simon Hjorth Jessing Lund, Peter Billeschou, and Leon Bonde Larsen. High-bandwidth active impedance control of the proprioceptive actuator design in dynamic compliant robotics. In *Actuators*, volume 8, page 71. Multidisciplinary Digital Publishing Institute, 2019.

[56] Walt Kester, Brian Erisman, and Gurjit Thandi. Section 4 switched capacitor voltage converters. In *Switched Capacitor Voltage Converters. Available online: https://www. analog. com/media/en/training-seminars/design-handbooks/Practical-Design-Techniques-Power-Thermal/Section4. pdf (accessed on 14 November 2020)*.

[57] Fang Lin Luo and Hong Ye. Small signal analysis of energy factor and mathematical modeling for power dc–dc converters. *IEEE Transactions on Power Electronics*, 22(1):69–79, 2007.

[58] António Manuel Santos Spencer Andrade, Everson Mattos, Luciano Schuch, Hélio Leães Hey, and Mario Lúcio da Silva Martins. Synthesis and comparative analysis of very high step-up dc–dc converters adopting coupled-inductor and voltage multiplier cells. *IEEE Transactions on Power Electronics*, 33(7):5880–5897, 2018.

[59] Jason Gu, Ghulam Abbas, Adnan Samad, Muhammad Usman Asad, and Umar Farooq. Set-point tracking of a dc-dc boost converter through optimized pid controllers. In *2016 IEEE Canadian Conference on Electrical and Computer Engineering (CCECE)*, pages 1–5, 05 2016.

[60] Mohamed Derbeli, Maissa Farhat, Oscar Barambones, and Lassaad Sbita. Control of pem fuel cell power system using sliding mode and super-twisting algorithms. *International journal of hydrogen energy*, 42(13):8833–8844, 2017.

[61] José de Jesús Rubio and Adrian Gustavo Bravo. Optimal control of a pem fuel cell for the inputs minimization. *Mathematical Problems in Engineering*, 2014, 2014.

[62] Song-Yul Choe, Jung-Gi Lee, Jong-Woo Ahn, and Soo-Hyun Baek. Integrated modeling and control of a pem fuel cell power system with a pwm dc/dc converter. *Journal of Power Sources*, 164(2):614–623, 2007.

[63] Fatima Zahra Belhaj, Hassan El Fadil, Zakariae El Idrissi, Mohamed Koundi, and Khawla Gaouzi. Modeling, analysis and experimental validation of the fuel cell association with dc-dc power converters with robust and anti-windup pid controller design. *Electronics*, 9(11):1889, 2020.

[64] JM Andujar, F Segura, and MJ Vasallo. A suitable model plant for control of the set fuel cell- dc/dc converter. *Renewable Energy*, 33(4):813–826, 2008.

[65] B. Alharbi, M. Alhomim, and R. McCann. Robust control of dc-dc boost converter by using μ-synthesis approach. *IFAC-PapersOnLine*, 52(4):200–205, 2019.

[66] Mustapha Habib, Farid Khoucha, and Abdelghani Harrag. Ga-based robust lqr controller for interleaved boost dc–dc converter improving fuel cell voltage regulation. *Electr. Power Syst. Res.*, 152:438–456, 2017.

[67] Zhidong Qi, Juntao Tang, Jin Pei, and Liang Shan. Fractional controller design of a dc-dc converter for pemfc. *IEEE Access*, 8:120134–120144, 2020.

[68] KPS Rana, Vineet Kumar, Nitish Sehgal, and Sunitha George. A novel dpdi feedback based control scheme using gwo tuned pid controller for efficient mppt of pem fuel cell. *ISA transactions*, 93:312–324, 2019.

[69] Ahmed Fathy, Mohammad Ali Abdelkareem, AG Olabi, and Hegazy Rezk. A novel strategy based on salp swarm algorithm for extracting the maximum power of proton exchange membrane fuel cell. *International Journal of Hydrogen Energy*, 46(8):6087–6099, 2021.

[70] Nedjem Eddine Benchouia, Abdallah Derghal, Bouziane Mahmah, Belgacem Madi, Lakhdar Khochemane, and Elias Hadjadj Aoul. An adaptive fuzzy logic controller (aflc) for pemfc fuel cell. *International Journal of Hydrogen Energy*, 40(39):13806–13819, 2015.

[71] Sy-Ruen Huang, Chiu-Yue Lin, Chueh-Cheng Wu, and Shin-Joe Yang. The application of fuzzy controller for fuel cell generating studies. *Int. J. Hydrog. Energy*, 33(19):5205–5217, 2008.

[72] Mohamed Derbeli, Lassaad Sbita, Maissa Farhat, and Oscar Barambones. Proton exchange membrane fuel cell—a smart drive algorithm. In *2017 International Conference on Green Energy Conversion Systems (GECS)*, pages 1–5. IEEE, 2017.

[73] Doudou N Luta and Atanda K Raji. Fuzzy rule-based and particle swarm optimisation mppt techniques for a fuel cell stack. *Energies*, 12(5):936, 2019.

[74] K Jyotheeswara Reddy and N Sudhakar. Anfis-mppt control algorithm for a pemfc system used in electric vehicle applications. *International Journal of Hydrogen Energy*, 44(29):15355–15369, 2019.

[75] Abdelghani Harrag and Sabir Messalti. How fuzzy logic can improve pem fuel cell mppt performances? *Int. J. Hydrog. Energy*, 43(1):537–550, 2018.

[76] M. Derbeli, L. Sbita, M. Farhat, and O. Barambones. Proton exchange membrane fuel cell — a smart drive algorithm. In *2017 International Conference on Green Energy Conversion Systems (GECS)*, pages 1–5. IEEE, March 2017.

[77] I. M. Safwat, X. Wu, X. Zhao, and W. Li. Adaptive fuzzy logic control of boost converter fed by stand-alone pem fuel cell stack. In *2017 IEEE Transportation Electrification Conference and Expo, Asia-Pacific (ITEC Asia-Pacific)*, pages 1–6, 2017.

[78] James D. Broesch. Chapter 7 - applications of dsp. In James D. Broesch, editor, *Digital Signal Processing*, pages 125–134. Newnes, Burlington, 2009.

[79] Chrysovalantou Ziogou, Spyros Voutetakis, Michael Georgiadis, and Simira Papadopoulou. Model predictive control (mpc) strategies for pem fuel cell systems: A comparative experimental demonstration. *Chemical Engineering Research and Design*, 131, 02 2018.

[80] Abderezak Lashab, Dezso Sera, and Josep M Guerrero. A dual-discrete model predictive control-based mppt for pv systems. *IEEE Transactions on Power Electronics*, 34(10):9686–9697, 2019.

[81] Naki Güler and Erdal Irmak. Mppt based model predictive control of grid connected inverter for pv systems. In *2019 8th International Conference on Renewable Energy Research and Applications (ICRERA)*, pages 982–986. IEEE, 2019.

[82] Shahram Golzari, Farzan Rashidi, and Hassan Feshki Farahani. A lyapunov function based model predictive control for three phase grid connected photovoltaic converters. *Solar Energy*, 181:222–233, 2019.

[83] Mostafa Ahmed, Mohamed Abdelrahem, and Ralph Kennel. Highly efficient and robust grid connected photovoltaic system based model predictive control with kalman filtering capability. *Sustainability*, 12(11):4542, 2020.

[84] Erdal Irmak and Naki Güler. A model predictive control-based hybrid mppt method for boost converters. *International Journal of Electronics*, 107(1):1–16, 2020.

[85] Omar Abdel-Rahim and Haoyu Wang. A new high gain dc-dc converter with model-predictive-control based mppt technique for photovoltaic systems. *CPSS Transactions on Power Electronics and Applications*, 5(2):191–200, 2020.

[86] Da Xue and Nael H El-Farra. Forecast-triggered model predictive control of constrained nonlinear processes with control actuator faults. *Mathematics*, 6(6):104, 2018.

[87] Wee Chin Wong, Ewan Chee, Jiali Li, and Xiaonan Wang. Recurrent neural network-based model predictive control for continuous pharmaceutical manufacturing. *Mathematics*, 6(11):242, 2018.

[88] Zhihao Zhang, Zhe Wu, David Rincon, and Panagiotis D Christofides. Real-time optimization and control of nonlinear processes using machine learning. *Mathematics*, 7(10):890, 2019.

[89] Helen Durand. Responsive economic model predictive control for next-generation manufacturing. *Mathematics*, 8(2):259, 2020.

[90] Stefan Banholzer, Giulia Fabrini, Lars Grüne, and Stefan Volkwein. Multi-objective model predictive control of a parabolic advection-diffusion-reaction equation. *Mathematics*, 8(5):777, 2020.

[91] Ahmed G Mahmoud A Aziz, Hegazy Rez, and Ahmed A Zaki Diab. Robust sensorless model-predictive torque flux control for high-performance induction motor drives. *Mathematics*, 9(4):403, 2021.

[92] Luis Valverde, Carlos Bordons, and Felipe Rosa. Integration of fuel cell technologies in renewable-energy-based microgrids optimizing operational costs and durability. *IEEE Transactions on Industrial Electronics*, 63(1):167–177, 2016.

[93] T. Hausberger, A. Kugi, A. Eder, and W. Kemmetmüller. High-speed nonlinear model predictive control of an interleaved switching dc/dc-converter. *Control Engineering Practice*, 103:104576, 2020.

[94] Shiyu Yang, Man Pun Wan, Wanyu Chen, Bing Feng Ng, and Swapnil Dubey. Experiment study of machine-learning-based approximate model predictive control for energy-efficient building control. *Applied Energy*, 288:116648, 2021.

[95] K Jyotheeswara Reddy and N Sudhakar. High voltage gain interleaved boost converter with neural network based mppt controller for fuel cell based electric vehicle applications. *IEEE Access*, 6:3899–3908, 2018.

[96] Jawad Chorfi, Malika Zazi, and Mohamed Mansori. A new intelligent mppt based on ann algorithm for photovoltaic system. In *2018 6th International Renewable and Sustainable Energy Conference (IRSEC)*, pages 1–6. IEEE, 2018.

[97] Derick Furquim Pereira, Francisco da Costa Lopes, and Edson H Watanabe. Neural generalized predictive control for tracking maximum efficiency and maximum power points of pem fuel cell stacks. In *IECON 2018-44th Annual Conference of the IEEE Industrial Electronics Society*, pages 1878–1883. IEEE, 2018.

[98] Ahmed Sabah Al-Araji, Hayder A Dhahad, and Essra A Jaber. A neural networks based predictive voltage-tracking controller design for proton exchange membrane fuel cell model. *Journal of Engineering*, 25(12):26–48, 2019.

[99] A Rezazadeh, A Askarzadeh, and M Sedighizadeh. Adaptive inverse control of proton exchange membrane fuel cell using rbf neural network. *Int. J. Electrochem. Sci.*, 6:3105–3117, 2011.

[100] Slimane Hadji, Jean-Paul Gaubert, and Fateh Krim. Real-time genetic algorithms-based mppt: study and comparison (theoretical an experimental) with conventional methods. *Energies*, 11(2):459, 2018.

[101] Alireza Abaspour, Nasrin Tadrisi Parsa, and Mohammad Sadeghi. A new feedback linearization-nsga-ii based control design for pem fuel cell. *Int. J. Comput. Appl.*, 97(10), 2014.

[102] Nida Khanam, Badrul Hasan Khan, and Tabish Imtiaz. Maximum power extraction of solar pv system using meta-heuristic mppt techniques: A comparative study. In *2019 International Conference on Electrical, Electronics and Computer Engineering (UPCON)*, pages 1–6. IEEE, 2019.

[103] Mustafa İnci and Abdullah Caliskan. Performance enhancement of energy extraction capability for fuel cell implementations with improved cuckoo search algorithm. *International Journal of Hydrogen Energy*, 45(19):11309 – 11320, 2020.

[104] Pi-Yun Chen, Kuo-Nan Yu, Her-Terng Yau, Jun-Ting Li, and Chih-Kang Liao. A novel variable step size fractional order incremental conductance algorithm to maximize power tracking of fuel cells. *Applied Mathematical Modelling*, 45:1067–1075, 2017.

[105] A Harrag and S Messalti. Variable step size ic mppt controller for pemfc power system improving static and dynamic performances. *Fuel Cells*, 17(6):816–824, 2017.

[106] Weidong Xiao, William G Dunford, Patrick R Palmer, and Antoine Capel. Application of centered differentiation and steepest descent to maximum power point tracking. *IEEE Transactions on Industrial Electronics*, 54(5):2539–2549, 2007.

[107] Lean Karlo S Tolentino, Febus Reidj G Cruz, Ramon G Garcia, and Wen-Yaw Chung. Maximum power point tracking controller ic based on ripple correlation control algorithm. In *Humanoid, Nanotechnology, Information Technology, Communication and Control, Environment and Management (HNICEM), 2015 International Conference on*, pages 1–6. IEEE, 2015.

[108] SM Ferdous, GM Shafiullah, Mohammad Abdul Moin Oninda, Md Asaduzzaman Shoeb, and Taskin Jamal. Close loop compensation technique for high performance mppt using ripple correlation control. In *Universities Power Engineering Conference (AUPEC), 2017 Australasian*, pages 1–6. IEEE, 2017.

[109] Manel Hammami and Gabriele Grandi. A single-phase multilevel pv generation system with an improved ripple correlation control mppt algorithm. *Energies*, 10(12):2037, 2017.

[110] A Harrag and H Bahri. A novel single sensor variable step size maximum power point tracking for proton exchange membrane fuel cell power system. *Fuel Cells*, 19(2):177–189, 2019.

[111] M Sarvi, M Parpaei, I Soltani, and MA Taghikhani. Eagle strategy based maximum power point tracker for fuel cell system. *International Journal of Engineering-Transactions A: Basics*, 28(4):529–536, 2015.

[112] Mun-Kyeom Kim. Optimal control and operation strategy for wind turbines contributing to grid primary frequency regulation. *Applied Sciences*, 7(9):927, 2017.

[113] N Kalaiarasi, Subranshu Sekhar Dash, Sanjeevikumar Padmanaban, S Paramasivam, and Pandav Kiran Morati. Maximum power point tracking implementation by dspace controller integrated through z-source inverter using particle swarm optimization technique for photovoltaic applications. *Applied Sciences*, 8(1):145, 2018.

[114] Antti Pohjoranta, Marco Sorrentino, Cesare Pianese, F Amatruda, and Tero Hottinen. Validation of neural network-based fault diagnosis for multi-stack fuel cell systems: stack voltage deviation detection. *Energy Procedia*, 81:173–181, 2015.

[115] Y Bicer, I Dincer, and M Aydin. Maximizing performance of fuel cell using artificial neural network approach for smart grid applications. *Energy*, 116:1205–1217, 2016.

[116] Mingxuan Chen, Suliang Ma, Jianwen Wu, and Lian Huang. Analysis of mppt failure and development of an augmented nonlinear controller for mppt of photovoltaic systems under partial shading conditions. *Applied Sciences*, 7(1):95, 2017.

[117] Giovanna Adinolfi, Giorgio Graditi, Pierluigi Siano, and Antonio Piccolo. Multiobjective optimal design of photovoltaic synchronous boost converters assessing efficiency, reliability, and cost savings. *IEEE Transactions on Industrial Informatics*, 11(5):1038–1048, 2015.

[118] Fang Fang and Le Wei. Backstepping-based nonlinear adaptive control for coal-fired utility boiler–turbine units. *Applied Energy*, 88(3):814–824, 2011.

[119] Mohamed Derbeli, Maissa Farhat, Oscar Barambones, and Lassaad Sbita. A robust mpp tracker based on backstepping algorithm for proton exchange membrane fuel cell power system. In *Compatibility, Power Electronics and Power*

Engineering (CPE-POWERENG), 2017 11th IEEE International Conference on, pages 424–429. IEEE, 2017.

[120] Mohamed Derbeli, Oscar Barambones, and Lassaad Sbita. A robust maximum power point tracking control method for a pem fuel cell power system. *Applied Sciences*, 8(12):2449, 2018.

[121] Aranzazu D Martin, JM Cano, J Fernando A Silva, and Jesús R Vázquez. Backstepping control of smart grid-connected distributed photovoltaic power supplies for telecom equipment. *IEEE Transactions on energy conversion*, 30(4):1496–1504, 2015.

[122] Sandipan Patra, Ankur, Modem Narayana, Soumya R Mohanty, and Nand Kishor. Power quality improvement in grid-connected photovoltaic–fuel cell based hybrid system using robust maximum power point tracking controller. *Electric Power Components and Systems*, 43(20):2235–2250, 2015.

[123] Abderrahim Taouni, Ahmed Abbou, Mohammed Akherraz, Abderrahmane Ouchatti, and Radouane Majdoul. Mppt design for photovoltaic system using backstepping control with boost converter. In *Renewable and Sustainable Energy Conference (IRSEC), 2016 International*, pages 469–475. IEEE, 2016.

[124] Moussa Reddak, Abdelmajid Berdai, Anass Gourma, and Abdelaziz Belfqih. Integral backstepping control based maximum power point tracking strategy for wind turbine systems driven dfig. In *Electrical and Information Technologies (ICEIT), 2016 International Conference on*, pages 84–88. IEEE, 2016.

[125] Hanen Nafaa, Maissa Farhat, and Sbita Lassaad. A pv water desalination system using backstepping approach. In *Green Energy Conversion Systems (GECS), 2017 International Conference on*, pages 1–5. IEEE, 2017.

[126] Muhammad Arsalan, Ramsha Iftikhar, Iftikhar Ahmad, Ammar Hasan, K Sabahat, and A Javeria. Mppt for photovoltaic system using nonlinear backstepping controller with integral action. *Solar Energy*, 170:192–200, 2018.

[127] Tousif Khan Nizami and Arghya Chakravarty. Neural network integrated adaptive backstepping control of dc-dc boost converter. *IFAC-PapersOnLine*, 53(1):549–554, 2020.

[128] Lijia Cao, Zhang Shengxiu, Li Xiaofeng, Liu Yinan, and Liu Ying. Nonlinear adaptive block backstepping control using command filter and neural networks approximation. *Information Technology Journal*, 10:2284–2291, 12 2011.

[129] Ramazan Coban. Backstepping integral sliding mode control of an electromechanical system. *Automatika*, 58:266–272, 07 2017.

[130] Il-Song Kim. Sliding mode controller for the single-phase grid-connected photovoltaic system. *Applied Energy*, 83(10):1101–1115, 2006.

[131] Bin Wang, Guangliang Ma, Dan Xu, Le Zhang, and Jiahui Zhou. Switching sliding-mode control strategy based on multi-type restrictive condition for voltage control of buck converter in auxiliary energy source. *Applied Energy*, 228:1373–1384, 2018.

[132] K. Sankar and Amiya K. Jana. Nonlinear multivariable sliding mode control of a reversible pem fuel cell integrated system. *Energy Conversion and Management*, 171:541–565, 2018.

[133] Lianhao Yin, Gabriel Turesson, Per Tunestål, and Rolf Johansson. Sliding mode control on receding horizon: Practical control design and application. *Control Engineering Practice*, 109:104724, 2021.

[134] Shankar Gambhire, D.Ravi Kishore, P. Londhe, and Shweta Pawar. Review of sliding mode based control techniques for control system applications. *International Journal of Dynamics and Control*, 9, 03 2021.

[135] Jenn-Kun Kuo and Chi-Fa Wang. An integrated simulation model for pem fuel cell power systems with a buck dc–dc converter. *Int. J. Hydrog. Energy*, 36(18):11846–11855, 2011.

[136] Mohamed Derbeli, Asma Charaabi, Oscar Barambones, and Lassaad Sbita. Optimal energy control of a pem fuel cell/battery storage system. In *2019 10th International Renewable Energy Congress (IREC)*, pages 1–5. IEEE, 2019.

[137] Mohamed Derbeli, Oscar Barambones, Maissa Farhat, and Lassaad Sbita. Efficiency boosting for proton exchange membrane fuel cell power system using new mppt method. In *2019 10th International Renewable Energy Congress (IREC)*, pages 1–4. IEEE, 2019.

[138] Seghir Benhalima, Rezkallah Miloud, and Ambrish Chandra. Real-time implementation of robust control strategies based on sliding mode control for standalone microgrids supplying non-linear loads. *Energies*, 11(10):2590, 2018.

[139] Michail Zak. Terminal attractors in neural networks. *Neural Networks*, 2(4):259–274, 1989.

[140] S. T. Venkataraman and S. Gulati. Control of nonlinear systems using terminal sliding modes. In *1992 American Control Conference*, pages 891–893, 1992.

[141] Yuqiang Wu, Xinghuo Yu, and Zhihong Man. Terminal sliding mode control design for uncertain dynamic systems. *Systems & Control Letters*, 34(5):281–287, 1998.

[142] Amin Mohammadpour Shotorbani, Saeid Ghassem-Zadeh, Behnam Mohammadi-Ivatloo, and Seyed Hossein Hosseini. A distributed secondary scheme with terminal sliding mode controller for energy storages in an islanded microgrid. *International Journal of Electrical Power & Energy Systems*, 93:352–364, 2017.

[143] Arie Levant, Adir Pridor, R. Gitizadeh, I. Yaesh, and Joseph Ben Asher. Aircraft pitch control via second-order sliding technique. *Journal of Guidance Control and Dynamics - J GUID CONTROL DYNAM*, 23:586–594, 07 2000.

[144] Mohamed Derbeli, Oscar Barambones, Maissa Farhat, Jose Antonio Ramos-Hernanz, and Lassaad Sbita. Robust high order sliding mode control for performance improvement of pem fuel cell power systems. *International Journal of Hydrogen Energy*, 45(53):29222–29234, 2020.

[145] Mohamed Derbeli, Oscar Barambones, Jose Antonio Ramos-Hernanz, and Lassaad Sbita. Real-time implementation of a super twisting algorithm for pem fuel cell power system. *Energies*, 12(9):1594, 2019.

[146] Mohammed Yousri Silaa, Mohamed Derbeli, Oscar Barambones, and Ali Cheknane. Design and implementation of high order sliding mode control for pemfc power system. *Energies*, 13(17):4317, 2020.

[147] Mohamed Derbeli, Oscar Barambones, Mohammed Yousri Silaa, and Cristian Napole. Real-time implementation of a new mppt control method for a dc-dc boost converter used in a pem fuel cell power system. In *Actuators*, volume 9, page 105. Multidisciplinary Digital Publishing Institute, 2020.

[148] Cristian Napole, Oscar Barambones, Mohamed Derbeli, Isidro Calvo, Mohammed Silaa, and Javier Velasco. High-performance tracking for piezoelectric actuators using super-twisting algorithm based on artificial neural networks. *Mathematics*, 9:244, 01 2021.

[149] Deepika Deepika, Sandeep Kaur, and Shiv Narayan. Integral terminal sliding mode control unified with ude for output constrained tracking of mismatched uncertain non-linear systems. *ISA Transactions*, 101:1–9, 2020.

[150] Mohammad Morshed and Afef Fekih. Design of a chattering-free integral terminal sliding mode approach for dfig-based wind energy systems. *Optimal Control Applications and Methods*, pages 1–17, 07 2020.

[151] Hammad Armghan, Ming Yang, Ammar Armghan, Naghmash Ali, MQ Wang, and Iftikhar Ahmad. Design of integral terminal sliding mode controller for the hybrid ac/dc microgrids involving renewables and energy storage systems. *International Journal of Electrical Power & Energy Systems*, 119:105857, 2020.

[152] Chian-Song Chiu and Chih-Teng Shen. Finite-time control of dc–dc buck converters via integral terminal sliding modes. *International Journal of Electronics*, 99:643–655, 05 2012.

[153] Satish Kumar Gudey and Rajesh Gupta. Recursive fast terminal sliding mode control in voltage source inverter for a low-voltage microgrid system. *IET Generation, Transmission & Distribution*, 10(7):1536–1543, 2016.

[154] Mohammed Yousri Silaa, Mohamed Derbeli, Oscar Barambones, Cristian Napole, Ali Cheknane, and José María Gonzalez De Durana. An efficient and robust current control for polymer electrolyte membrane fuel cell power system. *Sustainability*, 13(4):2360, 2021.

[155] C. Xiu and P. Guo. Global terminal sliding mode control with the quick reaching law and its application. *IEEE Access*, 6:49793–49800, 2018.

[156] H. Pan, G. Zhang, H. Ouyang, and L. Mei. A novel global fast terminal sliding mode control scheme for second-order systems. *IEEE Access*, 8:22758–22769, 2020.

[157] Gregor Hoogers. Handbook of fuel cell technology, 2003.

[158] Félix Grasser and Alfred C Rufer. An analytical, control-oriented state space model for a pem fuel cell system. In *2007 Power Conversion Conference-Nagoya*, pages 441–447. IEEE, 2007.

[159] Fauhan Rosli, Che Mohd Ruzaidi Ghazali, Mohd Mustafa Al Bakri Abdullah, and Kamarudin Hussin. A review: Characteristics of oil palm trunk (opt) and quality improvement of palm trunk plywood by resin impregnation. *BioResources*, 11(2):5565–5580, 2016.

[160] Cataldo Simari, Georgia Potsi, Alfonso Policicchio, Ida Perrotta, and Isabella Nicotera. Clay–carbon nanotubes hybrid materials for nanocomposite membranes: advantages of branched structure for proton transport under low humidity conditions in pemfcs. *The Journal of Physical Chemistry C*, 120(5):2574–2584, 2016.

[161] Feiqi Liu, Fuquan Zhao, Zongwei Liu, and Han Hao. The impact of fuel cell vehicle deployment on road transport greenhouse gas emissions: the china case. *International Journal of Hydrogen Energy*, 43(50):22604–22621, 2018.

[162] A Appleby. John y frank r. foulkes. *Fuel Cell Handbook. Van Nostrand Reinhold Co. 1989. New York*, 1989.

[163] José Manuel Andújar and Francisca Segura. Fuel cells: History and updating. a walk along two centuries. *Renewable and sustainable energy reviews*, 13(9):2309–2322, 2009.

[164] Rong-Heng Lin, Xue-Nan Xi, Pei-Nan Wang, Bu-Dan Wu, and Shi-Ming Tian. Review on hydrogen fuel cell condition monitoring and prediction methods. *International Journal of Hydrogen Energy*, 44(11):5488–5498, 2019.

[165] Tabbi Wilberforce, Zaki El-Hassan, FN Khatib, Ahmed Al Makky, Ahmad Baroutaji, James G Carton, James Thompson, and Abdul G Olabi. Modelling and simulation of proton exchange membrane fuel cell with serpentine bipolar plate using matlab. *International Journal of Hydrogen Energy*, 42(40):25639–25662, 2017.

[166] B Rismanchi and MH Akbari. Performance prediction of proton exchange membrane fuel cells using a three-dimensional model. *International Journal of Hydrogen Energy*, 33(1):439–448, 2008.

[167] MH Akbari. Pem fuel cell systems for electric power generation: An overview. In *Proceedings International Hydrogen Energy Congress and Exhibition IHEC*, 2005.

[168] Zhixiang Liu, Kevin Kendall, and Xieqiang Yan. China progress on renewable energy vehicles: Fuel cells, hydrogen and battery hybrid vehicles. *Energies*, 12(1):54, 2019.

[169] C EG Padro and Victoria Putsche. Survey of the economics of hydrogen technologies. Technical report, National Renewable Energy Lab., Golden, CO (US), 1999.

[170] Alexander E Farrell, David W Keith, and James J Corbett. A strategy for introducing hydrogen into transportation. *Energy Policy*, 31(13):1357–1367, 2003.

[171] SJC Cleghorn, X Ren, TE Springer, MS Wilson, C Zawodzinski, TA Zawodzinski, and S Gottesfeld. Pem fuel cells for transportation and stationary power generation applications. *International Journal of Hydrogen Energy*, 22(12):1137–1144, 1997.

[172] Hydrogen Properties. Course manual on hydrogen fuel cell engines and related technologies module 1. *College of the Desert, Palm Desert, CA, USA*, 2001.

[173] Chunto Tso and Shih-Yun Chang. A viable niche market—fuel cell scooters in taiwan. *International Journal of Hydrogen Energy*, 28(7):757–762, 2003.

[174] Steve Medwin. Application of fuel cells to fork lift trucks. *Industrial Utility Vehicle & Mobile Equipment Magazine*, 2005.

[175] Arnold R Miller and David L Barnes. Advanced underground vehicle power and control fuel cell mine locomotive. In *Proceeding of the 2002 US DOE Hydrogen Program Review*, pages 5–9, 2002.

[176] Henry Oman. Fuel-cell powered airplane propulsion. *IEEE Aerospace and Electronic Systems Magazine*, 19(1):12–13, 2004.

[177] Ahmed Al Amerl, Ismail Oukkacha, Mamadou Baïlo Camara, and Brayima Dakyo. Real-time control strategy of fuel cell and battery system for electric hybrid boat application. *Sustainability*, 13(16):8693, 2021.

[178] Leslie Eudy, Richard Parish, Jonathan Leonard, and Arthur D Little-Acurex Environmental. Hydrogen fuel cell bus evaluation. *2001 US DOE Hydrogen Program Review*, page 859, 2001.

[179] European Commission. High Level Group for Hydrogen, Fuel Cell Technologies, European Commission. Directorate-General for Energy, and European Commission. Directorate General for Research. *Hydrogen Energy and Fuel Cells: A Vision of Our Future:[final Report of the High Level Group].*, volume 20719. European Commission, Directorate-General for Research, 2003.

[180] Fuel Cell Handbook. Us department of energy, office of fossil energy, and national energy technology laboratory, eg&g technical services. *Inc, Science Application International Corporation*, 2002.

[181] Ronald F Mann, John C Amphlett, Michael AI Hooper, Heidi M Jensen, Brant A Peppley, and Pierre R Roberge. Development and application of a generalised steady-state electrochemical model for a pem fuel cell. *Journal of power sources*, 86(1-2):173–180, 2000.

[182] Bouziane Mahmah, Abdelhamid M'Raoui, Maïouf Belhamel, and Hocine Benmoussa. Experimental study and modelling of a fuel cell pemfc fed directly with hydrogen/oxygen. In *The 16th World Hydrogen Energy Conference (WHEC*, volume 16, 2006.

[183] Jeferson M Corrêa, Felix A Farret, Luciane Neves Canha, and Marcelo Godoy Simoes. An electrochemical-based fuel-cell model suitable for electrical engineering automation approach. *IEEE Transactions on industrial electronics*, 51(5):1103–1112, 2004.

[184] J Larminie and A Dicks. Fuel cell systems explained (west sussex, john willey & sons, ltd). 2000.

[185] S Elanayar Vt and Yung C Shin. Radial basis function neural network for approximation and estimation of nonlinear stochastic dynamic systems. *IEEE transactions on neural networks*, 5(4):594–603, 1994.

[186] Yahui Li, Sheng Qiang, Xianyi Zhuang, and Okyay Kaynak. Robust and adaptive backstepping control for nonlinear systems using rbf neural networks. *IEEE Transactions on Neural Networks*, 15(3):693–701, 2004.

[187] Kevin L Priddy and Paul E Keller. *Artificial neural networks: an introduction*, volume 68. SPIE press, 2005.

[188] Mohamed Derbeli, Asma Charaabi, Oscar Barambones, and Cristian Napole. High-performance tracking for proton exchange membrane fuel cell system pemfc using model predictive control. *Mathematics*, 9(11):1158, 2021.

[189] Hesam Karim, Sharareh R Niakan, and Reza Safdari. Comparison of neural network training algorithms for classification of heart diseases. *IAES International Journal of Artificial Intelligence*, 7(4):185, 2018.

[190] DS Falcão, José Carlos M Pires, C Pinho, AMFR Pinto, and Fernando Gomes Martins. Artificial neural network model applied to a pem fuel cell. In *IJCCI 2009: PROCEEDINGS OF THE INTERNATIONAL JOINT CONFERENCE ON COMPUTATIONAL INTELLIGENCE*, 2009.

[191] Dong Van Dao, Hojjat Adeli, Hai-Bang Ly, Lu Minh Le, Vuong Minh Le, Tien-Thinh Le, and Binh Thai Pham. A sensitivity and robustness analysis of gpr and ann for high-performance concrete compressive strength prediction using a monte carlo simulation. *Sustainability*, 12(3):830, 2020.

[192] Viet-Ha Nhu, Nhat-Duc Hoang, Van-Binh Duong, Hong-Dang Vu, and Dieu Tien Bui. A hybrid computational intelligence approach for predicting soil shear strength for urban housing construction: a case study at vinhomes imperia project, hai phong city (vietnam). *Engineering with Computers*, 36(2):603–616, 2020.

[193] Mehrdad Arabi, Ali dehshiri, and Mahdi Shokrgozar. Modeling transportation supply and demand forecasting using artificial intelligence parameters (bayesian model). *Istrazivanja i projektovanja za privredu*, 16:43–49, 01 2018.

[194] V. Mudunuru. Comparison of activation functions in multilayer neural networks for stage classification in breast cancer. *Neural, Parallel & Scientific Computations archive*, 24, 2016.

[195] D. Ashok Kumar and S. Murugan. Performance analysis of mlpff neural network back propagation training algorithms for time series data. In *2014 World Congress on Computing and Communication Technologies*, pages 114–119, 2014.

[196] Bhavna Sharma and K. Venugopalan. Comparison of neural network training functions for hematoma classification in brain ct images. *IOSR Journal of Computer Engineering*, 16:31–35, 2014.

[197] Kanchan V Shende, MR Ramesh Kumar, and KV Kale. Comparison of neural network training functions for prediction of outgoing longwave radiation over

the bay of bengal. In *Computing in Engineering and Technology*, pages 411–419. Springer, 2020.

[198] Maria Isabel Arteaga Orozco. *Control no lineal de convertidores conmutados CC/CC: Análisis de prestaciones y verificación experimental.* Universitat Politècnica de Catalunya, 2007.

[199] Eladio Durán Aranda et al. *Prototipo experimental para la medida y caracterización de las curvas IV y PV de módulos y Arrays FVs: diseño, modelado, implementación y pruebas.* 2010.

[200] Wuhua Li and Xiangning He. Review of nonisolated high-step-up dc/dc converters in photovoltaic grid-connected applications. *IEEE Transactions on Industrial Electronics*, 58(4):1239–1250, 2010.

[201] Fernando Lessa Tofoli, Dênis de Castro Pereira, Wesley Josias de Paula, and Demercil de Sousa Oliveira Júnior. Survey on non-isolated high-voltage step-up dc–dc topologies based on the boost converter. *IET power Electronics*, 8(10):2044–2057, 2015.

[202] Renan Diego de Oliveira Reiter, Leandro Michels, Adriano Péres, and Sérgio Vidal Garcia Oliveira. Analysis of pv arrays for residential applications using a three-phase step-up isolated dc-dc converter with high-frequency transformer. In *IECON 2011-37th Annual Conference of the IEEE Industrial Electronics Society*, pages 1208–1213. IEEE, 2011.

[203] Ahmad H El Khateb, Nasrudin Abd Rahim, Jeyraj Selvaraj, and Barry W Williams. Dc-to-dc converter with low input current ripple for maximum photovoltaic power extraction. *IEEE Transactions on Industrial Electronics*, 62(4):2246–2256, 2014.

[204] Antonio Luque and Steven Hegedus. *Handbook of photovoltaic science and engineering.* John Wiley & Sons, 2011.

[205] Richard Kaye, Akhtar Kalam, and Cagil Ozansoy. Selection of inductor and capacitor for buck converter using design equations comparison. *Journal of Scientific & Industrial Research*, 78(09):586–588, 2019.

[206] M Nayeripour and M Mahdi Mansouri. Analyze of real switching angle limits in tcsc on capacitor and inductor values and their selection factors. 2013.

[207] S Meikandasivam, Rajesh Kumar Nema, and Shailendra Kumar Jain. Selection of tcsc parameters: Capacitor and inductor. In *India International Conference on Power Electronics 2010 (IICPE2010)*, pages 1–5. IEEE, 2011.

[208] P Khazaei, SM Modares, M Dabbaghjamanesh, M Almousa, and A Moeini. A high efficiency dc/dc boost converter for photovoltaic applications. *International Journal of Soft Computing and Engineering (IJSCE)*, 6(2):2231–2307, 2016.

[209] Subramani Saravanan and Neelakandan Ramesh Babu. A modified high step-up non-isolated dc-dc converter for pv application. *Journal of applied research and technology*, 15(3):242–249, 2017.

[210] Mojtaba Forouzesh, Yam P Siwakoti, Saman A Gorji, Frede Blaabjerg, and Brad Lehman. Step-up dc–dc converters: A comprehensive review of voltage boosting techniques, topologies, and applications. *IEEE Transactions on Power Electronics*, 2017.

[211] Lars Alminde, Morten Bisgaard, Fjolnir Gudmundsson, Claus Kesjer, Toke Koustrup, Christian Lodberg, and Tor Viscor. Power supply for the aau cubesat. *Aalborg University, Aalborg Denmark*, 2001.

[212] Michel Girard, Hugues Angelis, and Magali Girard. *Alimentations à découpage: cours et exercices corrigés*. Dunod, 2003.

[213] Robert W Erickson and Dragan Maksimovic. *Fundamentals of power electronics*. Springer Science & Business Media, 2007.

[214] Adedamola Omole. Analysis, modeling and simulation of optimal power tracking of multiple-modules of paralleled solar cell systems. 2006.

[215] Feri Yusivar, MY Farabi, R Suryadiningrat, WW Ananduta, and Y Syaifudin. Buck-converter photovoltaic simulator. *International Journal of Power Electronics and Drive Systems*, 1(2):156, 2011.

[216] Muhammad H Rashid. Power electronics handbook, 2001.

[217] Ned Mohan, Tore M Undeland, and William P Robbins. *Power electronics: converters, applications, and design*. John wiley & sons, 2003.

[218] Mohammed A Elgendy, Bashar Zahawi, and David J Atkinson. Assessment of perturb and observe mppt algorithm implementation techniques for pv pumping applications. *IEEE transactions on sustainable energy*, 3(1):21–33, 2011.

[219] Abdul Motin Howlader, Naomitsu Urasaki, Tomonobu Senjyu, Atsushi Yona, and Ahmed Yousuf Saber. Optimal pam control for a buck boost dc-dc converter with a wide-speed-range of operation for a pmsm. *Journal of Power Electronics*, 10(5):477–484, 2010.

[220] Yingqi Zhang and Paresh C Sen. A new soft-switching technique for buck, boost, and buck-boost converters. *IEEE transactions on Industry Applications*, 39(6):1775–1782, 2003.

[221] Young-Joo Lee, Alireza Khaligh, Arindam Chakraborty, and Ali Emadi. Digital combination of buck and boost converters to control a positive buck–boost converter and improve the output transients. *IEEE Transactions on Power Electronics*, 24(5):1267–1279, 2009.

[222] Mark Gaboriault and Andrew Notman. A high efficiency, noninverting, buck-boost dc-dc converter. In *Nineteenth Annual IEEE Applied Power Electronics Conference and Exposition, 2004. APEC'04.*, volume 3, pages 1411–1415. IEEE, 2004.

[223] Biranchinath Sahu and Gabriel A Rincón-Mora. A low voltage, dynamic, noninverting, synchronous buck-boost converter for portable applications. *IEEE Transactions on power electronics*, 19(2):443–452, 2004.

[224] SJ Chiang, Hsin-Jang Shieh, and Ming-Chieh Chen. Modeling and control of pv charger system with sepic converter. *IEEE Transactions on industrial electronics*, 56(11):4344–4353, 2008.

[225] Elena Niculescu, Marius-Cristian Niculescu, and Dorina-Mioara Purcaru. Modelling the pwm sepic converter in discontinuous conduction mode. In *Proceedings of the 11th WSEAS International Conference on CIRCUITS*, pages 98–103, 2007.

[226] Mustafa A Al-Saffar, Esam H Ismail, Ahmad J Sabzali, and Abbas A Fardoun. An improved topology of sepic converter with reduced output voltage ripple. *IEEE Transactions on power electronics*, 23(5):2377–2386, 2008.

[227] Jingquan Chen and Chin Chang. Analysis and design of sepic converter in boundary conduction mode for universal-line power factor correction applications. In *2001 IEEE 32nd Annual Power Electronics Specialists Conference (IEEE Cat. No. 01CH37230)*, volume 2, pages 742–747. IEEE, 2001.

[228] Emilio Mamarelis, Giovanni Petrone, and Giovanni Spagnuolo. Design of a sliding-mode-controlled sepic for pv mppt applications. *IEEE Transactions on Industrial Electronics*, 61(7):3387–3398, 2013.

[229] Ahmad El Khateb, Nasrudin Abd Rahim, Jeyraj Selvaraj, and Mohammad Nasir Uddin. Fuzzy-logic-controller-based sepic converter for maximum power point tracking. *IEEE Transactions on Industry Applications*, 50(4):2349–2358, 2014.

[230] E. Vuthchhay and C. Bunlaksananusorn. Dynamic modeling of a zeta converter with state-space averaging technique. In *2008 5th International Conference on Electrical Engineering/Electronics, Computer, Telecommunications and Information Technology*, volume 2, pages 969–972, 2008.

[231] S. Singh, B. Singh, G. Bhuvaneswari, and V. Bist. Power factor corrected zeta converter based improved power quality switched mode power supply. *IEEE Transactions on Industrial Electronics*, 62(9):5422–5433, 2015.

[232] S. Narula, B. Singh, and G. Bhuvaneswari. Power factor corrected welding power supply using modified zeta converter. *IEEE Journal of Emerging and Selected Topics in Power Electronics*, 4(2):617–625, 2016.

[233] Vashist Bist and Bhim Singh. Reduced sensor configuration of brushless dc motor drive using a power factor correction-based modified-zeta converter. *IET Power Electronics*, 7(9):2322–2335, 2014.

[234] D. Murthy-Bellur and M. K. Kazimierczuk. Isolated two-transistor zeta converter with reduced transistor voltage stress. *IEEE Transactions on Circuits and Systems II: Express Briefs*, 58(1):41–45, 2011.

[235] Min-Sup Song, Young-Dong Son, and Kwang-Hyun Lee. Non-isolated bidirectional soft-switching sepic/zeta converter with reduced ripple currents. *Journal of Power Electronics*, 14(4):649–660, 2014.

[236] G Spiazzi and P Mattavelli. Design criteria for power factor preregulators based on sepic and cuk converters in continuous conduction mode. In *Proceedings of 1994 IEEE Industry Applications Society Annual Meeting*, volume 2, pages 1084–1089. IEEE, 1994.

[237] Vashist Bist and Bhim Singh. Pfc cuk converter-fed bldc motor drive. *IEEE Transactions on Power Electronics*, 30(2):871–887, 2014.

[238] CK Tse, YM Lai, and HHC Iu. Hopf bifurcation and chaos in a free-running current-controlled cuk switching regulator. *IEEE Transactions on Circuits and Systems I: Fundamental Theory and Applications*, 47(4):448–457, 2000.

[239] Ali Farzan Moghaddam and Alex Van den Bossche. A ćuk converter cell balancing technique by using coupled inductors for lithium-based batteries. *Energies*, 12(15):2881, 2019.

[240] Miao Zhu and Fang Lin Luo. Enhanced self-lift ćuk converter for negative-to-positive voltage conversion. *IEEE transactions on power electronics*, 25(9):2227–2233, 2010.

[241] JAM Bleijs and JA Gow. Fast maximum power point control of current-fed dc-dc converter for photovoltaic arrays. *Electronics Letters*, 37(1):5–6, 2001.

[242] MD Singh. *Power electronics*. Tata McGraw-Hill Education, 2008.

[243] Muhammad H Rashid. *Power electronics handbook: devices, circuits and applications*. Elsevier, 2010.

[244] Jean-Jacques E Slotine, Weiping Li, et al. *Applied nonlinear control*, volume 199. Prentice hall Englewood Cliffs, NJ, 1991.

[245] P Mattavelli, L Rossetto, G Spiazzi, and P Tenti. General-purpose sliding-mode controller for dc/dc converter applications. In *Proceedings of IEEE Power Electronics Specialist Conference-PESC'93*, pages 609–615. IEEE, 1993.

[246] Vadim I Utkin. Sliding mode control design principles and applications to electric drives. *IEEE transactions on industrial electronics*, 40(1):23–36, 1993.

[247] Leonid Fridman, Arie Levant, et al. Higher order sliding modes. *Sliding mode control in engineering*, 11:53–102, 2002.

[248] ST Venkataraman and S Gulati. Control of nonlinear systems using terminal sliding modes. 1993.

[249] Vadim Utkin, Jürgen Guldner, and Ma Shijun. *Sliding mode control in electro-mechanical systems*, volume 34. CRC press, 1999.

[250] M Toghiani Rizi and H Eliasi. Nonsingular terminal sliding mode controller for voltage and current control of an islanded microgrid. *Electric Power Systems Research*, 185:106354, 2020.

[251] Yong Feng, Xinghuo Yu, and Zhihong Man. Non-singular terminal sliding mode control of rigid manipulators. *Automatica*, 38(12):2159–2167, 2002.

[252] Xinghuo Yu and Man Zhihong. Fast terminal sliding-mode control design for nonlinear dynamical systems. *IEEE Transactions on Circuits and Systems I: Fundamental Theory and Applications*, 49(2):261–264, 2002.

[253] Yuxin Zhao, Tian Wu, and Yan Ma. A double power reaching law of sliding mode control based on neural network. *Mathematical Problems in Engineering*, 2013, 09 2013.

[254] SV Emel'Yanov, SK Korovin, and A Levant. High-order sliding modes in control systems. *Computational mathematics and modeling*, 7(3):294–318, 1996.

[255] Giorgio Bartolini, Arie Levant, A Pisano, and E Usai. 2-sliding mode with adaptation. In *Proc. of the 7th IEEE Mediterranean Conference on Control and Systems*, 1999.

[256] Igor Boiko, L Fridman, and R Iriarte. Analysis of chattering in continuous sliding mode control. In *American Control Conference, 2005. Proceedings of the 2005*, pages 2439–2444. IEEE, 2005.

[257] Igor Boiko, Leonid Fridman, Alessandro Pisano, and Elio Usai. Analysis of chattering in systems with second-order sliding modes. *IEEE transactions on Automatic control*, 52(11):2085–2102, 2007.

[258] David J Perreault, Kenji Sato, RL Selders, and John G Kassakian. Switching-ripple-based current sharing for paralleled power converters. *IEEE Transactions on Circuits and Systems I: Fundamental Theory and Applications*, 46(10):1264–1274, 1999.

[259] Giorgio Bartolini, Antonella Ferrara, Elio Usai, and Vadim I Utkin. On multi-input chattering-free second-order sliding mode control. *IEEE transactions on automatic control*, 45(9):1711–1717, 2000.

[260] Arie Levant. Sliding order and sliding accuracy in sliding mode control. *International journal of control*, 58(6):1247–1263, 1993.

[261] Arie Levant. Principles of 2-sliding mode design. *automatica*, 43(4):576–586, 2007.

[262] SV Emelyanov. High order sliding modes in control systems. *Differential equations*, 29:1627–1647, 1993.

[263] Qun Zong, Jie Wang, Bailing Tian, and Yang Tao. Quasi-continuous high-order sliding mode controller and observer design for flexible hypersonic vehicle. *Aerospace Science and Technology*, 27(1):127–137, 2013.

[264] Arie Levant. Homogeneity approach to high-order sliding mode design. *Automatica*, 41(5):823–830, 2005.

[265] SV Emel'Yanov, SK Korovin, and LV Levantovskii. Higher-order sliding modes in binary control systems. In *Soviet Physics Doklady*, volume 31, page 291, 1986.

[266] SV Emelyanov, SK Korovin, and LV Levantovskiy. A drift algorithm in control of uncertain processes. *PROB. CONTROL INFO. THEORY.*, 15(6):425–438, 1986.

[267] Charles Ronald Harahap and Tsuyoshi Hanamoto. Fictitious reference iterative tuning-based two-degrees-of-freedom method for permanent magnet synchronous motor speed control using fpga for a high-frequency sic mosfet invertermosfet inverter. *Applied Sciences*, 6(12):387, 2016.

[268] Eduardo Espíndola-López, Alfonso Gómez-Espinosa, Roberto V Carrillo-Serrano, and Juan C Jáuregui-Correa. Fourier series learning control for torque ripple minimization in permanent magnet synchronous motors. *Applied Sciences*, 6(9):254, 2016.

[269] Jui-Ho Chen, Her-Terng Yau, and Jin-Han Lu. Implementation of fpga-based charge control for a self-sufficient solar tracking power supply system. *Applied Sciences*, 6(2):41, 2016.

[270] Marwan Rosyadi, SM Muyeen, Rion Takahashi, and Junji Tamura. A design fuzzy logic controller for a permanent magnet wind generator to enhance the dynamic stability of wind farms. *Applied Sciences*, 2(4):780–800, 2012.

[271] Tan-Jan Ho and Chun-Hao Chang. Robust speed tracking of induction motors: An arduino-implemented intelligent control approach. *Applied Sciences*, 8(2):159, 2018.

[272] J. Mendel. *Type-1 Fuzzy Systems: Design Methods and Applications*, chapter 4, pages 229–234. Springer International Publishing, 2003.

[273] J. Rodriguez, M. P. Kazmierkowski, J. R. Espinoza, P. Zanchetta, H. Abu-Rub, H. A. Young, and C. A. Rojas. State of the art of finite control set model predictive control in power electronics. *IEEE Transactions on Industrial Informatics*, 9(2):1003–1016, 2013.

[274] Jose Rodriguez and Patricio Cortes. *Predictive control of power converters and electrical drives*, volume 40. John Wiley & Sons, 2012.

[275] Andres Larrea, Oscar Barambones, and Jose A Ramos-Herran. Design and implementation of a predictive control system for a photovoltaic generator. In *2016 IEEE 21st International Conference on Emerging Technologies and Factory Automation (ETFA)*, pages 1–7. IEEE, 2016.

[276] Panagiotis E Kakosimos and Antonios G Kladas. Implementation of photovoltaic array mppt through fixed step predictive control technique. *Renewable energy*, 36(9):2508–2514, 2011.

[277] Long Cheng, Pablo Acuna, Ricardo P Aguilera, Jiuchun Jiang, Shaoyuan Wei, John E Fletcher, and Dylan DC Lu. Model predictive control for dc–dc boost converters with reduced-prediction horizon and constant switching frequency. *IEEE Transactions on Power Electronics*, 33(10):9064–9075, 2017.

[278] S Bououden, O Hazil, S Filali, and M Chadli. Modelling and model predictive control of a dc-dc boost converter. In *2014 15th International Conference on Sciences and Techniques of Automatic Control and Computer Engineering (STA)*, pages 643–648. IEEE, 2014.

[279] Dawei Wu, Mou Chen, Huajun Gong, and Qingxian Wu. Robust backstepping control of wing rock using disturbance observer. *Applied Sciences*, 7(3):219, 2017.

[280] Li-Hsin Chen and Chao-Chung Peng. Extended backstepping sliding controller design for chattering attenuation and its application for servo motor control. *Applied Sciences*, 7(3):220, 2017.

[281] Keun Uk Lee, Yoon Ho Choi, and Jin Bae Park. Backstepping based formation control of quadrotors with the state transformation technique. *Applied Sciences*, 7(11):1170, 2017.

[282] Qing Guo, Yili Liu, Dan Jiang, Qiang Wang, Wenying Xiong, Jie Liu, and Xiaochai Li. Prescribed performance constraint regulation of electrohydraulic control based on backstepping with dynamic surface. *Applied Sciences*, 8(1):76, 2018.

[283] Kairong Duan, Simon Fong, Yan Zhuang, and Wei Song. Artificial neural networks in coordinated control of multiple hovercrafts with unmodeled terms. *Applied Sciences*, 8(6):862, 2018.

[284] Sisi Wang, Lijun Wang, Zixuan Qiao, and Fengshan Li. Optimal robust control of path following and rudder roll reduction for a container ship in heavy waves. *Applied Sciences*, 8(9):1631, 2018.

[285] Hadeed Ahmed Sher, Ali Faisal Murtaza, Abdullah Noman, Khaled E Addoweesh, Kamal Al-Haddad, and Marcello Chiaberge. A new sensorless hybrid mppt algorithm based on fractional short-circuit current measurement and p&o mppt. *IEEE Transactions on Sustainable Energy*, 6(4):1426–1434, 2015.

[286] KR Bharath and Eenisha Suresh. Design and implementation of improved fractional open circuit voltage based maximum power point tracking algorithm for photovoltaic applications. *International Journal of Renewable Energy Research (IJRER)*, 7(3):1108–1113, 2017.

[287] Jirada Gosumbonggot. Maximum power point tracking method using perturb and observe algorithm for small scale dc voltage converter. *Procedia Computer Science*, 86:421–424, 2016.

[288] Xavier Serrano-Guerrero, José González-Romero, Xavier Cárdenas-Carangui, and Guillermo Escrivá-Escrivá. Improved variable step size p&o mppt algorithm for pv systems. In *Power Engineering Conference (UPEC), 2016 51st International Universities*, pages 1–6. IEEE, 2016.

[289] M Sarvi and MM Barati. Voltage and current based mppt of fuel cells under variable temperature conditions. In *Universities Power Engineering Conference (UPEC), 2010 45th International*, pages 1–4. IEEE, 2010.

[290] Carlo Cecati, Hassan Abdullah Khalid, Mario Tinari, Giovanna Adinolfi, and Giorgio Graditi. Dc nanogrid for renewable sources with modular dc/dc llc converter building block. *IET Power Electronics*, 10(5):536–544, 2016.

[291] Nicu Bizon, Phatiphat Thounthong, Marian Raducu, and Luminita M Constantinescu. Designing and modelling of the asymptotic perturbed extremum

seeking control scheme for tracking the global extreme. *International Journal of Hydrogen Energy*, 42(28):17632–17644, 2017.

[292] Nicu Bizon. Energy optimization of fuel cell system by using global extremum seeking algorithm. *Applied Energy*, 206:458–474, 2017.

[293] J Jiao and X Cui. A real-time tracking control of fuel cell power systems for maximum power point. *J Comput Inf Syst*, 9(5):1933–1941, 2013.

[294] Jianxin Liu, Tiebiao Zhao, and YangQuan Chen. Maximum power point tracking of proton exchange membrane fuel cell with fractional order filter and extremum seeking control. In *ASME 2015 International Design Engineering Technical Conferences and Computers and Information in Engineering Conference*, pages V009T07A026–V009T07A026. American Society of Mechanical Engineers, 2015.

[295] Osama Elbaksawi. Design of photovoltaic system using buck-boost converter based on mppt with pid controller. *Universal Journal of Electrical and Electronic Engineering*, 6:314–322, 12 2019.

[296] Nedia Aouani and Carlos Olalla. Robust lqr control for pwm converters with parameter-dependent lyapunov functions. *Applied Sciences*, 10(21), 2020.

[297] Mohamed Derbeli, Lassaad Sbita, Maissa Farhat, and Oscar Barambones. Pem fuel cell green energy generation—smc efficiency optimization. In *Green Energy Conversion Systems (GECS), 2017 International Conference on*, pages 1–5. IEEE, 2017.

[298] Imen Mrad, Mohamed Derheli, Lassaad Shita, Jean Pierre Barhot, Maissa Farhat, and Oscar Baramhones. Sensorless and robust pemfec power system drive based on z (tn) observability. In *Green Energy Conversion Systems (GECS), 2017 International Conference on*, pages 1–6. IEEE, 2017.

[299] Jehun Hahm, Hyoseok Kang, Jaeho Baek, Heejin Lee, and Mignon Park. Design of incremental conductance sliding mode mppt control applied by integrated photovoltaic and proton exchange membrane fuel cell system under various operating conditions for bldc motor. *International Journal of Photoenergy*, 2015, 2015.

[300] Yunmei Fang, Yunkai Zhu, and Juntao Fei. Adaptive intelligent sliding mode control of a photovoltaic grid-connected inverter. *Applied Sciences*, 8(10):1756, 2018.

[301] Samia Charfeddine, Attia Boudjemline, Sondess Ben Aoun, Houssem Jerbi, Mourad Kchaou, Obaid Alshammari, Zied Elleuch, and Rabeh Abbassi. Design of a fuzzy optimization control structure for nonlinear systems: A disturbance-rejection method. *Applied Sciences*, 11(6), 2021.

[302] KM Tsang and WL Chan. Maximum power point tracking for pv systems under partial shading conditions using current sweeping. *Energy Conversion and Management*, 93:249–258, 2015.

[303] Nedjem Eddine Benchouia, Abdallah Derghal, Bouziane Mahmah, Belgacem Madi, Lakhdar Khochemane, and Elias Hadjadj Aoul. An adaptive fuzzy logic controller (aflc) for pemfc fuel cell. *International Journal of Hydrogen Energy*, 40(39):13806–13819, 2015.

[304] Carlos Robles Algarín, John Taborda Giraldo, and Omar Rodríguez Álvarez. Fuzzy logic based mppt controller for a pv system. *Energies*, 10(12):2036, 2017.

[305] Woonki Na, Pengyuan Chen, and Jonghoon Kim. An improvement of a fuzzy logic-controlled maximum power point tracking algorithm for photovoltic applications. *Applied Sciences*, 7(4):326, 2017.

[306] John Macaulay and Zhongfu Zhou. A fuzzy logical-based variable step size p&o mppt algorithm for photovoltaic system. *Energies*, 11(6):1340, 2018.

[307] Mohamed Redha Rezoug, Rachid Chenni, and Djamel Taibi. Fuzzy logic-based perturb and observe algorithm with variable step of a reference voltage for solar permanent magnet synchronous motor drive system fed by direct-connected photovoltaic array. *Energies*, 11(2):462, 2018.

[308] Saban Ozdemir, N. Altin, and Ibrahim Sefa. Fuzzy logic based mppt controller for high conversion ratio quadratic boost converter. *International Journal of Hydrogen Energy*, 42, 03 2017.

[309] Imane Worighi, Thomas Geury, Mohamed El Baghdadi, Joeri Van Mierlo, Omar Hegazy, and Abdelilah Maach. Optimal design of hybrid pv-battery system in residential buildings: End-user economics, and pv penetration. *Applied Sciences*, 9:1022, 03 2019.

[310] Isa Nasiri Avanaki and M Sarvi. A new maximum power point tracking method for pem fuel cells based on water cycle algorithm. *Journal of Renewable Energy and Environment*, 3(1):35, 2016.

[311] Hassan Fathabadi. Novel highly accurate universal maximum power point tracker for maximum power extraction from hybrid fuel cell/photovoltaic/wind power generation systems. *Energy*, 116:402–416, 2016.

[312] Alivarani Mohapatra, Byamakesh Nayak, Priti Das, and Kanungo Barada Mohanty. A review on mppt techniques of pv system under partial shading condition. *Renewable and Sustainable Energy Reviews*, 80:854–867, 2017.

[313] Nabil Karami, Nazih Moubayed, and Rachid Outbib. General review and classification of different mppt techniques. *Renewable and Sustainable Energy Reviews*, 68:1–18, 2017.

[314] Marinko Barukcic, Željko Hederić, and Željko Špoljarić. The estimation of i–v curves of pv panel using manufacturers' i–v curves and evolutionary strategy. *Energy Conversion and Management*, 88:447–458, 2014.

[315] Tamer Khatib, Wilfried Elmenreich, and Azah Mohamed. Simplified i-v characteristic tester for photovoltaic modules using a dc-dc boost converter. *Sustainability*, 9, 2017.

[316] Roland Szabo and Aurel Gontean. Photovoltaic cell and module i-v characteristic approximation using bézier curves. *Applied Sciences*, 8(5), 2018.

[317] Mehmet Ali Yildirim and Marzena Nowak-Ocłoń. Modified maximum power point tracking algorithm under time-varying solar irradiation. *Energies*, 13(24), 2020.

[318] Ali Faisal Murtaza, Hadeed Ahmed Sher, Filippo Spertino, Alessandro Ciocia, Abdullah M. Noman, Abdullrahman A. Al-Shamma'a, and Abdulaziz Alkuhayli. A novel mppt technique based on mutual coordination between two pv modules/arrays. *Energies*, 14(21), 2021.

[319] Hyeon-Seok Lee and Jae-Jung Yun. Advanced mppt algorithm for distributed photovoltaic systems. *Energies*, 12(18), 2019.

[320] Wenbing Chang, Xinpeng Ji, Yinglai Liu, Yiyong Xiao, Bang Chen, Houxiang Liu, and Shenghan Zhou. Analysis of university students' behavior based on a fusion k-means clustering algorithm. *Applied Sciences*, 10(18), 2020.

[321] Alex Mouapi, Nadir Hakem, and Nahi Kandil. Piezoelectric energy harvesting prediction and efficient management for industrial wireless sensor. *Applied Sciences*, 10, 2020.

[322] Gasim Hayder, Mahmud Iwan Solihin, and Hauwa Mohammed Mustafa. Modelling of river flow using particle swarm optimized cascade-forward neural networks: A case study of kelantan river in malaysia. *Applied Sciences*, 10, 2020.